# Measurement of MAST edge ion temperatures and velocities

Thomas Morgan

PhD

The University of York

Department of Physics

September 2011

# Abstract

A novel experimental method using gas puffing of neutrals to stimulate charge exchange emission has been developed to measure ion temperatures and toroidal rotation velocities in the edge of MAST. This uses cold deuterium gas puffing as the source of neutrals in place of the more usual method of donation from neutral beams. A pre-existing spectroscopy system with 60 toroidal chords with spatial resolution of 1.5 mm and temporal resolution of 10 ms was adopted for this purpose. The $C^{6+}(n = 8 \rightarrow 7)$ transition at 5290.5Å was identified as the optimal emission line, while a resonance in the cross section between the $D^0(n = 2)$ and $C^{6+}(n = 8)$ energy levels makes the measurement feasible.

In order to assess the potential of this measurement method a model of the expected performance of the system was created. All important processes in the edge regime were identified and density profiles of electrons, carbon ions and deuterium neutrals were modelled. These were combined to produce a prediction of performance.

The spectrum observed was complicated by molecular deuterium emission and a fitting routine to this complex data was developed and benchmarked. Correction factors were also identified and calculated for the emission line. System improvements were made including a new bandpass filter, gas valve and camera.

Analysis of the measured intensity profiles showed a good response to gas puffing and toroidal velocity and ion temperature results are presented. A large reverse shear in the toroidal rotation is observed close to the separatrix in normal operation, but not in counter-rotation experiments. This is attributed to parallel Pfirsch-Schlüter flow. The ion temperature results display a large difference between ion and electron temperature in the pedestal region in many H-mode discharges. This is linked to the collisionality of the ions such that flux surface coupling in the banana regime leads to small ion gradients.

# Contents

# List of Figures

# List of Tables

# Acknowledgements

I would like to first of all thank my research supervisor Hendrik Meyer, whose insight and wisdom has been invaluable during the past few years. I would also like to thank my York supervisor Greg Tallents whose encouragement and guidance has been greatly appreciated. I am much indebted to Darren Temple, whose advice and forbearance in the early years was of great use in helping me find my feet at Culham.

A great many people at Culham have been very helpful to me and patiently answered my questions. My admiration and gratitude go out to Neil Conway, Rob Akers, Maarten de Bock, Marco Wisse, Martin O'Mullane, Rory Scanell, Martin Valovic, Andy Kirk, Geoff Cunningham, Sarah Newton, Clive Michael, Stuart Robertson, Nick Hawkes and Manfred von Hellermann. Thanks also to Mike Driscoll and the MAST team for working so hard to get my experiment working again when bits broke. In York my thanks also go to Roddy Vann and Howard Wilson.

There have been many students at Culham without whose help whom I would not have made it through. Thanks to Simon Freethy, Peter Denner, John McCone, Tom O'Gorman, Sarah Elmore and all who have dwelt in the 'Ghetto' for often useful and usually tangential discussions. I owe a debt of thanks particularly to Peter Hill and David Dickinson for teaching me gyrokinetic theory, and to Thijs Versloot, David Moulton, Oliver Ford and Adam Foster for their helpful input. Thanks also to Pete Buxton, Simon Myers and Alex Lampson for making my early days in York an easy transition.

I would like to express my gratitude to my sister and to my parents, for their love and support as well as multiple cups of coffee which got me through at the final stages. Despite both being English graduates they have always supported me in pursuing physics and following my dreams, wherever they have led.

Finally I would like to thank Margreet, who has made the last two years so much fun I can't believe they've flown by. She has been a great sounding board and kept me sane throughout the writing process.

# Chapter 1

# Introduction

## 1.1 Fusion

The world's fossil fuel energy resources are finite and peak production of coal, oil and natural gas are all expected within the $21^{\text{st}}$ century. Furthermore $CO_2$ emissions due to fossil fuels are believed to be driving global warming and a move away from energy production through fossil fuels is a stated goal of most major nations. Renewable energy sources are generally deemed too intermittent and low energy density to produce consistent base load power without future improvements in technology. The other major established source of power, nuclear fission, has the problem of nuclear waste disposal and limited resources of uranium, which will also become depleted over time. The impact of the Fukushima disaster in Japan has also influenced politicians to move away from nuclear fission power in countries such as Germany and its future looks uncertain.

Concurrently humanity's population is growing at an increasing rate and is predicted to peak at $\sim 9$ billion by 2050 [1]. As more of the third world industrialises, the worlds energy demands are likely to increase by 52% by 2035 [2]. There is therefore a demand for alternative sources of energy to keep up with this demand and to supplant other sources as they become unavailable, and fusion offers one of the brightest possibilities.

Fusion works by fusing isotopes of low atomic number elements together through the strong nuclear force. The most promising reaction for the near future is between two isotopes of hydrogen, deuterium ($D$) and tritium ($T$). If these isotopes can be made to overcome their electrostatic repulsion they can fuse together, releasing large amounts of energy with every reaction as mass difference through Einstein's famous equation $E = mc^2$, as

$$D + T \rightarrow He + n + 17.6 \quad \text{MeV} \tag{1.1}$$

The produced helium nucleus (or alpha particle) is stable while the neutrons can cause activation of materials. However, this does not generally produce long lived radioactive isotopes, unlike nuclear fission, and so energy production from fusion would not suffer the same waste disposal issues.

Due to the ratio of their masses and conservation of momentum the helium nucleus receives 3.5 MeV, the neutron receiving 14.1 MeV, and it is the neutron which is generally useful in extracting energy from the process while the helium may provide the heat for the reaction to be sustained. This energy is around three orders of magnitude greater than most chemical reactions, implying a great potential for large quantities of power to be produced from only a small amount of fuel. Deuterium is abundant on Earth as one atom in 6400 in water is deuterium. Tritium is unstable and has a half life of $\sim 12.3$ years [3], but can be produced from lithium. Lithium resources worldwide are estimated at 25.5 million tonnes [4] which would supply world total energy consumption at current rates for $\sim 30,000$ years [5]. If fusion power can be made to reliably work, fusion has the potential to supply the world with its stable base load generation for the foreseeable future.

## 1.2 Tokamaks

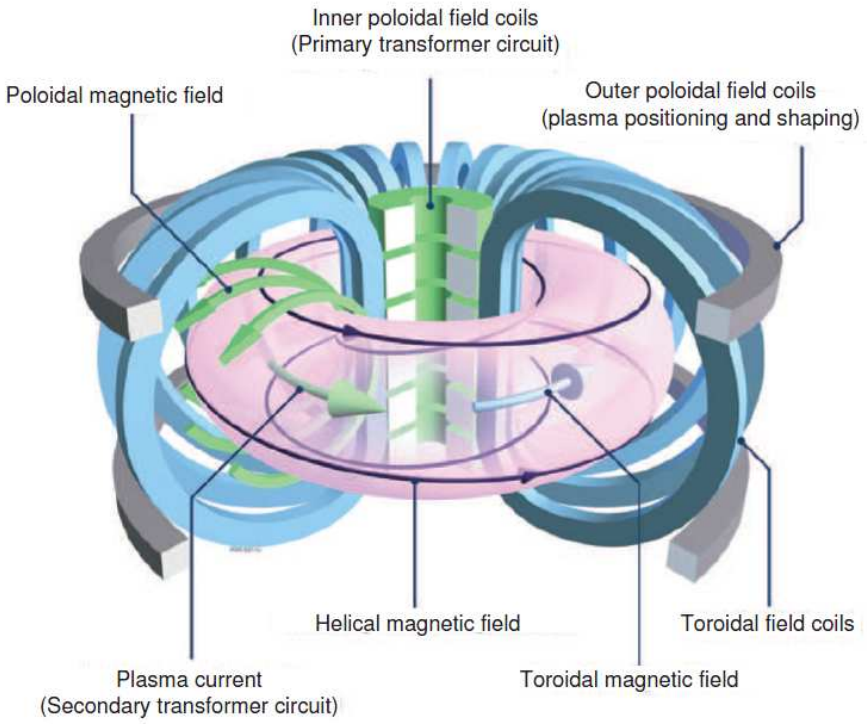


**Figure 1.1:** *Schematic of a tokamak explaining the major components, currents and fields.*

For nuclear fusion to become a reality, a way of sustaining enough fusion reactions to

produce a valuable amount of power must be found. This necessitates overcoming the Coulomb repulsion between the nuclei, which requires giving the particles a large kinetic energy. To give the nuclei enough energy to maximise the cross section for fusion to occur between $D$ and $T$, the gas mixture needs to be heated to approximately $T_i \sim 11$ million K, or $T_i \sim 10$ keV. At these temperatures all electrons are stripped from the atoms through collisions and the gas becomes a plasma.

It is also necessary for enough reactions to take place to maintain a useful energy output so that the energy created through fusion can be used to produce a self-sustaining reaction. Therefore the density of particles $n_i$ must be kept high. A further criteria is that the characteristic time at which energy is lost to the plasma, $\tau_E$ (the energy confinement time) must be maximised so that the energy does not leave the plasma more quickly than it is being produced, which would lead the process to die out without external heating.

For the fusion reaction to be self sustaining it can be summarised by the Lawson criterion that the product of the above three factors must be

$$n_i T_i \tau_E > 5 \times 10^{21} \quad \text{keV} \quad \text{s} \quad \text{m}^{-3} \tag{1.2}$$

One way to maximise this value is to use magnetic fields to confine the plasma so that it does not collide with solid objects which would cause the plasma to cool down. Tokamaks are one such magnetic confinement device.

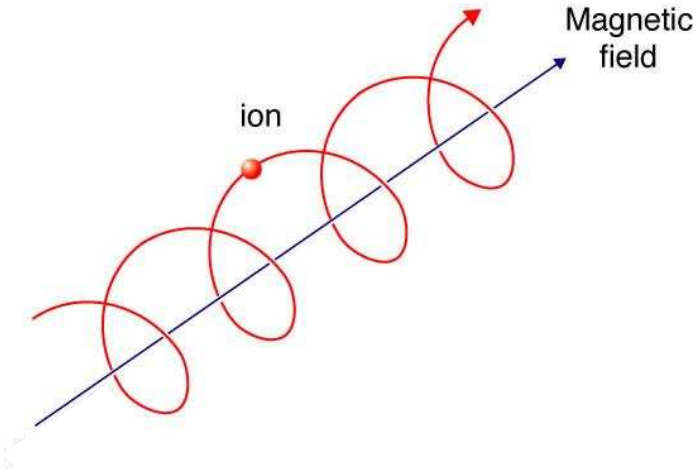


**Figure 1.2:** *Cyclotron motion of an ion about a magnetic field line [6]*

A property of charged particles is that in a magnetic field they will tend to follow field lines. As all particles in the plasma are ionised this can be used to confine the plasma to the field lines. The Lorentz force causes the particles to gyrate around the field line with cyclotron frequency for species $j$ of $\omega_{cj} = (e_j B)/m_j$ and Larmor radius $\rho_L^j = v_\perp/\omega_{cj}$,

where $e_j$ and $m_j$ are the charge and mass respectively of the particle, $B$ the magnetic field strength and $v_\perp = \sqrt{(2k_B T_j)/m_j}$ the perpendicular velocity to the magnetic field.

If the field lines are closed upon themselves in a torus shape then the particles will be confined along the field lines. Cross field diffusion is many orders of magnitude slower than transport along it so the particles are essentially trapped to move along these orbits.

The word tokamak derives from Russian and is an shortening of "Toroidal chamber with magnetizing coils". It consists of a vacuum vessel shaped in a torus, the vacuum removing collisions of the plasma with atmospheric gases which would otherwise cool it. The main confinement arises from toroidal field coils which produce a solenoidal magnetic field which is closed upon itself by the torus shape to form a toroidal field. In plasma physics toroidal refers to the 'long' way around the torus while poloidal refers to the 'short' way.

Confinement by toroidal field alone is not sufficient to hold the plasma. The curvature of the field lines leads to a drift of the ions and electrons in opposite directions towards the top and bottom of the vessel. This sets up an electric field which causes the plasma to move outwards and hit the outer wall of the vessel. To counter this a solenoid in the centre of the vessel induces a toroidal current in the plasma through transformer action (the plasma itself acting as the secondary winding). This has two effects, firstly it heats the plasma through resistive (Ohmic) dissipation, and secondly it creates a magnetic field in the poloidal direction. The sum of the toroidal and poloidal fields is a helical field. This counteracts the curvature drift by redistributing ions and electrons to the top and bottom of the plasma so that the electric field does not arise.

Due to surface area differences between the inside and outside of the plasma a hoop force arises which pushes the plasma outwards towards the walls. To act against this poloidal field coils are added which help to stabilise this and also shape the plasma.

As the current is driven inductively the plasma can only last as long as there is a flux in the transformer. Therefore the tokamak is a pulsed device at present. Methods of non-inductive current drive are being investigated and other toroidal shapes such as stellerators do not require inductive drive, implying that in the future fusion devices can be made at least quasi-constant in power output.

## 1.3 The MAST tokamak

A limiting factor in the development of power generating fusion devices is the ratio of outward plasma pressure to inward magnetic pressure. This ratio is known as $\beta$, defined as

$$\beta = \frac{2\mu_0 \langle p \rangle}{B^2} \tag{1.3}$$

In conventional tokamaks this ratio is generally less than 10% and has a hard limit before the plasma becomes unstable to ballooning modes [7]. Theoretical work [8] suggested that an improvement in confinement could be achieved if the aspect ratio ($A = R_0/a$ is the ratio of major and minor axes) were reduced to below 2. These tokamaks are referred to as spherical tokamaks. The improvement is partly due to high safety factor values ($q$) at the plasma edge in low aspect ratio tokamaks, which means the particles spend a long time in the 'good' confinement region of the plasma, which is close to the centre column of the plasma (see figure 1.3). This improves the stability of MHD modes in the plasma [9].

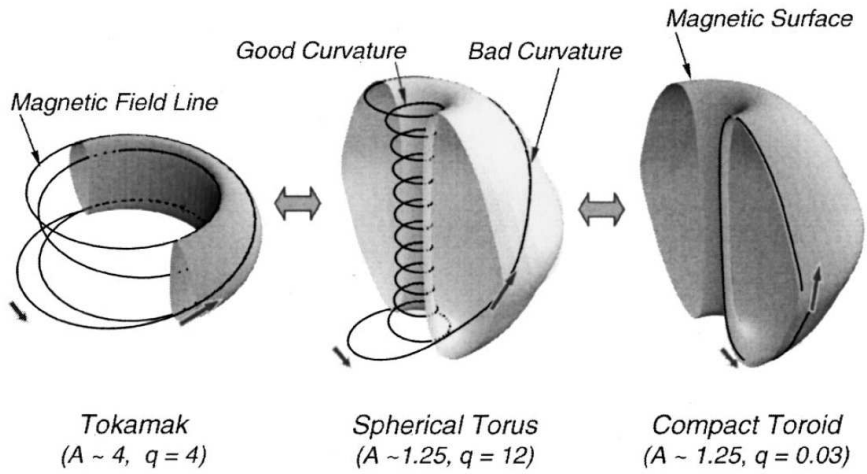


**Figure 1.3:** *Magnetic configuration of conventional tokamaks and spherical tokamaks. Ions and electrons follow the field lines around the tokamak, and therefore in spherical tokamaks the particles spend more time close to the centre column, in the region of good curvature. From Peng (2000) [9]*

Spherical tokamaks are characterised by increased natural elongation and triangularity (which also improves stability) and higher bootstrap current resulting in smaller requirements to externally (inductively) drive current in the plasma [10]. As they are compact they are cheaper to construct and run than conventional tokamaks of similar size, magnetic field and plasma current.

The compact shape produced by removing as much material as possible from the centre of the machine also means that the plasma is closer to the centre column and that the plasma feels a greater magnetic field produced by the toroidal field coils for a given nominal value of magnetic field produced, than would be experienced in conventional tokamaks. This results in higher $\beta$ values in spherical tokamaks than could be achieved otherwise. The START (Small Tight Aspect Ratio Tokamak) tokamak [11] was constructed at Culham, UK, to test the spherical tokamak concept and achieved $\beta$ values of 40% [12], around 4 times higher than in conventional tokamaks. This small machine was operational between

1991 and 1998. Typical parameters are shown in table 1.1.

| Tokamak | $A$ | $R_0$ (m) | $B_\phi$ (T) | $I_p$ (kA) | $t$ (ms) | $T_e(0)$ (eV) |
|---|---|---|---|---|---|---|
| START | 1.25 | 0.32 | 0.5 | 310 | 40 | $\sim 500$ |
| MAST | 1.4 | 0.85 | 0.6 | 1300 | $< 1000$ | $\sim 2500$ |
| NSTX | 1.4 | 0.85 | 0.6 | 1400 | $< 1600$ | $\sim 2000$ |

**Table 1.1:** *Plasma parameters of important spherical tokamaks, from left to right aspect ratio, major radius, vacuum toroidal field, plasma current, pulse length and typical core electron temperature.*

The success of this experiment lead to the construction of two larger spherical tokamaks: NSTX (National Spherical Tokamak eXperiment) [13, 14], based at Princeton Plasma Physics Laboratory, USA, and MAST (Mega-Ampere Spherical Tokamak) [15–18], based at Culham, UK, both of which have been in operation since 1999. Their parameters are listed above. The two tokamaks are the two largest spherical tokamaks currently in the world, and often co-operate in mutually beneficial areas of research as their main parameters are broadly similar (see table 1.1).

In MAST the toroidal field in the plasma is generated by 24 field coils in 12 pairs which surround the vacuum vessel wall and form a closed loop through the plasma centre column. A solenoid running through this column drives startup and induces toroidal current in the plasma. The main sources of heating in MAST are through Ohmic heating and approximately 5 MW of heating from two JET style PINI (Positive Ion Neutral Injection) neutral beams [18] injected with accelerator energies between 65 and 75 kV. The machine contains two divertors located at the top and bottom of the machine. This allows operation in several different divertor configurations: as single null operation using predominantly only the top or bottom divertor or both divertors in a double null configuration operation with two X-points at the top and bottom of the plasma. In normal operational mode the ion $\nabla B$ drift is towards the lower divertor.

The MAST tokamak is contained within a vacuum vessel $\sim 4.4$ m in height with a radius of $\sim 2$ m. The large vessel allows the poloidal field coils to be located within the MAST vessel close to the plasma. As the plasma only occupies around 20% of the interior volume of the plasma vessel this also allows a level of access for diagnostics which is unparalleled by most other tokamaks in the world. Apart from the ECELESTE diagnostic discussed in detail in this thesis the most important diagnostics used during this research include a 130 chord ND:Yag Thomson scattering system producing measurements of $T_e$ and $n_e$ with a spatial resolution of $\sim 1$ cm and time resolution of 4 ms in normal operation [20], and a

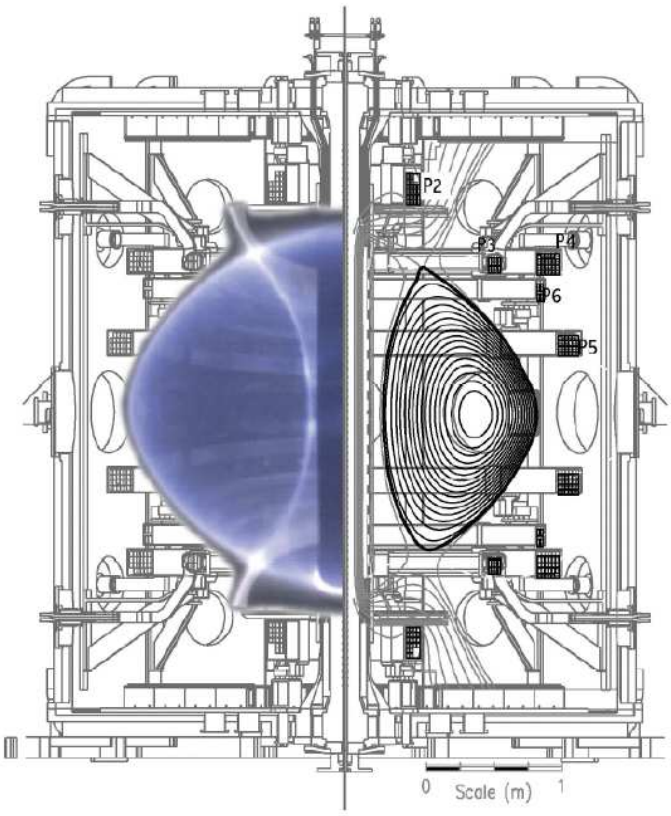


**Figure 1.4:** *A schematic showing the structure and dimensions of the MAST tokamak. The left hand side shows a superimposed image of $D_\beta$ emission while the right shows lines of constant poloidal magnetic field. From Temple (2010) [19].*

core charge exchange spectroscopy system which will be described in more detail in section 1.5.

## 1.4 The plasma edge

The edge of the plasma refers here to the last 5 to 10 cm inside the last closed flux surface (LCFS) in the MAST plasma. This region interacts both with the scrape-off layer (SOL) and the inner region of the plasma. In the SOL open field lines carry hot ions and electrons from the plasma to the divertor while neutrals and impurities enter across the separatrix (flux surface containing the X-point[1]) into the plasma and become ionised. The majority of visible emission from the plasma occurs from this thin layer. Compared to the core the temperatures are cool and densities low requiring consideration of different processes than are important compared to the hot core. The region is a transition from core processes and SOL processes.

[1]in MAST the terms LCFS and separatrix can generally be used interchangeably

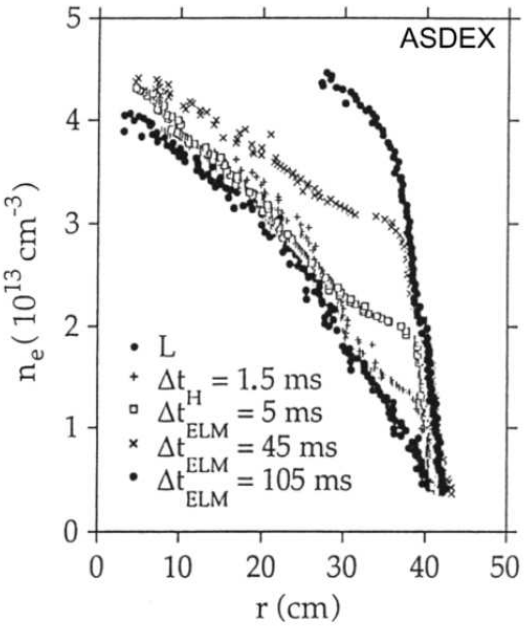


**Figure 1.5:** *Evolution of the electron density in the edge of the ASDEX tokamak during a transition from L-mode to H-mode showing the development of the pedestal gradient. Recovery after ELM emission proceeds with a similar increase in the gradient over time. From Manso (1993) [21].*

Plasmas can be divided into two main confinement regimes. In 1982 a regime of improved confinement was discovered in the ASDEX tokamak [22] which improved the confinement time $\tau_E$ by a factor $\sim 2$. This mode was designated the High-confinement mode or H-mode, plasmas not displaying this improvement are now denoted as Low-confinement (or L-mode) or Ohmic dependent upon whether they are heated by neutral beams. The difference in these cases is that the L-mode has lower confinement than Ohmic plasmas as the neutral beam heating drives turbulence. H-mode has since been observed on many other tokamaks including spherical tokamaks and stellerators, indicating this is a general phenomena of toroidal plasma devices. It appears to require a threshold heating level to enter and is characterised by formation of a transport barrier in the form of a pedestal (region of steep gradient) in the pressure at the plasma edge (see figure 1.5) and a large reduction in turbulence in the same region. The formation of the edge transport barrier and transition to H-mode confinement is still a subject of study but the most widely accepted explanation involves turbulence suppression through sheared poloidal flows in the plasma edge [23].

A feature of the H-mode is an MHD (Magneto-HydroDynamic) instability called the Edge Localised Mode (ELM). These are characterised as a rapid expulsion of plasma material and a collapse of the edge pedestal. The pedestal gradient recovers and steepens until

another expulsion occurs, producing a periodic cycle of ELM events. These are believed to be driven by MHD peeling-ballooning modes [24].

For a machine the size of MAST ELMs are not a serious problem in terms of damage. However the next generation tokamak, ITER, which is currently under construction in Caderache, France, will be $\sim 8$ times the volume of JET, the largest tokamak now in existence. In a large future tokamak device such as ITER the energy expelled by the plasma during ELMs could be sufficient to quickly damage the wall materials unless ELMs can be controlled [25]. Understanding edge pedestal physics will play a crucial role in controlling ELMs and mitigating their effects, as well as maximising the tokamak performance in the H-mode to ensure the confinement requirements for net fusion power can be realised. Ion temperatures are an important component of the pressure, so a good diagnostic measurement of these temperatures is important in understanding the plasma edge. Similarly ion toroidal velocities play a role in flow shear transport suppression, locked modes and ELM control via RMP's (Resonant Magnetic Perturbations) [26]. Therefore detailed diagnosis in the plasma edge of these values is of great interest.

## 1.5 Charge Exchange Recombination Spectroscopy

Since its inception in the 1970's charge exchange recombination spectroscopy (CXRS) using neutral beams has been developed into a widely used and reliable diagnostic technique in tokamaks around the world. It was originally put to use in determining impurity densities [27, 28]. However, it quickly became widely used in determining ion temperatures [29, 30] and rotational velocities [31, 32] where it has become the most reliable tool in detecting these quantities [33] and a CXRS system has been installed for these purposes in many modern tokamaks [34–40].

Temperatures and velocities can generally be inferred from Doppler spectroscopy of gases and plasmas which are in thermodynamic equilibrium and thus possess a Maxwellian distribution of energies. This requires spectroscopic emission from the observation location to provide information about the energy distribution however. If impurities have a long enough lifetime in the plasma they will become equilibrated with the bulk ions (generally deuterium in most fusion experiments) so that one can infer the bulk (majority) ion temperature from them, which is normally the quantity of more interest (due to mass differences bulk rotation speeds cannot necessarily be inferred as readily from impurity rotation however). The centre of tokamak plasmas are generally so hot that all low Z impurities are fully ionized and so do not produce spectral emission. High $Z$ impurities are generally not fully ionized, but tend to emit at ultraviolet wavelengths and below where inferring

temperatures and velocities is more difficult and where the spectra themselves are harder to measure and require vacuum lines of sight which are more complex and expensive [33]. Emission from low-$Z$ hydrogen-like impurities on the other hand is typically in the visible spectrum which is far more convenient to use for spectroscopic purposes. Therefore if fully ionised low-$Z$ impurities can become hydrogen-like by gaining an electron this provides a way to gain information about ions in the core.

Neutral beams are used as a heating source on many tokamaks including MAST. Essentially these are collimated beams of neutral atoms produced via breakdown of source gas on filaments, acceleration via grids to energies between 10 keV and 100 keV, followed by neutralisation through a second tank of gas, where some ions receive an electron and become neutralised. The fraction which does not is diverted into a beam dump using a bend magnet, while the rest enters the plasma. As the particles are neutral they are not influenced by the strong magnetic fields in the plasma, allowing them to enter the core of the plasma where the heating is most effective. As the neutrals become ionised they impart both heating and torque (if, as is usual, orientated at an angle with a tangent to the plasma) as they are designed to be of higher energy than the temperature of the ions in the core. The neutral beams are most commonly composed of deuterium, although diagnostic beams of other species have been implemented [38]. Neutral beams provide a means of donating electrons to these hot impurities as they can penetrate to the core, producing emission which is localised at the beam location.

Neutrals also penetrate the plasma from gas present at the plasma edge, fueling from gas valves, and recycling from the walls. In all cases charge exchange between a neutral donor and an ionised receiver proceeds in the same way. The neutral atom $D$ donates an electron to the receiver $R$ through collisions via

$$D^0 + R^{Z+} \rightarrow D^+ + R^{(Z-1)+*}. \tag{1.4}$$

This process generally does not greatly perturb the state of the receiver due to the mass difference between the ion and the donated electron, so its energy is not greatly disturbed. This allows us to assume that the state of the receiving ion after the charge exchange process is a reflective sampling of the entire population.

Generally the electron will transfer into an excited state and then cascade down to the ground state through emission of photons, i.e.

$$R^{(Z-1)+*} \rightarrow R^{(Z-1)+} + \gamma \tag{1.5}$$

By observing these photons from a given spatial location they can tell us the temper-

ature and velocity of the emitting particles if the spectrum is examined by processing the light via a spectrometer. These photons will have a Doppler broadened distribution due to the Maxwellian distribution of energies such that the distribution function for a species $j$ is given by

$$P_j(\lambda)\mathrm{d}\lambda = \sqrt{\frac{m_j c^2}{2\pi k_B T_j}}\exp\left(-\frac{m_j c^2\left(\lambda-\lambda_S\right)^2}{2k_B T\lambda_0^2}\right)\mathrm{d}\lambda \tag{1.6}$$

where $\lambda_0$ is the natural (rest) wavelength of the photon and $\lambda_S$ the observed central wavelength due to the Doppler effect from net rotation either towards or away from the point of observation. By fitting a Gaussian function to the emission

$$f(x) = A\exp\left(-\frac{(x-x_0)^2}{2\sigma^2}\right) + c \tag{1.7}$$

we can equate $x_0 = \lambda_S$ as the centrum of the Gaussian and $\sigma = \sqrt{(k_b T_j \lambda_0^2)/(m_j c^2)}$ as the standard deviation of the Gaussian, $A = (m_j c^2)(2\pi k_B T_j)$ being the amplitude of the emission, while $c$ is the baseline.

The velocity $v$ can be inferred from $\lambda_S$ as

$$\frac{\lambda_S}{\lambda_0} = \sqrt{\frac{1+v/c}{1-v/c}} \tag{1.8}$$

In the non-relativistic limit (which is generally true for ion rotations, which are of the order $10^5$ m s$^{-1}$ in MAST) we can use the binomial theorem to simplify this expression as

$$\sqrt{1\pm\frac{v}{c}} \approx 1 \pm \frac{1}{2}\frac{v}{c} \tag{1.9}$$

where rearranging and assuming $\lambda_S \approx \lambda_0$ the rotational velocity can be determined as

$$v \approx c\left(1-\frac{\lambda_S}{\lambda_0}\right). \tag{1.10}$$

The temperatures can simply be inferred from the standard deviation of the fitted Gaussian i.e.

$$k_B T_j = \frac{\sigma^2}{\lambda_0^2} m_j c^2. \tag{1.11}$$

While in principle simple the measurements are complicated by a variety of factors. Firstly the line emission selected must have a great enough intensity to be observed, which depends on the distribution of neutrals and receiving ions in the plasma, as well as the rate coefficients for charge exchange between the two species. Furthermore there are several background processes which can complicate the observed emission as well as reducing

the signal to background ratio. This requires a solid understanding of the atomic physics involved as well as modelling of the population and distribution within the plasma of all relevant species. Furthermore, there are factors which distort the lineshape from a Gaussian, such as the instrument function of the measurement system, fine structure broadening etc, which must be corrected for. Therefore determination of true values of ion temperature and velocity requires maximising the signal received due to active stimulation as well as fully understanding all background processes, as well as isolating the Doppler broadening from other factors. This will be discussed in chapter 3.

## 1.6 Motivation for using ECELESTE to produce ion temperatures and velocities

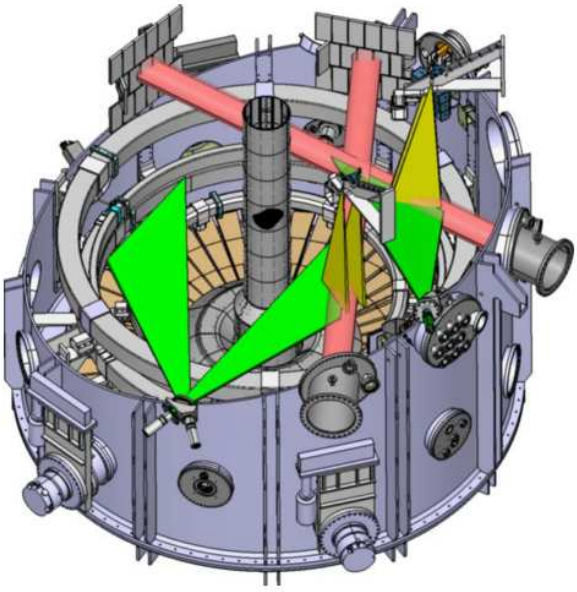

**Figure 1.6:** *A schematic showing the core CXRS system in the MAST tokamak. The heating beams are depicted as pink, the green views are toroidal chords while the yellow views are poloidal chords. From Conway et. al. (2006) [40].*

As discussed in section 1.5, charge-exchange recombination spectroscopy (CXRS) has a long and successful history in plasma diagnostics. On MAST the core ion temperature and velocities have been measured via CXRS utilising the neutral beams using the spectrometer CELESTE-3 [40]. In summary the CELESTE-3 system consists of two toroidal views, each with 64 chords,one viewing across each beam, plus a toroidal view for background of 28 chords. In the poloidal direction it has two sets of views for each beam, each with 32 chords, 16 of which sample background and 16 of which sample the beam. A summary is shown in

figure 1.6. Overall it has a spectral resolution of $\sim 1$ cm and a time resolution of 5 ms [40]. This provides high quality ion temperature ($T_i$) and velocity measurements in the toroidal ($v_\phi$) and poloidal directions ($v_\theta$) in the plasma core in scenarios where the beam is on.

It is desirable to know the edge ion temperatures and toroidal velocities across the pedestal region of the plasma (see section 1.4). The ECELESTE system used in this thesis is an edge spectroscopy system, at the commencement of this thesis used for measuring the radial electric field ($E_R$) [41]. It consists of 64 viewing chords in poloidal and toroidal directions (although in this thesis only 60 of the toroidal chords were used and none of the poloidal chords). A more detailed description is given in chapter 2. While the core charge exchange system covers the entire plasma radius with a 1 cm radial resolution the ECELESTE system is focused solely on the plasma edge, covering approximately the last 10 cm inside the separatrix with a maximum radial resolution of $\sim 1.5$ mm. This allows detailed examination of the edge region which should be complementary to the core CXRS system by investigating here in much more detail than would be available otherwise.

The edge region of the plasma is an area of transition between the cool temperature behaviour of the scrape-off layer (SOL) and the hot temperature behaviour of the core, often incorporating steep gradients which affect the entire interior due to the pedestal in H-mode. The electron temperatures and densities are reliably diagnosed with very high spatial and temporal resolution by a Thomson scattering system which covers the plasma over its entire extent, including the scrape off layer [20]. At the plasma edge electron temperatures (and densities) generally display a pedestal (a region of steep gradient) during H-mode which is usually between 5 and 20 mm in width [42]. It is possible that an ion temperature pedestal gradient exists on a similar length scale to the electrons. If this is the case then this will not be studied in detail by the beam based system as the radial resolution is $\sim 10$ mm. The ECELESTE system has a maximum radial resolution of $\sim 1.5$ mm covering the outer $\sim 10$ cm of the plasma so any pedestal in the ions will be well diagnosed.

In the edge region the CELESTE-3 system also has drawbacks which it was hoped the ECELESTE system could be adapted to compensate for. Firstly without the beams no information is available. Secondly the system often gives spurious results in its outermost chords. This can be at least partially attributed large instrument function of the CELESTE-3 diagnostic, which is around 400 eV [43], as well as a large background of passive charge exchange emission caused by neutral influx into the plasma which locally complicates the total signal and can dominate over the emission due to the beam.

In order for spatially localised measurements in the plasma edge to be made by ECELESTE, a source of neutrals that would stimulate charge exchange emission was required.

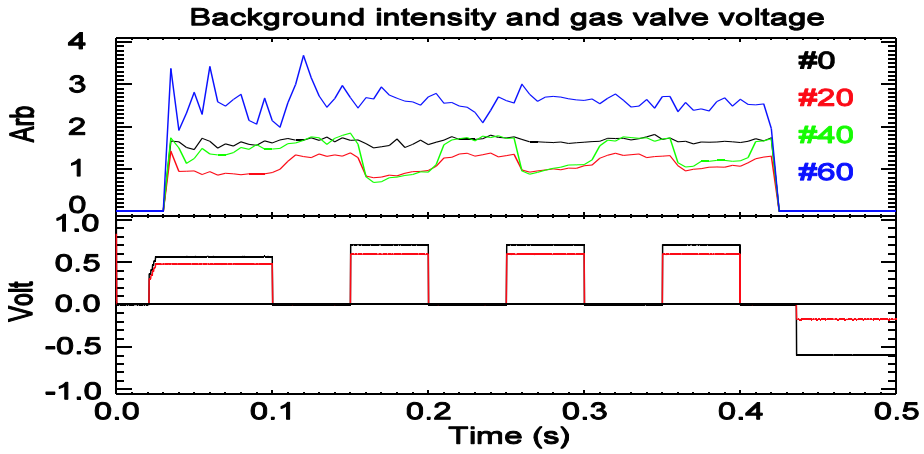


**Figure 1.7:** *(top) Recorded background emission intensity as a function of time for several toroidal background viewing chords showing that turning gas puffing on and off directly stimulates charge exchange emission. (bottom) Gas puff signal voltage, where zero indicates gas puffing on [44]*

The ECELESTE system focuses at a location where gas can be puffed into the system from an injection nozzle HELIOS, so if a suitable gas were to be identified this could be delivered locally. It was noted during 2007 that gas puffing affected some of the toroidal background viewing chords [44] (see figure 1.7) which indicated that neutral deuterium which was fueling the plasma was also stimulating charge exchange emission in the edge, which was being picked up by these lines of sight. While problematic for the core CXRS system as it affected the background subtraction process, this indicated a way to produce localised charge exchange emission without neutral beams in the edge of the plasma. By locally injecting cold neutral deuterium at the location observed by the ECELESTE viewing chords, this produces an additional source of neutrals, locally boosting the 'passive' emission observed as background by the core CXRS system. This additionally added perturbation can boost the signal and can then be subtracted from the remaining passive emission.

## 1.7 Thesis summary

The method of measuring ion temperatures and velocities at the edge of the MAST tokamak involved modifying the setup of the ECELESTE system and the HELIOS nozzle used to inject the neutrals. An overview of the system is made and its capabilities assessed in chapter 2.

Edge CXRS diagnostics have generally used neutral beams to provide the neutrals [38, 39, 45], combined with a dedicated edge spectroscopy system. Measurements of poloidal rotation and ion temperature at the high field side of the C-Mod tokamak have recently been produced using neutral deuterium gas puffing charge exchange with $B^{5+}$ [46],[45]

while measurements of electron temperatures and densities using helium gas puffing at the low field side edge of MAST has also been performed [47]. To the knowledge of the author however, measuring ion temperatures and toroidal velocities through CXRS at the low field side plasma edge using gas puffing as a neutrals source has not previously been presented in literature. This is also the first measurement of this kind to be made in spherical tokamaks and the radial resolution of the ECELESTE system is much higher than that available at C-Mod allowing greater insight.

The processes involved in producing charge exchange in this regime are quite different from those involving neutral beams due to the large energy difference between cold neutral deuterium with an energy of a few eV from gas puffing and hot neutral beams with energies of tens of keV. Therefore, it was necessary to investigate fully the processes involved in charge exchange in this regime to assess the feasibility of the technique. This is discussed in detail in chapter 3 where identification of a suitable line of sufficient intensity was the first priority. All rate coefficients of relevant processes were then collated or calculated in this regime and the contribution of background processes is assessed. Collisional radiative modelling of the deuterium energy level population was made to asses each level's contribution to the emission. The expected radial density profiles of electrons, deuterium neutrals and carbon ions are discussed and where required modelled. A model of the gas puff penetration and collimation was also made. From this an expected performance of the ECELESTE system in terms of active to background signal ratio is determined for both H-mode and L-mode scenarios.

In chapter 4 the complex spectra recorded are examined and complicating emission from molecular deuterium is identified. The development of a fitting routine capable of fitting to this complex edge spectra is discussed and benchmarked against simulated data. Identification of all corrections to the data from line distorting factors is made and the size of their influence assessed. Where necessary the correction factor has been calculated. An assessment is made of all uncertainties in the results for velocities and temperatures as well as radial uncertainties.

In chapter 5 the performance of the gas puffing in producing active spectra is assessed as well as the limitations of the system. Improvements to the ECELESTE system are also discussed. The author's contribution to the hardware upgrades in these cases was the full design and purchase of a bandpass filter, the physics basis for a gas valve located in the HELIOS nozzle head and assisting in commissioning two new CCD cameras, but in each case the impact of the upgrades are discussed and results of the improvement presented where available.

Finally in chapter 6 typical results for toroidal velocities and ion temperatures are presented. In the velocity results a large reverse shear in the flow close to the separatrix is observed and possible explanations for this behaviour are investigated. In the case of the ion temperatures a large discrepancy between ion and electron temperatures is observed in the pedestal region in some H-mode shots. The causes of this are also investigated. In the case of the velocity shear this is attributed to parallel Pfirsch-Schlüter flow while for the temperature results this is linked to the collisionality and suggested to be due to flux surface coupling in the banana regime limiting the ion temperature gradient in the pedestal region. The impact that this has upon the scrape off layer is also considered, and the results found to be compatible with expectations.

# Chapter 2

# The ECELESTE system

## 2.1 Introduction

The work of this thesis centres around the observation of visible spectral emission arising from charge exchange at the MAST plasma edge, caused by the deliberate introduction of neutral gas. This chapter will describe the ECELESTE spectrometer used to record these spectra, as well as the HELIOS nozzle used to deliver the gas puff. Collectively these are designated the ECELESTE system. An overview of the system is described below, while a more detailed description of the main components follows this. Description of calibrations and systematic improvements made are given in Appendix C and section 5.4.

## 2.2 ECELESTE overview

The ECELESTE spectrometer was originally used as part of the COMPASS-D tokamak, when it was called CELESTE ('Charge Exchange Light Emission Spectroscopy for Temperature Evaluation') and used to determine core ion temperatures $T_i$, as well as toroidal and poloidal plasma rotation velocities $v_\phi^i$ and $v_\theta^i$ [48]. It was later adapted into a combined diagnostic with HELIOS (see below) called HELCEL to measure the radial electric field $E_R$ [49]. Following COMPASS-D's decommissioning and the construction of MAST, the spectrometer was removed and installed with adaptations as an edge diagnostic ('Edge-CELESTE'). Originally the set-up was used to determine the edge radial electric field $E_R$ using helium injection at the plasma edge [41], but this work returns the system to the purpose of determining $T_i$ and $v_\phi^i$.

The HELIOS gas puff nozzle was also part of a COMPASS-D diagnostic (HELIOS, 'HELium Injection and Optical Spectroscopy') [50], originally used to determine $T_e$ and $n_e$ via line intensity ratios of He I injected via the nozzle. Again the nozzle was fitted to

MAST and re-purposed to provide impurity injections, although the rest of the HELIOS system was not retained.

The HELIOS nozzle delivers a puff of cold impurity gas (in this case deuterium) to the plasma at the outer midplane. The subsequent emission is collected by two lenses, at poloidal and toroidal viewing locations (although the poloidal views have not been used in this study). Light collected by the lenses is fed into optical fibre bundles which transfer the light via a patch panel to a lens at the entrance of a Czerny-Turner spectrometer. This lens focuses the light into the spectrometer through an entrance slit array, which is optimised to provide good spectral resolution. The spectrometer splits the light into spectra with a 2400 lines/mm grating which are then coupled through a de-magnifying lens into a CCD camera. This records the dispersed light intensity as a digital signal and sends the output to a computer, where the signal is processed. An overview is shown in figure 2.1 [19]

### 2.2.1 The HELIOS nozzle

The nozzle system consists of a gas supply, a plenum, a pipe connection and a nozzle head at the plasma edge. The gas supply is introduced into the plenum prior to a plasma shot, the species of which can be changed from shot to shot. The plenum has a volume of around 3 litres, which is more than sufficient to supply gas with no discernible loss of pressure over the duration of the discharge. The supply of gas is controlled by a series of high volume fast acting piezoelectric valves the last of which is located approximately 1.5 m from the nozzle, and which are rated to approximately 1.5 bar (which is the limiting factor for the pressure in the system). When the piezoelectric valve is activated the gas flows along a 1.5 m section of 4.72 mm internal diameter pipe to the end of the nozzle and into the plasma. The nozzle head is boron-nitride which has a high heat capacity to protect the steel pipe from plasma interaction. The head also contains ceramic breaks to prevent currents propagating in the nozzle.

In order to get a high level of localization the nozzle needs to be located within a few cm of the plasma separatrix. However, the plasma radius can vary widely between 1.3 m and 1.6 m. Moreover, the whole system needs to be retractable outside the vessel wall and gate valve for testing and in order to allow conditioning of the MAST vacuum vessel. Therefore the entire nozzle can be driven with an accuracy of $\pm 1$ mm radially away from and towards the plasma between shots via a stepping motor over a range of -0.05 to 1 m from the vacuum vessel wall.

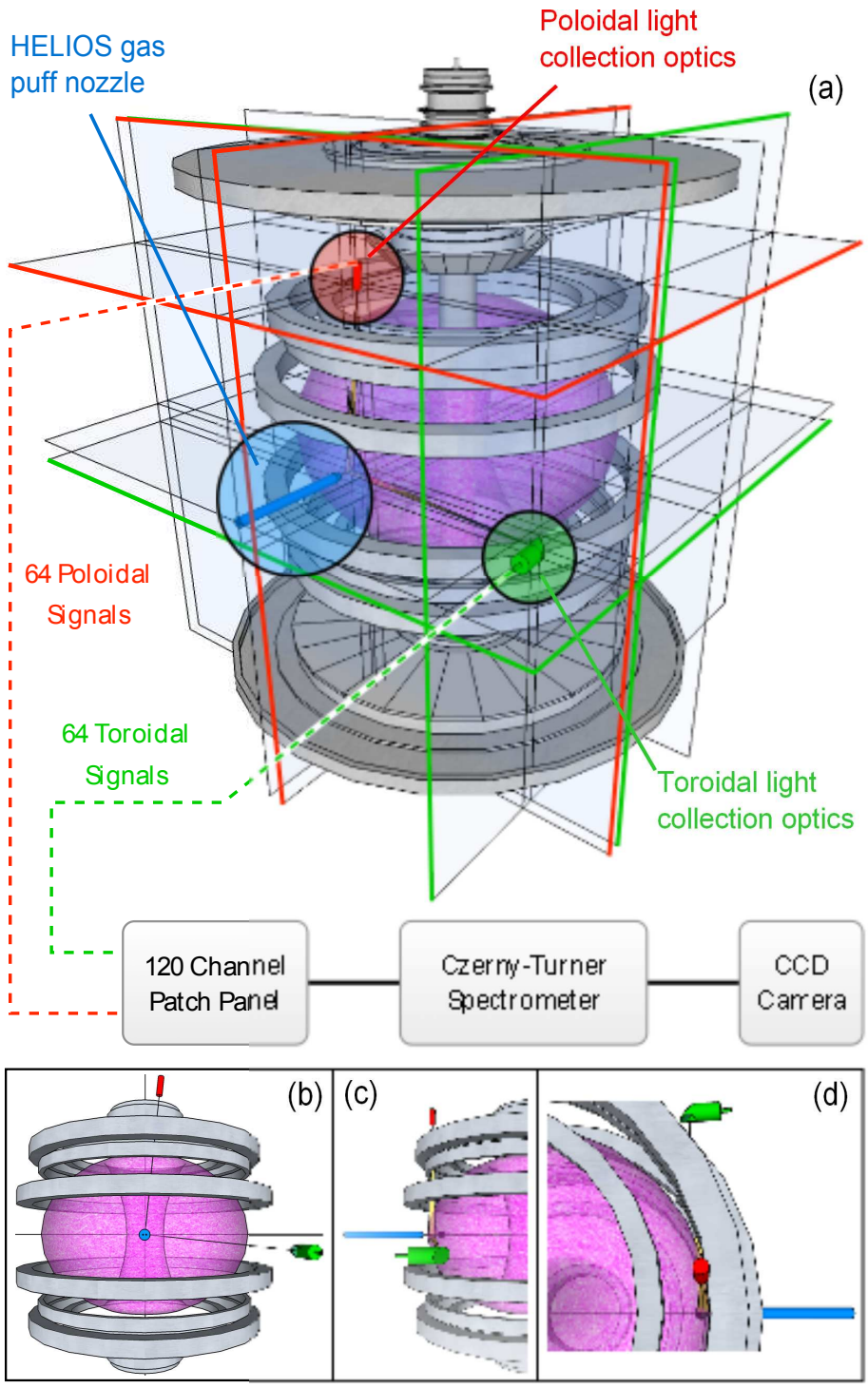


**Figure 2.1:** *(a) An overview of the ECELESTE system showing the position of the HELIOS nozzle (blue), the positions of the poloidal (red) and toroidal (green) collection optics and a schematic of the rest of the system. (b) view from behind the HELIOS nozzle (c) view from the toroidal optics location (d) view from the poloidal optics location indicating the relative positioning of these components [19]*

### 2.2.2 ECELESTE collection optics and fibres

The ECELESTE spectrometer system consists of two sets of viewing optics, one at a poloidal viewing location located on a strut looking down from the top of the vessel, and one at a toroidal location looking through a window near the midplane of the vessel, looking tangentially at the end of the HELIOS nozzle (see figure 2.1). Each set of optics consists of 64 viewing chords covering approximately a 10 cm radial extent.

The poloidal optics are an $f/7$ custom built lens, while the toroidal optics are an $f/2$ off the shelf Canon camera lens, which looks into the plasma via a mirror. Therefore due to its smaller aperture the poloidal signal is much weaker as the lens couples much less light into the system. Due to the width of the Doppler broadened spectral images in this experiment it was not possible to accommodate both sets of poloidal and toroidal spectra on the CCD[1] and so in order to maximise the signal strength and spatial resolution only the toroidal fibres were connected to the spectrometer. Therefore, while in theory poloidal rotation $v_\theta^i$ could be determined using this technique it has not been determined during this investigation and for the purposes of this thesis the poloidal system can be ignored.

The toroidal optics can be moved between shots using a micrometer to view different parts of the plasma edge in order to study particularly large or small plasmas, which is an additional advantage as the poloidal view is fixed. However, as the MAST machine area (the area inside the radiological safety wall) is closed during operations this is typically only possible at the start or end of a day, not on an ad-hoc basis.

To provide easy access the spectrometer is located outside of the machine area and requires a fibre optic feed from the collection optics to the spectrometer. This allows a more flexible set-up by permitting changes to the fibre alignments to the spectrometer outside the machine area, and makes the system easier to maintain. A direct relay inside the machine area would also not permit 120 chords in the way a fibre optic array allows. The disadvantage of this is attenuation of the signal along the fibre of approximately -20 dB $km^{-1}$. Over the 32 m of fibre optic cable this equates to $\sim 86\%$ transmission so this is not a significant issue.

Instead of a single fibre for each toroidal chord, each view consists of a three fibre array aligned to have the same radial location, but spaced vertically over a region of $\sim 1.5$ cm. This allows for finer radial and spatial resolution by using thinner fibres while maintaining the same etendue. At the outer midplane edge flux surfaces are approximately vertically aligned. As gradients in temperature and velocity in the direction of the magnetic field are

[1] This is not true when measuring helium spectra in $E_R$ experiments, as the helium does not equilibrate and so has less broadening

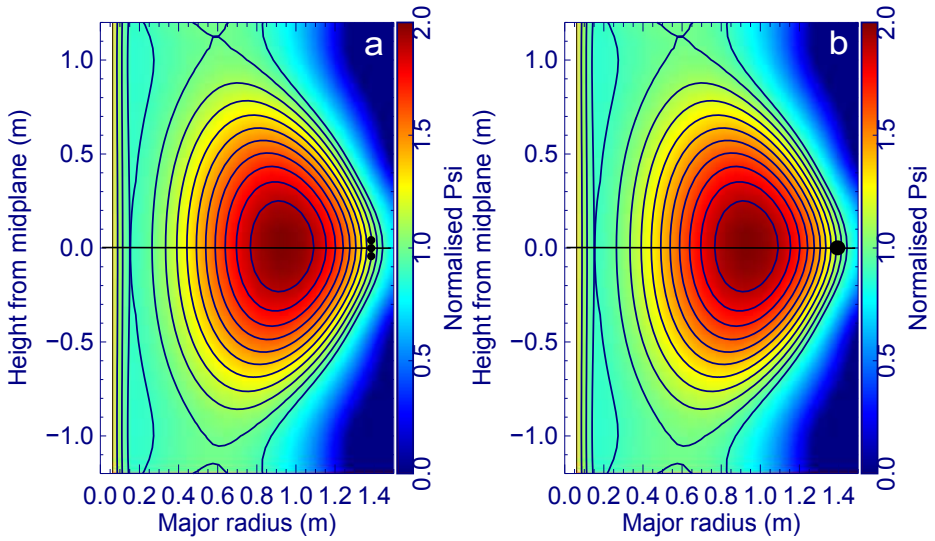


**Figure 2.2:** *An improvement of spatial and radial resolution due to using an array of fibres (a) rather than a single fibre (b) arises due to each chord cutting fewer flux surfaces, while maintaining the same etendue.*

much smaller than those in the radial direction, by sampling from regions of approximately constant poloidal field a more representative sample of the nominal position observed by the chord is recorded than for a chord with greater radial width. The spacing of the fibres in this manner consequently covers fewer flux surfaces than a single circular cross section collecting the same amount of light would do (see figure 2.2). The three fibres are then bundled into a single fibre (see figure 2.3) and can be treated as a single source at the spectrometer.

The focal spot size diameter of each of the toroidal optics is 3.0 mm. As the radial range of the viewing chords is $\sim$ 10 cm this means the maximum radial resolution[2] possible under ideal conditions is $\sim$ 1.5 mm, so the fibres are mounted in six rows to avoid overlapping. Although the spots are focused at the gas puffing location each viewing chord can be closely approximated as a long cylinder of diameter 3 mm as the focal plane is 1.73 m from the optics' location and so almost focused at infinity. This means that the amount of background light detected along the line of sight in regions far from the gas puffing position is minimised due to the narrow field of view, compared to an optic focused on that position from a closer location (as the volume of background enclosed by the line of sight would be larger). By focusing at the gas puffing location rather than actually at infinity however the spatial localisation is maximised at that position.

[2]Radial resolution refers to the accuracy of positioning of individual chords with respect to one another and the overall geometry of the plasma while spatial resolution refers to the spread in possible positions of each chord

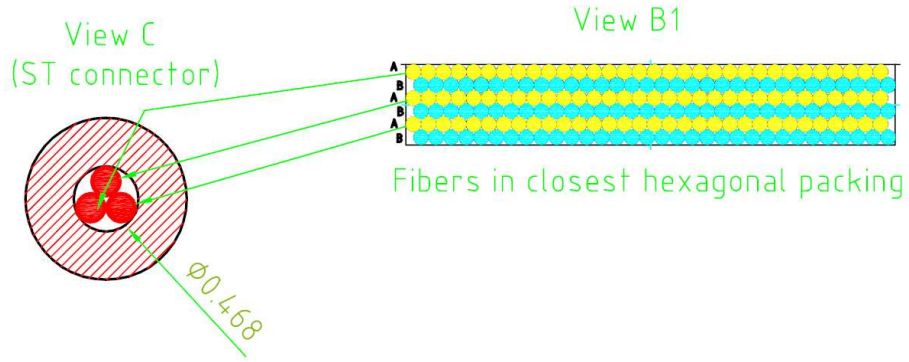


**Figure 2.3:** *The design of the toroidal fibres showing the arrangement of the fibres as they receive light from the plasma behind the collection optics (right) and how they are packed into a single fibre during transmission to the spectrometer (left)*

The system also contains a view located at the midplane but located toroidally around from the gas puffing location looking radially into the plasma. As radial velocities are much smaller compared to poloidal or toroidal velocities this signal essentially provides a measure of the unshifted signal as a zero-point for the velocity measurements, as well as a measure of changes to the background signal level while the gas puffing is activated.

Between the fibres from the tokamak and the spectrometer there is a patch panel consisting of 120 fibre to fibre connections which allows the inputs to the spectrometer to be reconfigured. As measurements of $E_R$ were also being made using the same system [19, 41] this allowed easy reconfiguration to take place without having to change the inputs at the spectrometer entrance which could misalign the fibres to the entrance slits and grating.

### 2.2.3 The spectrometer

The light from the fibres is focused onto a set of entrance slits via an input lens (see figure 2.4 [51]). The slit set consists of ten 400 $\mu m$ vertical slits each of which accommodates twelve fibres to produce a possible $10 \times 12$ array. Due to the width of the broadened spectra however, only every other fibre was connected to produce a $5 \times 12$ 'chequerboard' array. As this is less than the number of usable toroidal chords (64) typically five chords (to also accommodate the radial chord) viewing at the inner radius are not connected, halving the radial resolution at that point.

The spectrometer is a 1m Monospek 1000 Czerny-Turner spectrometer manufactured by Hilger Analytical. It consists of two 10cm diameter toroidal mirrors and a 2400 lines/mm holographic reflecting grating made by Milton-Roy (see figure 2.5). The grating is manually rotatable via an external wheel to allow different wavelengths of light to be aligned to the exit. The holographic grating has the advantage of reducing stray light and thus errors

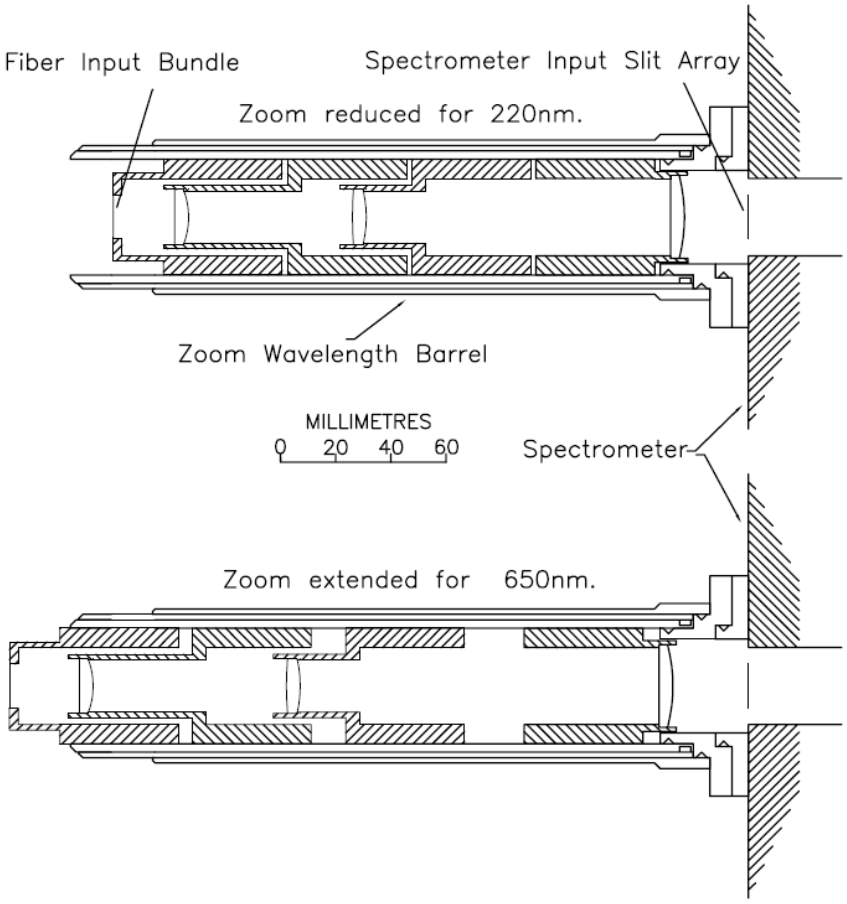


**Figure 2.4:** *The ECELESTE spectrometer input lens is adjustable to focus light between 220 and 650 nm and has a magnification of 2.0 [51]*

while maintaining a similar level of efficiency compared to a traditional mechanically ruled grating [51].

The spectrometer produces an array of spectra of the same dimensions as that at the input slits (i.e. the $10 \times 5$ chequerboard array) so a wavelength specific filter is used to select the region around the charge-exchange line in order to remove unwanted crosstalk due to photons from adjacent chords in the array (see section 5.4.2 for more details). The large length of the spectrometer and high line ruling of the grating produces a high dispersion such that the spectra array would overspill the CCD image region. Consequently the dispersed light is de-magnified using another coupling lens behind the filter which reduces the apparent size of the array to $\sim 7 \times 7$ mm on the CCD.


**Figure 2.5:** *The ECELESTE spectrometer (top) and detail of the entrances side (bottom). Light from each fibre is focused onto the entrance slits (1) and collimated by a toroidal mirror (2). The diffraction grating (3) disperses the light chromatically and this is focused by a second mirror (4) onto the spectrometer filter and exit (5) and out of the spectrometer into a demagnifying lens and camera (6)*

### 2.2.4 The CCD and data acquisition

The CCD (Charge Coupled Device) used on ECELESTE is a custom built frame transfer Wright Instruments device consisting of a 2D array of 22.5 $\mu$m$\times$ 22.5 $\mu$m pixels arranged in a $340\times1152$ grid. Each pixel consists of a photoactive semiconductor sensor which produces conduction band electrons when exposed to light due to photon absorption. The number of electrons produced in each pixel is proportional to the number of photons incident upon it, so this provides a measure of light intensity at that point on the CCD. The CCD signal is dependent on the quantum efficiency of the detector (the rate at which photons are converted to electrons), which is wavelength dependent (see figure 2.6). While the optical fibres limit the wavelength range measurable in the blue/UV range, due to the low transmission of optical fibres in this wavelength region, the CCD has very poor efficiency above $\sim$ 950 nm, which effectively limits spectroscopic measurements using this system to the visible or near infra-red. In order to improve the efficiency and reduce noise the camera is Peltier cooled to 200 K.

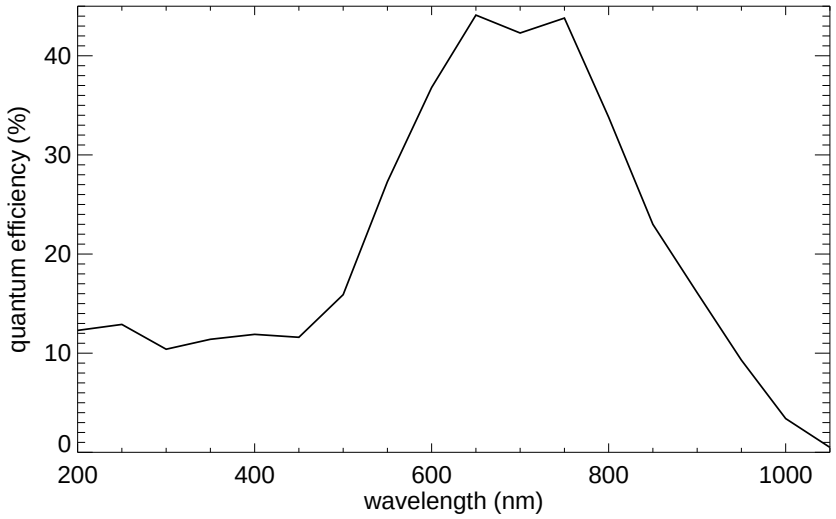


**Figure 2.6:** *The quantum efficiency of the CCD as a function of wavelength*

The light has been distributed chromatically in the x-direction (referred to here as the row or horizontal direction, the y-direction being referred to as the column or vertical direction) by the spectrometer. Each column of pixels acts as a shift register separated by oxide channel stops and by applying voltages in sequence (see figure 2.7) the electrons are moved down vertically from the image region (the top $340\times576$ region) to the store region (a masked $340\times576$ area which is shielded from the light source). When the electrons reach the line read out region they are shifted horizontally into an output amplifier (see

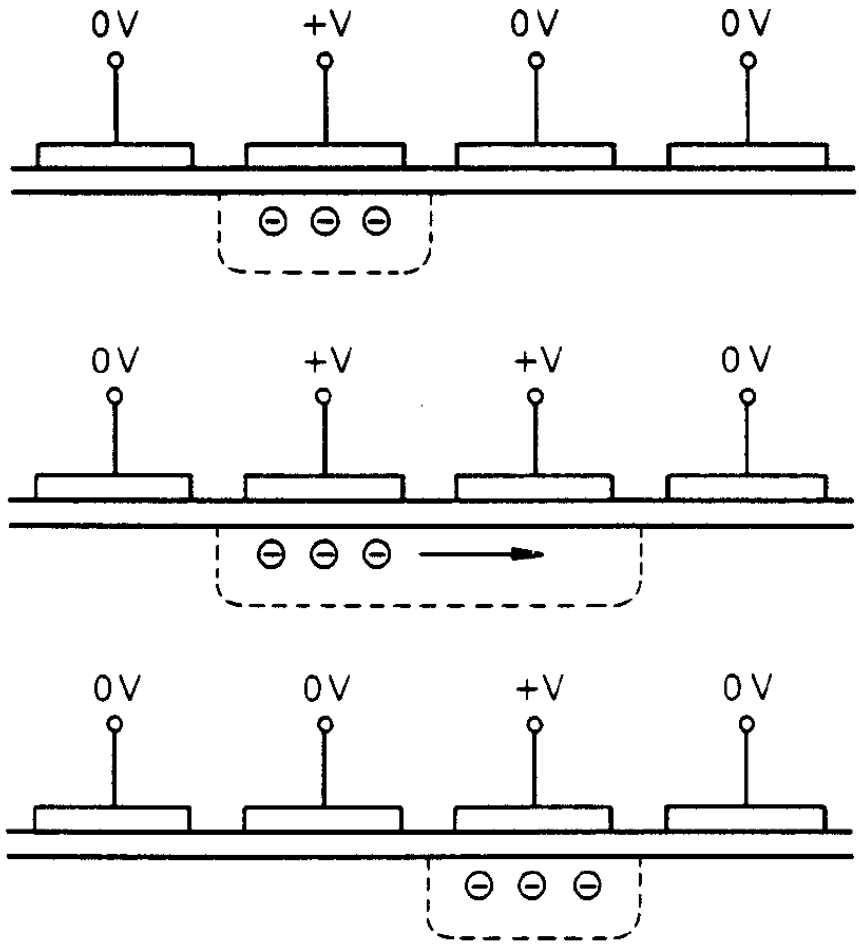


**Figure 2.7:** *Diagram of charge transfer in a typical CCD: The electrons are collected in the second potential well by applying a positive bias voltage to the gate electrode (top). These are transferred by applying a voltage to the third gate which allows the electrons to move into this adjacent potential well (middle). The voltage at the second electrode is then switched off and the electrons now all move into the third well (bottom). By repeating this process the electrons are shifted down the CCD [51]*

figure 2.8).

The reason for the store region on the ECELESTE CCD camera is to hold the data to be read out. Typically CCD shift times are much quicker than readout times. At high speed the pixel read out cycle time is 5.2 $\mu$s so to read out the entire active image region takes 893 ms. As the typical MAST shot time is 300-500 ms this is therefore completely inadequate. Moreover, while the data is slowly being read out the data is also slowly moving down the chip (at a speed of 1.5 ms per row if this were the case for this camera), which produces a vertical smear from positions of high intensity in those columns as they are moved down the CCD under that exposure area. With high and low intensity sources

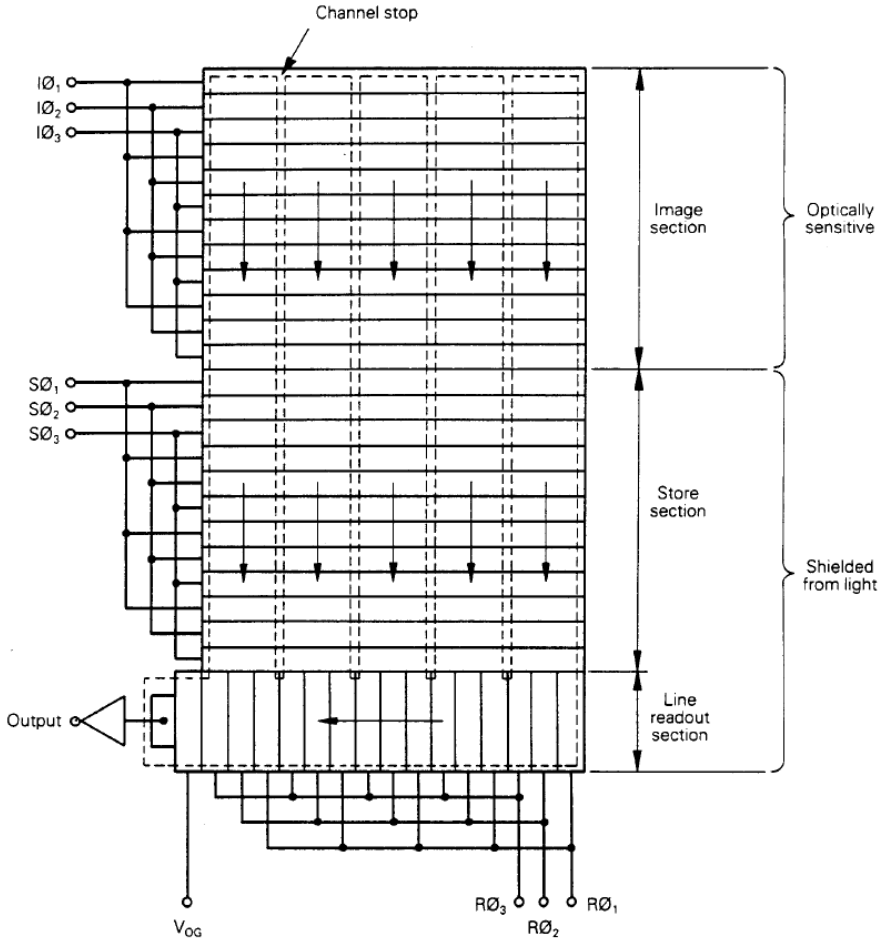


**Figure 2.8:** *Typical layout of a frame transfer CCD, showing direction of movement of electrons from image region to store region to readout region to output amplifier [51]*

in the same columns this could overwhelm weak signals with strong ones.

To avoid this the entire image region is quickly moved down to the store region, allowing the image region to accumulate data in the meantime. To down transfer a row takes 300 ns, so in order to shift all 576 takes $\sim 1.7\mu$s. Test shots showed that exposure times of 5-10 ms are required to record enough light to detect the spectra with good photon statistics (see section 4.4) so this value is only a small fraction of the exposure time. Therefore vertical smearing is virtually eliminated as each row is exposed for approximately 300ns per row as it passes under illuminated areas of the CCD.

However, the above arrangement would still only allow one unsmeared image to be taken per shot. To enable multiple time resolved spectra to be recorded the rows of the image section are binned together in groups of approximately 25 and the total photons in each column of the bin are added together to produce a single total row which contains all the data from one row of the spectral array. This has the added advantage of reducing the noise

to signal ratio at read-out. As the spectral array does not completely cover the image region there are approximately 275 pixel rows at the top which are essentially unilluminated and can be ignored as they are not recorded. This produces twelve rows of data per timeslice, which can be transferred to the store region. This allows up to 48 timeslices (576/12) to be taken per shot before it must be read out. At 10 ms this would be sufficient for all but the longest shots, while at 5 ms the majority of the shot can be covered. The added advantage of this is that the data can be read out slowly after the shot, as noise from the amplifier is inversely proportional to the speed at which it operates.

While use of a store region and binning largely avoids the effect of vertical smearing, smearing of the charge exchange signal can also occur due to inefficient transfer of electrons between rows, where some electrons can be left behind if transfer is not 100% efficient. If low intensity sources are higher up the CCD than high intensity sources this can provide an additional spurious signal on the low intensity spectra. In order to quantify the effect of this and any residual vertical smearing (which would provide a similar effect as both are proportional to incident intensity) the spectra incident on the CCD were arranged in a chequerboard pattern so that binned rows above and below did not contain a viewing chord but were empty except for any light from these effects. Analysis of these regions during measurements showed that electrons in these regions were very close to background and that smearing is not an important problem.

The output from the amplifier is transformed to a digital signal by an ADC (Analogue-to-Digital Converter) and deposited in the MAST data stores. This is processed via a series of analysis codes to produce data, as discussed in section 4.3.

Due to the high speed nature of the shot the CCD operation is pre-programmed and triggered by a signal from the MAST control system. This allows the start of data collection to be set with an accuracy only limited by the clock signal of the computer. The binning regions, exposure times and trigger point can all be adjusted using custom software between shots, allowing a high degree of flexibility in the operation of the ECELESTE system.

## 2.3 Conclusion

The overall system is capable of providing up to 48 sets of 60 channels of 3 mm spatial resolution, 1.5 mm radial resolution data at a time resolution of 5-10 ms. This allows the entire edge region to be surveyed throughout the majority of the plasma discharge, providing a suitable diagnostic for the investigations of ion temperature and velocity in the plasma edge if a suitable charge exchange line is found in this region. Identification of a suitable line and its modelled performance will be discussed in chapter 3.

# Chapter 3

# Modelling of the charge exchange signal

## 3.1 Introduction

Prior to attempting to measure the charge exchange signal it was necessary to assess the feasibility of the proposed method of stimulating charge exchange by using a gas puff to inject cold deuterium into the plasma. This required answering several questions to assess the feasibility of the diagnostic. These included deciding which emission line was best to utilise and how large a signal would be expected, based on which impurities exist in the MAST plasma and which emission lines are in the visible range, and also whether the impurity chosen would be in thermal equilibrium with the plasma. It was also necessary to understand what background processes exist and how large a contribution these would make in affecting the signal to noise ratio.

In order to assess this it was also necessary to model how the gas puff would perform by determining how far the gas puff would penetrate into the plasma, how localized the gas puff would be, and what density of gas puff would be required to create a good signal.

This chapter therefore firstly discusses the candidate species that could be used to produce charge exchange emission and which emission lines would be the most promising. It then considers the question of whether or not the impurity would be in equilibrium with the bulk ions in the plasma and whether the impurity's use as a proxy for ion temperature and velocity would therefore be valid. The cross sections and rate coefficients for charge exchange with cold deuterium are determined and the contributions from ground state and excited state deuterium atoms are analysed. The background processes that are significant are then identified and rate coefficients for all processes compared. A model for the density of carbon in the plasma is produced as well as models for the neutral deuterium present as

background and from gas puffing. Finally the individual model profiles and rate coefficients are combined together to produce overall model profiles of background and active emission rates as would be seen by the ECELESTE spectrometer views, and the validity of these results assessed.

## 3.2 Issues with charge exchange recombination spectroscopy

The use of hydrogen (and its isotopes) as the receiver ion in CXRS to diagnose the temperature and velocities within a tokamak plasma is not easily viable as imaging $H^0$ emission after charge exchange recombination gives poor spatial resolution. Once the $H^+$ ions regain an electron they are then neutral and no-longer bound to the field lines. Velocities in the core can be of the order 100km $s^{-1}$, while for transitions in the Balmer series in the visible range the largest transition probabilities $A_{ik}$ are in the range $10^6 - 10^7$ $s^{-1}$ [52], leading to movement of several mm before emission of a photon.

It is necessary to use an impurity ion for CXRS which remains charged even after accepting an electron. Ideally the impurity ions are in thermal equilibrium with the $H^+$ ions so that they have the same temperature.

In tokamaks the main impurities come from the wall materials, air that has been absorbed into the wall between shots and then released during the shot, and any injected impurities, which can also linger in the vacuum vessel after their use on previous shots. The main impurity ions present in the MAST tokamak are helium, carbon, iron and oxygen, as shown in figure 3.1. The most abundant of these is carbon, which is ablated and sputtered from the surface tiles and divertor plates, both of which are made from fine grain graphite. Therefore carbon is the leading impurity to consider for CXRS.

Throughout the majority of the MAST plasma the dominant impurity is fully ionized carbon (see figure 3.2). At higher temperatures intermediate ionization species may not be in equilibrium with the plasma even if they are present as they will be ionized before they can equilibrate if the thermalization time is longer than the ionization time (although generally this is not true at the plasma edge, see section 3.3). Moreover the intermediate ionization states will generally be spatially localised over a small radial extent, meaning measurements across most of the plasma using that state are impossible.

Given the need for the impurity line in CXRS to be from a fully ionized impurity this limits the number of possible emission lines to those from hydrogen-like emission. This immediately rules out iron as a source as it will only be fully ionized in the core, if at all, (the ionization potential of hydrogen-like iron is 9278 eV [55]).

High-Z impurities tend to have their strongest emission lines in the UV range. However

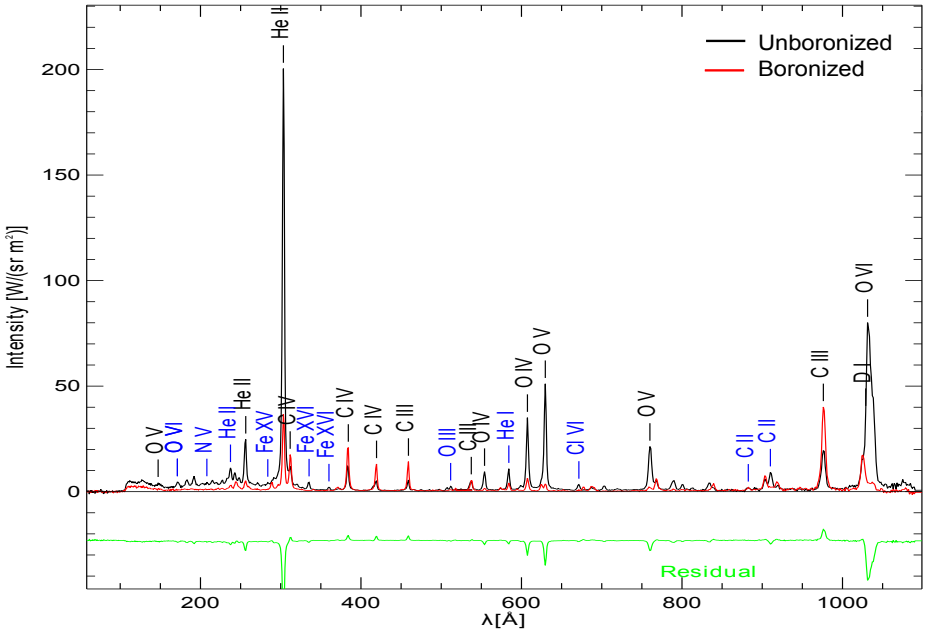


**Figure 3.1:** *Comparison of emission lines in the VUV region (before and after a boronization), showing the predominant impurity species in the plasma [53]*

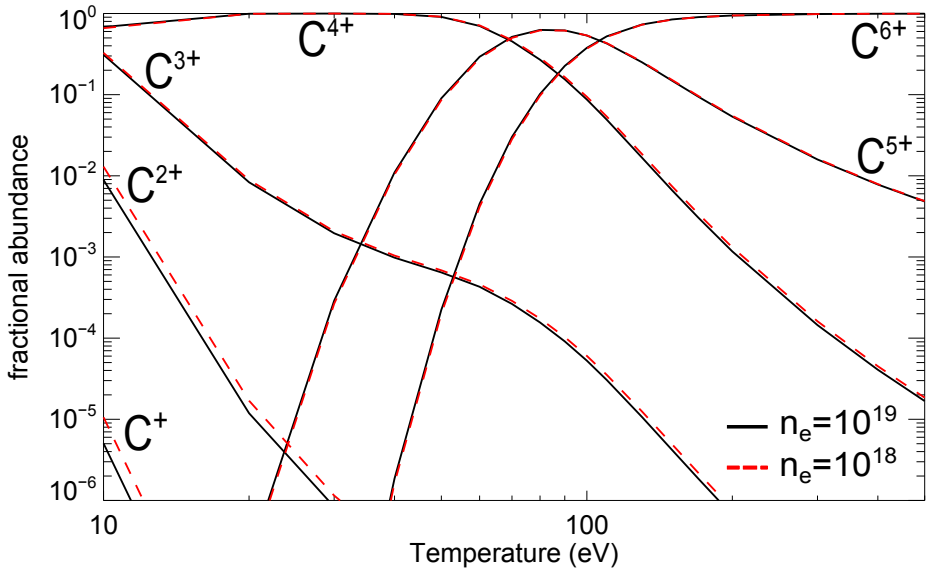


**Figure 3.2:** *Equilibrium fractional abundances of carbon ionization stages calculated from a collisional radiative model available from ADAS [54]*

UV spectroscopy requires much more complex and expensive optics such as a vacuum lines-of-sight which must be situated in the torus chamber meaning this was not a viable option. The ECELESTE system uses optical fibres which do not transmit UV well. The available camera also only has a large quantum efficiency in the visible and near infrared (see section 2.2.4), thus limiting the upper wavelengths available. Limiting the wavelength to the visible/near IR range thus implies that the transitions should be of the type $n \rightarrow m$

where $n, m \gg 1$. All transmissions which are not electric dipole (E1) transitions are likely to be too weak to be visible above noise so transitions other than electric dipole are not considered. As the transition probabilities are strongest for transitions of the type $n = m + 1$ this further limited the number of possibilities. These are listed in table 3.1 with their nearest neighbours in the spectrum in the infrared or ultraviolet [56, 57]. As carbon is the most abundant impurity this implies that $C^{5+}(8 \rightarrow 7)$ at 529 nm is the most promising line to utilise.

| Helium | | Carbon | | Oxygen | |
|---|---|---|---|---|---|
| Line | $\lambda$ (nm) | Line | $\lambda$ (nm) | Line | $\lambda$ (nm) |
| $He^{+}(3 \rightarrow 2)$ | 163.89 | $C^{5+}(7 \rightarrow 6)$ | 343.37 | $O^{7+}(8 \rightarrow 7)$ | 297.58 |
| $\mathbf{He^{+}(4 \rightarrow 3)}$ | **468.52** | $\mathbf{C^{5+}(8 \rightarrow 7)}$ | **529.05** | $\mathbf{O^{7+}(9 \rightarrow 8)}$ | **434.06** |
| $He^{+}(5 \rightarrow 4)$ | 1011.99 | $C^{5+}(9 \rightarrow 8)$ | 771.28 | $\mathbf{O^{7+}(10 \rightarrow 9)}$ | **606.30** |
| | | | | $O^{7+}(11 \rightarrow 10)$ | 819.77 |

**Table 3.1:** *List of usable spectral lines for charge exchange measurements (visible range (380-700nm) in bold)*

## 3.3 The equilibrium between D and carbon impurity

Beam heating of the plasma favours the heavier impurity ions over the deuterium ions as the slowing down time of the fast ions by the plasma ions is proportional to $\frac{m_z}{(m_b+m_z)Z^2}$ [5] where $m_b$ is the mass of the beam ions while the energy coupling efficiency from the beam is proportional to $m_b/(m_b + m_z)$ so that overall each carbon ion receives six times as much power as each deuterium ion [51].

For the measurement of temperature and velocity to be valid using CXRS, it is necessary for the impurity and bulk ions to be in equilibrium with each other. Therefore it is necessary that any differences between ion and impurity heating are quickly equilibrated. This requires that the thermal transport time is longer than the thermalization time ($\tau_{trans} >> \tau_{zi}$), thus allowing the ions to equilibrate with each other at each flux surface. The thermalization time between impurity and deuterium is given by [5]

$$\tau_{zi} = \frac{3\sqrt{2}\pi^{3/2} m_z m_i}{n_z e^4 Z_i^2 Z_z^2 \ln\Lambda} \left( \frac{k_B T_z}{m_z} + \frac{k_B T_i}{m_i} \right)^{3/2} \tag{3.1}$$

and is proportional to temperature and inversely proportional to density. A range of values for thermalization between $C^{6+}$ and $D^{+}$ are shown in figure 3.3. Although these are calculated using the assumption that the impurity temperature $T_z = T_i$, the deuterium tem-

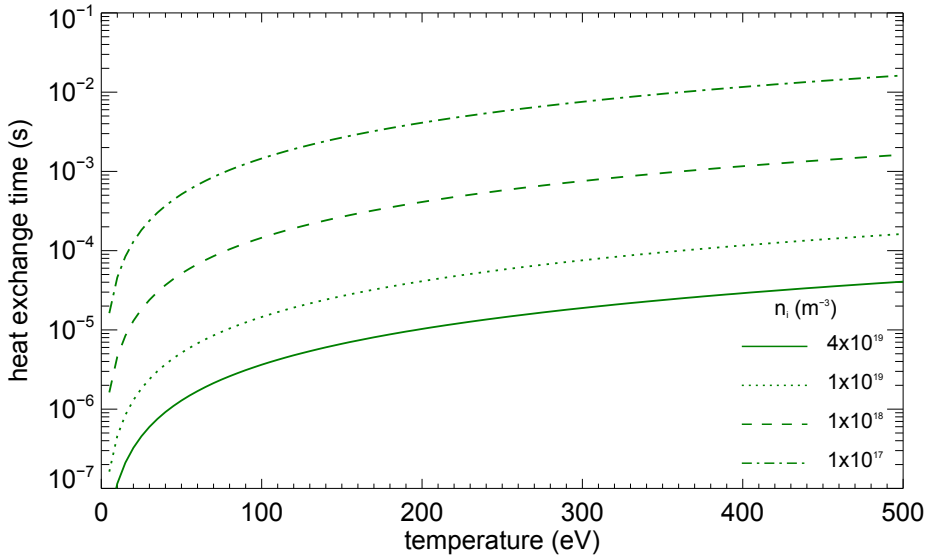


**Figure 3.3:** *Thermalization times as a function of $n_i$ and $T_i$ for $C^{6+}$ and $D^+$ under the assumption that $T_z = T_i$ calculated using equation 3.1*

perature, altering this does not significantly change the results due to the mass difference between deuterium and carbon.

The thermal transport time can be estimated as

$$\tau_{trans} \approx \frac{L_p^2}{\chi_i} \tag{3.2}$$

where $L_p = p/\nabla p$ and the neoclassical thermal diffusivity can be estimated as [5]

$$\chi_i \approx \frac{k_B T}{\tau_e \omega_c^2 m}. \tag{3.3}$$

The true thermal diffusivity is normally in the range $0.1 < \chi_i < 10$ and the estimate of equation 3.3 provides a reasonable estimate in H-mode for the true value, while in L-mode this tends to underestimate the true value of $\chi_i$ by up to a factor of 10 higher [58]. Figure 3.5 indicates that this should not significantly influence the below conclusions.

As $L_p$ and $\chi_i$ are changing functions of radius, to estimate $\tau_{trans}$ model profiles of $n_z$ and $T_z$ were made for L- and H-mode in the edge region under the assumptions that $n_i = n_e$ and $Z_{eff} = 1.5$ (see figure 3.4). These were based on typical electron temperature and density profiles from Thomson scattering and provide order of magnitude estimates of the size of $\tau_{trans}$. There are several uncertainties involved in this approach, especially given the difficulty in calculating accurately the slope of the pressure gradient $\nabla p$. Nonetheless figure 3.5 shows that except when the density is very low at the edge of the plasma (where it is unlikely that there would be any significant signal in any case) $\tau_{trans} >> \tau_{zi}$ and therefore deuterium and carbon are expected to be in thermal equilibrium with each other.

The carbon must also remain in its fully ionized state for longer than the thermalization time in order to equilibrate. The criterion for this is that the recombination time (given as $\tau_{rc} = (n_e \langle \sigma v \rangle_{rc})^{-1}$) is much greater than the thermalization time. The total recombination rates for $C^{6+}$ are of order $10^{-17} - 10^{-18}$ $\mathrm{m^3 s^{-1}}$ (see section 3.5.1) while densities are of the order $10^{17} - 10^{19}$ $\mathrm{m^{-3}}$ in the plasma edge, meaning $\tau_{rc}$ is of the order 10-1000 ms, much larger than the thermalization time shown in figure 3.5. The fact that the transport times are also calculated to be smaller than the recombination time implies that higher ionisation states can be present in the edge at larger radii and lower temperatures than could be expected from equilibrium abundances (see figure 3.2). However, the equilibrium profiles will still remain a good first order assumption in producing model carbon density profiles (see section 3.6.1).

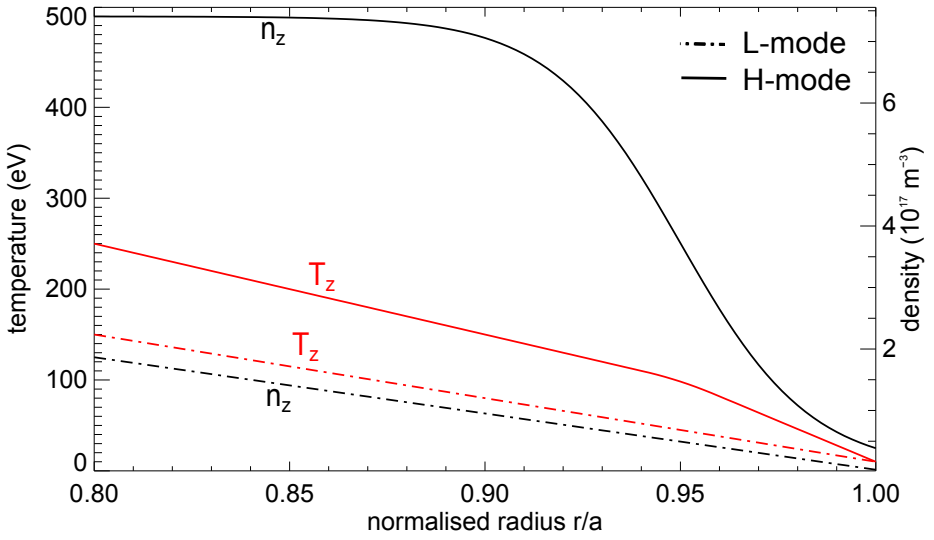


**Figure 3.4:** *Model profiles of carbon density and temperature used to estimate* $\tau_{trans}$

The mass ratio between electrons and ions is large which means the electron and ion temperature can become decoupled from one another if the electrons and ions have a large equilibration time. However, $T_i$ and $T_z$ could also become decoupled if the gradient scale length $L^i_\perp$ of the deuterium ions becomes very small. As deuterium is the bulk ion, the carbon will generally be coupled to its temperature. If the gradient scale length of the deuterium is smaller than the Larmor radius of the carbon $\rho^C_L$, then the temperatures can be decoupled from one another in steep gradient regions. However, the Larmor radius for carbon is a factor $\sqrt{\frac{m_i}{m_z}}Z = \sqrt{6}$ smaller than the Larmor radius $\rho^i_L$ of deuterium. Therefore as generally $L^i_\perp > \rho^i_L$ the carbon will respond to any changes in deuterium over short scales and remain in equilibrium at all flux surfaces.

A measurement of $T_z$ via charge exchange can be construed to be a measurement of $T_i$ as it has been shown that the carbon remains ionized for long enough that equilibration

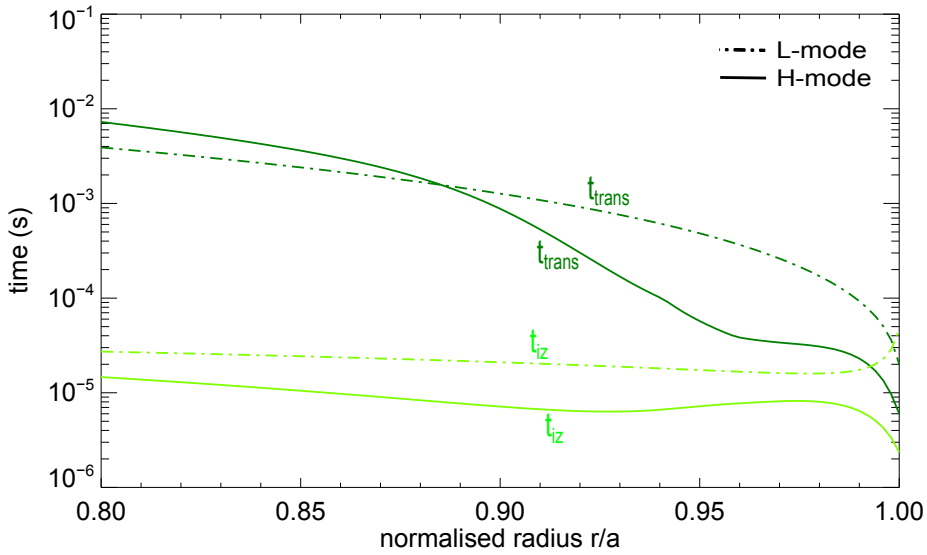


**Figure 3.5:** *Calculated values of $\tau_{trans}$ and $\tau_{zi}$ for the model profiles in figure 3.4*

can take place. Furthermore as the carbon and deuterium ions equilibrate with each other more quickly than they are transported and the gradient scale length of carbon is smaller than that of deuterium the two species should be in equilibrium on every flux surface. This allows measurements of $C^{6+}$temperature and velocity to be used to infer the temperature and velocity of $D^{+}$.

## 3.4 Size of active signal

### 3.4.1 Cross sections

Given that $C^{6+}$ appears the most promising of the impurities available in the MAST plasma, and that the $n = 8 \rightarrow 7$ line is the most probable emission line to use, it is necessary to estimate whether this interaction will produce a large active signal. This is determined both by the overall rate for charge exchange leading to emission of light at this wavelength and by the relative rate compared to other processes which would contribute to the background emissions.

To determine the contribution to an emission process from charge exchange it is first necessary to determine the cross section for the interaction for the relevant plasma conditions. Cross sections are difficult to measure and complex to calculate. As well as charge-transfer into the excited level directly, electrons may end up in this level by transfer into a higher level followed by cascade to the $n$-level of interest [32]. Additionally, within the $n$-level the states are split into different orbital angular momentum states $l$ and into different total angular momentum states $j$ where $j = l \pm 1/2$ due to spin-orbit coupling.

This fine structure is also populated by different amounts and this must also be accounted for.

An initial estimate of which levels will be preferentially populated can be found by following a semi classical approach, as outlined in Hutchinson (2005) [57]. We consider a collision between a fully stripped ion of charge $Z_i$ and a singly charged ion or atom of charge $Z_p$ with the electron in the principle quantum level $n_p$. The two nuclei are passing at a relative constant velocity $v$ (which in this particular case will be essentially the thermal speed of the ions) and with impact parameter $R$, and as they pass their potential wells are interacting so that the electron moves in a joint potential $V(t)$.

Initially we consider collisions where $v << v_e$, the electron's orbital velocity in the magnetic field. As the nuclei approach each other there is a resonance or 'level crossing' at a separation $b = a_0 r_r$ where the total electron energies are equal, due to the lowering of the potential well of the atom by the interaction with the ion. The electron can thus transfer across while conserving total energy and angular momentum. In reality this is a quantum mechanical effect: the resonance is due to the energy of the electron wavefunction attached to either nuclei being approximately equal, therefore allowing the probability of the electron being attached to the carbon ion to gradually increase, much like two coupled pendula. However, treating the problem classically leads to a similar result.

Solving the equation for the electron energies and for the electric potential at the saddle point leads us to an equation for $r_r$ and the ratio of the resonant energy levels $n_i/n_p$ (see appendix A):

$$r_r = \frac{2{n_p}^2}{{Z_p}^2}\left(Z_p + 2\sqrt{Z_i Z_p}\right) = \frac{2{n_i}^2}{{Z_i}^2}\left(Z_p + 2\sqrt{Z_i Z_p}\right) \tag{3.4}$$

$$\frac{n_i}{n_p} = \left(\frac{Z_i}{Z_p}\right)^{3/4}\left(\frac{2\sqrt{Z_i} + \sqrt{Z_p}}{2\sqrt{Z_p} + \sqrt{Z_i}}\right)^{1/2} \tag{3.5}$$

From equation 3.5 the resonant state for $n_p = 1$, $Z_p = 1$, $Z_i = 6$ is $n_i \approx 4.4$ while for $n_p = 2$ the resonant state is $n_i \approx 8.8$. This immediately implies that the first excited state for the donor deuterium will be important at low energies as the majority of the charge exchange from ground state will be into lower excited states of the carbon ion. As the wavelengths for these transitions are in the UV there will therefore be no visible light emitted as it cascades down the energy levels to the ground state.

If we now assume that nuclei which approach closer than $b$ have an equal probability of emerging attached to either atom and that the probability of charge exchange is zero for $R > b$ then we can estimate the cross section probability as

$$\sigma_{low} \approx \frac{1}{2}\pi {a_0}^2 {r_r}^2 = 8\frac{\pi {a_0}^2 {n_p}^4 Z_i}{{Z_p}^3}\left[1+\sqrt{Z_p/Z_i}+Z_p/4Z_i\right] \tag{3.6}$$

From this it can be immediately seen that there is no energy dependence at low energies, so it should be expected that the real cross sections will follow a similar shape. The scaling of $\sim {n_p}^4 Z_i/{Z_p}^3$ follows what would be intuitively expected, that electrons in high $n_p$ states in low $Z_p$ atoms will be loosely bound to the nucleus, and that the larger the charge of the interacting ion $Z_i$ the stronger the attraction, the larger $r_r$ is and thus the larger the cross section is. Thus for $n_p = 1$, $\sigma \approx 70\pi {a_0}^2$ but for $n_p = 2$, $\sigma \approx 1114\pi {a_0}^2$ due to the strong ${n_p}^4$ dependency, a factor $\sim 16$ greater. This scaling indicates that the cross section is not only resonant at approximately the correct level for this visible line but that the probability of charge exchange is much greater as well. This further adds to the evidence that the $n_p = 2$ state of the $D$ excitation will be at least important, if not dominant, in the analysis of the overall rate of exchange.

At large collision velocities such that $v \approx v_e$, the resonance condition is broken, and the probability of interaction will decrease with increasing $v$. For intermediate energies it can be estimated as follows, again following Hutchinson (2005) [57].

If the electron is to transfer from the deuterium atom to the carbon ion it must have enough kinetic energy, in the rest frame of the atom, to match the speed of the ion as it moves past. Therefore the saddle potential must be at least $\frac{1}{2}m_e v^2$. If the probability of capture is postulated to be P(Capture) $\approx (b/v)(v_e/a)$ for an impact parameter $b$ and electric orbital radius $a = (a_0 {n_p}^2)/Z_p$ then the capture cross section can be calculated as $\sigma \approx \pi b^2$P(Capture), i.e (see appendix A)

$$\sigma_{med} \approx \pi {a_0}^2 \frac{{Z_m}^3 {Z_p}^2}{\sqrt{2}{n_p}^3}\left(\frac{2R_y}{\frac{1}{2}m_e v^2}\right)^{7/2} \tag{3.7}$$

where $Z_m = \left(\sqrt{Z_p}+\sqrt{Z_i}\right)^2$. Defining

$$\varepsilon = \frac{\frac{1}{2}m_e v^2}{2R_y} \quad \text{and then} \quad \hat{\varepsilon} = \frac{2\varepsilon {n_p}^2}{{Z_i}^{4/7}{Z_p}^{10/7}} \tag{3.8}$$

interpolation of the cross section for charge exchange between the low and intermediate energy results can be achieved using the formula

$$\sigma_{interpol} = \sigma_{low}/(1+\hat{\varepsilon}^{7/2}) \tag{3.9}$$

.

This interpolation procedure is illustrated in figure 3.6. As this is a sum over all final $n$-levels it cannot be determined what proportion of this will be to the $n_i = 8$ final level.

However, at low energies it would be expected that the resonance would hold strongly, such that only $n$-levels lying close by in energy would be significantly populated. Therefore for $n_p = 1$ this will be mostly $n_i = 4, 5$, while for $n_p = 2$ this will be mostly $n_i = 8, 9$. At higher and intermediate energies where this resonance breaks down, the spread of $n$-levels should be broader. For $l$-states at low energies the electron is most likely to transfer into the state $n_{max} = l$ where $n_{max} = n_p Z^{3/4}$ (or $n - 1 = l$ for $n < n_{max}$). At higher energies the population is more skewed towards higher $l$ states, particularly $l = n - 1$ states in all cases due to angular momentum conservation [32, 59]. Calculations by Olson and Schultz (1989) [33, 60] show this for $O^{8+}$ at beam energies between 40 and 80 keV (see figure 3.7). At the lower energies of interest here this $nl$ state preference will be even more pronounced, although the $l = n - 1$ dominance can be rebalanced to a more statistical state by l-mixing effects (see section 4.6.1).

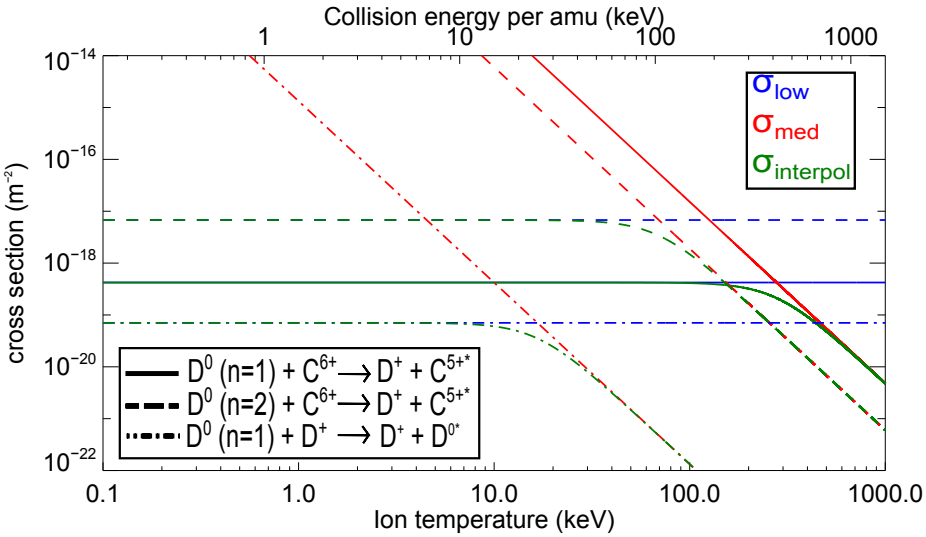


**Figure 3.6:** *Semiclassical cross sections for charge exchange, showing the low (equation 3.6), and medium (equation 3.7) energy solutions as well as the calculated from equation 3.9 for three different processes: charge exchange of ground state deuterium with $C^{6+}$ (solid line), charge exchange of deuterium in the first excited state with $C^{6+}$ (dashed line), and, for comparison, ground state deuterium with $D^+$.*

There is a large body of literature discussing the cross section for emission from the $n = 8 \rightarrow 7$ line in $C^{6+}$ [60–69]. Preferred cross sections for carbon [65, 68, 70], oxygen [65, 70], beryllium and boron [71, 72] etc. have been collected and ADAS [54] also has a comprehensive set of data. Although few experiments have been possible to test this data [66] there is a good enough agreement between all methods that a good level of confidence is possible (for example see figure 3.8).

Much of the published literature on charge exchange cross sections is concerned with

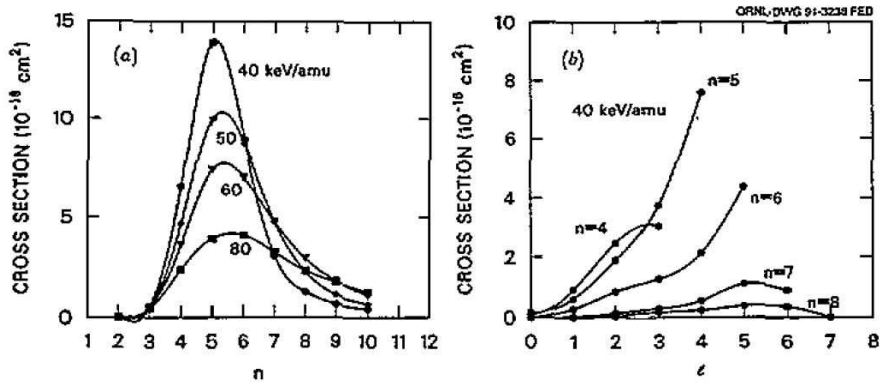


**Figure 3.7:** *(a) Partial cross sections at a variety of beam energies for the charge exchange reaction* $H^0(1s) + O^{8+} \longrightarrow H^+ + O^{7+}(n)$*. (b) Partial cross sections at 40 keV amu*$^{-1}$ *into specific l-levels for a variety of n-levels. From Isler (1994) [33] based on data from Olson and Schultz (1989) [60].*

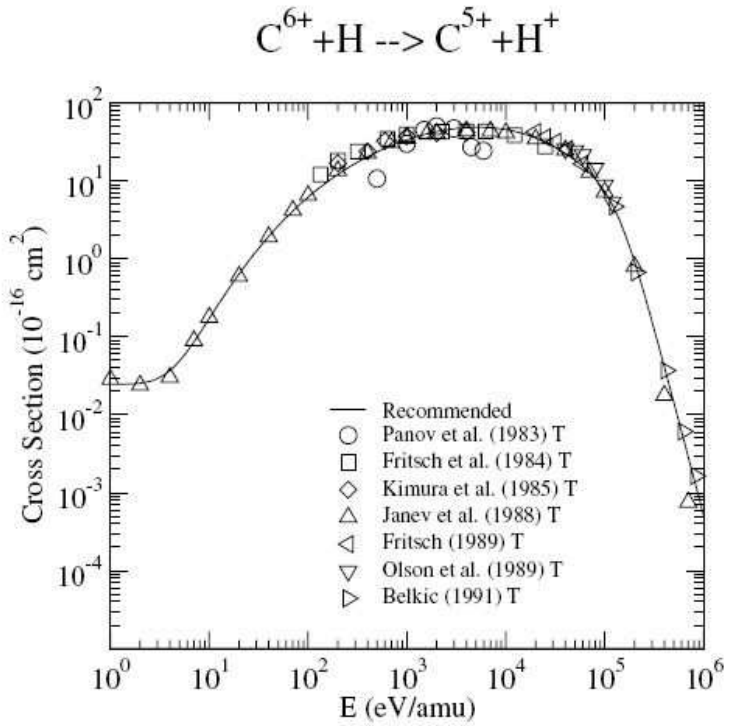


**Figure 3.8:** *Total cross section data for* $C^{6+} + H^0 \longrightarrow C^{5+} + H^+$ *collated by Suno and Kato (2007) [68].*

charge exchange at the keV energy range of neutral beams for the purposes of determining heating deposition within the plasma and for CXRS using neutral beams. This is a well established technique on many tokamaks to measure ion temperatures and velocities and the emission line in question has often been employed [39, 40, 73–75]. However, using a gas puff to provide the source of neutral deuterium is a novel technique and so little study

has been made of cross sections for charge exchange in the relevant plasma conditions. A gas puff of cold deuterium will have energies 1000 times smaller than the cross section ranges generally quoted for deuterium accelerated in an NBI system and so much of the cross section literature is therefore not relevant. The temperatures of the neutral atoms provided by the gas puff will generally be in the range 2-8 eV due to the energy released by Franck-Condon dissociation of the molecular $D_2$ into its atomic constituents. Therefore the energies of collision are not those of the neutrals, but of the plasma itself, except at very low energies, so the region of interest is energies ranging from a few eV up to several hundred eV. Suno and Cato (2006) [76] give a summary of preferred cross sections and their database provides data in the eV range, but only for total cross section from ground state and for $n_i$-levels up to $n_i$=5.

Despite this, however, some data at low energies is available from ADAS [54]. Several sets of data for $n_p = 1$ and $n_p = 2$ are available and shown in figure 3.9. Preferred data for $n_p = 2$ is from Hoekstra *et. al.* (1998) [67] calculated via classical trajectory Monte-Carlo method (CTMC) and preferred data for $n_p = 1$ is combined data by Fritsch (1989), Frirsch and Lin (1984) and Ryufuku (1982) [63, 77, 78] using the close-coupling molecular orbital (CCMO) and unitarised distorted wave approximation (UDWA) methods. This has been spline interpolated between 10 and 1000 eV as no data is available, but this should nevertheless give an order of magnitude estimate of the contribution from $n_p = 1$ neutrals. As can be seen the data is qualitatively consistent with what is expected, with the cross section for $n_p = 2$ neutrals much larger than that for $n_p = 1$ at low energies. The shape for $n_p = 2$ is also similar to the semi-classical prediction, as the transition to $n_i = 8$ is the dominant contributor to the total cross section, while for $n_p = 1$ this is only a small fraction of the total cross section.

### 3.4.2 Rate coefficients

The rate coefficients for these charge exchange reactions can be calculated within ADAS (see figure 3.10). The rate coefficient is defined as

$$\langle \sigma_{ij} v \rangle = \int \sigma_{ij} f(\mathbf{v}) v d^3 v \Big/ \int f(\mathbf{v}) d^3 v \tag{3.10}$$

for a cross section (for some reaction $i \rightarrow j$) $\sigma_{ij}$. As $f(\mathbf{v})$ is normally assumed to be a Maxwellian $\langle \sigma_{ij} v \rangle$ is a function of temperature $T$. Effective emission rates $\langle \sigma_{i \rightarrow j} v \rangle^{eff}$ can also be calculated which take into account the additional population of the upper level $j$ from transitions into higher $n$-states $> j$, followed by decay into the upper level of interest. The total effective emission rate for charge exchange into $C^{6+}(n = 8)$ from all $D^0(n = i)$

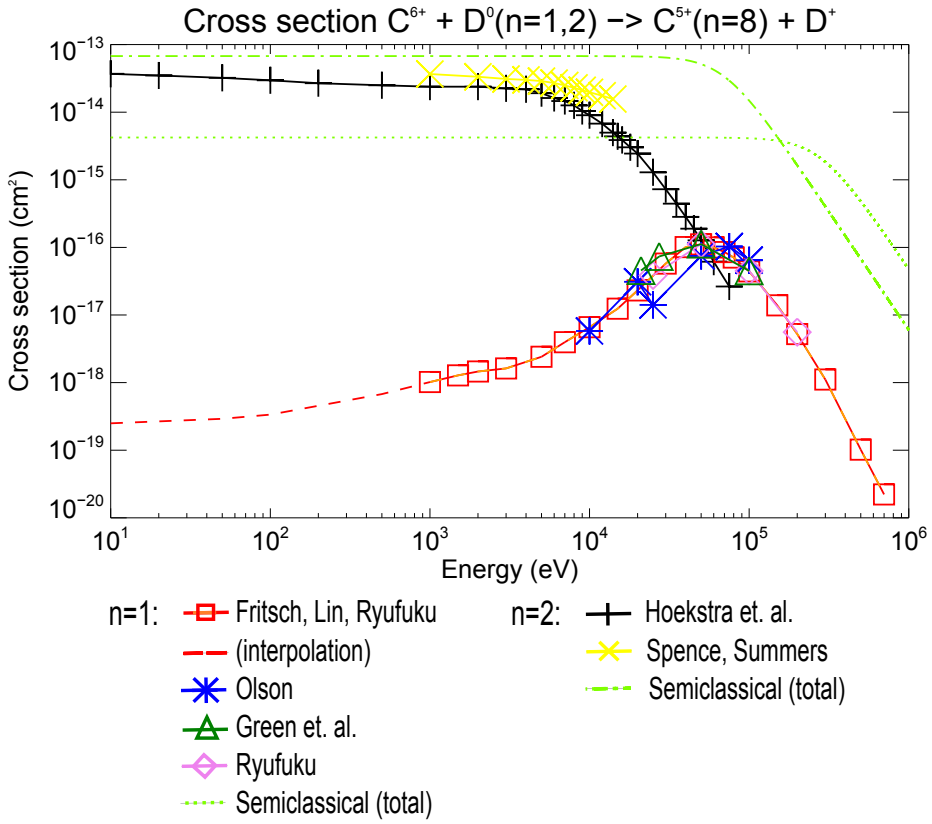


**Figure 3.9:** *Cross section data for $C^{6+} + H^0(n = 1, 2) \longrightarrow C^{5+}(n = 8) + H^+$ from various sources [61–63, 67, 77–79], sourced from ADAS [54]. Also total semi-classical cross sections (into all final states) for the two processes as calculated from equation 3.9*

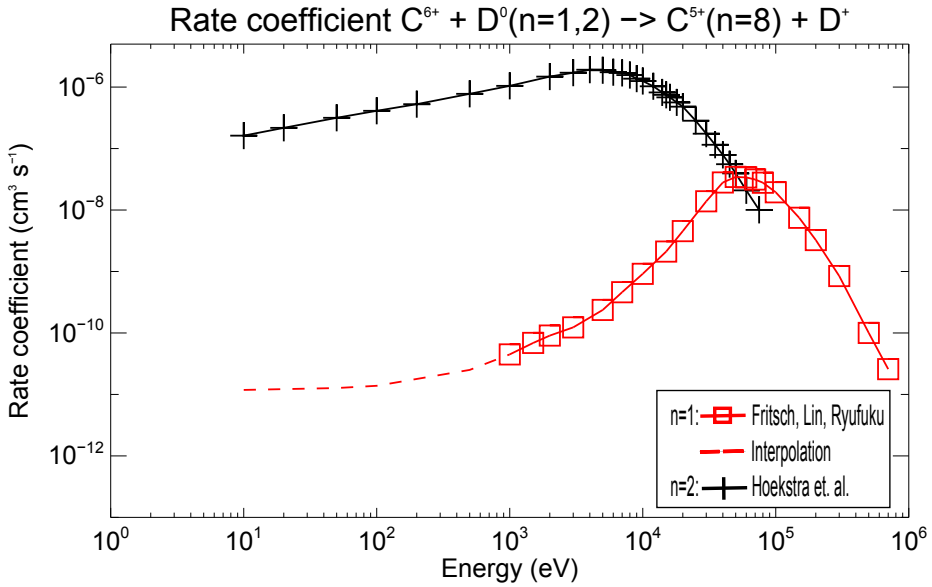


**Figure 3.10:** *Effective rate coefficient data for $C^{6+} + H^0(n = 1, 2) \longrightarrow C^{5+}(n = 8) + H^+$ from various sources [63, 67, 77, 78], sourced from ADAS [54]*

states is therefore

$$\Phi^{CX} = B_{8\to7} \sum_i n_{D^0}(n=i) n_{C^{6+}} \langle \sigma_{i\to8} v \rangle^{eff} \tag{3.11}$$

where $B_{j\to i} = A_{ji} / \sum_{k\neq j} A_{jk}$ is the branching ratio. As discussed previously the primary line of interest is where $j = 8$, $i = 7$. In order to understand the full contribution from ground and first excited state it is necessary to know what fraction of the neutral deuterium population is in the first excited state to work out the total charge exchange emission. The total emission can be defined as

$$\Phi^{CX} = B_{8\to7} \left( n_{D^0} n_{C^{6+}} \left( (1-f) \langle \sigma_{1\to8} v \rangle^{eff} + f \langle \sigma_{2\to8} v \rangle^{eff} \right) \right) \tag{3.12}$$

where $f = n_2/n_1$ assuming that the population of other excited states are negligible (a good assumption, except at high densities, see below). Generally tokamak plasmas are not in total thermal equilibrium as radiation tends to be weakly coupled, mostly being lost without re-absorption. In the case where electron densities are large and collisions dominate then there will be a local equilibrium between states, the criterion for which can be given as [57]

$$n_e \gg 10^{19} T(eV) (\Delta E(eV))^3 \quad \mathrm{m}^{-3} \tag{3.13}$$

Equation 3.13 is satisfied for most species only at high $n$-levels where $\Delta E$ is small. At lower energies a more general collisional-radiative model must be used. In equilibrium situations the general equation for the population of a level $i$ can be given as a sum over all other states $j$ [57]

$$0 = \sum_{j\neq i} [n_i A_{ij} - n_j A_{ji} + (n_i B_{ij} - n_j B_{ji}) \rho(\nu_{ij}) + n_e n_i \langle \sigma_{ij} v \rangle - n_e n_j \langle \sigma_{ji} v \rangle] \tag{3.14}$$

where $A_{ij}, A_{ji}, B_{ij}, B_{ji}$ are the Einstein coefficients for spontaneous and stimulated transitions, $\rho(\nu_{ij})$ is the radiation density and $\langle \sigma_{ji} v \rangle, \langle \sigma_{ij} v \rangle$ are electron collisional excitation/dexcitation rate coefficients. By solving the set of coupled equations for each level $i$ the populations of all levels can be found, assuming the Einstein coefficients and rate coefficients for all processes are known. As this is highly complex, a simple assumption of coronal equilibrium can be applied as a first approximation, where all excitations are collisional, and all de-excitations radiative. This is a good approximation in the regime where densities are low and the plasma is optically thin, such that most photons emitted from excited states are lost from the plasma without re-absorption, and therefore radiative

excitation will be negligible compared to electron excitation. If the electron collision time $\tau_e$ is much greater than the excitation time $\tau_{ex}$ this will be a valid approximation. The electron collision time is given as [5]

$$\tau_e = 12\pi^{3/2}\frac{\epsilon_0^2 m_e^{1/2}(k_B T_e)^{3/2}}{n_e m_e e^4 \ln\Lambda} \tag{3.15}$$

while the excitation time for a level $i$ is given as $\tau_{ex} = 1/\sum_{j<i} A_{ij}$. In the edge the collision time for electrons is of the order 1 $\mu$s while the excitation time is of the order 1-100 ns. Therefore coronal equilibrium is a good approximation for the plasma edge, which is the region of interest.

In coronal equilibrium the rate of downward radiative transitions depends only on the Einstein coefficient for spontaneous emission $A_{ij}$, so a plasma which is of sufficiently low density will have a rate of collisional de-excitation negligible in comparison to this, while upward excitations will be overwhelmingly from collisional electron excitation of the ground state. Therefore all but the first and last terms in equation 3.14 can be ignored, so that the excited state population can be calculated as

$$\frac{n_i}{n_1} = \frac{n_e\langle\sigma_{1\to i}v\rangle}{\sum_j A_{ij}}. \tag{3.16}$$

While this will give a good approximation of the excited states in many situations, it does not well approximate the case of the first excited state of deuterium, due to the metastable nature of the $2S_{1/2}$ excited state. This occurs as the spontaneous emission from $2S_{1/2}$ to the ground state is first order forbidden, with $A_{ij} = 2.495\times10^{-6}$ (compared with $A_{ij} = 6.270\times10^{8}$ for the $2P_{3/2}$ state for example). Coronal equilibrium of the $2S_{1/2}$ is not applicable, as most de-excitation will be collisional. A simplified model therefore is to treat sublevels $2S_{1/2}$ and $2P_{1/2} + 2P_{3/2} = 2P_J$ separately, using only collisional transitions between levels $n = 1 \leftrightarrow 2(2S_{1/2})$ and $n = 2(2S_{1/2}) \leftrightarrow 3$, truncating the summation at this point (i.e. ignoring higher $n$-states), and ignore all radiative population of the $n = 2$ level from $n = 3$ and above and other radiative terms. Equation 3.14 then becomes

$$\frac{D_0(2S_{1/2})}{D_0(1S_{1/2})} = \frac{\langle\sigma_{2S_{1/2}\to1S_{1/2}}v\rangle}{\langle\sigma_{1S_{1/2}\to2S_{1/2}}v\rangle + \sum_{L=S,P,D}\langle\sigma_{2S\to3L_J}v\rangle}. \tag{3.17}$$

Population values using this simplified model for $2S_{1/2}$ and the coronal equilibrium model for $2P_J$ are shown in figure 3.11, as well as calculations for both using a full collisional-radiative model [54], which includes the effect of neutral hydrogen charge exchange, ionization and recombination. The simplified models are accurate to within 25% in the case of the coronal equilibrium model and within 75% in the case of the collisional

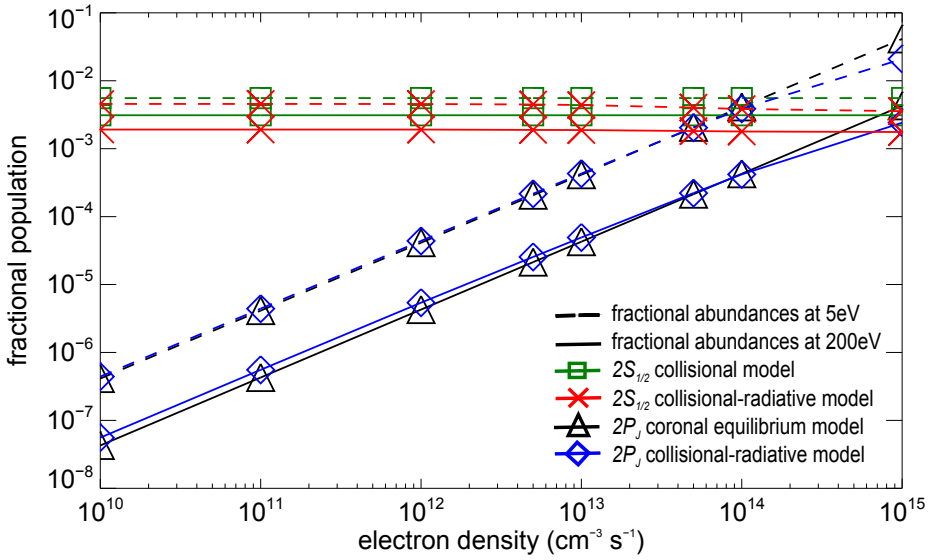


**Figure 3.11:** *Fractional abundances of the first excited state of deuterium as a function of electron density, for both 5 eV and 200eV using both a full collisional-radiative model [54] and simplified models (equations 3.16 and 3.17)*

model over the density and temperature range shown, up to $n_e \approx 10^{15}$ cm$^{-3}$, far higher than the density of tokamak plasmas.

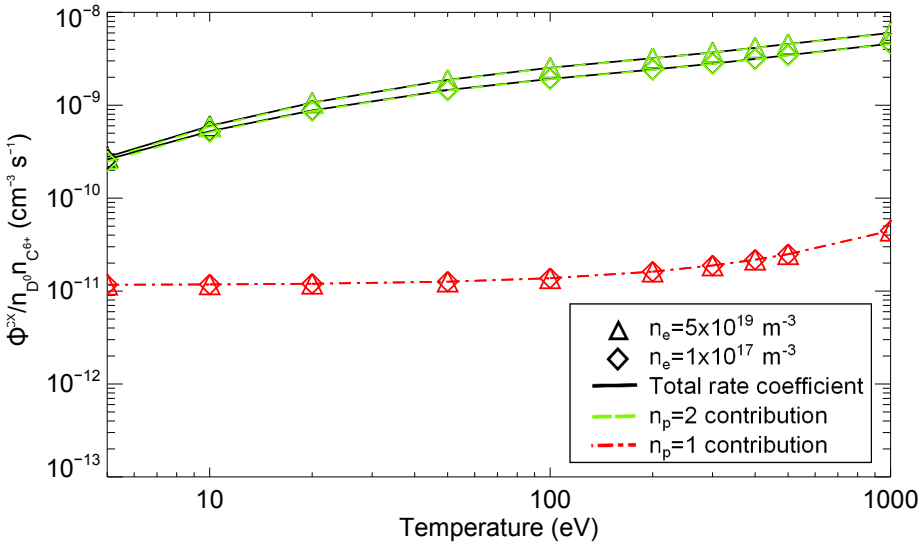


**Figure 3.12:** *Effective rate coefficients for charge exchange of $C^{6+}$ into $n_i = 8$ from $D^0(n_p = 1, 2)$*

The relative contributions of the $2S_{1/2}$ and $2P_J$ levels to the overall rate of charge-exchange emission can be determined. At all but very high densities the population of the $2P_J$ excited state is negligible compared to the $2S_{1/2}$ state, so the fraction is almost independent of electron density. Therefore, the overall fraction can be calculated as a function only of electron temperature, so that the overall contribution to charge exchange

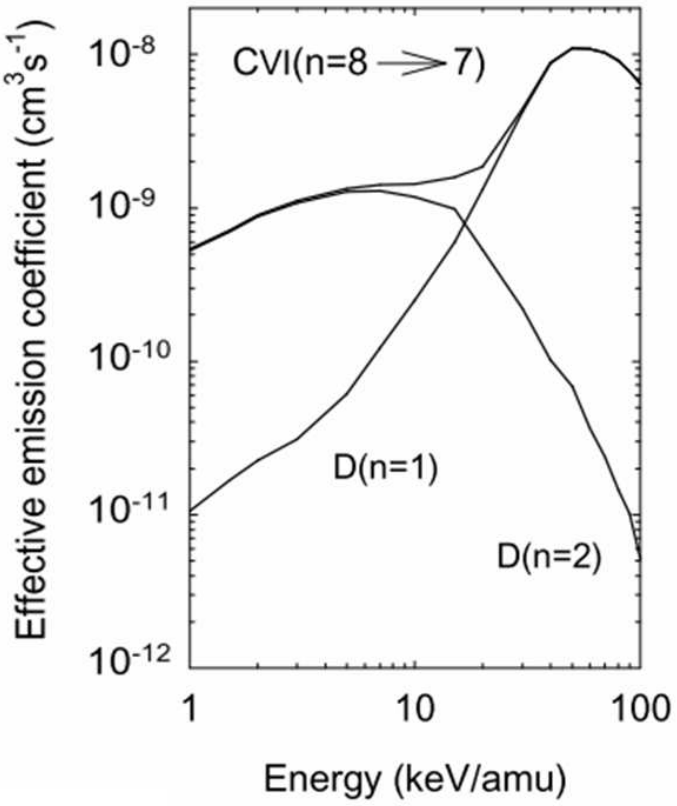


**Figure 3.13:** *Photon emission coefficients for charge exchange emission* $C^{6+}$ $n_i = 8 \rightarrow 7$ *from* $D^0(n_p = 1, 2)$ *at keV beam energies, calculated by Hoekstra et. al. (1998) [67], under the assumptions that* $T_i = T_e = 8$ keV *and* $n_e = 5 \times 10^{13}$ cm$^{-3}$

from $n_p = 1$ and $n_p = 2$ can also be found in terms solely of temperature, assuming $T_i = T_e$, as shown in figure 3.12. This shows that for cold neutrals in the plasma edge the charge exchange signal comes almost totally from exchange with $n_p = 2$ neutrals, the contribution from ground state being negligible in comparison, so that equation 3.12 can be reduced to its second term only. This is compatible with the calculations of Hoekstra *et. al.* (1998) [67] which uses the same cross section data to calculate this at keV beam energies (see figure 3.13).

The active charge exchange signal can therefore be calculated if the density of $C^{6+}$ and of $D^0$ is known. The active charge exchange signal will be visible above background charge exchange if the value of $n_{D^0}(active)$ from the gas puff is large compared with $n_{D^0}(background)$ (see section 3.6.2). However it is also necessary to determine whether charge exchange is the dominant process producing radiation at this wavelength in the plasma, as otherwise any perturbation in the charge exchange signal will be unobservable compared to background even if the number of deuterium atoms from the gas puff is much greater than the number

naturally in the plasma. This will be investigated in section 3.5.

In this analysis contributions from higher excitation levels of the donor deuterium atoms ($D^0(n_p \geq 3)$) have been ignored, which will provide an additional source of charge exchange ions and thus CX emission. However, for $n_p = 3$ the cross section into $n_i = 8$ will be small as the dominant level according to equation 3.5 will be $n_i = 13.2$ with only a fraction entering the $n_i = 8$ state during cascade to the ground state. Furthermore the population of $n_p \geq 3$ will be small as none of these states are metastable, and thus the equilibrium population will be well described by coronal equilibrium, and thus negligible (the fraction of the total population in the $n_p = 3$ state is $\sim 1 \times 10^{-4}$ over most of the temperature and density ranges of interest, while for higher states the fraction will be even smaller).

## 3.5 Background processes

### 3.5.1 Rate coefficients

At the wavelength of interest there are several processes which contribute to the background signal recorded by the ECELESTE system. These include radiative recombination of $C^{6+}$ into the $n = 8$ state and electron excitation of $C^{5+}$ to the $n = 8$ state, both of which are wavelength specific. Bremsstrahlung and cyclotron radiation across the wavelength spectrum, which increase the overall broadband noise produced must also be considered. For a general emission line, dielectronic recombination would also make a contribution, but not for fully ionized ions as this process is only possible in the presence of an atomically bound electron. As an optically thin plasma has been assumed, radiative excitation is also assumed to be negligible. Therefore the background signal can be characterized as

$$\Phi^{BG} = \Phi^{CX(BG)} + \Phi^{EE} + \Phi^{RC} \tag{3.18}$$

or more specifically:

$$\begin{aligned} \Phi^{BG} &= B_{8\to7}\left(n_{D^0}^{BG} n_{C^{6+}}\left(f\langle\sigma_{2\to8}v\rangle_{CX}^{eff} + (1-f)\langle\sigma_{2\to8}v\rangle_{CX}^{eff}\right) + \cdots \right. \\ &\quad \left. + n_e n_{C^{5+}} \sum_{i<8} f'_i \langle\sigma_{i\to8}v\rangle_{EE}^{eff} + n_e n_{C^{6+}} \langle\sigma_{\infty\to8}v\rangle_{RC}^{eff}\right) \end{aligned} \tag{3.19}$$

where $f'_i$ and is the fraction of $C^{5+}$ in state $n = i$.

As there is no ADAS data available for radiative recombination of $C^{6+}$ above the $n = 5$ level an approximate rate coefficient assuming a Maxwellian electron temperature distribution was used to calculate $\langle\sigma_n v\rangle_{RC}$ for the $n = 8$ level and above from Hutchinson (2005) [57], given as

$$\langle \sigma_n v \rangle_{RC} = \bar{g}_n 5.2 \times 10^{-20} Z \left(\frac{\chi_n}{T}\right)^{3/2} \exp(\chi_n/T) E_1(\chi_n/T) \quad \mathrm{m^3 s^{-1}} \tag{3.20}$$

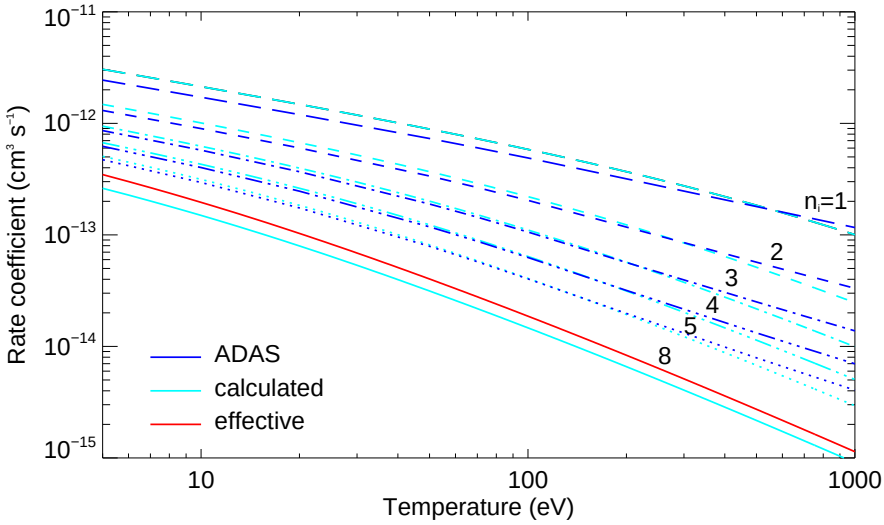


**Figure 3.14:** *Rate coefficients for radiative recombination of $C^{6+}$ into $n_i = 1-5, 8$ from ADAS [54] and equation 3.20 and effective rate coefficient for recombination into $C^{6+}(n = 8)$*

where $\bar{g}_n$ is an average Gaunt factor over the Maxwellian distribution, $\chi_n = Z^2 R_y / n^2$ for recombination to a given level $n$, i.e. the ionization energy of that level and $E_1(x) = \int_y^\infty (exp(-x)/x)\, ds$ is the first exponential integral function. It is assumed that $\bar{g}_n = 1$, which is accurate to within 20% [80], while the approximation $\ln(|1 + 1/x|) - (0.56/1 + 4.1x + 0.9x^2) \approx \exp x E_1(x)$ gives a further inaccuracy of up to 0.5% [57]. When compared to fully calculated values from ADAS for $C^{6+}(n = 1 \rightarrow 5)$ this approximation is accurate to within 25% over the temperature range $5(\mathrm{eV}) \leq T \leq 1000(\mathrm{eV})$ for $n = 1 \rightarrow 5$, such that a similar level of accuracy can readily be assumed for $n \geq 8$. In order to calculate the effective rate coefficient knowledge of the branching fraction for decay into the $n = 8$ level is required. Calculation of this requires solution of a full collisional radiative model for these high level states, but a first order approximation assumes equal decay into lower principle quantum levels such that the branching fraction into level $i$ from upper level $j$ is $1/(j-1)$ (assuming degenerate sub-levels). This is likely to be an overestimate for levels where $j \gg i$ and an underestimate for levels where $j \approx i$ as the spontaneous emission coefficient $A_{ji}$ is proportional to $1/\lambda_{ji}^3$. This correction increases the effective rate coefficient by approximately 10%. This is also shown in figure 3.14

As there is no electron excitation data available from ADAS for electron excitation to levels above $n = 5$ again an analytical approximation is used [57], given as

$$\langle\sigma_n v\rangle_{EE} = 1.925\times10^{-14}\frac{8R_y}{\sqrt{\pi}\Delta E_{nm}}\sqrt{\frac{R_y}{T}}e^{-u}\left(\frac{R_y 2Z^2}{\Delta E_{nm}n_j^3}\left[1-aue^{u+au}E_1(a+au)\right]+\cdots\right.$$
$$\left.+f_{nm}\left[e^u+E_1u-\frac{u}{s+u}e^{s+u}E_1(s+u)\right]\right)\quad \mathrm{m^3s^{-1}} \tag{3.21}$$

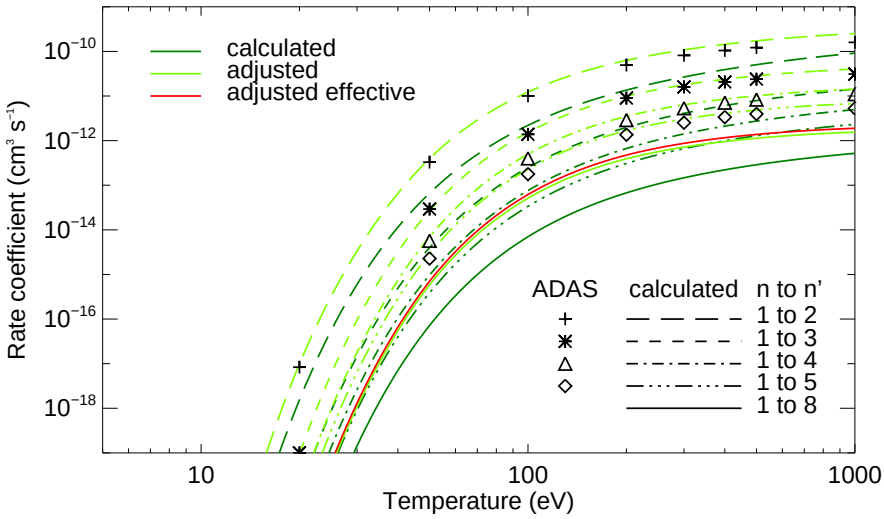


**Figure 3.15:** *Rate coefficients for electron excitation from ground state of $C^{5+}$ into $n_i = 2-5, 8$ from ADAS [54] and equation 3.21, empirically adjusted values and effective rate coefficient for excitation into $C^{5+}(n=8)$*

where $u = \Delta E_{nm}/T$, $a = 4\chi_n/\Delta E_{nm}$, $s = 1/a$ and the oscillator strength $f_{nm} = (32/3\sqrt{3}\pi)n_n(\chi_n/\Delta E_{nm}n_m)^3 g$, with $g$ a Gaunt factor taken to be 1. The results are shown in figure 3.15. Comparison with known values for excitation from ADAS for $C^{5+}(n = 1 \rightarrow 2-5)$ shows that this is a significant underestimate of the true values by a fitted empirical factor in the range 2.7-5.7 over the temperature range 20-1000 eV. Multiplying the analytical results with this factor results in a fit within 30% for temperatures $20 < T < 500$ eV. By making the same assumption as for recombination for the branching ratios, the branching from higher excitations results in increasing the effective rate coefficient by a factor of 22%. Contributions from excited levels of $C^{5+}$ into the $n = 8$ state are negligible, removing the necessity for a summation in equation 3.19.

The rate coefficients of the four processes populating the $n = 8$ state of $C^{5+}$ are shown for convenience together in figure 3.16.

While bremsstrahlung, cyclotron and synchrotron radiation will all produce additional background emission, this is essentially all broad spectrum emission which can be subtracted from the emission spectrum if measured at a wavelength away from the $n = 8 \rightarrow 7$

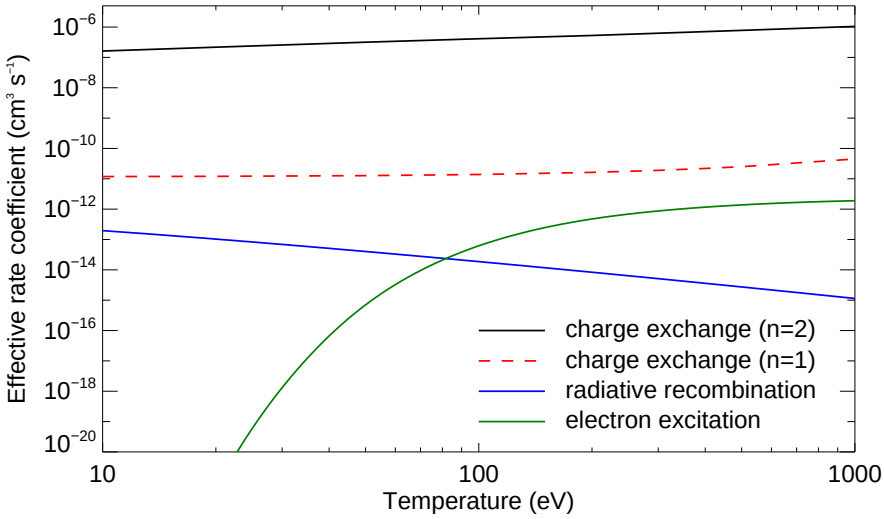


**Figure 3.16:** *Effective rate coefficients for charge exchange, electron excitation and radiative recombination into the final state* $C^{5+}(n = 8)$

charge exchange line. As this radiation can separately be quantified by measurement and subtracted from recorded spectra, consideration of these processes in more detail is unnecessary.

### 3.5.2 The plume effect

In the theory discussed so far the only source of active data is assumed to be due to charge exchange of the donor deuterium with $C^{6+}$ leading to emission from the $n = 8 \rightarrow 7$ transition. The charge exchange process followed by decay to the ground state, however, will mean that there is an extra source of $C^{5+}$ ions produced by the gas puff and which are prompt with its introduction into the plasma. These $C^{5+}$ ions will drift around the torus following the magnetic field lines. If they drift into the line of sight of a viewing chord and are excited by electrons into the $n = 8$ state then this will produce a source of emission which is non-localized to the gas puff and which is likely to be a different temperature and velocity to that attempting to be deduced (see figure 3.17). Therefore it is important to deduce the contribution from this plume emission. Fonck *et. al.* (1984) [32] discuss this for neutral beams and determine that this is most significant for the $n = 2 \rightarrow 1$ transitions of low $Z$ elements, as the electron excitation rates are highest in these transitions. Bell *et. al.* (2006) [81] have expanded on this work and applied it to the neutral beam CXRS system at NSTX and find that for the $n = 8 \rightarrow 7$ transition of $C^{5+}$ it is of most importance in the core. This is due to the fact that the magnetic pitch angle in spherical tokamaks is large at the edge due to the small difference between the toroidal and poloidal magnetic fields

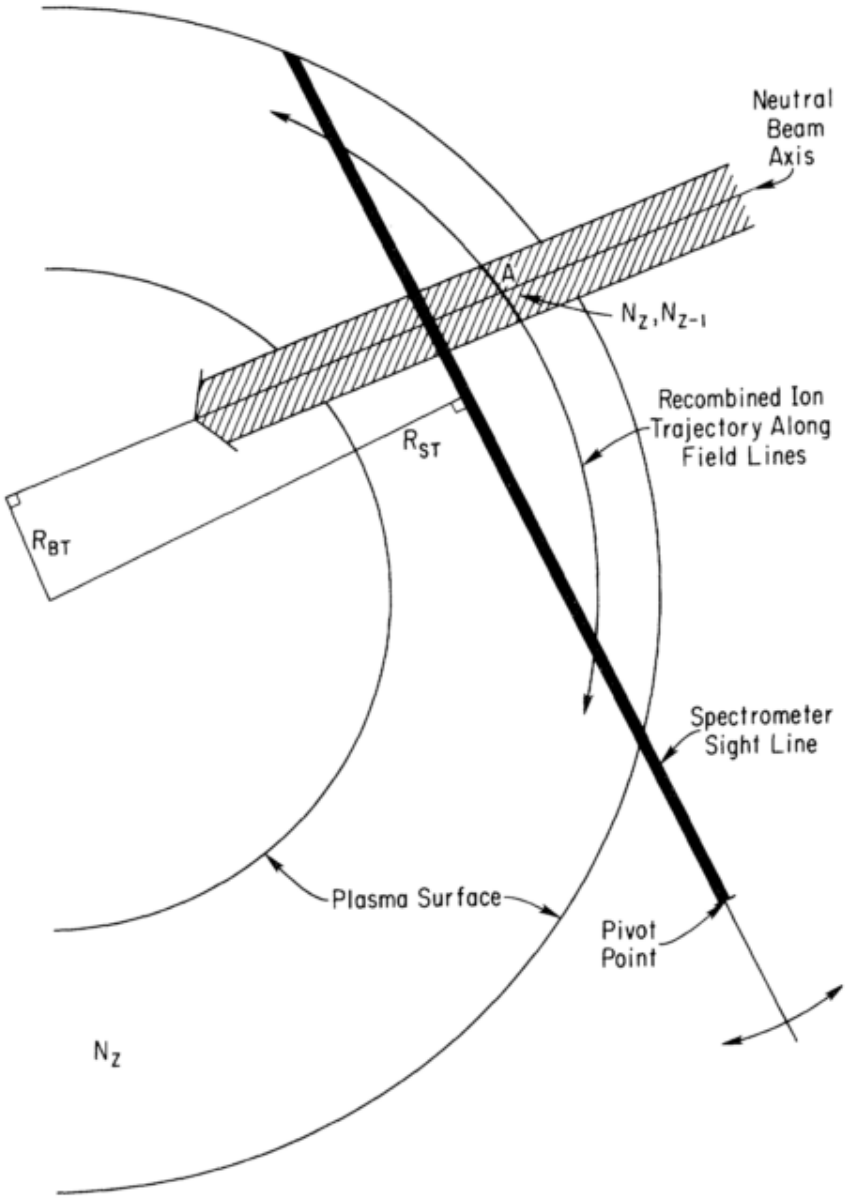


**Figure 3.17:** *A diagrammatical explanation of the plume effect as it affects neutral beam facilitated CXRS. The extra $C^{5+}$ created by a neutral beam can drift around the field lines. If it is excited as it moves across the lines of sight of the spectrometer it can cause spurious emission from locations not at the neutral beam line of sight intersection, giving a false temperature and velocity [32].*

compared to conventional tokamaks. In this case it is therefore only necessary to consider what plume emission is produced locally at the gas puffing location.

The extra $C^{5+}$ produced by the gas puff is balanced by the ionization rate of $C^{5+}$ back to $C^{6+}$. Therefore the density of the extra $C^{5+}$ is given by

$$n_{C^{5+}}^{plume} = \frac{n_{D^0}^{GP} n_{C^{6+}} \langle \sigma v \rangle_{CX}^{TOT}}{n_e \langle \sigma v \rangle_{ION}} \tag{3.22}$$

The extra $C^{5+}$ will only contribute to the emission if it is excited by electrons before it leaves the region observed by the ECELESTE lines of sight. After this it moves away from the midplane and will not be observed if it is excited before ionization. The region covered, as discussed in section 2.2.2, is 1.5 cm in height, and the pitch angle in the plasma edge region is approximately 36° (see section 4.6.2). This gives a maximum observable path length $l$ of $\sim 25$ mm. Using the excitation rate coefficients from section 3.5.1 the path length between excitations is approximately $\lambda_{EE} = v_{||}\tau_{EE}$ where $v_{||} \sim 1 \times 10^5$ m s$^{-1}$ is the parallel velocity of the ions and $\tau_{EE} = 1/(n_e \langle \sigma_{1\to 8} v \rangle_{EE})$. The fraction $f_{EE} = l/\lambda_{EE}$ then gives the ratio of observable to total electron excitation, and is of the order $10^{-7} - 10^{-8}$. From this we can therefore determine the ratio of plume emission to charge exchange emission as

$$\frac{B_{plume}}{B_{CX}} = \frac{n_e n_{C^{5+}}^{plume} \langle \sigma_{1\to 8} v \rangle_{EE} B_{8\to 7} V}{n_{D^0}^{GP}(n=2) n_{C^{6+}} \langle \sigma_{2\to 8} v \rangle_{CX} B_{8\to 7} V} f_{EE} \tag{3.23}$$

where V is the volume enclosed by the intersection of the gas puff and the lines of sight. This can be simplified using equation 3.22 to

$$\frac{B_{plume}}{B_{CX}} = \frac{n_{D^0}^{GP}}{n_{D^0}^{GP}(n=2)} \frac{\langle \sigma v \rangle_{CX}^{TOT}}{\langle \sigma_{2\to 8} v \rangle_{CX}} \frac{\langle \sigma_{1\to 8} v \rangle_{EE}}{\langle \sigma v \rangle_{ION}} f_{EE}. \tag{3.24}$$

This can be evaluated for the edge region using the model profiles used in section 3.3 and can be found to be smaller than $10^{-3}$ everywhere in H-mode and smaller than $10^{-4}$ everywhere in L-mode (see figure 3.18). Therefore the plume effect is not important in this case.

## 3.6 Particle modelling

Given these processes the contribution for each can be calculated if the density of $e^-$, $D^0$, $C^{5+}$ and $C^{6+}$ are known. The density of electrons is well diagnosed by the Thomson scattering diagnostic to a high accuracy, while $n_{C^{5+}}$ can be determined from $n_{C^{6+}}$ and the fractional abundance ratios shown in figure 3.2 as the ratios of the two are assumed to be rigidly coupled. The densities of background and active $D^0$ and of $C^{6+}$ are left to be determined.

All of these data are assumed to be global quantities upon a given flux surface as the transport time around the tokamak is very short, in the region of $10^{-5}$ s, with the exception of the active signal which is localized at the gas puffing region. Therefore it is sufficient to model $n_{C^{6+}}$, $n_{C^{5+}}$ and $n_{D^0_{BG}}$ as functions only of radius.

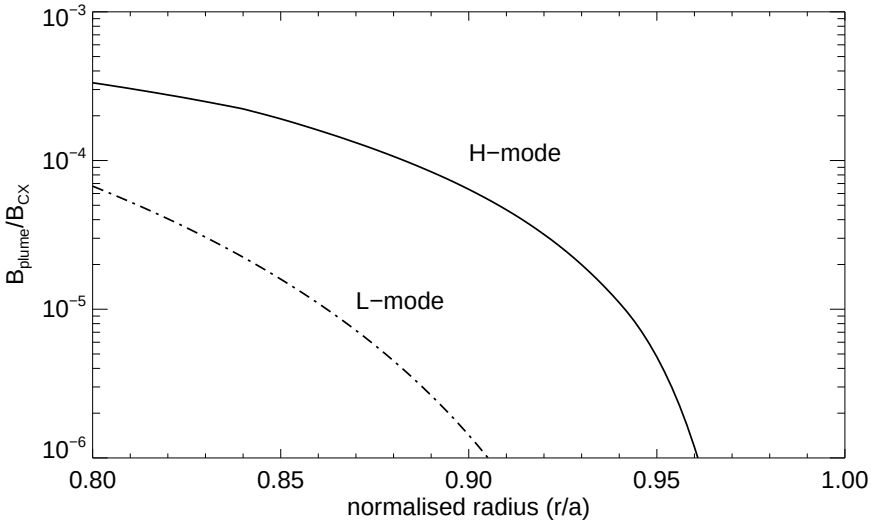


**Figure 3.18:** *Calculated ratio of $B_{plume}$ to $B_{CX}$ using equation 3.24 and the model profiles of section 3.3*

### 3.6.1 Carbon density modelling

The density of carbon is not directly diagnosed, but can be inferred indirectly from measurements of $Z_{eff}$ (assuming carbon is the dominant impurity) or from measurements using neutral beam modelling to reconstruct the impurity density. Within MAST both of these methods are possible but the first allows us to infer the density of both $C^{6+}$ and $C^{5+}$ from the edge $n_e$ and the pre-existing carbon abundance data and has therefore been utilized in this analysis using the definition of $Z_{eff}$ as [5]

$$Z_{eff} = \frac{\sum_j n_j Z_j^2}{\sum_j n_j Z_j}. \tag{3.25}$$

The carbon density profile can vary considerably from shot to shot and between the various modes of operation, as well as change through these modes. Typical profiles are shown in figure 3.19 for beam cut-on (approximately Ohmic), L-mode and H-mode discharges [43]. As can be seen the carbon impurity level is much higher in H-mode than L-mode, implying that signal levels from charge exchange could be stronger in this case. As seen in figure 3.20 the carbon density also builds up through the course of an H-mode. Therefore a typical carbon profile can vary greatly with discharge conditions. To create a generic profile to be used here to estimate the signal level the general shape of the L-mode and H-mode have been retained. A constant value for $Z_{eff} = 1.5$ has been assumed for L-mode, while to construct a model H-mode profile an underlying shape with $Z_{eff} = 1.5$ relative to $n_e$ was combined with a Gaussian shape with a peak value at $Z_{eff} = 2.5$, $\sigma = 0.05r/a$ and centred

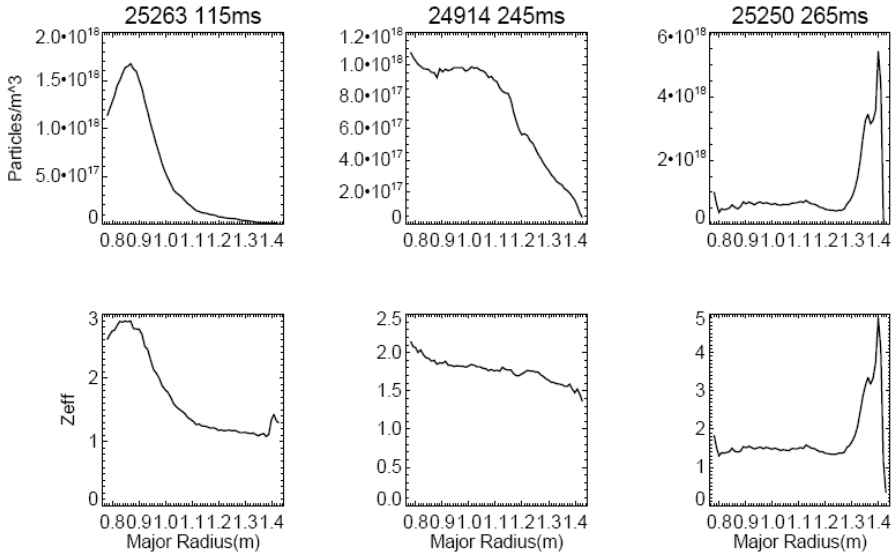


**Figure 3.19:** *Carbon ($C^{6+}$) density profiles in particles $m^{-3}$ (above) that each characterize a typical profile at beam cut-on (approximately Ohmic conditions) (left) during L-mode (centre) and during H-mode (right). Corresponding $Z_{eff}$ values calculated from these are given below. From McCone (2011) [43].*

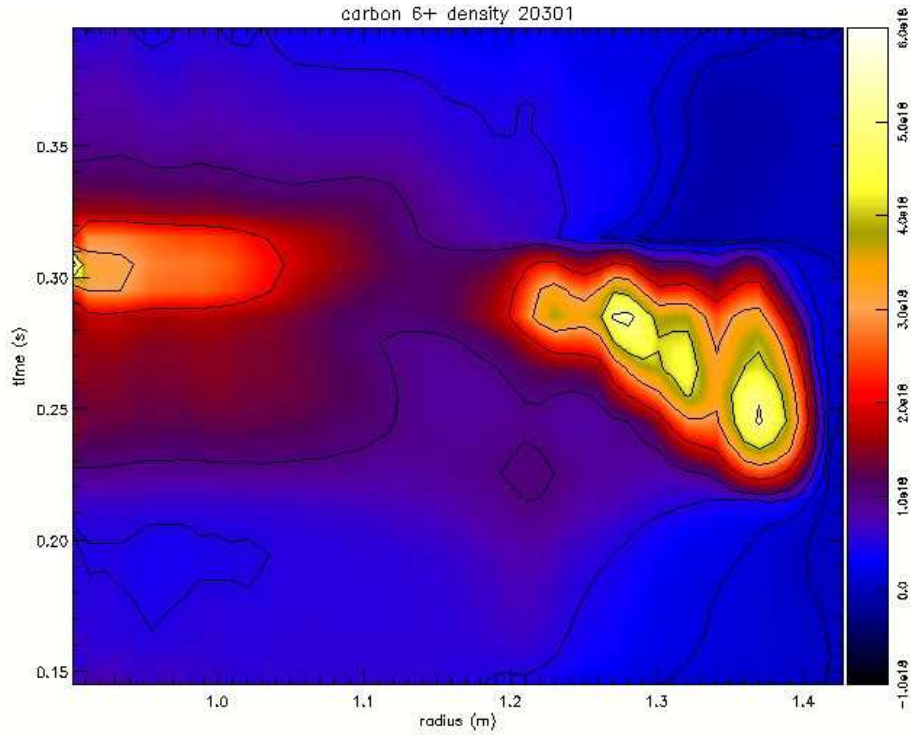


**Figure 3.20:** *Contours of $C^{6+}$ density profiles in particles $m^{-3}$ showing evolution of the carbon profile through H-mode*

at $r/a = 0.92$, which is consistent with measured values [43]. The $Z_{eff}$ profiles used are shown in figure 3.21.

To determine the values of $n_{C^{6+}}$ and $n_{C^{5+}}$, $Z_{eff}$ is approximated as

$$Z_{eff} \approx 1 + \frac{n_c}{n_e}\langle Z \rangle \tag{3.26}$$

where $\langle Z \rangle = \sum_i f_i Z_i^2 / \sum_i f_i Z_i$ is the average charge of carbon in the plasma, assuming carbon is the sole impurity, and $f_i$ are the temperature dependant fractional abundances shown in figure 3.2. Rearranging this given the generic $Z_{eff}$ profiles for L-mode and H-mode gives equations for $n_{C^{i+}}$ as

$$n_{C^{i+}} = f_i n_e \frac{Z_{eff} - 1}{\langle Z \rangle} \tag{3.27}$$

The generic profiles generated are shown in figure 3.22.

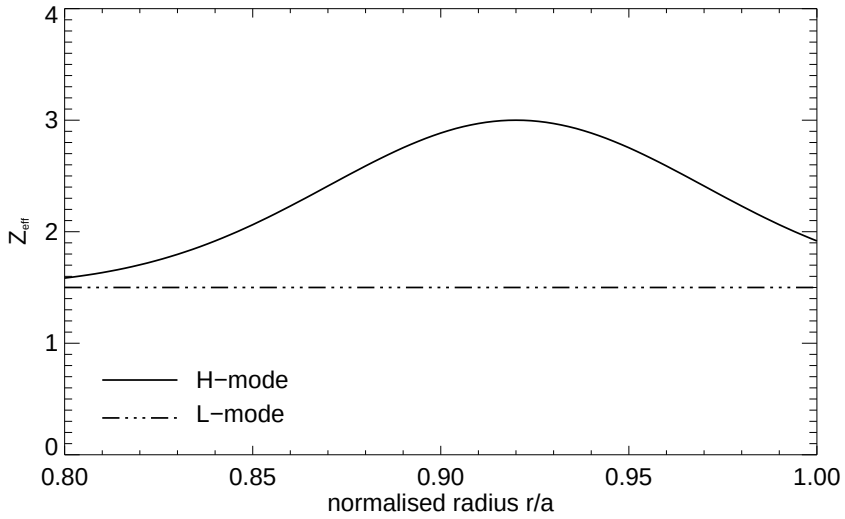


**Figure 3.21:** *model $Z_{eff}$ profiles used in the production of model carbon density profiles of $C^{6+}$ and $C^{5+}$ in figure 3.22*

### 3.6.2 Neutral density modelling

The density of neutrals was calculated using the kinetic transport model KN1D [82]. This is a 1-D in space (minor radius), 2-D in velocity (perpendicular and parallel to the minor geometric axis) slab geometry transport code which calculates the distribution functions $f_H$, $f_{H_2}$ of the atomic and molecular deuterium respectively. From this the density of the atomic and molecular deuterium as a function of minor radius are determined. The model uses a numerical grid to calculate the density using an algorithm which incorporates all

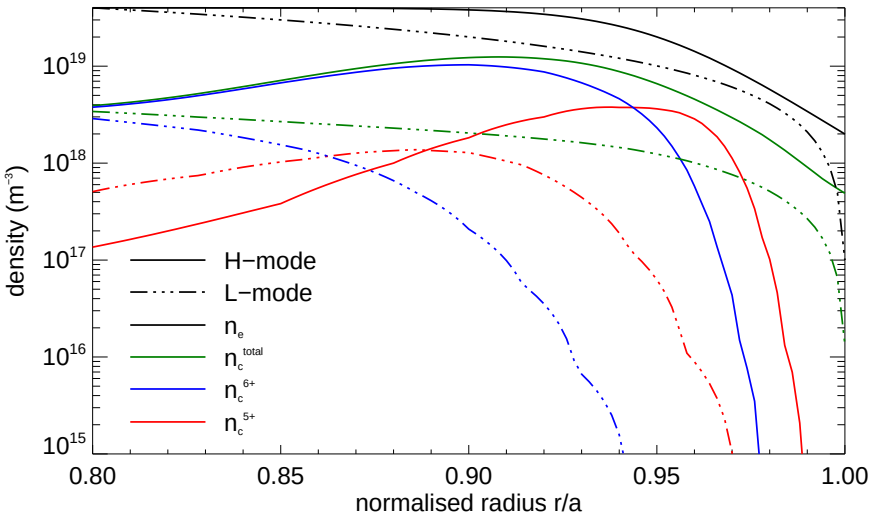


**Figure 3.22:** *model carbon density profiles used in construction of model intensity profiles in section 3.7*

major atomic and molecular processes. The required inputs include the machine geometry as well as profiles for $n_e$, $T_e$ and $T_i$. The model profiles for a typical MAST L-mode and H-mode shown in figure 3.4 were used under the same set of assumptions. The model also required the pressure of $D_2$ neutrals at the vessel wall. In MAST this is provided by a fast ion gauge [83]. In typical shots the value ranges from $1 - 5 \times 10^{18}$ m$^{-3}$. The modelling results are shown in figure 3.23 for a range of different fast ion gauge values. Overall the results for H-mode show a much larger gradient in neutral density as the neutrals enter the plasma due to the higher densities and temperatures typical of H-modes resulting in more rapid ionization.

The charge exchange emission produced by a localized gas puff requires a more complex model for the density of neutral deuterium than outlined above. GTNEUT [84] is a 2-D transmission-and-escape-probabilities code which calculates neutral transport fluxes and densities. The code calculates the flux of particles through each side of the mesh of convex cells specified by the user through a series of time-steps and calculates the number of particles escaping as neutrals during each timestep until equilibrium is reached. Neutrals are unaffected by magnetic fields so the variations in the third dimension can be assumed symmetrical to spatial variations in the second dimension and therefore a full three dimensional image of the gas puff can be created. The code was set up in a slab geometry with boundaries sufficiently far from the gas puffing region to produce no effect on the result and benchmarked using the calculated background flux to ensure that the two codes were compatible for comparison. The results of this are shown in figure 3.24 and show reasonable

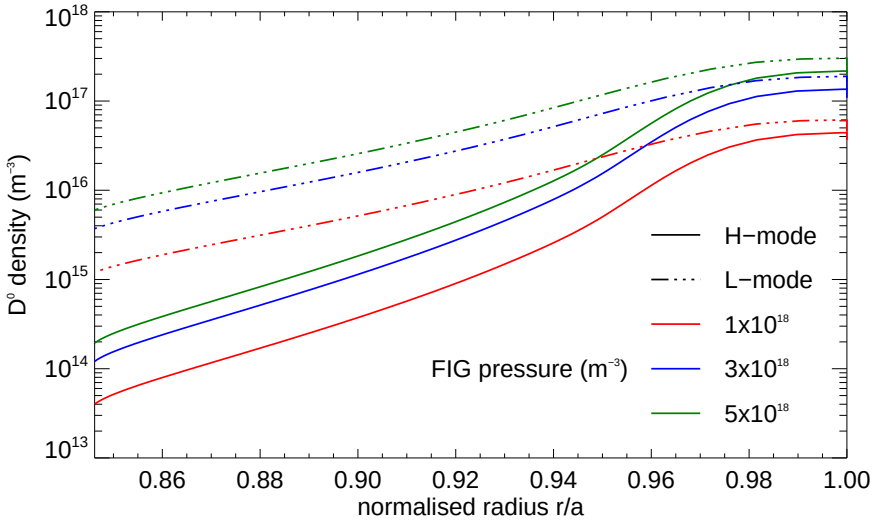


**Figure 3.23:** *Density of atomic $D^0$ as a function of normalized radius in a typical L-mode and H-mode for a range of molecular deuterium wall pressures as measured by the fast ion gauge (FIG) (indicating the maximum, minimum and most likely values for the FIG pressure) calculated by KN1D*

agreement when the total $D^0$ particle flux calculated by KN1D are applied uniformly as a source along the separatrix edge of the GTNEUT model geometry.

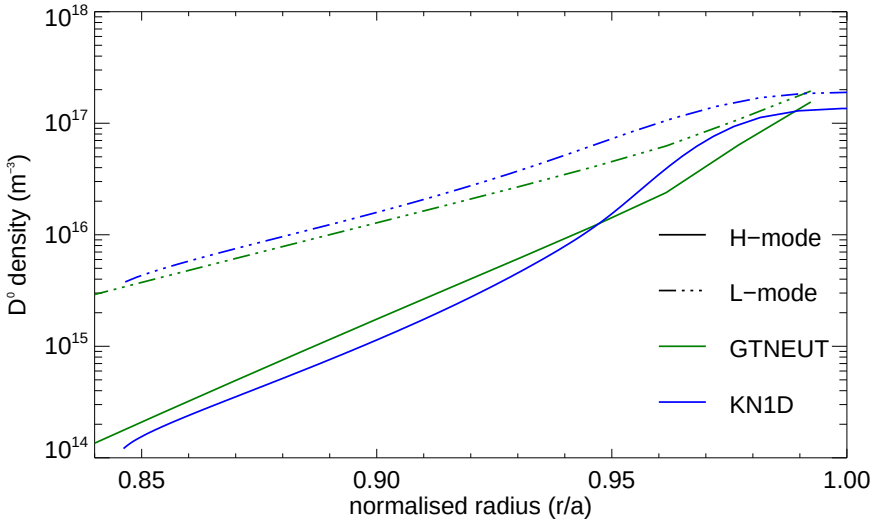


**Figure 3.24:** *Comparison of density of atomic $D^0$ as a function of normalized radius in a typical L-mode and H-mode between KN1D and GTNEUT at fast ion gauge pressure of* $3 \times 10^{18}$ $\mathrm{m}^{-3}$

While the radial variation of the gas puff can be found given an arbitrary source rate for particle influx to the plasma due to the gas puff, it is necessary to make an estimate of

the rate in order to determine the ratio of background to active signal.

The mass flow rate is defined as $\dot{m} = \rho v A$ where $\rho$ is the particle density, $v$ the flow velocity and $A$ the flow area. In MAST the gas puff is provided by the HELIOS nozzle, an external pipe injecting gas at the separatrix supplied from a plenum located outside the vessel (see section 2.2.1). This is large enough that the supplied pressure does not drop during the puff. The flow is regulated by a fast acting piezoelectric valve located $\sim 1.5$ m from the end of the pipe, which has an inner diameter of 4.76 mm. The maximum rating of this valve is 1.5 bar (the absolute upstream pressure $p_u$), while the density at the pipe outlet (i.e. at the plasma edge, the downstream pressure $p_d$) is around $5 \times 10^{-5}$ bar. If the flow regime is that of choked flow, the limit on flow rate is governed by the Mach number of the gas. The criteria for this to be true is that

$$\frac{p_u}{p_d} > \left(\frac{\gamma+1}{2}\right)^{\gamma/(\gamma-1)} \tag{3.28}$$

where $\gamma = C_p/C_V$ is the ratio of specific heats of the gas, which for molecular hydrogen is 1.41, so that the ratio is 1.9, which is greatly exceeded in this case, so the gas flow is indeed in the choked flow regime. Molecular hydrogen is a small and non-polar gas, so can be well approximated as ideal.

If we assume isentropic flow (as there should be no shocks in the flow) the molecular flow rate (molecules $s^{-1}$) can be defined as (see appendix B)

$$\dot{N} = \frac{\dot{m}}{m} = A\sqrt{\frac{\gamma}{mk_B}}\frac{p_u}{\sqrt{T_u}}\left(\frac{\gamma+1}{2}\right)^{-\frac{\gamma+1}{2(\gamma-1)}} \tag{3.29}$$

where $T_u$ is the absolute upstream temperature. The atomic mass flow rate will be double this if it is assumed that all the molecular $D_2$ is quickly dissociated upon contact with the plasma. This is borne out by the KN1D modelling. Given this the atomic flow rate can be calculated as $7 \times 10^{23} \pm 5 \times 10^{22}$ atoms $s^{-1}$. Inserting this into GTNEUT gives an equilibrium density profile, shown in figure 3.25. While the gas puff is a transient phenomenon, as long as the equilibrium is reached on a shorter timescale than the gas puff timescale then these results will be accurate. The timescale for this is approximately the ionization time of deuterium $\tau_{ion}$, defined as

$$\tau_{ion} = \frac{1}{n_e\langle\sigma_{ion}v\rangle} \tag{3.30}$$

The ionization rate coefficient is of the order $10^{-14}$ $m^3$ $s^{-1}$ [85] meaning ionization occurs on a timescale of $10 - 100$ $\mu$s, much less than the gas puff duration (around 10 ms). Equilibrium ionization of the gas puff deuterium can thus be assumed.

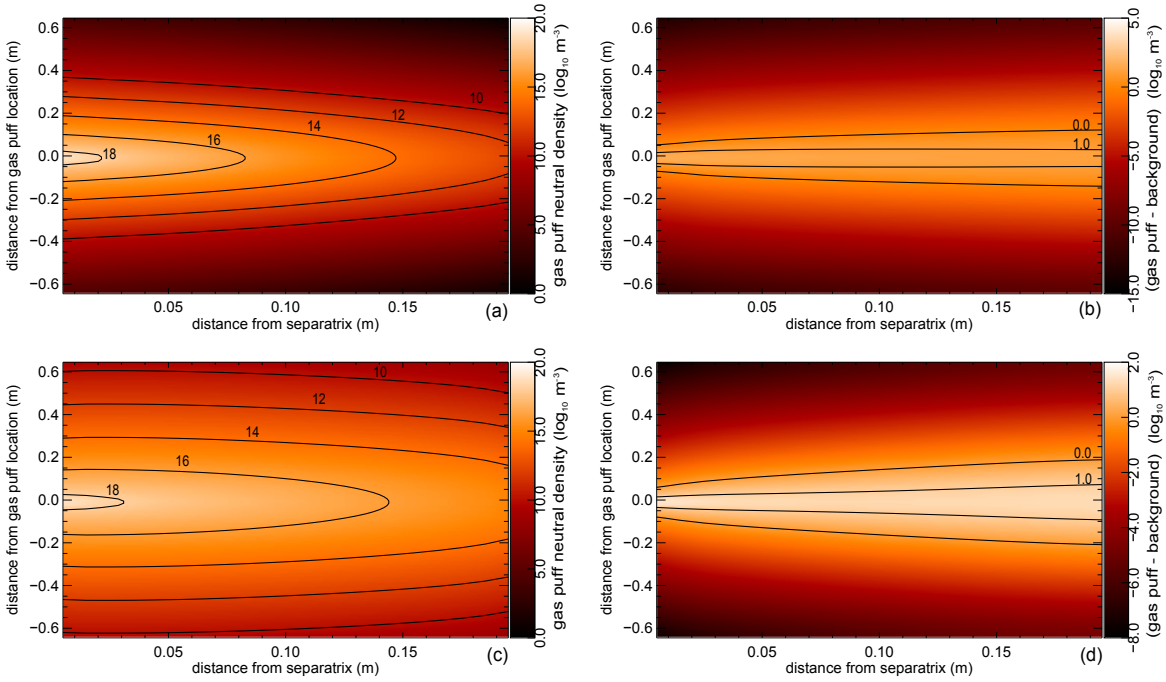


**Figure 3.25:** *Results of modelling of gas puff injection, showing the calculated profiles (a and c) and differential profiles between the gas puff and background (b and d) for H-mode (a and b) and L-mode (c and d)*

The GTNEUT modelling also answers the important question of whether the gas puff atoms will be localized. Figures 3.25(b) and 3.25(d) show the density of the gas puff relative to the background, demonstrating that the gas puff density is as high or higher than background density levels over a radius of 5-10cm (from the vector between the gas puff location and the centre column centre at $z = 0$m) between 0-10 cm inside the separatrix in H-mode, and has a radius of 6-12 cm between 0-10 cm from the separatrix in L-mode. The effect of this finite width will be to produce a measurement over different flux surfaces and therefore reduce the spatial resolution of the diagnostic. The extent of this effect will be dealt with in section 4.7.

## 3.7 Model intensity profiles of charge exchange emission

### 3.7.1 Effect of tokamak geometry

In order to determine the effective penetration depth of the gas puff into the plasma it is necessary to transform the 1D models of densities and temperatures, as well as the 2D model of gas puffing into the toroidal geometry through which the spectrometer collects emission. As the viewing chords of the ECELESTE spectrometer look tangentially through

the edge of the plasma their orientation needs to be taken into account when determining the strength of the active signal relative to the passive (background) signal, as the background will be a line-integrated measurement along the length of the chord, while the active signal also has a finite width along which it is integrated, as shown in section 3.6.2.

To generate model profiles of L- and H-mode signal intensity the outside edge region of the plasma was assumed to be spherical with respect to the centre column centre at $z = 0$m with an outer major radius of 1.45 m. This is approximately correct in the toroidal direction. At the outer radial positions this closely fits the shape of the flux surfaces over the small region of interest and allows the modelling to remain in 2D with the third dimension implicitly symmetrical with the second.

The viewing chords were also assumed to all intersect the gas puff vector tangentially. This is not entirely the case as the chords intersect at small angles to the normal but this assumption is sufficiently close to reality for these purposes.

Transforming to this system the effect is to curtail the penetration depth of the gas puff as the signal strength from the edge background can overcome the active signal on some inner chords.

### 3.7.2 Model profiles

The local emissivity as a function of radius for H-mode and L-mode background processes are shown in figure 3.26. The major contributing factor over most of the region is from charge exchange (dominated by the charge exchange from $D^0(n = 2)$ process) but neither recombination nor electron excitation are negligible. The position of the background well within the position of the separatrix is predominantly due to a lack of carbon at the plasma edge due to the cold ions and electrons used in the model profiles.

The geometry adjusted contour profiles (see figure 3.27) imply a narrow band of high emissivity from the gas puff injection as indicated by figure 3.25. When line integrated along the spectrometer lines of sight the total, signal and background intensities indicate that the active signal is significantly larger than the background over a radially narrow window of approximately 10cm in both scenarios (see figure 3.28). This is similar to the radial extent covered by the ECELESTE spectrometer and would be wide enough to detect a pedestal in the ions with a size of the same order as the electron pedestal (0.5-2 cm [86]). Figure 3.29 also shows that the upstream pressure should be maximised as a reduction produces a proportionally smaller active signal. The modelling implies that the higher temperatures of H-mode plasmas and higher overall density of carbon impurities in the plasma (partially due to the effects of quasineutrality and the electron density pedestal)

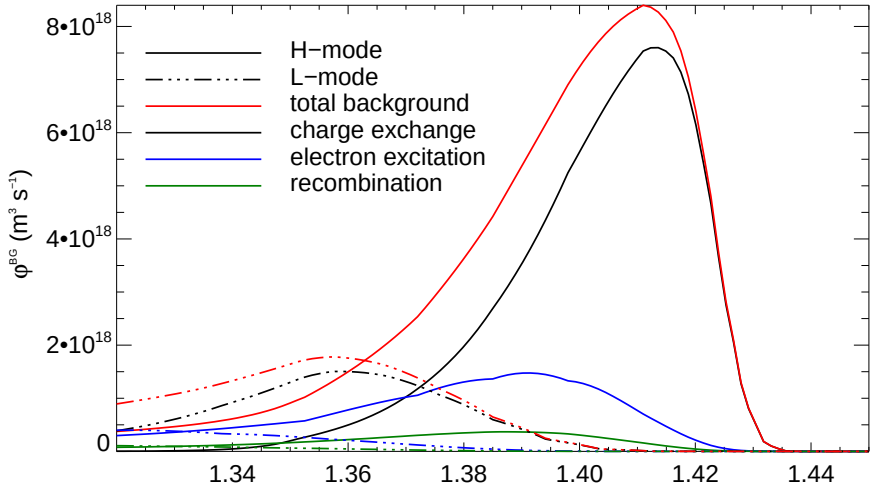


**Figure 3.26:** *Comparison of background emission contributions as a function of radius between H-mode and L-mode model profiles showing the contributions from charge exchange with background deuterium (black), electron excitation of $C^{5+}$ (blue) and electron recombination with $C^{6+}$ (green), as well as the total of these three processes (red)*

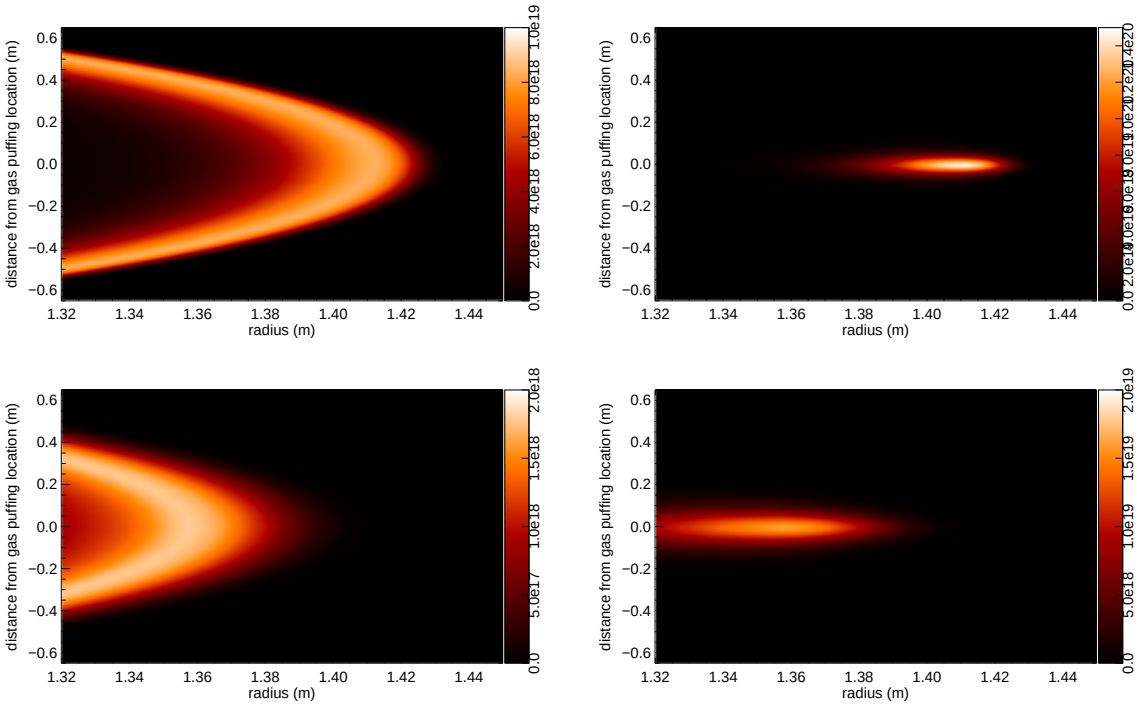


**Figure 3.27:** *Geometry adjusted contour profiles of background (a and c) and active (b and d) emission for H-mode (a and b) and L-mode (c and d) scenarios*

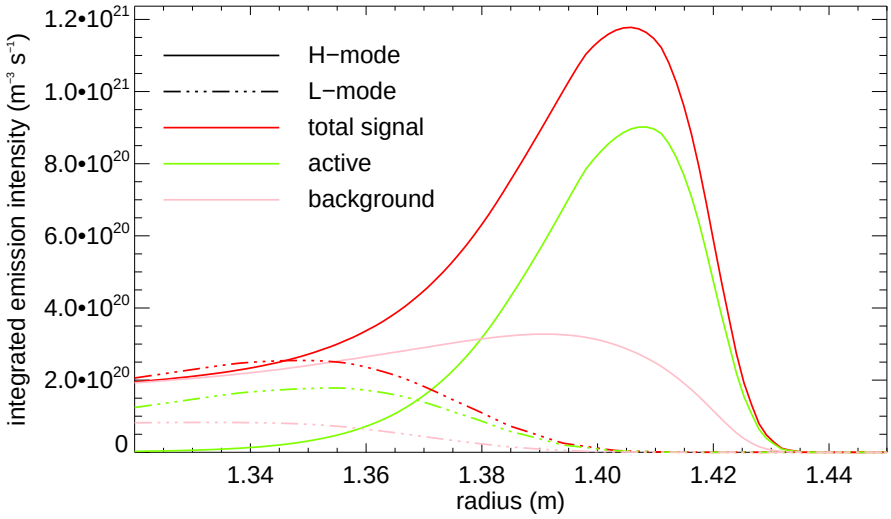


**Figure 3.28:** *Comparison of integrated emission intensities along the spectrometer lines of sight as a function of radius for H-mode and L-mode model profiles*

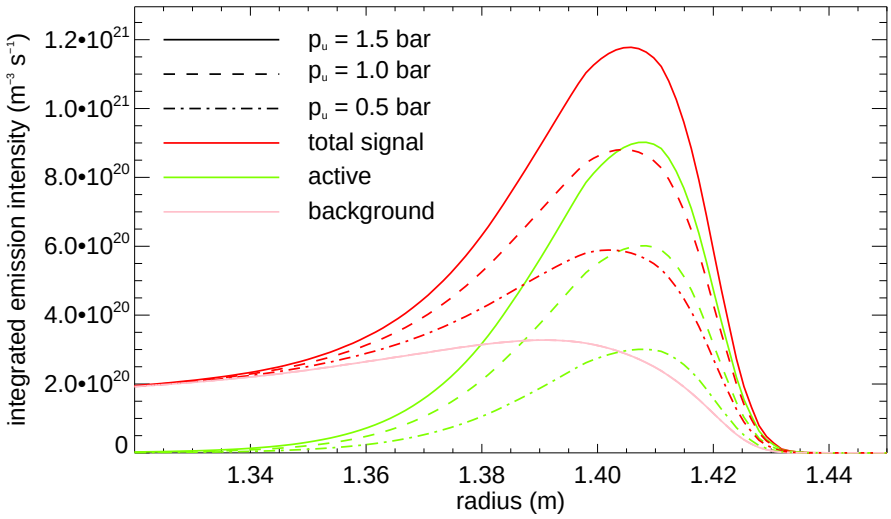


**Figure 3.29:** *Comparison of integrated emission intensities along the spectrometer lines of sight for H-mode scenarios where the upstream pressure in the plenum of the HELIOS nozzle is set at different values, showing the effect on gas puffing signal*

should ensure an approximately 10 times higher signal level in the edge region, despite the lower neutral penetration, in H-mode scenarios.

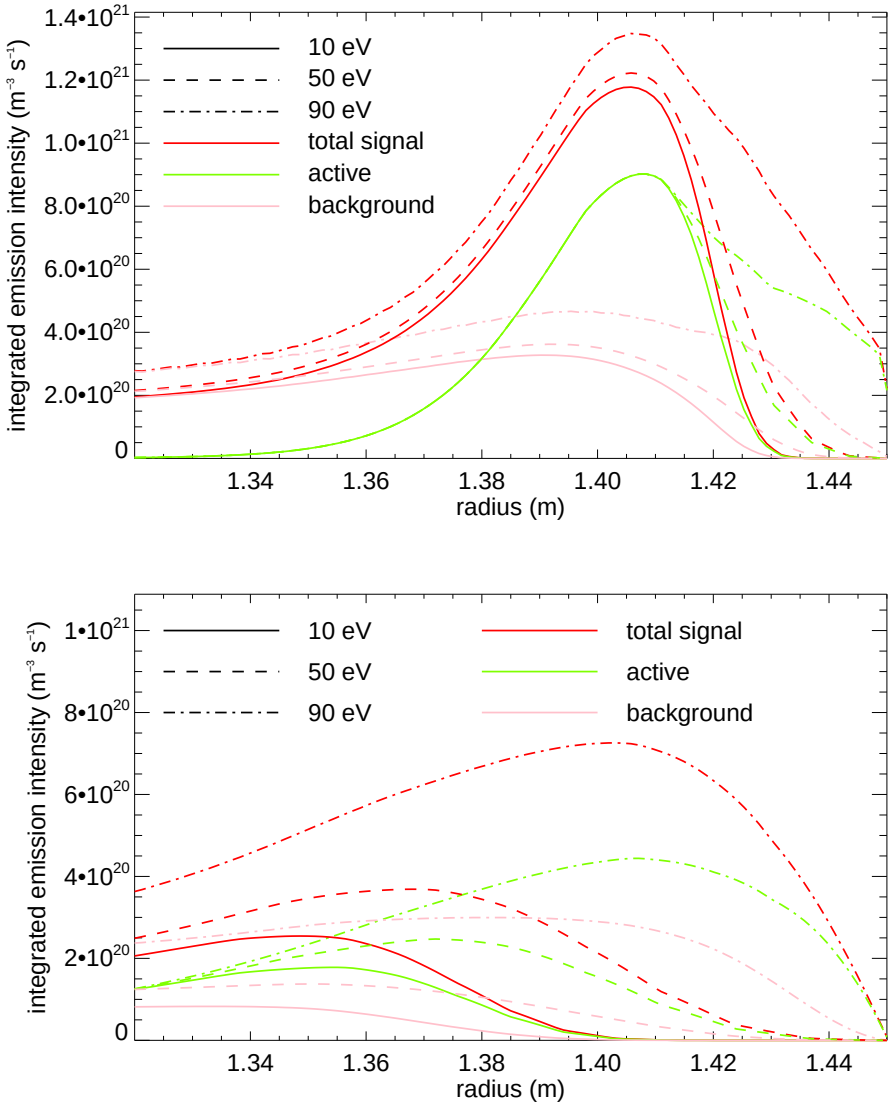


**Figure 3.30:** *Effect of adjusting minimum edge $T_i$ on model emission profiles for H-mode (above) and L-mode (below)*

### 3.7.3 The effect of edge temperatures

Throughout this analysis there have been many assumptions which make the results only an approximation. In the model profiles (figure 3.4) the ion temperature $T_i$ is assumed to equal $T_e$, which falls to 10 eV at the plasma edge. Therefore the density of $C^{6+}$ falls off quickly as the separatrix is approached. This has the effect that the combined signal is only significant approximately 2 cm or 6 cm from the plasma edge in H-mode and L-

mode respectively. A hotter plasma edge for the ions would result in a larger population of $C^{6+}$ (and $C^{5+}$). The L-mode and H-mode scenarios were therefore repeated with a higher edge ion temperature ($T_i(r/a = 1.0) = 50$ eV or 90 eV) to investigate this. The overall results are shown in figure 3.30, and imply that measurements could be made much closer to the plasma edge if ion temperatures remain higher than originally modelled in the near separatrix region. The results also imply the measurement range would also be extended in this case, most significantly in L-mode, where the measurement region could be greater than 13 cm if this scenario were to be realistic. However, due to the inferior penetration of the deuterium neutrals measurements at radii more than 10cm from the plasma edge appear unlikely regardless of edge temperature in H-mode.

The radial extent of charge exchange emission could also theoretically provide a measure of carbon densities. However the modelling challenges are large which would mean the uncertainties in the measurement are likely to be larger than those of existing measurement techniques, so this has not been further investigated here.

### 3.7.4 Analysis of modelling errors

As seen in figures 3.26 and 3.28 the main contribution to overall signal levels is from charge exchange, both background and active. As both rely on the same rate coefficients and $C^{6+}$ density differences between the two signal levels result from the relative densities of neutral deuterium. Therefore the calculations were repeated in both a worst- and best-case scenario, based on the range of uncertainties in neutral pressure at the wall used in KN1D (a range between $1 - 5 \times 10^{18}$ $\mathrm{m}^{-3}$) and neutral particle flux calculated using equation 3.29 (a range between $6.5 - 7.5 \times 10^{23}$ atoms $\mathrm{s}^{-1}$) as well as the most likely scenario calculated above. The results (figure 3.31) show that the radial measurement range would be unaffected, but that the signal to background ratio could vary at the peak signal position from approximately 2:1 in the worst case scenario to approximately 10:1 in the best case in H-mode, and between approximately 3:2 in the worst case and 6:1 in the worst case in L-mode. This indicates that measurements using this technique are likely to be successful, most significantly in H-mode.

### 3.7.5 Conclusion

By assessing the impurities present in the MAST plasma and their ionization distribution over the plasma, as well as the available diagnostic system and line strengths of candidate lines, the best line to use for CXRS measurements is found to be the $C^{5+}(n = 8 \rightarrow 7)$ line. The $C^{6+}$ in the plasma was calculated to be ionized for long enough to be equilibrated

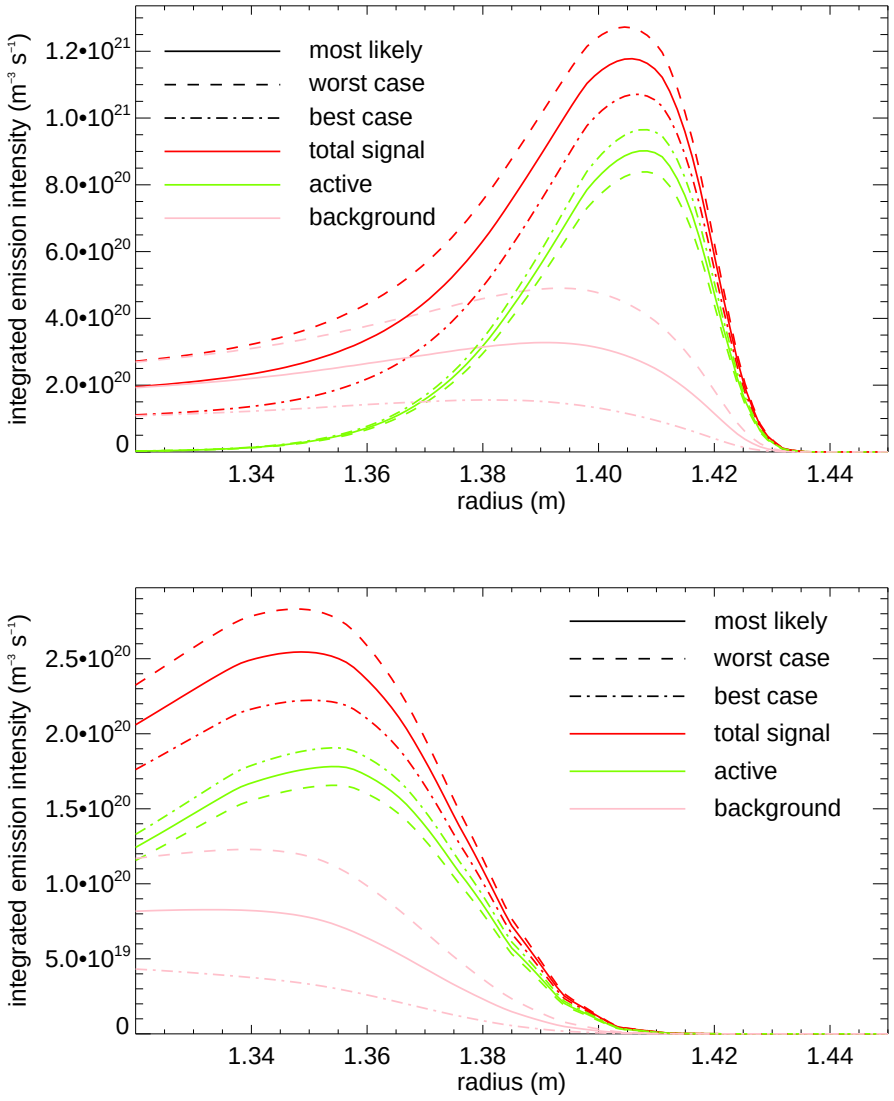


**Figure 3.31:** *Best- and worse-case predictions of emission intensity profiles for H-mode (above) and L-mode (below) scenarios*

with the bulk deuterium in the plasma, and by using model profiles of L-mode and H-mode found to be in equilibrium with it over all flux surfaces. This allows $C^{6+}$ to be used as a proxy for $D^{+}$ in determining ion temperatures and velocities via charge exchange with neutral deuterium provided by a gas puffing nozzle.

Cross sections and effective rate coefficients for the charge exchange process were then produced using the ADAS [54] database, and the contributions from the ground state and first excited state of neutral deuterium to the overall charge exchange signal assessed by calculating the equilibrium population of the deuterium atom. This implied that the dominant process by which deuterium atoms exchanged an electron to $C^{6+}$ is from the first

excited state of the deuterium, and that the ground state and higher state contributions are negligible. The main background processes producing the same $C^{5+}$ $(n = 8 \rightarrow 7)$ emission were identified to be charge exchange from background deuterium ions via the same process as discussed in section 3.4, electron excitation of $C^{5+}$ and recombination of plasma electrons with $C^{6+}$. The effective rate coefficients for these were calculated from analytical expressions and compared to available ADAS data.

Modelling of the densities of $D^0$ present as background, as well as introduced via gas puffing were made, as well as the densities of $C^{6+}$ and $C^{5+}$. The carbon density models were model profiles based on measured $Z_{eff}$ data and the models of $n_e$ and $T_e$ used in section 3.3 along with equilibrium population models for the different ionization states. The model of background neutral deuterium was made using the kinetic transport model KN1D [82]. The active signal was modelled by GTNEUT [84], a 2-D transmission-and-escape-probabilities code. Having benchmarked the two codes against one another to ensure consistency, the modelling showed that the gas puffing would provide a narrow localised region of neutral density which was higher than background in both H-mode and L-mode scenarios over at least 10 cm from the plasma edge, implying that the active signal would be confined to that region and that good spatial resolution would be achieved.

By combining the effective rate coefficients and model profiles for all processes an artificial intensity profile in the geometry of the spectrometer was created for H-mode and L-mode scenarios. This showed a narrow region of good active to background signal ratio, but similar in length to the ECELESTE systems radial coverage. The modelling also implied that the L-mode signal would be much smaller than H-mode signals as $C^{6+}$densities are much lower in L-mode. Furthermore if the plasma edge was cool ($\ll 100eV$) this would mean that measurement near the separatrix would be impossible as there would be no $C^{6+}$in cool regions to provide signal. Overall, however, the modelling in this chapter shows that measurement of ion temperatures and velocities in the plasma edge using CXRS via cold deuterium gas puffing is a viable diagnostic within the first several cm of the plasma's separatrix on MAST, and allows progression to measurements using the ECELESTE system to proceed with confidence. A description of the process of producing measurements of ion temperature and velocity from the data will be made in 4.

# Chapter 4

# Spectra analysis

## 4.1 Introduction

In this chapter the method of determining ion temperatures and toroidal velocities from the width and spectral peak position of the line recorded by the ECELESTE spectrometer after excitation by charge exchange following a deuterium gas puff will be discussed. The complex spectral shape of the spectra is first examined and additional lines to the charge exchange emission identified and investigated. The fitting routine applied to the spectral lineshape is then described, followed by an analysis of the sources of noise in order to assess the size of errors in the temperature and toroidal velocity measurements. The fitting routine is benchmarked to investigate any distortions due to the multi-Gaussian fitting necessary to incorporate the additional lines. A series of correction factors to the width and position of the spectral lineshape are then identified, and the size of these are quantified.

## 4.2 The complex spectrum

In order to produce an ansatz for the fitting function some initial raw data was recorded. These preliminary experiments proceeded by injecting deuterium gas at 1.5 bar as discussed in chapter 2. The data recorded was divided into subsections each containing a single viewing chord. The raw spectral line profiles produced by this proved more complex than the simple Gaussian shape that would be expected from Doppler broadening of a single emission line alone, and this shape varied considerably over the plasma radius. A typical set of spectra as recorded are shown in figure 4.1.

The charge exchange emission line is the sum of hundreds of emission lines of very similar wavelength, split by fine structure degeneracy breaking and Zeeman splitting, amongst other effects. It is also convolved with the instrument function of the system. Each line

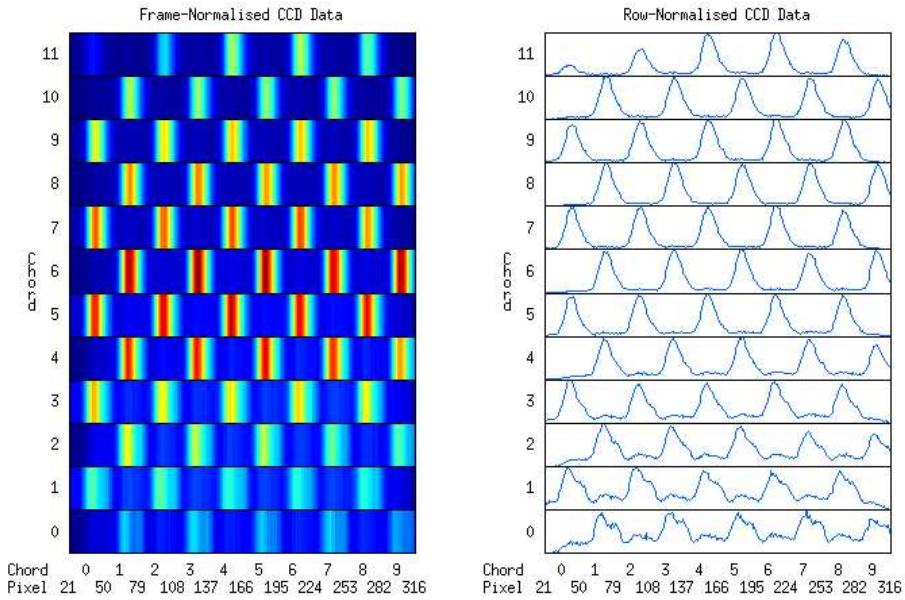


**Figure 4.1:** *Typical raw (binned) spectra produced in initial experiments (shot 20301, time 300 ms). The data is not in radial order but higher row numbers refer to smaller radii, while for each spectra the wavelength increases towards the left. The left hand side indicates the overall intensity recorded normalised over the entire set of spectra while on the right each row has been normalised to the highest peak within that row.*

is broadened by Doppler and Stark broadening. However, it is shown in section 4.6 that the total sum is well represented by a single Gaussian if corrections for all of these effects are made. Therefore the shape of the emission spectrum will highly resemble a Gaussian shape and will be well fitted by one.

The observed spectra show a much more complex spectra, especially at the plasma edge, while further inside a single Gaussian shape produces a much better fit (see figure 4.2). It therefore appears clear that there is at least one other line emitted from the plasma close to the emission wavelength at the plasma edge.

From an initial examination of the spectra it appeared clear that there was at least one other line which is very strong at the edge, often becoming stronger than the charge exchange line (which can be identified from its position at inner radii) at the outermost few chords. As it does not penetrate in as far as the charge exchange line it can be isolated from the charge exchange emission. Fitting to the unidentified line over several shots shows that it has a width very close to the instrument function, and that its spectral position does not change over the radius, implying that this is a line positioned at a constant wavelength around 5288-5289 Å . When deuterium is injected the line integrated intensity increases as shown in figure 4.3. This reduces the identity of the unidentified line to two options. Either

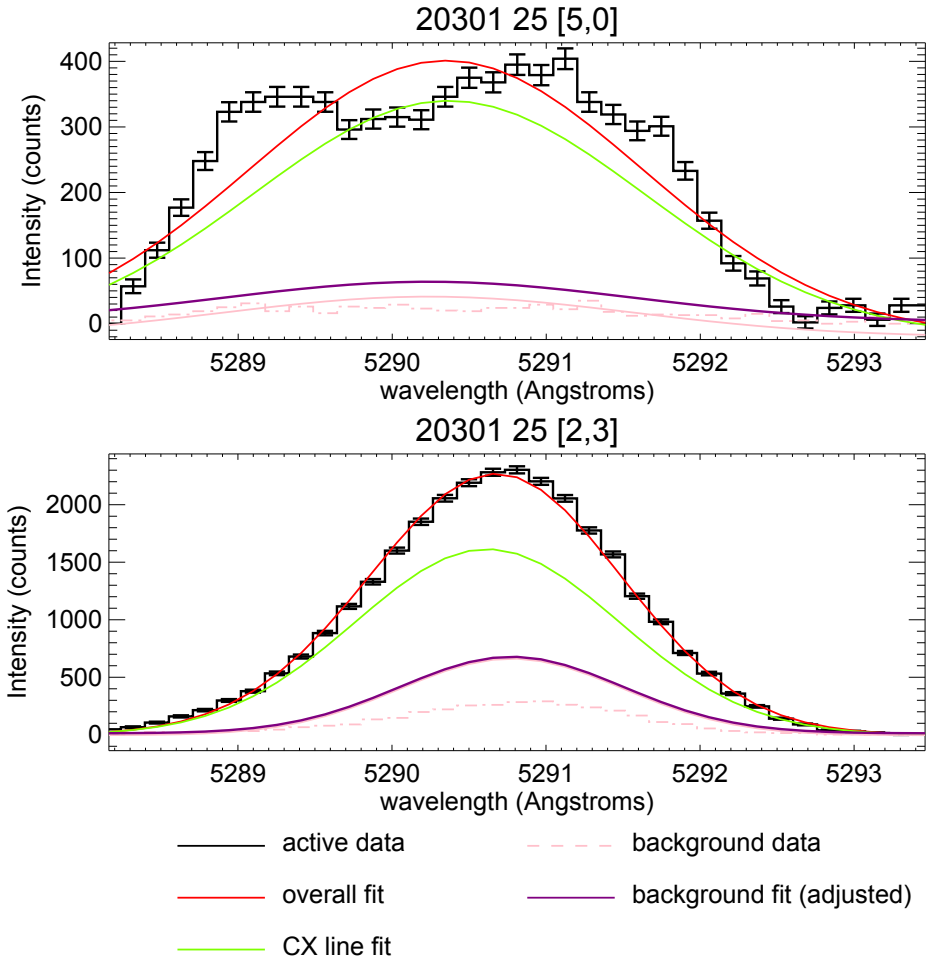


**Figure 4.2:** *A comparison of two raw spectra showing that one-Gaussian fitting does not fit the emission close to the edge (top, major radius 1.413 m) but provides an excellent fit further inside the separatrix (bottom, major radius 1.388 m). From shot 20301, time = 246 ms.*

this is a cold impurity ion which is stimulated to emit by charge exchange due to the added deuterium, or it is a molecular deuterium line where the addition of extra deuterium boosts the emission. Molecular deuterium has over 5000 emission lines over the range 4500-5500 Å [88] so this is a distinct possibility in the plasma edge.

A broad spectrum survey of the plasma edge was conducted using an edge chord of the Motional Stark Effect (MSE) diagnostic [91]. The results show the same line present next to the carbon emission line (see figure 4.4 (b)), removing any doubt that this could be an instrumental effect. As the impurity must have a reasonable prevalence within the plasma the NIST database [90] provides only one plausible line from Fe I at 5288.52 Å [89]. However, the broad spectrum survey does not show the other stronger Fe I emission lines that should be present when compared to an LTE spectrum generated from the line

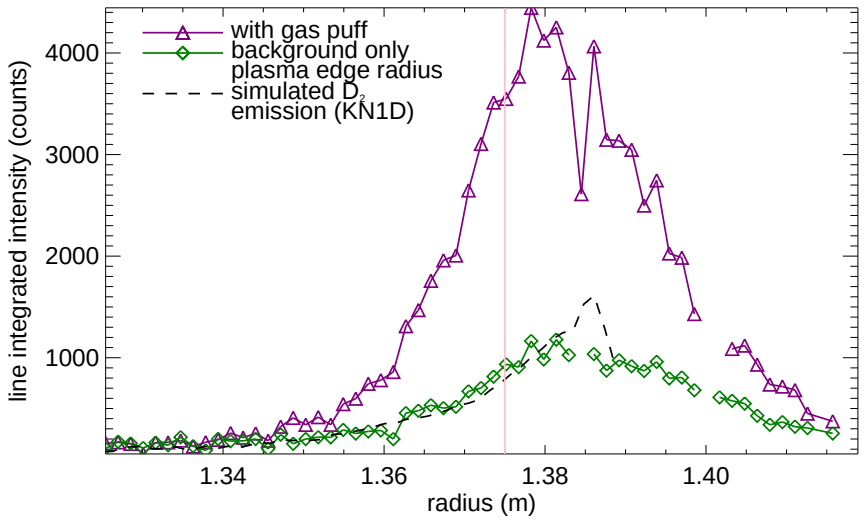


**Figure 4.3:** *A comparison between the line integrated emission intensity profile before and during a gas puff of the unidentified line. The emission profiles are from shot 20262, time = 240 ms (background only) and time = 250 ms (with gas puff). The plasma edge was identified using the HOMER linear camera [87]. The simulated $D_2$ emission was produced from KN1D-generated H-mode profiles and is scaled to fit by dividing by $5 \times 10^{15}$ m$^{-3}$.*

strengths and wavelengths from the NIST database [90] (see figure 4.4 (a)). This eliminates the possibility that the line is an Fe I emission line and leaves only the possibility that this is a molecular deuterium emission line.

A comparison of the line integrated emission spectrum compared with simulated line integrated emission produced from the KN1D data generated in section 3.6.2 shows a similar profile shape which adds strength to the argument that the additional line is $D_2$ molecular emission (see figure 4.3).

To investigate further whether the emission is $D_2$ molecular emission a spectrum from a low pressure deuterium lamp was recorded using a PI Acton lab spectrometer with a 2400 line grating. This has a larger dispersion than the ECELESTE spectrometer, allowing narrow and weak lines to be identified more easily. Fitting to the data recorded from this shows that the already identified line is likely to be the deuterium line at 5288.8 Å (line $a$). There is also a weaker, broader line at 5292.0 Å (line $b$) (see figure 4.5). It seems likely that conditions in the lamp and at the plasma edge are sufficiently similar to assume that this second line is also present and must be accounted for when fitting to the recorded charge exchange spectra, especially considering the obvious existence of line $a$ in the recorded spectra. If this first deuterium line is strong then it is likely that line $b$ is also important in the fitting process. However, the more free parameters are available, the less reliable

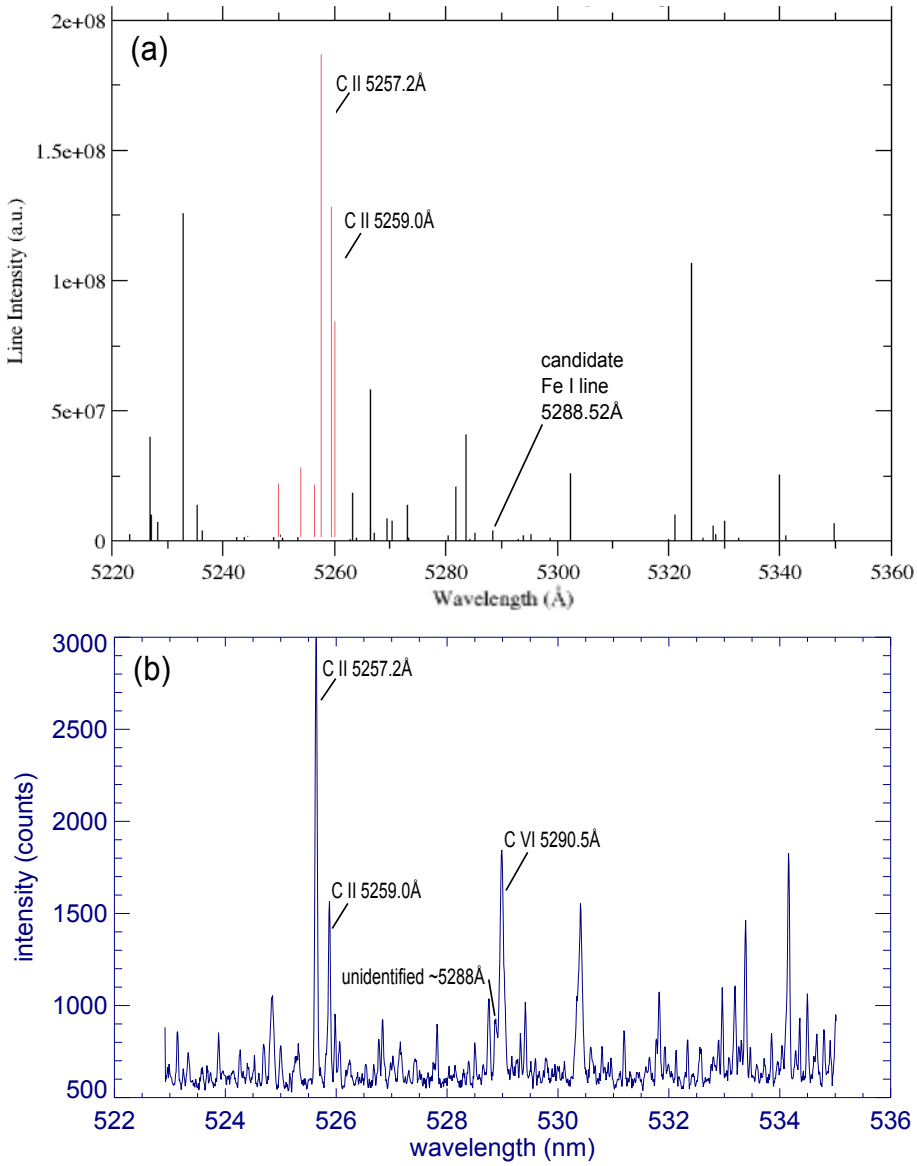


**Figure 4.4:** *A comparison between (a) the expected Fe I emission line spectrum (black) and C II spectrum (red) generated from data by Nave et. al. (1994) [89] via NIST [90] and (b) the measured emission spectrum over the same wavelength range from MAST plasma shot 20879, time = 61 ms. The two strong C II lines have also been identified.*

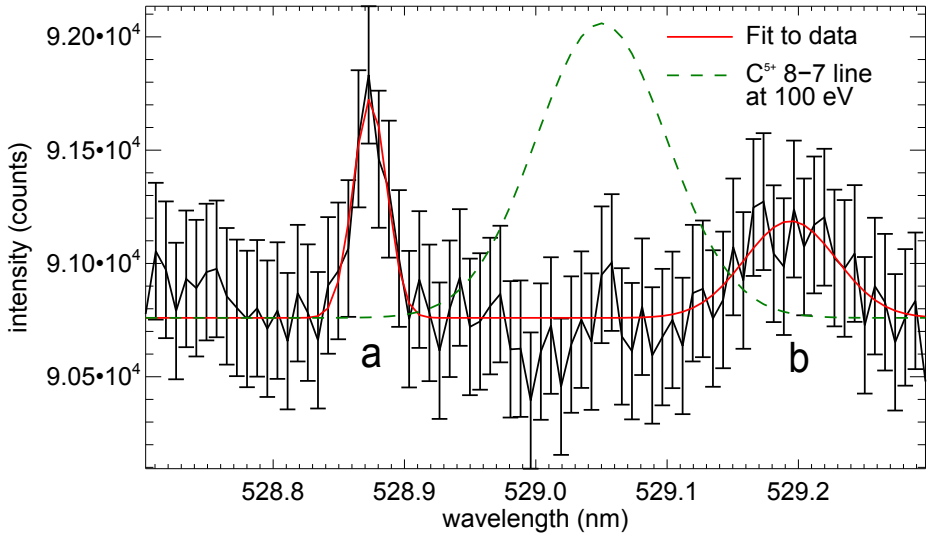


**Figure 4.5:** *The deuterium lamp spectrum around 5290 Å covering the wavelength region in which the $C^{5+}$ emission spectra are recorded using a PI Acton spectrometer. Two emission lines (a and b) are identified by fitting to this. For reference the simulated spectra of the $C^{5+}$ emission line at 100 eV and zero rotation has been added, assuming a negligibly small instrument function. The recorded ECELESTE spectra are more complicated than this due to additional broadening by a variety of effects.*

the fitting routine will be. Therefore only two Gaussian fitted lines are considered for most spectra, with three Gaussian fitting triggered if the measured height of line $a$ is sufficiently large. Benchmark testing (see section 4.5) shows that line $b$ is only important when line $a$ is large, while leaving the line $b$ as a free parameter in all fits significantly reduces the quality of the fit if the height of lines $a$ and $b$ are small. Fitting of spectra where line $a$ is intense shows a marked improvement in the quality of the fit, where spuriously high temperatures at the edge of the plasma were produced if line $b$ was not considered (see figure 4.6).

It is concluded that the unidentified additional lines are due to molecular emission of $D_2$. As the molecular deuterium will be cold and with a small or zero toroidal velocity, the assumptions of severely constrained width and position in the fitting algorithm, as discussed in section 4.3 can be used with confidence.

## 4.3 The fitting routine

In order to determine the position (for velocities) and width (for temperatures) of the active spectral emission it was necessary to fit the data with an analytical curve $f(x, \mathbf{a})$ (where $x$ is the pixel number and $\mathbf{a}$ the fitting parameters). As discussed in section 4.2 it was necessary to fit multiple Gaussians to the spectrum. The fitting equation to the line

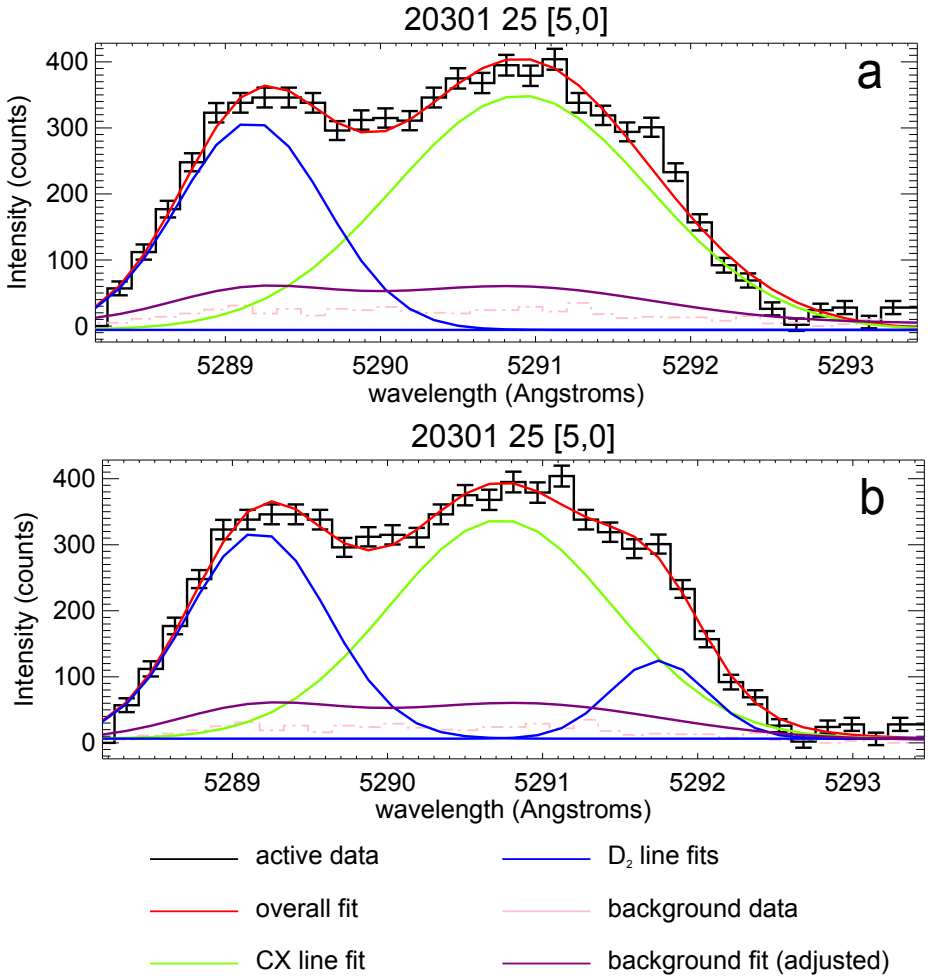


**Figure 4.6:** *Comparison of two (a) and three (b) Gaussian fitting for an example profile near the plasma edge (∼ 1 cm inside separatrix). The top fit with only two Gaussians shows a poor fit on the red wing of the data which is corrected by the three-Gaussian fit.*

profiles was initially set to be

$$f(x,(a)) = \sum_{i=0}^{n} a_{3i} \exp\left(-\frac{(x - a_{3i+1}^2}{2a_{3_i+2}^2}\right) + a_{3n+1}. \tag{4.1}$$

where $n$ is the number of Gaussian fits. Comparison with equation 1.7 shows that $a_{3i}$ are the maxima of the Gaussians, $a_{3i+1}$ the centroids, and $a_{3i+2}$ the standard deviations and $a_{n+1}$ the baseline. We will define $a_0$, $a_1$ and $a_2$ as the maxima, centroid and standard deviation of the charge exchange line. Generally $n = 2$ but if triggered three Gaussian fitting to the data is made.

Equation 4.1 was fitted to the data using the IDL fitting code MPFIT [92]. This uses the Levenberg-Marquardt non-linear least squares fitting algorithm. A general overview of this technique can be found in, for example, 'Numerical Recipes in C' by Press *et. al.*

(1998) [93].

The fit to each line profile recorded for a viewing chord begins with $N$ data points representing the spectral variation of the line profile intensity variation in the form of the number of photoelectrons $y_i$ at CCD pixel positions $[x_1 \dots x_i \dots x_N]$. The $\chi^2$ value of the fit of $f(x, \mathbf{a})$ to this set of data is therefore

$$\chi^2(\mathbf{a}) = \sum_{i=1}^{N} \frac{(y_i - f(x_i, \mathbf{a}))^2}{\sigma_i^2} \tag{4.2}$$

where $\sigma_i$ are the individual independent, normally distributed standard deviations on each measured datum $y_i$.

The MPFIT routine calculates the spectrum and derivatives of the fitting function $f(x, \mathbf{a})$ using the initial guesses $\mathbf{a}_{initial}$ supplied by the user. Then the $\chi^2(\mathbf{a})$ value of this fit is calculated. The method minimises the $\chi^2$ function through the use of two algorithms. The method of steepest descent is applied far from the minimum and then switches to the inverse-Hessian method as the minimum is approached. It does this by iteratively adjusting a step size parameter $\delta\mathbf{a}$ which interpolates from the method of steepest descent when $\delta\mathbf{a}$ is small to the inverse-Hessian method when $\delta\mathbf{a}$ is large. The routine finds the value of $\chi^2(\mathbf{a} + \delta\mathbf{a})$. If the iteration $\chi^2(\mathbf{a} + \delta\mathbf{a}) \geq \chi^2(\mathbf{a})$ then $\delta\mathbf{a}$ is decreased and $\chi^2(\mathbf{a} + \delta\mathbf{a})$ is recalculated. If $\chi^2(\mathbf{a} + \delta\mathbf{a}) < \chi^2(\mathbf{a})$ then $\delta\mathbf{a}$ is increased, $\mathbf{a}$ is replaced by $\mathbf{a} + \delta\mathbf{a}$ in the function $f(x, \mathbf{a})$ and the function and $\chi^2$ recalculated. Once the reduction in $\chi^2$ reaches a tolerance limit from one step to the next the iteration stops and the best fit is found.

The advantage of this profile fitting method is that it is more robust than the inverse-Hessian method alone as it can often find the solution even if the initial ansatz is far from the final minimum. However, it does not find a global minimum, only the local one. In order to reduce this problem and maximise the chances of finding the global minimum, the fitting parameters $\mathbf{a}$ were constrained with upper and lower bounds close to the expected parameters, while leaving a large enough range to cover all possible values. To further improve fitting the fitting parameters $a_4$ and $a_5$ (and $a_7$ and $a_8$ where applicable) were constrained very closely to their ansatz values. This is justified in section 4.2 and the impact of this assessed in section 4.5.

## 4.4 Sources of noise

In order to minimise $\chi^2$ using the above technique, the statistical error $\sigma_i$ on each pixel must be known. The individual pixels will each have an independent error which consists of several sources.

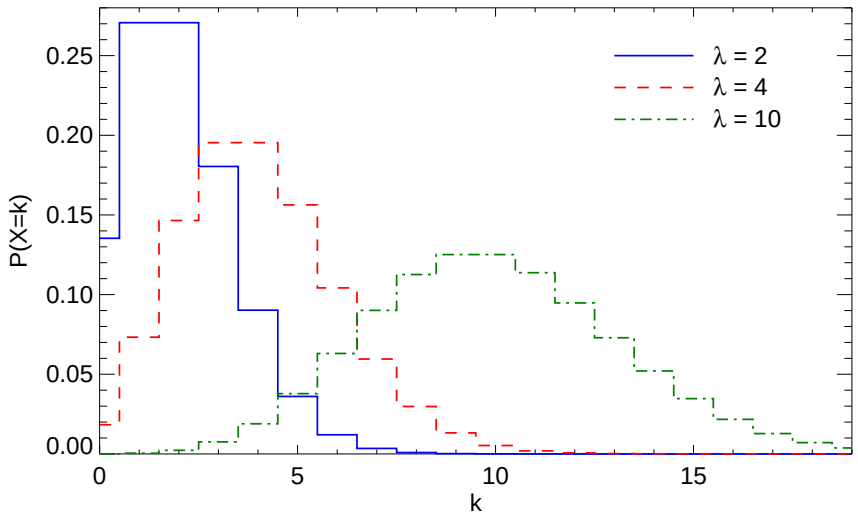


**Figure 4.7:** *The probability that $k$ events will be recorded for a Poisson distribution with expectation value $\lambda$ for several values of $\lambda$, calculated using equation 4.3.*

1. Shot noise: Any system which measures quantized variables that are emitted randomly will be subject to shot noise. A source emitting photons (such as the charge exchange process within the MAST plasma) will emit an average number of random independent photons over time. The number of photons collected in a given time interval will not necessarily be the average, but may be more or fewer. This spread about the average will be a Poisson distribution, where the expectation that there will be $k$ events (where $k$ is a positive integer) is given by

$$f(\lambda, k) = \frac{\lambda^k e^{-\lambda}}{k!} \tag{4.3}$$

   where $\lambda$ is the expected value (i.e. average photons recorded) and also the variance. Although the number of photoelectrons at each individual pixel can be accurately measured, the spread due to this variation produces a variation over the total spectra which is analogous to other forms of noise, and can thus be regarded as such.

   As illustrated in figure 4.7 this distribution approaches a normal distribution when $\lambda$ is large, as implied by the central limit theorem. This is important as least squares fitting assumes that the errors are normally distributed independent values. At all but very low intensities this will therefore be true as shot noise is generally dominant over other forms of noise. Each pixel can therefore be classified as an independent variable with mean $\lambda$ counts and standard deviation $\sigma = \sqrt{\lambda}$ counts to first order.

2. Dark noise: Even when no light is incident upon the CCD, electrons and holes are

still randomly generated in the CCD's potential wells. The number generated is proportional to the temperature of the CCD and is the main reason the camera is Peltier cooled to 200 K. At this temperature the number of electrons generated is only 0.71 per second per pixel. Considering that frame exposure times range from 5 to 10 ms this can therefore be largely disregarded as negligible (0.0071 electrons RMS at 10 ms).

3. Readout noise: As described in section 2.2.4 the camera reads out each pixel of data through an amplifier and ADC. The process of transforming clumps of electrons to a digital signal has an inherent error associated with it. The readout noise is the average variation in reading out the same data multiple times (e.g. taking several unilluminated zero exposure time frames and calculating the standard deviation in the difference between them). This provides another advantage of using a store region and binning data by allowing the data to be read out slowly after the discharge is over. As the error is related to the speed at which the data is read out, faster readout times produce noisier data. For the Wright Instruments CCD the low speed readout produces a standard deviation of 4.3 electrons RMS for each pixel, independent of the frame exposure time.

4. Continuum noise: Bremsstrahlung, cyclotron and synchrotron radiation produce a continuous background upon which line emission is superposed. As these processes produce a background which varies only weakly over the small wavelength range measured the emission is therefore simply a constant background source of photons which add to the overall shot noise. By fitting a non-zero baseline to the overall emission this can therefore be accommodated.

A further complication to calculating the noise is that each digital count represents approximately $\mu = 2.5$ electrons at the maximum gain available. Therefore the Poisson noise in photoelectrons for $N$ counts is $\sigma_{shot} = \sqrt{\mu N}$.

The total noise in counts can be calculated as a combination of all sources of error, i.e.

$$\sigma = \sqrt{\sigma_{shot}^2 + \sigma_{dark}^2 + \sigma_{readout}^2} \tag{4.4}$$

At large counts the shot noise dominates and the error becomes approximately normally distributed. At low counts, however, the error is larger than the expected normal distribution for this number of counts, leading the fitting algorithm to give less weight to pixels which are actually within the true standard deviation of the measurement. Therefore, this tends to produce bad fitting when the overall pixel count is low. However, due

to the continuum noise, recorded data tends to be dominated by shot noise everywhere on the CCD and pixel counts are large enough to avoid this problem.

## 4.5 Fitting benchmarking

Benchmark testing (testing using known centroids, maxima and widths) of the fitting routine was carried out to ascertain whether two-Gaussian fitting would be reliable or create systematic fitting errors to be corrected or excluded. In order to do this sets of 100 model profiles each of varying height, width, position and height ratio were created over the expected data range of the fitting parameters. These were given a randomly seeded Poisson error and then fitted using the above methodology. Any systematic errors should therefore produce deviations in the fitted parameters from the originals.

The parameters $a4$ and $a5$ in equation 4.1 were fixed for the purposes of benchmarking. Table 4.1 shows results from an example comparison fit between fixing the position and width of the deuterium line, as opposed to leaving all parameters free. While fixing parameters should in theory improve the fitting quality, this might also lead to a systematic error if the fixed positions are not correct. However no systematic error of this kind can be detected while there is a reduction in the error and in the standard deviation of the deduced line width and position if the parameters are fixed.

| Parameter | Model values | Free | Fixed |
|---|---|---|---|
| Width (pixels) | 5.0 | 4.931 ± 0.288 | 4.962 ± 0.192 |
| Position (pixels) | 15.0 | 14.940 ± 0.303 | 14.999 ± 0.219 |

**Table 4.1:** *Comparison between free and fixed parameters for the deuterium line on fitting of model spectra*

Using the fixed parameters $a4$ and $a5$ for deuterium line width and position a more thorough survey of the parameter space was conducted by varying intensities, height ratios, widths and heights of the modelled emission lines. The most obvious and expected effect of doing so was that increasing spectra signal height resulted in better statistics, due to the Poisson noise error being proportional to signal height (figures 4.8,4.9). For the width fitting it was found that there were large discrepancies at low intensities with a very large range of fitting results when the width was large, thus indicating that all fitting here should be disregarded as unreliable. Therefore the fitting was discarded if

$$a_2 \geq 0.086 a_0 + 2.57 \text{ (pixels)} \tag{4.5}$$

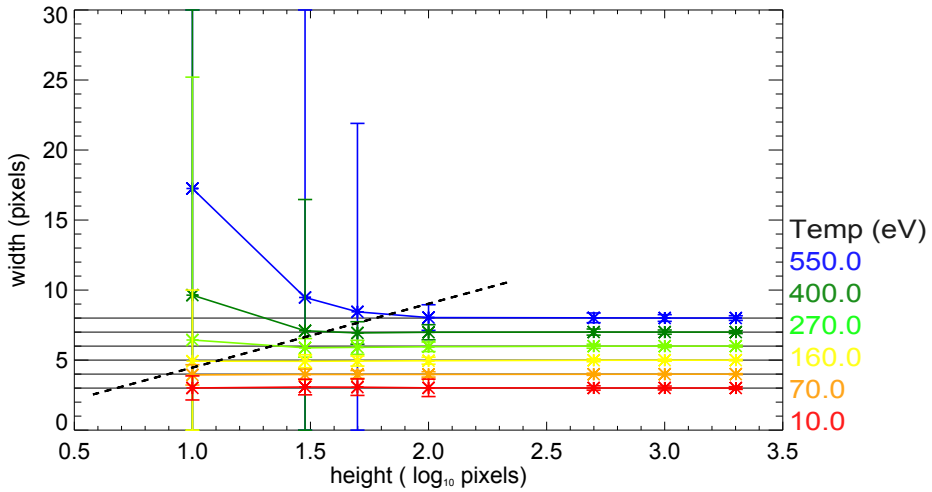


**Figure 4.8:** *Relationship between modelled height and fitted and model widths of two-Gaussian fitting technique also showing the cut to discard the fitting results where the fitting becomes unreliable.*

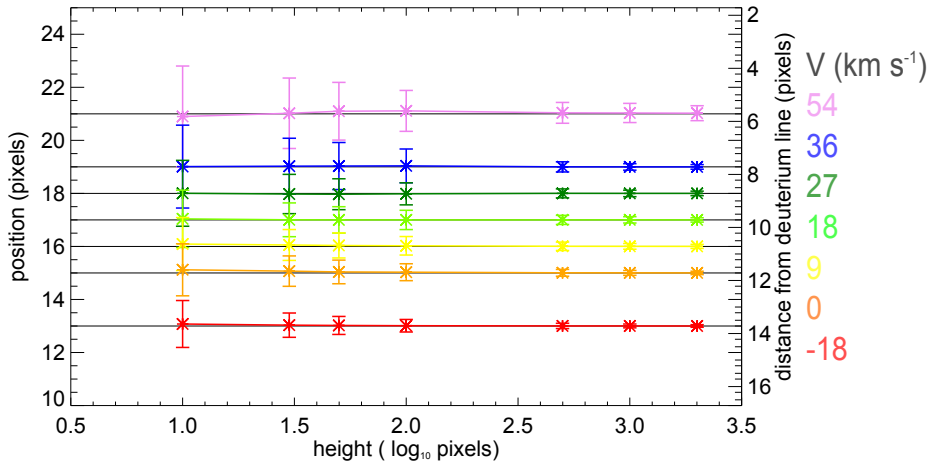


**Figure 4.9:** *Relationship between modelled height and fitted and model positions of two-Gaussian fitting technique*

where $a_0$ and $a_2$ are defined in equation 4.1. In fitting the spectral positions of the carbon emission line the fitting routine was able to replicate the input parameters at all values, albeit at increased uncertainty at lower intensities.

An analysis of the height ratio between the carbon line and the deuterium line (defined as $a_3/a_0$ from equation 4.1) shows that the distance between the peaks has a distinct effect upon the fitting when the carbon peak height was low, tending to overestimate the width when the modelled width was large and the spacing between peaks was large, and underestimate the width when the spacing is small (see figures 4.10,4.11). At low heights the height ratio has a moderate effect when the height of the two peaks was similar, but generally there was little correlation with the modelled ratio of peak height and failure of

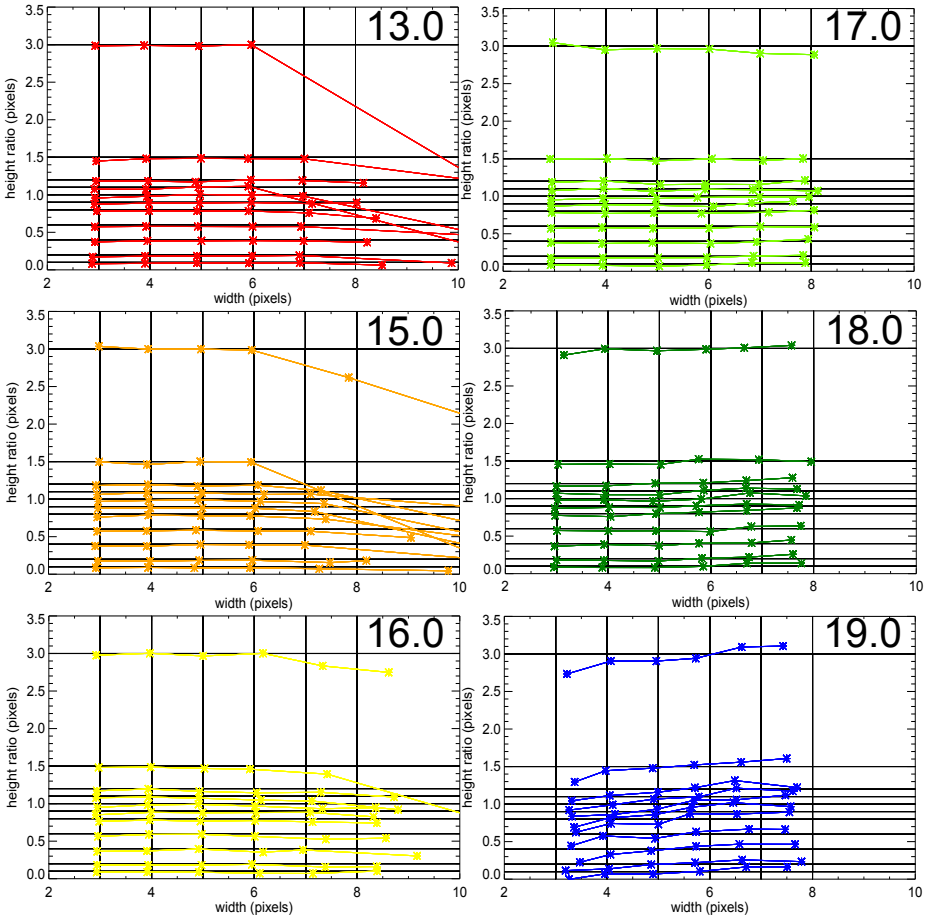


**Figure 4.10:** *Relationship between modelled height ratio at a carbon line height of 30 counts and fitted and model heights of two-Gaussian fitting technique for each modelled position (in pixels at top right of each plot, $v_\phi$=0 when pixel number is 15 and one pixel equated to $\sim$ 9000 km s$^{-1}$ in terms of plasma rotation.). The modelled position is shown as a black grid while the average measured position is shown on top.*

the fitting to replicate the modelled values. Most of the bad fitting is due to the fitting routine misidentifying the two separate peaks as one large carbon peak and a much smaller deuterium peak, leading to an overestimation of the width of the carbon peak, and an underestimation of the deuterium peak height as shown in figure 4.12. However, this is mostly confined to low height fitting so introducing a threshold requirement on the height of the carbon emission line can eliminate this analysis problem. From figure 4.13 it can be seen that there is no correlation between position fitting and this bad fitting effect however as the average position fit is always correct.

Though this benchmarking survey does not address the background subtraction or the effect of placing limits on the fitting parameters, the study provides an indication of the limits of the fitting procedure and suggests reliable ranges within the fitting parameter

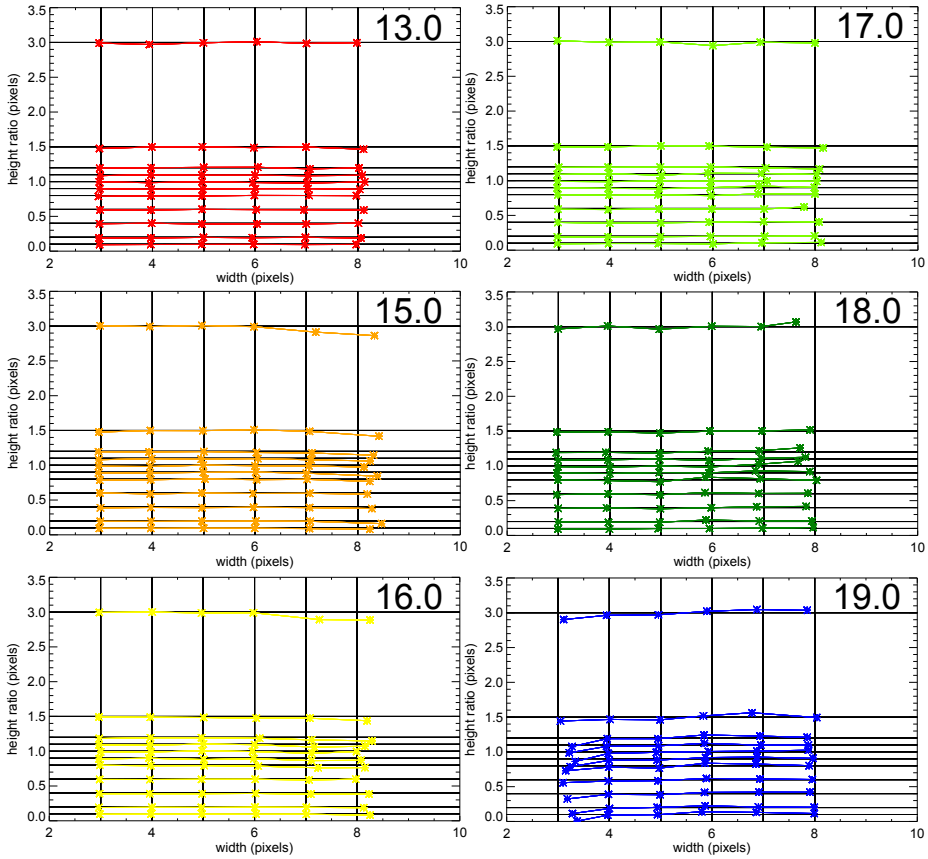


**Figure 4.11:** *Relationship between modelled height ratio at a carbon line height of 100 counts and fitted and model heights of two-Gaussian fitting technique for each modelled position (in pixels at top right of each plot, $v_\phi$=0 when pixel number is 15 and one pixel equated to $\sim$ 9000 km s$^{-1}$ in terms of plasma rotation.). The modelled position is shown as a black grid while the average measured position is shown on top.*

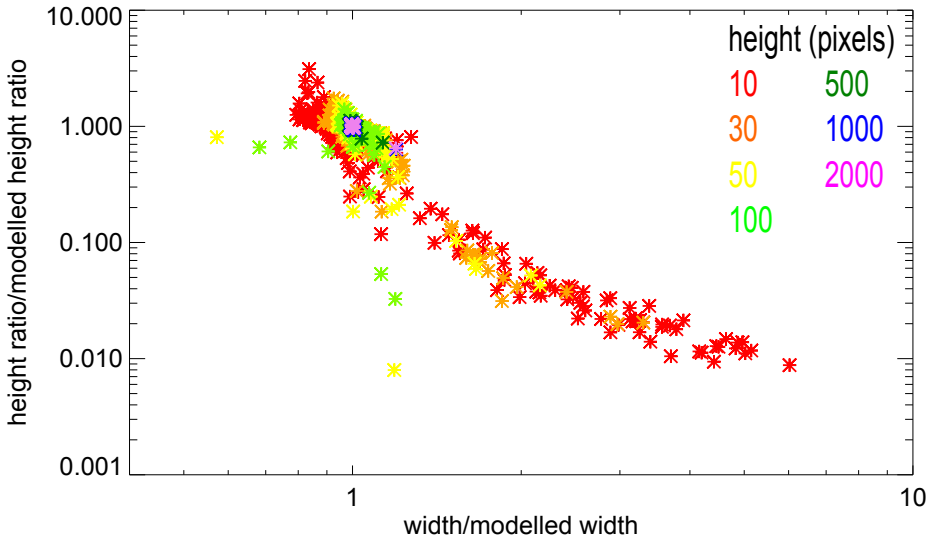


**Figure 4.12:** *Correlation between the ratio of fitted and modelled widths and the ratio of fitted and modelled height ratios between the two emission lines*

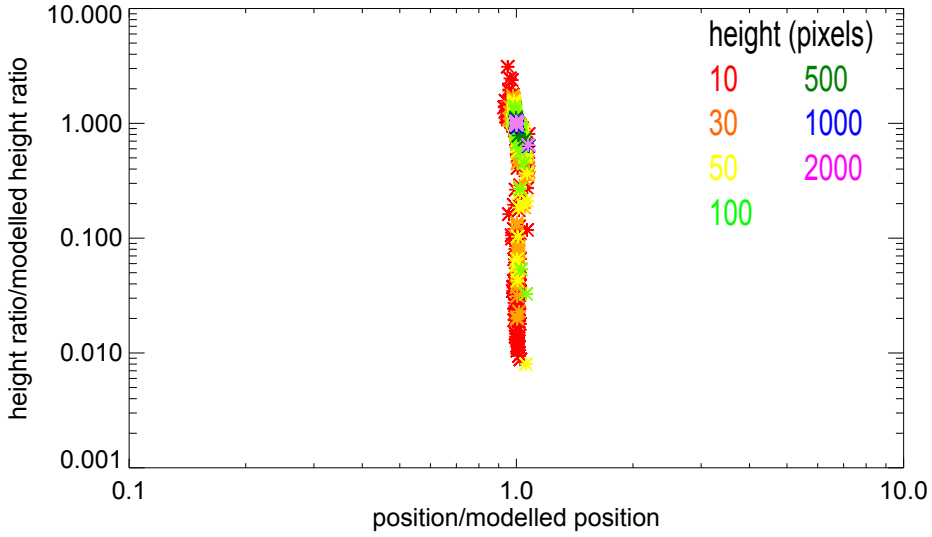


**Figure 4.13:** *Correlation between the ratio of fitted and modelled positions and the ratio of fitted and modelled height ratios*

space. In summary, as well as the limit imposed in equation 4.5 spectral widths fitted to the carbon emission line where the line height is below 50 counts should not be regarded as reliable, and error estimations should reflect this.

## 4.6 Fitting corrections

Beyond Doppler broadening and Doppler shift other processes can introduce uncertainties in the width and position of the charge exchange emission line. Other effects can also change the shape of the line from Maxwellian which affects the validity of the fitting process. The size and effect of these processes must be considered in order for the results to be reliable, and if the effect is large, corrections made. The various processes are discussed in this section and their effect on the resulting temperature and velocity profiles assessed.

### 4.6.1 Fine structure effects

Until now the charge exchange emission line has been considered to be a single wavelength transition between the $n = 8$ and $n = 7$ principle quantum levels of $C^{6+}$. However, the energy levels are split into different $l$-levels, each of which is split further into two $j = l \pm \frac{1}{2}$ levels (see figure 4.14) [59]. Levels with the same $j$ value are generally degenerate and are coupled in tokamak plasmas by ion microfields for all levels except for $n = 2$ [94]. Therefore $j$ becomes the good quantum number.

As described in section 3.4.1 certain resonant $n$-levels are dominantly populated by the charge exchange process, the dominant average level being given by equation 3.5. For

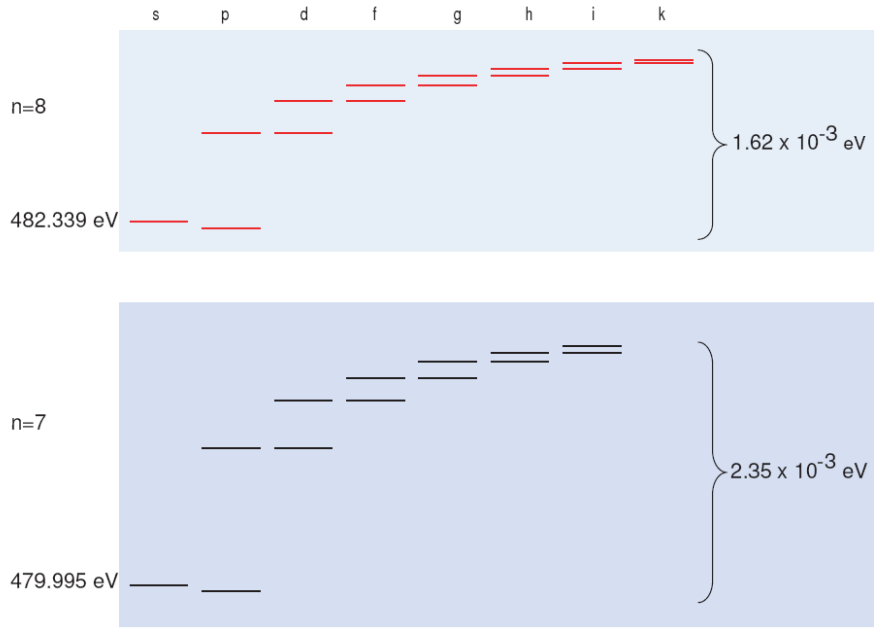


**Figure 4.14:** *Fine structure of the $n = 8$ and $n = 7$ levels of $C^{5+}$, from Wisse (2007) [59], data from Erickson et. al. (1977) [56] via NIST [90]*

levels where $n \leq n_i$ ($n_i$ being the resonant level), the highest $l$ states (y-rast states where $l = n - 1$) are dominantly populated by the charge exchange processes due to momentum conservation. For levels where $n > n_i$ the $l \approx n_i$ levels are dominantly populated [32]. This is accounted for in the cross sections and rate coefficients given in section 3.4.

However, these fine-structure states can be further coupled together by several processes, producing a redistribution of the sub-level populations before a photon is emitted. These $l$-mixing processes include ion-ion collisions and mixing by the motional Stark effect. The criteria for these to produce significant mixing are given by Fonck *et. al.* (1984) [32] and are shown in figure 4.15. For typical MAST edge plasma conditions ($B = 0.1 - 0.3$ T, $T = 50 - 500$ eV $Z_{eff} = 1.5 - 4$ and $n_e = 1 \times 10^{17} - 5 \times 10^{19}$ m$^{-3}$) the ion-ion collisions are shown to be an important mechanism while the linear and quadratic motional Stark effect only becomes an important mechanism for higher $n$-levels than $n = 8$.

The ion-ion collisions are most strongly dependent on density. For the plasma edge in MAST the large density range means that the $l$-mixing regime is transitional between full and no $l$-mixing. When full $l$-mixing occurs the $l$-levels are relatively populated within a given $n$-level according to their statistical distribution $(2l + 1)$. It is therefore simple to calculate the relative emission strengths of the electric dipole transitions using the Burger-Dorgelo-Ornstein sum rule [95] and produce a spectrum composed of all $\Delta j = \pm 1, 0$ transitions. For the intermediate case the calculations become more complex and require fuller

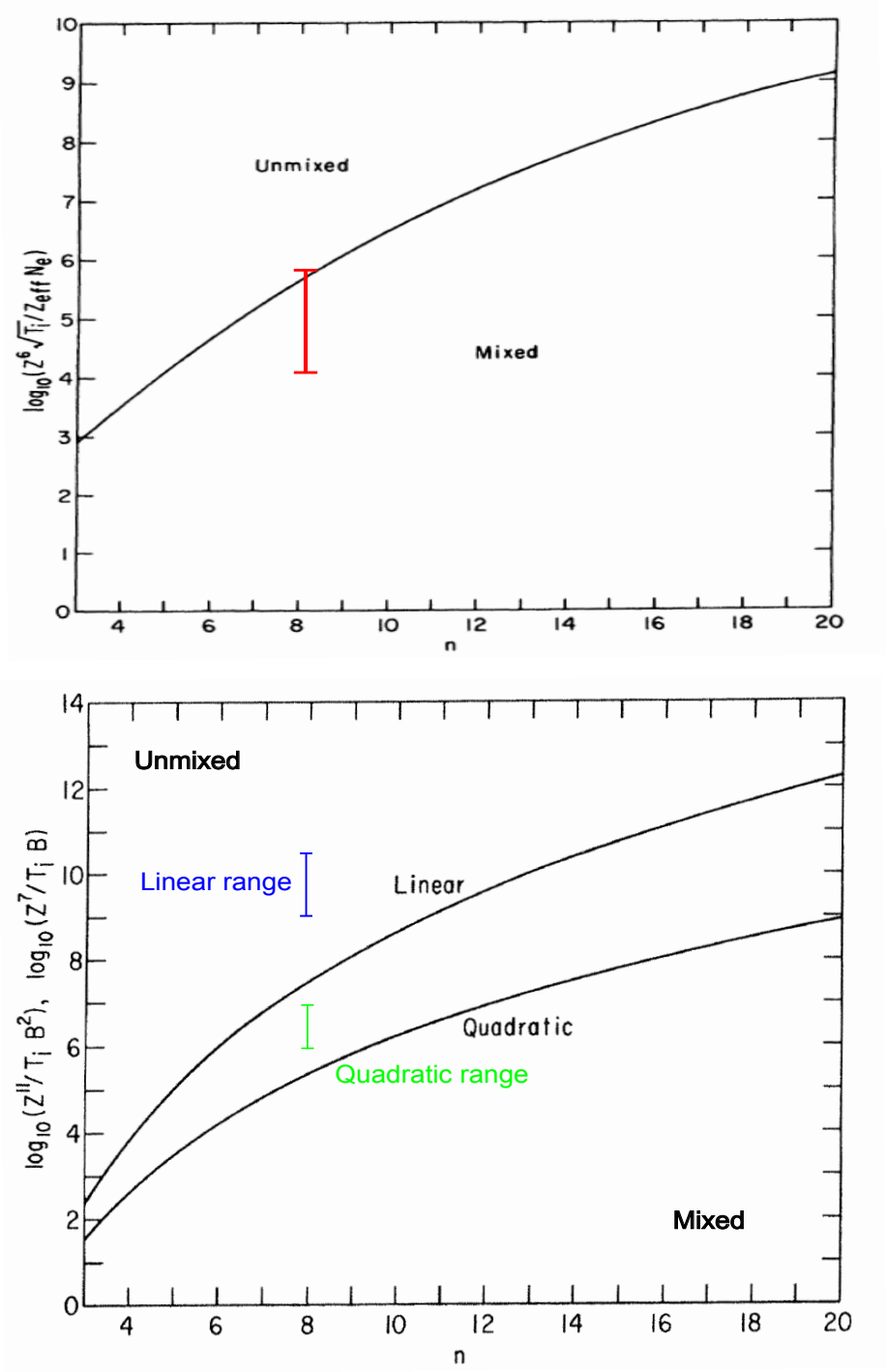


**Figure 4.15:** *Criteria for onset of l-mixing due to ion-ion collisions (top) and due to the linear and quadratic motional Stark effect (bottom). The bars shown for $n = 8$ show the range of values calculated for typical MAST edge plasma conditions (data from Fonck et. al. (1984) [32])*

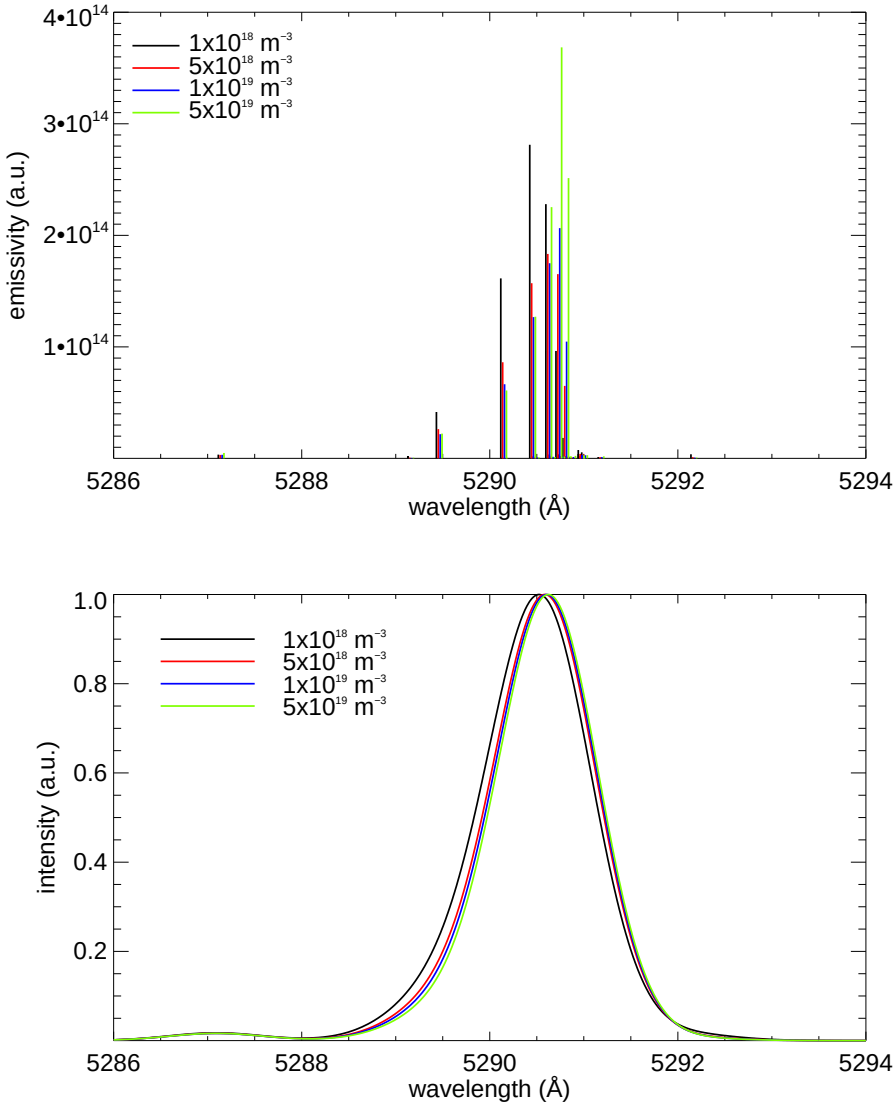


**Figure 4.16:** *The l-mixed $\Delta j$ transitions, including j-coupling effects, for several densities (top). The emissivities for $5 \times 10^{18} m^{-3}$, $1 \times 10^{19} m^{-3}$ and $5 \times 10^{19} m^{-3}$ have been increased in wavelength by 0.02, 0.04 and 0.06 Å for presentational purposes. The resultant net spectra are also shown for $T_i(real) = 100$ eV (bottom). Data calculated through ADAS [54]*

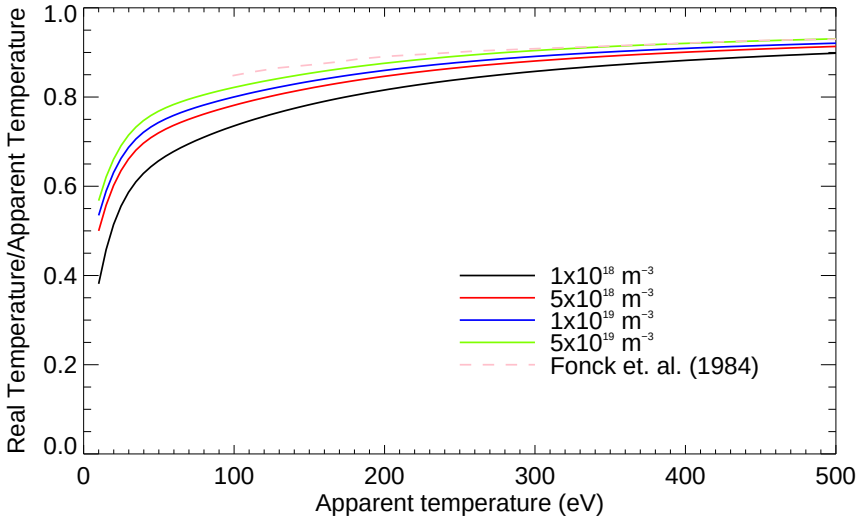


**Figure 4.17:** *Correction curves for calculating the real ion temperature from apparent temperatures broadened by fine structure effects. Comparison with data calculated by Fonck et. al. (1984) [32] shows good agreement.*

modelling. The spectral positions and relative intensities are calculated using an ADAS subprogram (ADAS306) [54] for several different densities (shown in figure 4.16 *(top)*) while the resultant spectra at 100 eV are shown in figure 4.16 *(bottom)*.

The result of the fine structure effects are three-fold. Firstly the multiple lines create a small distortion in the shape of the overall emission spectrum (although not enough to produce a large enough deviation from a Gaussian shape that alternative fitting must be considered for temperatures greater than 10-20 eV). Secondly the net spectrum is broadened spuriously by the combination of multiple closely spaced emission lines, producing an apparent temperature which is larger than the true temperature for each individual line. By fitting a Gaussian curve to the overall spectrum a correction curve can be calculated, as shown in figure 4.17. Comparison with Fonck *et. al.* (1984) [32] who calculated this using the same method for 25 keV donor atoms at temperatures greater than 100 eV (and which assumes full $l$-mixing for the $n = 8$ level) shows good agreement when the densities are large and full $l$-mixing is approached. A two dimensional array of correction values has been created for various values of $n_i$ and apparent $T_i$ . The ion density is assumed equal to the electron density and the Thomson scattering measurements of $n_e$ are used. The correction values for each measured point are then interpolated from this and applied to each point independently.

Thirdly, the centrum of the overall lineshape varies as a function of temperature and density (see figure 4.18). This can be explained as a shift in the population in the upper

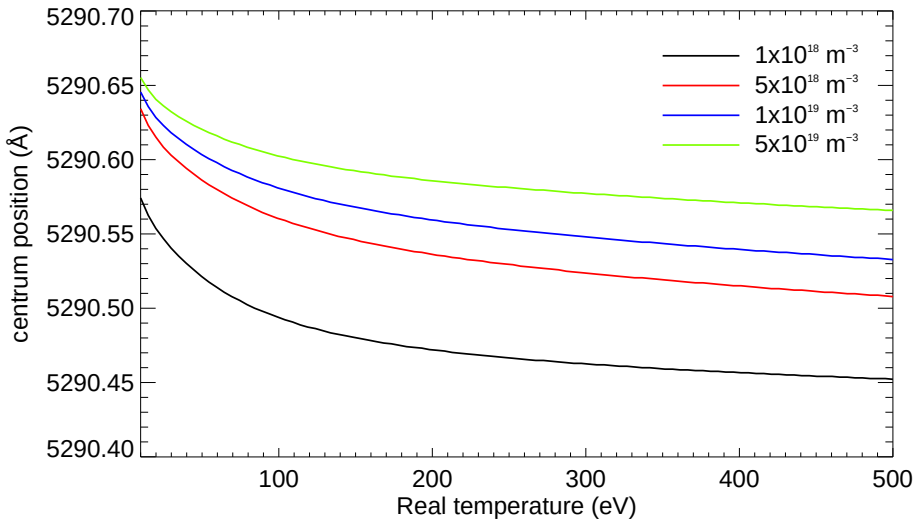


**Figure 4.18:** *Apparent line centra as a function of real temperature and for a range of densities. This must be accounted for when calculating toroidal ion velocities.*

states due to the $l$-mixing effect from unmixed to mixed as the density and temperature increase. This variation must be accounted for when calculating the velocity from the fitted measurements. The variation is of the same order as toroidal rotational speeds in the plasma edge ($\sim 1 \times 10^4$ m s$^{-1}$) so an accurate correction is essential to remove uncertainty in the rotational velocity.

### 4.6.2 Zeeman effect and motional Stark effect broadening

As well as broadening due to the fine structure each transition is also effected by the magnetic fields present in the plasma. This produces two effects.

Firstly the interaction of the magnetic field with the magnetic moment of the $C^{5+}$ atom produces a splitting in the energy level of each previously degenerate $j$-state according to the values of each state's spin projection along the magnetic field $m_j$ so that the splitting is

$$\Delta E_Z = g_j \mu_B m_j B \tag{4.6}$$

where $g_j$ is the Landé g-factor and $\mu_B$ the Bohr magneton. This splitting produces an extremely complex spectrum of 944 separate transitions in the $C^{5+}$ $n = 8 \rightarrow 7$ transition [96]. The spectra are polarised with three components ($\pi$ and $\pm\sigma$) which vary in intensity according to the viewing angle with respect to the magnetic field direction ($\vartheta$), which is given by [96]

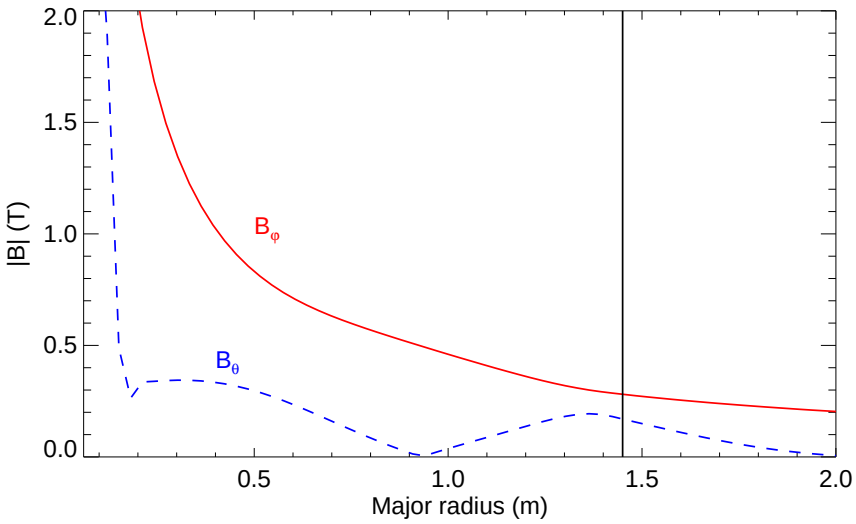


**Figure 4.19:** *Typical profiles for $B_\phi$ and $B_\theta$ in the MAST tokamak during the current flat-top across the midplane radius. The vertical black line denotes the approximate position of the separatrix at the midplane in the majority of MAST plasma scenarios during the flat-top*

$$\frac{I_\pi}{I_\sigma} = \frac{2\sin^2\vartheta}{1+\cos^2\vartheta} \tag{4.7}$$

Blom and Jupen (2002) [96] have fully analysed this problem and produced an empirical fitting which assumes each polarisation group can be treated separately as a Gaussian, so that the overall line can be fitted as a sum of three Gaussians with the overall broadening given by

$$W_{fitted} = \sqrt{W_D^2 + W_{FS}^2 + W_Z^2} \tag{4.8}$$

where $W_D$ is the Doppler broadening, $W_{FS}$ is the fine structure broadening as found in subsection 4.6.1 and $W_Z$ the broadening due to the Zeeman effect. The splitting between the two $\sigma$ components and the central $\pi$ component is given empirically as $\Delta\lambda_Z(\text{Å}) = \pm 0.1307 B(\text{T})$ [96]. In MAST plasmas typically $B_\phi \approx 0.3$ T, $B_\theta \approx 0.2$ T at the outer midplane edge (see figure 4.19) and therefore $B \approx 0.36$ T and $I_\pi/I_\sigma \approx 0.36$ when viewing toroidally . By creating three copies of the fine structure spectrum found in section 4.6.1 with the appropriate splitting and intensity ratio and fitting to the resultant spectrum the effect of the Zeeman splitting was therefore assessed for all relevant temperatures (see figure 4.20) and the correction curve and values of $W_Z$ are shown in figure 4.21. For most temperatures in the relevant range the Zeeman effect is small but it becomes especially important for temperatures below 100 eV where smaller Doppler broadening leads to a larger effect overall.

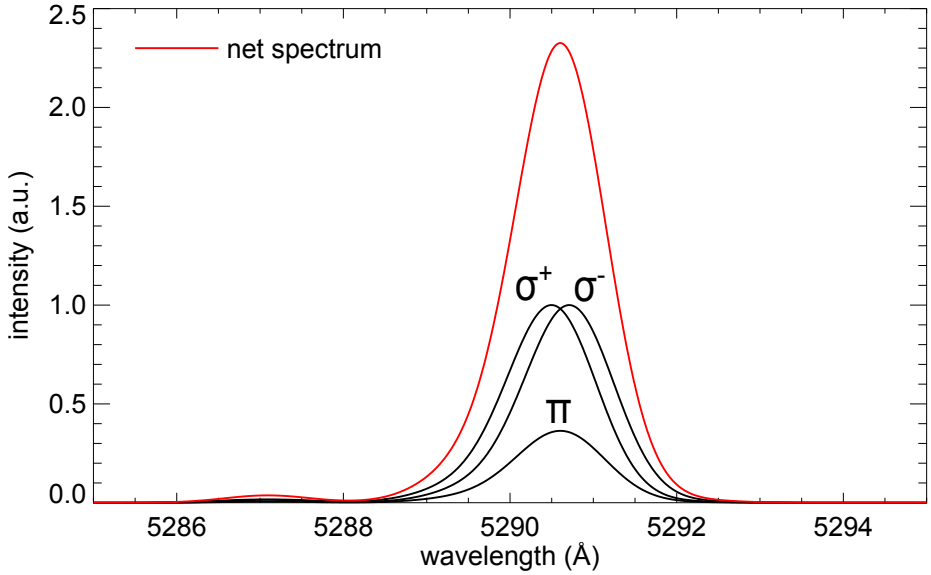


**Figure 4.20:** *The spectra of each component of the Zeeman effect, and the net spectrum resulting from it at 100 eV*

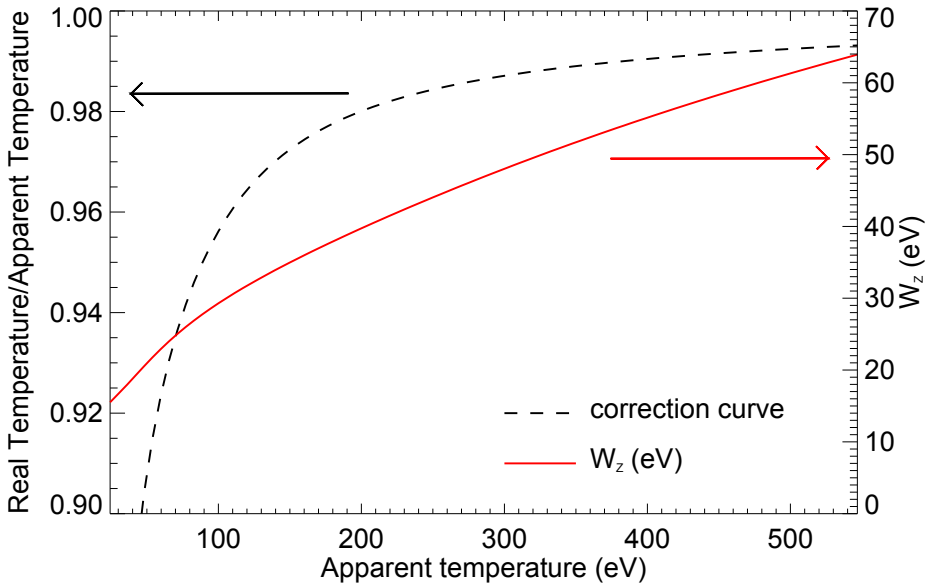


**Figure 4.21:** *Correction curves for calculating the real ion temperature from apparent temperatures broadened by the Zeeman effect (dotted curve) and corresponding values for $W_Z$ as described in equation 4.8*

The second way in which the magnetic field affects the level structure of the atom is due to Lorentz force felt by the atom as it moves through the magnetic field. The atom therefore experiences an electric field in its own frame of reference. This produces a broadening through the quadratic Stark effect given by[32]

$$\Delta E_S^Q \approx (e(\mathbf{v} \times \mathbf{B}))^2 \frac{n^4 a_0^2}{Z^2 \mu_0 B}. \tag{4.9}$$

For typical $B$-fields at the outer midplane plasma edge of 0.36 T and typical thermal velocities (perpendicular to the magnetic field) for a carbon ion at 500 eV of $\sim 6 \times 10^4$ m s$^{-1}$ the splitting in the degeneracy of the energy levels is approximately $1 \times 10^{-5}$ eV. By comparison the splitting due to the Zeeman effect is of order $2 \times 10^{-4}$ eV for the largest values of $m_j$. Therefore, it is safe to conclude that the motional Stark effect broadening is negligible.

### 4.6.3 Lifetime and pressure broadening

Two other mechanisms can lead to line broadening. Firstly, according to the Heisenberg uncertainty principle, if a system survives in a quantum state for a time $\tau$, the energy of that state cannot be known to better accuracy than

$$\Delta E = \frac{\hbar}{\tau} \tag{4.10}$$

This uncertainty produces a fundamental minimum spread in the possible energies of a given transition. The shape of this broadening is a Lorentzian, with a characteristic linewidth $\Delta E_L = h\gamma$ where $\gamma = 1/2\pi\tau$. For the $n = 8 \rightarrow 7$ transition of $C^{5+}$ the value of $\tau$ is approximately $3 \times 10^{-9}$ s (scaling lifetime data for H I from Wiese and Fuhr (2009) [97] (data via NIST [90]) by $Z^4$). For this case therefore the perturbation on the energy of the transition is $\approx 2 \times 10^{-7}$ eV. By comparison with the values in section 4.6.2 it is clear that this broadening is negligible.

Perturbations in the energy of the system can also be induced due to the interaction of nearby charged particles with the excited ion. This perturbing electric field produces Stark broadening, similarly to the motional Stark effect discussed previously, although as the source of the electric field here and in section 4.6.2 are different they must be treated separately. The surrounding perturber ions are slow moving by comparison with the natural excitation times $\tau$ so the quasi-static regime is appropriate. In this approximation the half width of the spectral line shape due to the pressure broadening using the Helmholtz approximation for the electric field is given by [98]

$$\Delta\nu_{SB} \approx \frac{12 Z_p \hbar}{Z m_z} \left(n_i^2 - n_f^2\right) n_p^{2/3} \tag{4.11}$$

where $Z_p$ and $n_p$ are the charge and density of the perturber respectively and $n_i$ and $n_f$ the principal quantum numbers of the initial and final states of the transition. For our transition of interest at a density of $1 \times 10^{19}$ m$^{-3}$ this produces a half width value of

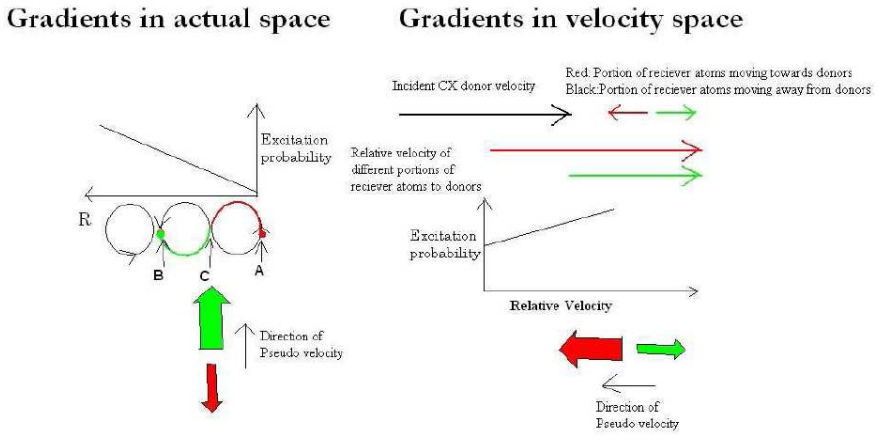


**Figure 4.22:** *Diagram showing the origin of pseudo velocities due to spatial gradients (left) and velocity gradients (right) from McCone (2011) [43]*

$\approx 880$ kHz or $\Delta E_{SB} \approx 4 \times 10^{-9}$ eV, which again is negligible in its effect on the lineshape. This should not be surprising as the densities are very low, and the temperatures very high compared to laboratory conditions when the converse is normally true and where Stark broadening often dominates over Doppler broadening.

### 4.6.4 Pseudo velocity and cross sectional effects

If the emitting ions do not have the same velocity distribution as the overall ion population then this can give rise to a non-representative emission profile. If there is a greater probability for some ions to charge exchange with others due to either spatial gradients or velocity gradients then this effect can arise.

With spatial gradients velocity dependent emission can arise due to the gyromotion of the ions. With reference to figure 4.22 charge exchange occurs at positions A and B and the ions move around their Larmor-orbits to position C before emitting. If there is a gradient in the charge exchange probability across this region such that there is a greater probability that charge exchange will occur at B then A then this will produce a false net velocity in the Doppler spectrum.

This will only be important if the ions are excited for long enough to precess a significant distance along their Larmor orbits. The angle precessed before emission is approximately $\omega_c \tau$ where $\omega_c = (ZeB)/m_z$ is the cyclotron frequency and $\tau$ the lifetime of the excited state. The lifetime can be approximated as $\sim 3$ ns by simple scaling (see section 4.6.3), while Bell and Synkowski (2000) [99] estimate it to be 0.7 ns using a collisional radiative model and measure it to be 1.1 ns. By comparison the cyclotron frequency in the plasma edge for $C^{6+}$ is $\sim 1 \times 10^7$ rad s$^{-1}$ . Clearly therefore this source of pseudo velocity is not

important.

In neutral beams the donor atoms (in each energy component) are normally close to monoenergetic and generally of much higher energy than that of the carbon ions. Therefore if the donor atoms have a component of velocity in the toroidal direction then the relative collisional energy between the carbon and deuterium can vary in the positive and negative toroidal direction for ions of the same energy. This could give rise to a pseudo velocity in the ion distribution if there is a gradient in the charge exchange probability as a function of energy (see figure 4.22). However, the deuterium gas puff is pointed radially into the plasma, so that any toroidal component will be very small. Therefore this effect can again be ignored.

### 4.6.5 Contribution from other lines

Several other impurities have emission lines which are close to 5290.5 Å. Of these the most likely to be important based on expected abundances in the plasma is the O VI $n = 8 \rightarrow 7$ line. This has an almost identical wavelength (separated by -8 pm [75]), the main differences are due incomplete screening by the $1s^2$ electrons in O VI [75]. Due to the small difference, identifying the lines separately is impossible given the dispersion of the available spectrometers, so it is necessary to estimate its possible effect on the temperature and velocity measurements.

Although $C^{6+}$ is assumed to be the main impurity in the plasma some contribution to the measured charge exchange emission could come from the oxygen ions. Due to their differing masses the O VI line is a factor of $\sqrt{3/4}$ narrower at the same temperature. Therefore, if we were to assume that all the measured emission was in fact from O VI this would lead to an underestimation of the true temperature of by a factor 0.81 at $T_i(Real) = 10eV$ to 0.76 at $T_i(Real) = 500eV$ once fine structure corrections are accounted for. However, a more realistic upper bound would be a 10% contribution from O VI. This leads to a deviation from the true temperature of only 2-3%. Given that the contribution from oxygen to the emission is unknown, it is reasonable therefore to neglect the effect this would have on the measurement.

### 4.6.6 Spatial smearing of strong velocity gradients

In a region with strong velocity gradients the finite width of the observation chord can have an effect upon the temperature results, resulting in artificial broadening of the temperature spectrum. This occurs if emission from regions with different toroidal rotations is observed in a single chord, which results in the observed spectrum being a sum of multiple Gaussians

each with slightly different central wavelengths. An upper limit for this effect may be estimated by assuming a very large gradient of $\Delta v = 10$ km s$^{-1}$ over the 3mm diameter of a single chord. This would result in a maximum range of central wavelengths of $\Delta\lambda_{SS}$ of 0.176 Å. This results in a distribution of Gaussians of

$$P_j(\lambda)\mathrm{d}\lambda = \int A(\lambda_S)\exp\left(-\frac{m_j c^2\left(\lambda-\lambda_S\right)^2}{2k_B T\lambda_0^2}\right)\mathrm{d}\lambda_S\mathrm{d}\lambda \tag{4.12}$$

where $A(\lambda_S)$ is given by

$$A(\lambda_S) = \sqrt{\Delta\lambda_{SS}^2 - (\lambda-\lambda_S)^2} \tag{4.13}$$

This gives a Gaussian overall from this slightly wider set of Gaussians. By fitting to this we can compare the true and observed temperatures in this case (See figure 4.23). From this it is clear that even at the upper limit the effect of this is very small. Generally velocity gradients are likely to be a tenth of the proposed limit (approximately 1 km s$^{-1}$ over 3 mm) in the edge and therefore corrections for this effect are likely to be very small and have therefore not been made.

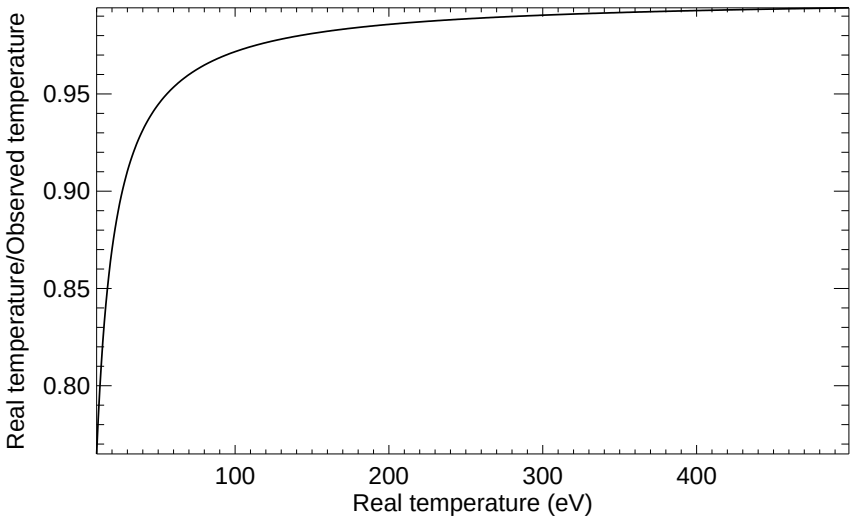


**Figure 4.23:** *Ratio of true to observed temperatures in the upper limit case of temperature broadening due to spatial smearing of high velocity gradient regions.*

## 4.7 Radial uncertainties

While the uncertainties in measured temperature and velocity is largely calculated from the errors inherent in the fitting routine there are also mechanisms which produce uncertainty in

the spatial direction. This includes calibration errors, as well as unavoidable uncertainties due to the extended nature of the gas puff and the effect of the gyration of the carbon ions about the magnetic field lines.

As discussed in section 4.6.4 the ions emit almost instantaneously when in the $n = 8$ state, so any uncertainty in the position of the carbon emission due to this is negligible. The innate width is due to the finite area of each viewing chord, which are three separate chords each of radius of 1.5 mm. There is also a calibration uncertainty in the position of all chords relative to the MAST centre column. This is determined by using two light sources to back-illuminate the two outermost chords. When these strike the HELIOS nozzle at a known radius the toroidal optics are therefore directed at a known position in the vessel. They can then be positioned at the desired radius using a micrometer screw with a fixed relationship between its value and the movement of the chords along the axis between HELIOS nozzle and the MAST centre column. This produces a further uncertainty of $\pm 1$ mm in the position of the chords with respect to the MAST geometry, though not to each other as the chord spacings are known with better than 0.1 mm accuracy.

An infinitely narrow gas puff would intersect with only a single flux surface and maximise the localisation. However, due to its extended nature, the gas puff cuts across several surfaces and therefore stimulates active emissions from a broader region which introduces additional spatial uncertainty. Based on the modelling of section 3.6.2 at the plasma edge it can be estimated that the width of the gas puff $W_e(r)$ (defined as where the density of neutrals equals the background) as it enters the plasma is $\sim$ 6 cm. This broadens approximately linearly so that 10 cm inside the edge it is $\sim$ 15 cm in L-mode and $\sim$ 11 cm in H-mode (see figure 3.25), as the H-mode puff tends to become ionized in a smaller region due to the increased density in H-mode, producing a narrower puff. The combination of all these uncertainties results in a spatial error in the range of 1.9 mm at the plasma edge and 4.5 mm and 8.5 mm 10 cm inside the edge in H-mode and L-mode respectively. It should be noted that halo neutrals (neutrals created due to charge exchange of the cold injected neutrals with the hot bulk deuterium) are included in the GTNEUT modelling of section 3.6.2 and that this effect has therefore been included in the model.

The combination of these effects is that the uncertainty in the position of the emission recorded by cannot be known to better accuracy than approximately $\pm 4.4$ mm at the edge and approximately $\pm 7 - 11$ mm at the innermost region covered by the system. This must therefore be accounted for when considering the accuracy of the measurements.

## 4.8 Fitting routine overview

Having defined and benchmarked the fitting routine and discussed corrections the fitting process can now be fully described. Firstly active and background timeslices are selected manually, using the gas puff waveform and line-integrated emission intensity as a guide. The radial chord at background and active timeslices is then fitted. This gives both the zero position for toroidal velocity measurements but also a measure of the change in background intensity between the background and active shots. Once each background chord has been fitted the active chords are fitted using a four Gaussian fitting method where the background lines are included as fixed parameters which have been scaled (either up or down) by the ratio of the background to active peak line intensity (i.e. the ratio of $a_0(active) : a_0(background)$ in equation 4.1) recorded by the radial chord. Although this does not account for any radial variation in background intensity this can still account for the majority of the effect a spuriously large or small background could have on the fitting accuracy.

As the background line fitting parameters are fixed the four-Gaussian fitting is equivalent to two-Gaussian fitting with the background subtracted. Therefore the benchmarking of section 4.5 is still applicable. If the deuterium line $a$ is found to be large fitting to background and active signals is repeated using three and six-Gaussian fitting respectively where the second deuterium line $b$ is also included and the background is fixed as before. Once these fits have been made cuts are applied to remove poorly fitted profiles and areas where the fitting is known to be unreliable and that can give spurious results. These apply a cut on the reduced chi-squared value $\frac{\chi^2}{\nu} > 2$ (where $\nu$ is the degrees of freedom) and the cut described in equation 4.5. For a fit to be accepted as good the reduced chi-squared value should normally be close to one. However, due to the uncertainties in determining the error variance as discussed in section 4.4 a smaller reduced chi-squared cut would most likely result in excluding good fits where the variance has been under-estimated, so the value of two has been selected in order to automatically exclude only very poor fits. The fitting process also permits manual examination and removal of obviously poor fits (prior to temperature and velocity calculation to avoid human cherry-picking) in order to compensate for this.

Once the fits to active data have been made temperatures and velocities are calculated from the fitting parameters using equations 1.10 and 1.11 and the calibrations made in Appendix C. At this point corrections to the data are made for fine structure, the Zeeman effect and cross section effects, as discussed in section 4.6.

# Chapter 5

# The performance of the system

## 5.1 Introduction

In chapter 4 the calibration of the ECELESTE system for recording $C^{5+}$ charge exchange emission has been described. In this chapter it is shown that it is possible to assess the effect that the gas puffing had on the emission spectra, and to compare this with the predictions of emission intensity made using the forward model of chapter 3. A qualitative analysis of the carbon density in L-mode and H-mode is also made as well as assessing the effect of ELMs on the particle density.

It is also necessary to determine the limitations of the ECELESTE system in terms of time resolution and data quality. A series of system improvements are discussed in this chapter, including designing and installing a new bandpass filter and a new valve for the HELIOS nozzle as well as adding a new CCD camera. These adaptations are assessed in terms of their improvement to the system and future improvements are also discussed to determine the potential of the ECELESTE system in the future.

## 5.2 Intensity results

### 5.2.1 Effect of gas puffing

By examining the time evolution of the data recorded by the ECELESTE system, the effect of the gas puffing on recorded charge exchange emission intensity profiles can be determined. In figure 5.1 the effect of gas puffing on L-mode data is shown. It is clear that the gas puffing has a significant effect on both the charge exchange emission and the edge molecular deuterium emission (see figure 5.3), boosting the charge exchange emission by up to a factor of 3-4 in terms of peak height ($a0$ in equation 4.1) and increasing the edge molecular deuterium emission by a similar factor in both L-mode and H-mode (see figures

4.3 and 5.3(a)). Figure 5.2 shows that as predicted from the carbon density in the edge (see figure 3.20) the emission in H-mode is much greater than in L-mode, and the boost to emission from gas puffing is correspondingly greater (although similar in numerical factor at approximately 3-4 for certain chords). Gas puffing is an effective method of locally boosting the emission from charge exchange, as predicted in chapter 3.

It is also possible to examine whether or not the gas puffing has a significant effect on the performance of the plasma overall. As this measurement should essentially be used in a non-perturbative manner, should the gas puff affect the discharge then this could limit the viability of it's use as a diagnostic. By using similar repeated shots (25221 and 25224) with either gas puffing on or off it is possible to assess whether a perturbation is observed. As shown in figure 5.4 there are no significant differences in the radius of the shot or electron density in the core that might be expected if the gas puff had a significant fueling effect. Furthermore no systematic differences were ever observed when operating with or without gas puffing. Therefore this indicates that the gas puffing can be regarded as non-perturbative.

### 5.2.2 Comparison with modelling

It is possible to estimate the accuracy of the modelling of expected profiles of charge exchange emission in chapter 3 by comparison with recorded charge exchange emission data from ECELESTE. As the modelling simulated the expected intensity profile that would be recorded by the ECELESTE spectrometer, a direct comparison between prediction and reality is possible. The intensity data recorded in several typical H-mode profiles is shown in figure 5.5, as well as the prediction of the emission profile modelling (the same data as in figure 3.30) which has been scaled in the y-axis so as to fit the total emission data. The measured ion and electron temperatures (from Thomson scattering) are shown in figure 6.6.

The shape of the original modelled profile is similar to the measured profiles, as the active parts both have a peaked shape, while the background emission is broader and less peaked. However, the peak position is further inside the separatrix in the model than in reality, while the overall profile shape is narrower than predicted.

It seems most likely that both of these differences are due to the limitations of using model profiles of $T_i$ , $T_e$ and $n_e$, as well as possibly inaccuracies in the neutral density modelling or carbon density modelling. In order to help distinguish between these possible origins of discrepancy the measured profiles of $T_i$ from ECELESTE and $T_e$ and $n_e$ from Thomson scattering for these timeslices are used in the emission model, with $n_{C^{5+}}$ and

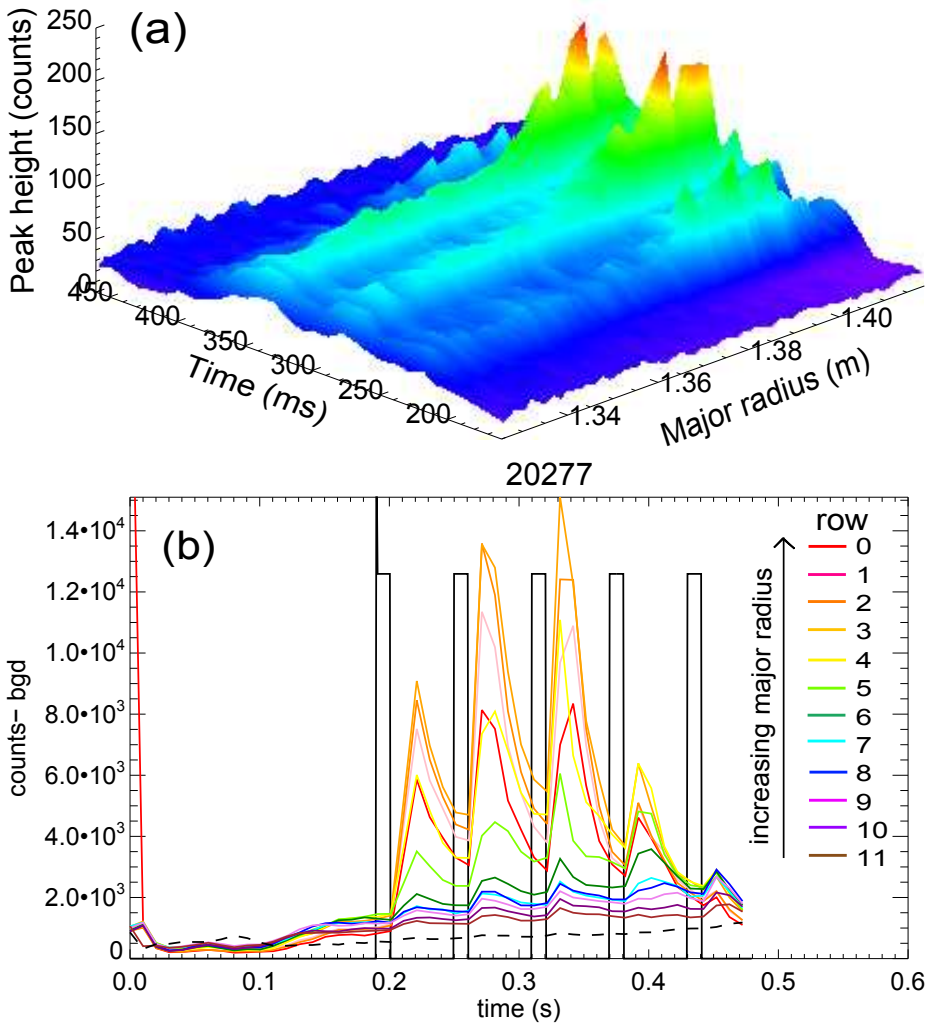


**Figure 5.1:** *(a) a 3D surface plot showing the effects of gas puffing on the recorded peak height of the carbon charge exchange emission for shot 20277 (b) Typical line integrated intensity time profile for various rows of the CCD, where increasing row number denotes decreasing radius. The counts are for the entire line integrated emission for a single chord in each row (i.e. both charge exchange and molecular emission), showing the effect of the gas puffing and the delay in the effect of the puffing on the recorded spectra for a typical L-mode shot. The black line denotes the voltage signal to the HELIOS piezoelectric valve (i.e. when it is opened) and the black dashed line the recorded radial chord data (i.e. plasma background)*

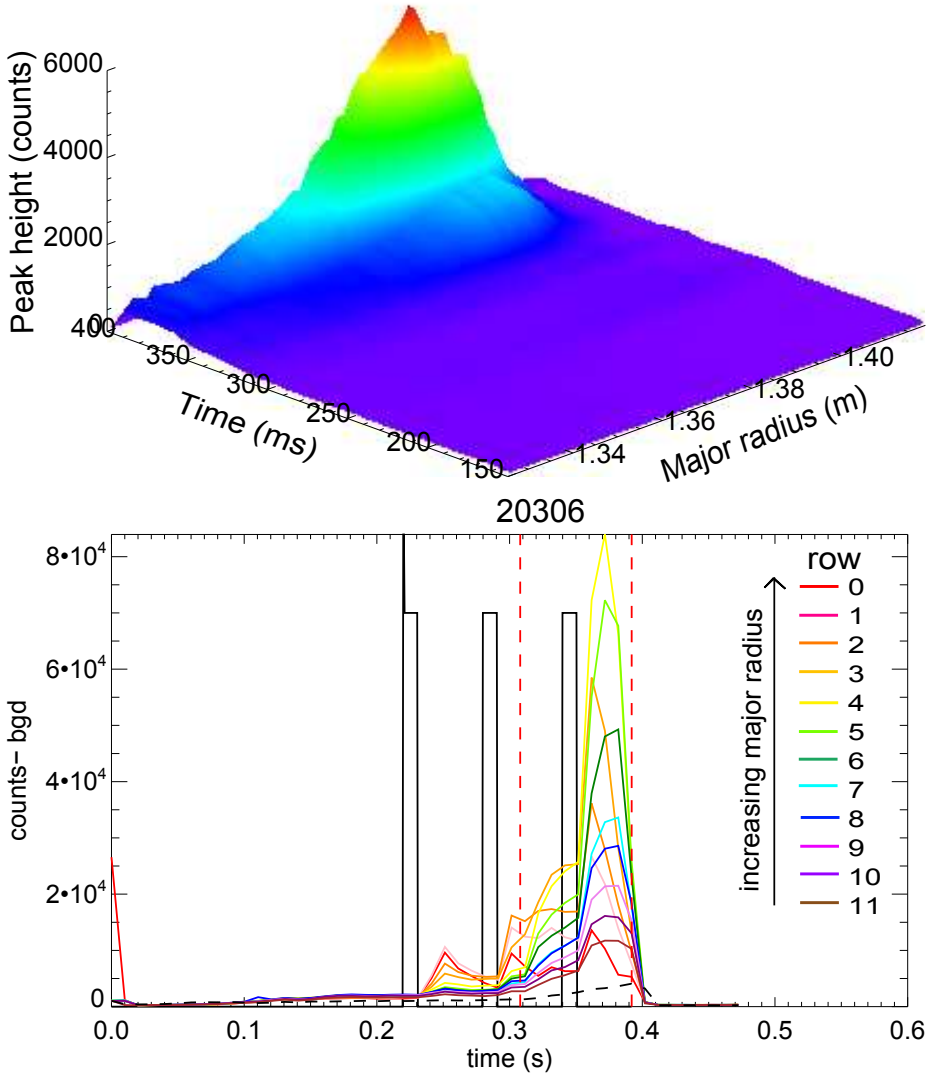


**Figure 5.2:** *(a) a 3D surface plot showing the effects of gas puffing on the recorded peak height of the carbon charge exchange emission for shot 20306 (b) Typical line integrated intensity time profile for various rows of the CCD, where increasing row number denotes decreasing radius. The counts are for the entire line integrated emission for a single chord in each row (i.e. both charge exchange and molecular emission), showing the effect of the gas puffing and the delay in the effect of the puffing on the recorded spectra for a typical H-mode shot. The black line denotes the voltage signal to the HELIOS piezoelectric valve (i.e. when it is opened) and the black dashed line the recorded radial chord data (i.e. plasma background). The red dashed lines indicate the position of the H-mode according to line integrated D-alpha emission.*

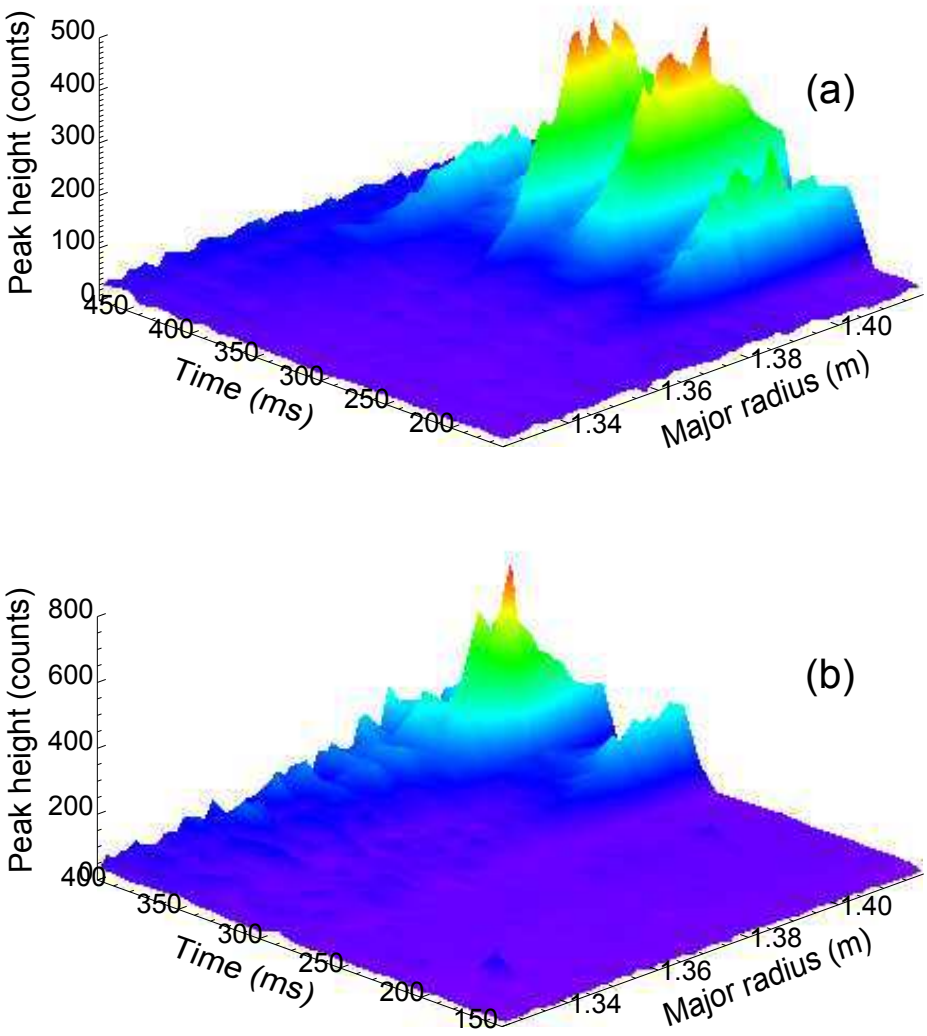


**Figure 5.3:** *a 3D surface plot showing the effects of gas puffing on the recorded peak height of the deuterium line emission for (a) a typical L-mode (shot 20277) and (b) a typical H-mode shot (shot 20306)*

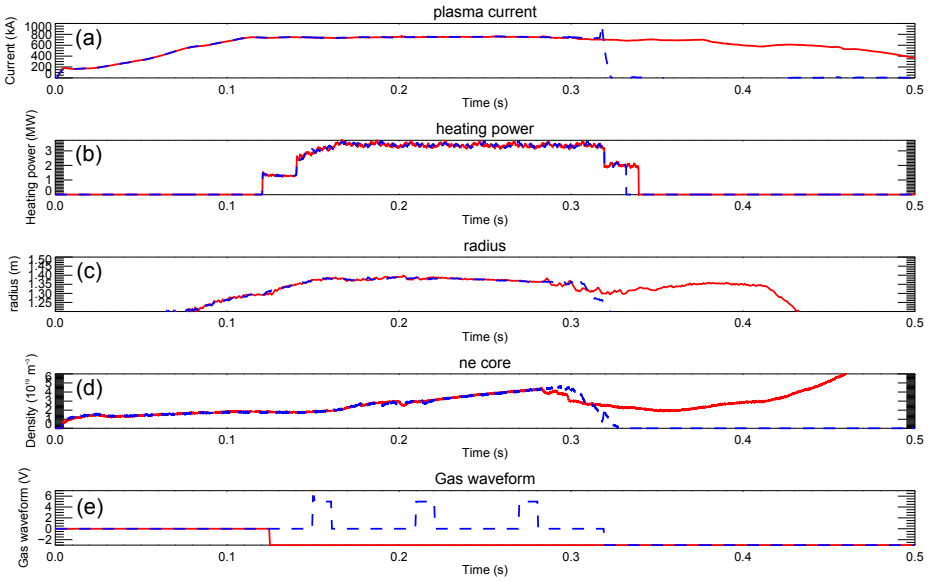


**Figure 5.4:** *Comparison between similar repeated shots (using the same reference shot) with either gas puffing on (shot 25221 blue, dashed) or off (shot 25224 red, solid). The traces of plasma current (a) and heating power (b) show there was good replication of the first shot in the second prior to disruption at 320 ms, while the traces of plasma radius (c) and core electron density (d) show no perturbations from the gas puffs (e).*

$n_{C^{6}+}$ calculated as in section 3.6.1. The results of this improved modelling are also shown in figure 5.5. This shows a much closer resemblance between measured and modelled intensity profiles, both in position and overall shape. The discrepancy in the ratio between background and active emission seems likely to be due to uncertainties in the intensity of the gas puff relative to modelled background.

Following the same principles the experimental and simulated L-mode intensity data can be compared. The results are shown in figures 5.6. The agreement here is much weaker, although the fit between model and measurement is again greatly improved by using true values for $T_i$ , $T_e$ and $n_e$ measured with ECELESTE and Thomson scattering. In particular the measured data extends much closer to the separatrix than predicted. This also appears to be true to a lesser extent in the case of H-mode profiles. This is most likely to be due to $C^{6+}$ extending closer from the core to the edge than predicted by the model. As shown in section 3.3 the recombination times for $C^{6+}$ are longer than the characteristic transport times calculated. This implies that fully ionised carbon can be transported outwards further beyond its equilibrium position given by figure 3.22 before it recombines, which could explain this observation. Generally transport times are higher in L-mode than H-mode plasmas leading to a larger outward drift in these cases prior to recombination, which is also consistent with what is seen. Furthermore the position where

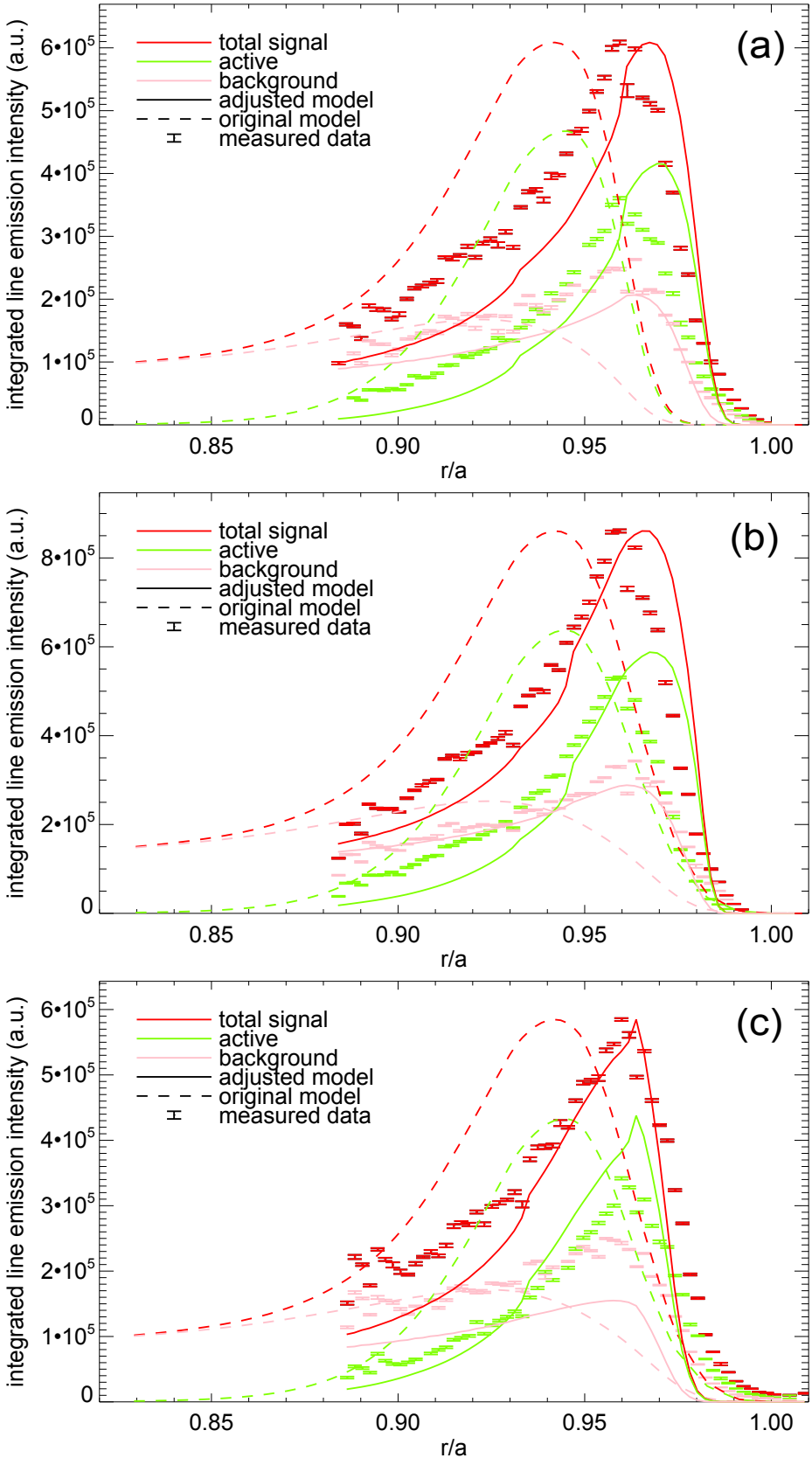


**Figure 5.5:** *Typical H-mode intensity profiles from shots (a) 20304, time = 296 ms, (b) 20306, time = 357 ms and (c) 20302, time = 296 ms. These are compared with the original modelling from chapter 3 (see figure 3.30) and updated modelling where measured profiles of $T_i$, $T_e$ and $n_e$ have been used.*

$C^{6+}$ density sharply decreases is highly sensitive to the temperature of the ions (see figures 3.2 and 3.22) so small discrepancies either in the model or measurements can significantly change the position where this occurs. This could also be due to stronger diffusion or a smaller neoclassical inward pinch velocity.

The close agreement between modelled and measured intensity profiles indicates that the modelling theory is a reasonably accurate one to use and helps validate the underlying assumptions within it (see chapter 3). The self consistent results also indicate that the measured values of $T_i$ can be regarded as reliable. As the recorded emission is consistently recorded closer to the plasma edge than predicted by the modelling, this implies that measurements in the pedestal region will have a better signal to background ratio than expected as recorded intensity levels will be higher, which will increase the reliability of the results.

### 5.2.3 Impurity density and the effect of ELMs

As shown clearly in the previous two sections the emission intensity recorded by the ECE-LESTE system is significantly higher in H-mode than L-mode. This can be ascribed to a build-up of carbon in the edge as discussed in section 3.6.1. The main transient events which could affect the recorded emission are ELMs. From the recorded measurements it is clear that the carbon builds up over several timeslices in ELM free H-modes and decreases when ELMs occur. The loss appears to be right across the edge region. Examples of ELM free and high ELM presence H-mode plasma shots are shown in figures 5.7 and 5.8 where for the sake of clarity no gas puffing has been applied. This is in agreement with theory that ELMs are associated with particle losses [24] and observations of electron density which show similar losses due to ELMs [100].

As the integration time of the ECELESTE system is typically 10 ms, it is not possible to determine any other influences from the ELMs as typical filament bursts are on the order $\approx 100$ $\mu$s in MAST (see figure 5.9(c)). However, it appears clear that the ELMs do not significantly affect the intensity profile recorded by the system. This is consistent with measurements of the ELM recovery time of 600-1000 $\mu$s, at which point the profile shape of the electron density returns to its pre-ELM shape, although normally at a lower density that slowly increases [100]. It is expected that the carbon should follow a similar recovery if it is consistent with fast measurements of carbon density recorded at DIII-D [101].

Figure 5.9 shows the recorded intensity profile of an H-mode where the emission intensity increase from the gas puff is spread over several consecutive timeslices. The lack of significant change in the profile shape for the timeslice recorded from 250 to 260 ms,

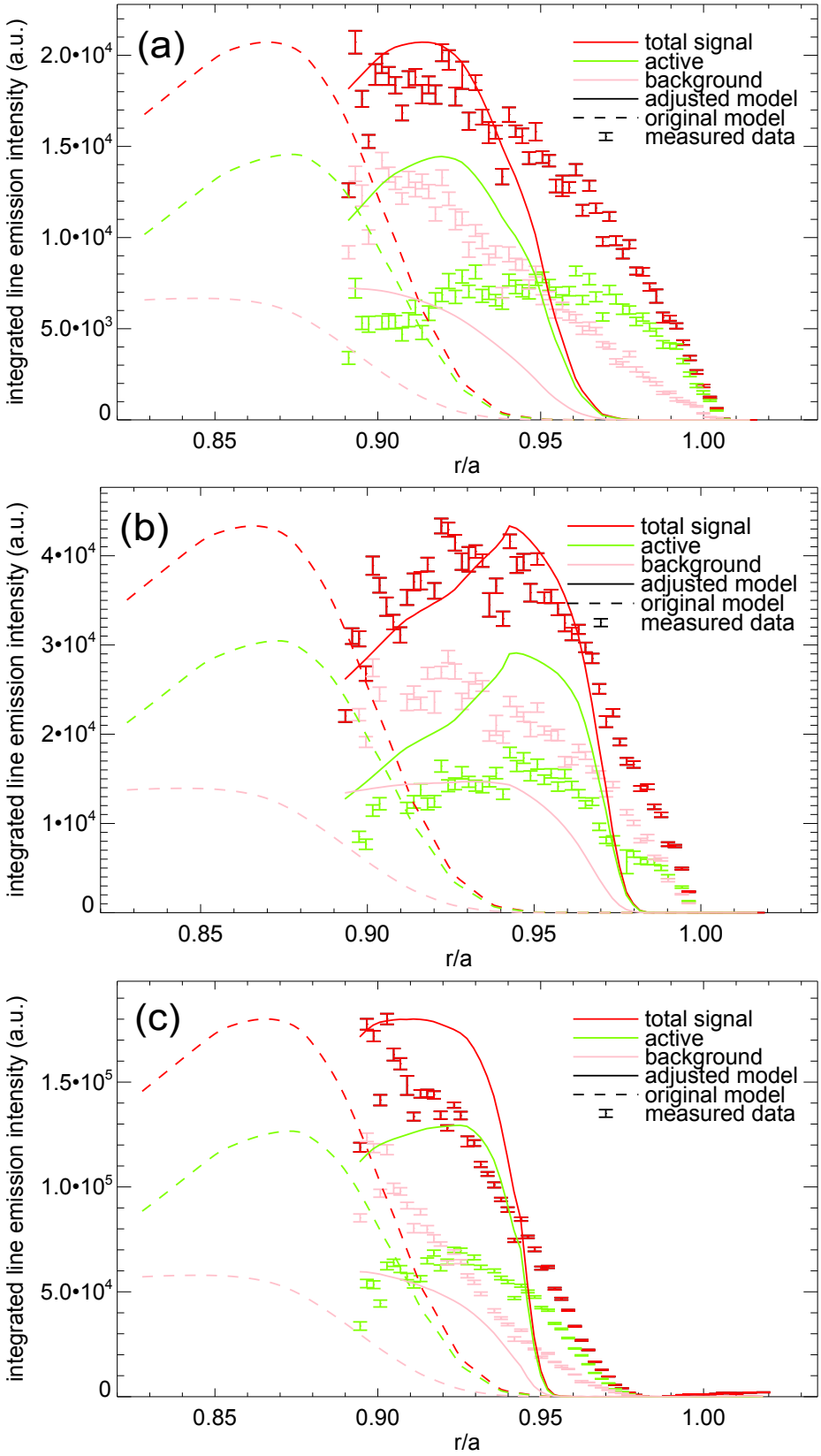


**Figure 5.6:** *Typical L-mode intensity profiles from shots (a) 20306, time = 246 ms, (b) 20299, time =246 ms and (c) 20169, time = 286 ms. These are compared with the original modelling from chapter 3 (see figure 3.30) and updated modelling where measured profiles of $T_i$, $T_e$ and $n_e$ have been used.*

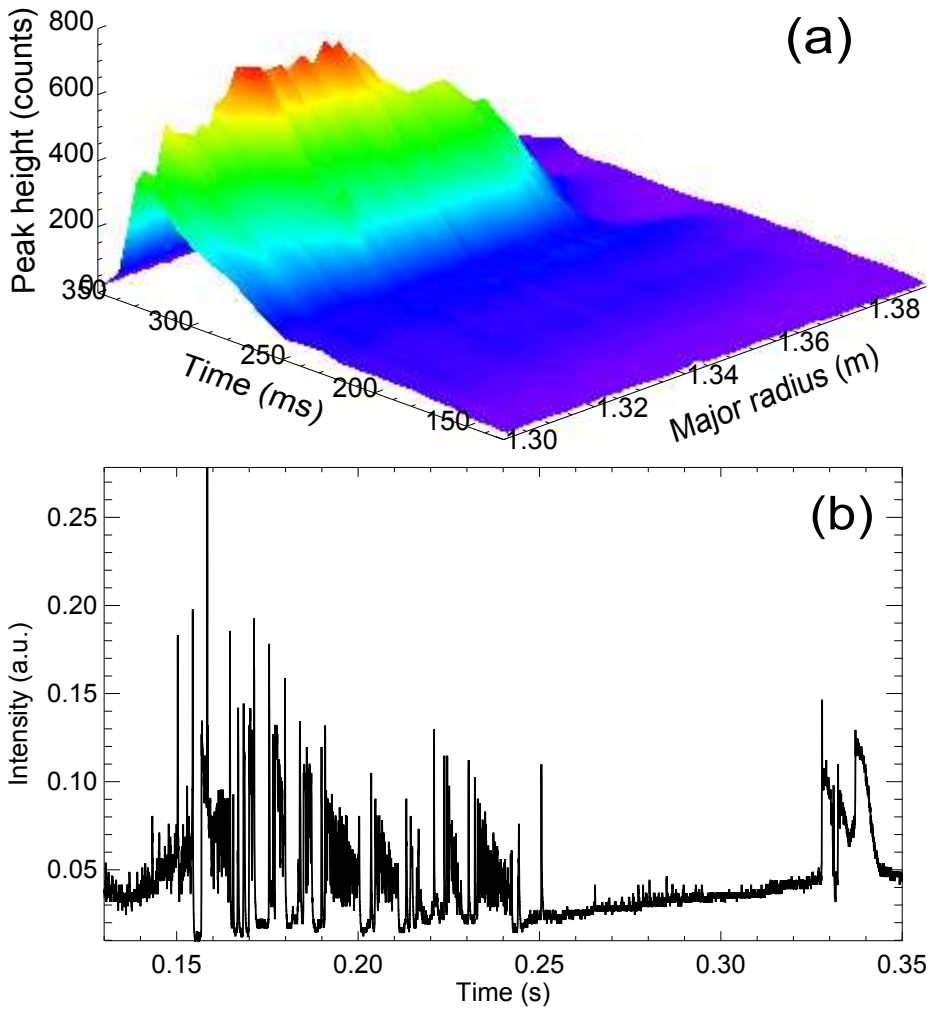


**Figure 5.7:** *(a) a surface plot showing the recorded background intensity of the recorded data in a typical ELM free H-mode (shot 25162) (b) The D-alpha integrated emission recorded by a photomultiplier tube.*

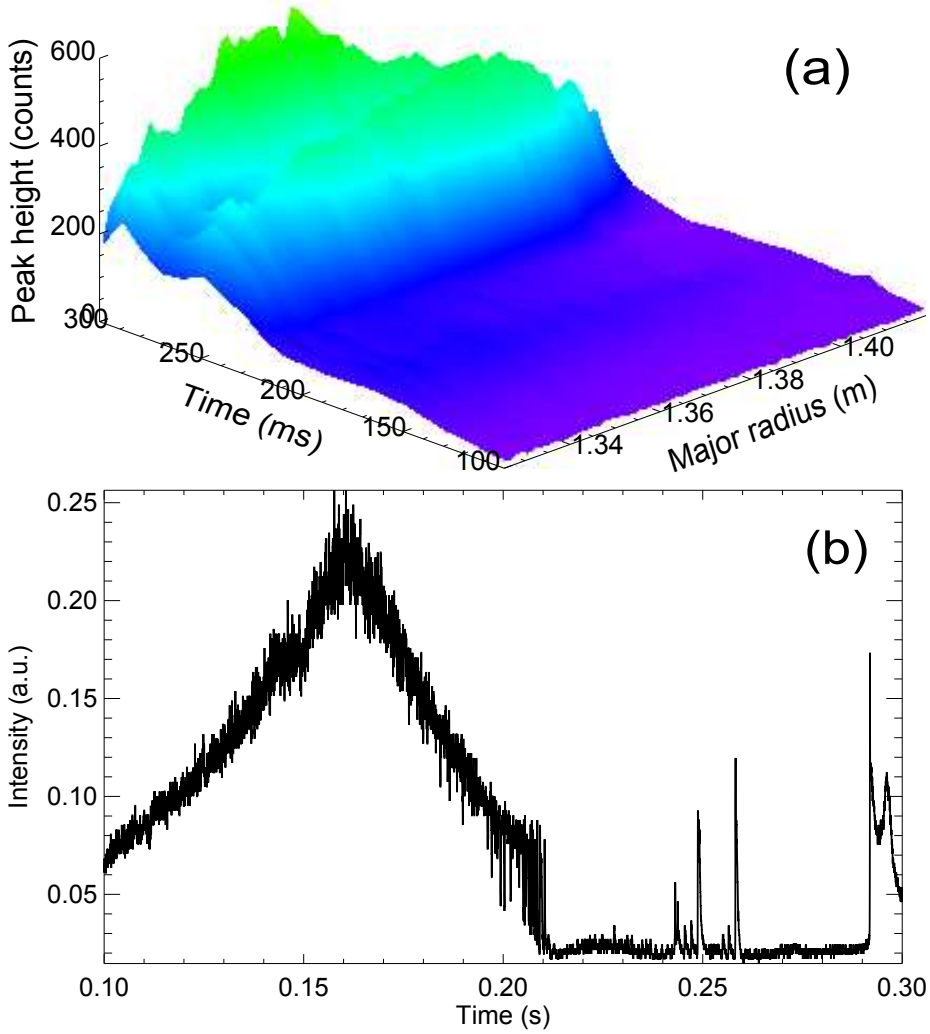


**Figure 5.8:** *(a) a surface plot showing the recorded background intensity of the recorded data in a typical H-mode with Type-I ELMs (shot 25162) (b) The D-alpha integrated emission recorded by a photomultiplier tube.*

despite an ELM recorded at 0.258 ms, compared to the ELM free timeslice prior to this and after this, implies that ELMs do not have a significant influence on the emission profile beyond removing $C^{6+}$ from the plasma and causing a resultant reduction in signal. The higher intensity for the later timeslice is most likely to be due to higher input gas intensity which peaks at 260 ms as shown in figure 5.9(b).

For ion temperatures and velocities it is difficult to disambiguate the effects of ELMs from other changes in the plasma between timeslices. The effect of ELM expulsion is likely to be an addition of hot and fast ions from further into the plasma onto the outer chords as they are expelled. However, the dwell time of these ions in any given radial position as they are expelled is likely to be very short as an entire ELM burst is approximately one hundredth of the integration time. Therefore it is reasonable to assume that any effect of ELMs on these results is likely to be small.

## 5.3 Measurement limitations

While a good deal of information can be gleaned from the recorded emission data, the ECELESTE system does have several limitations, and it is necessary to discuss where these lie. Improvements to the ECELESTE system made in the course of this work and future improvements that are proposed are described in section 5.4.

In order for useful and accurate data to be recorded with ECELESTE, several factors must be in favourable alignment. Firstly, the plasma must be at a correct radius. As the radial extent of the viewing chords is only around 10 cm, the edge region of plasmas with very large or small radius cannot be satisfactorily observed. Small plasmas will not be viewed at all, while the emission observed from very large plasmas will not have a large perturbation from the gas puffing, as the penetration is only significant up to $\sim$ 10 cm from the plasma edge. All plasmas grow from a small merging compression in MAST at start-up, and so the early part of the shot is never captured for all measurements currently existing. Often the plasma will shrink at ramp down, so this is usually not captured either, meaning often only the current flat top is observed. While the position of the chords can be set at different major radii to accommodate large or small plasmas, this requires an entry to the MAST machine area, and is not something that can be done from plasma shot to plasma shot on an ad hoc basis.

Another limitation arises from the position of the plasma nozzle. The strength of the modulation in the emission signal intensity is proportional to the position of the nozzle. In the modelling this was assumed to be within $\sim$ 1 cm of the plasma edge. However, if the plasma radius grows unexpectedly due to ELMs or vertical displacement events (VDE's) for

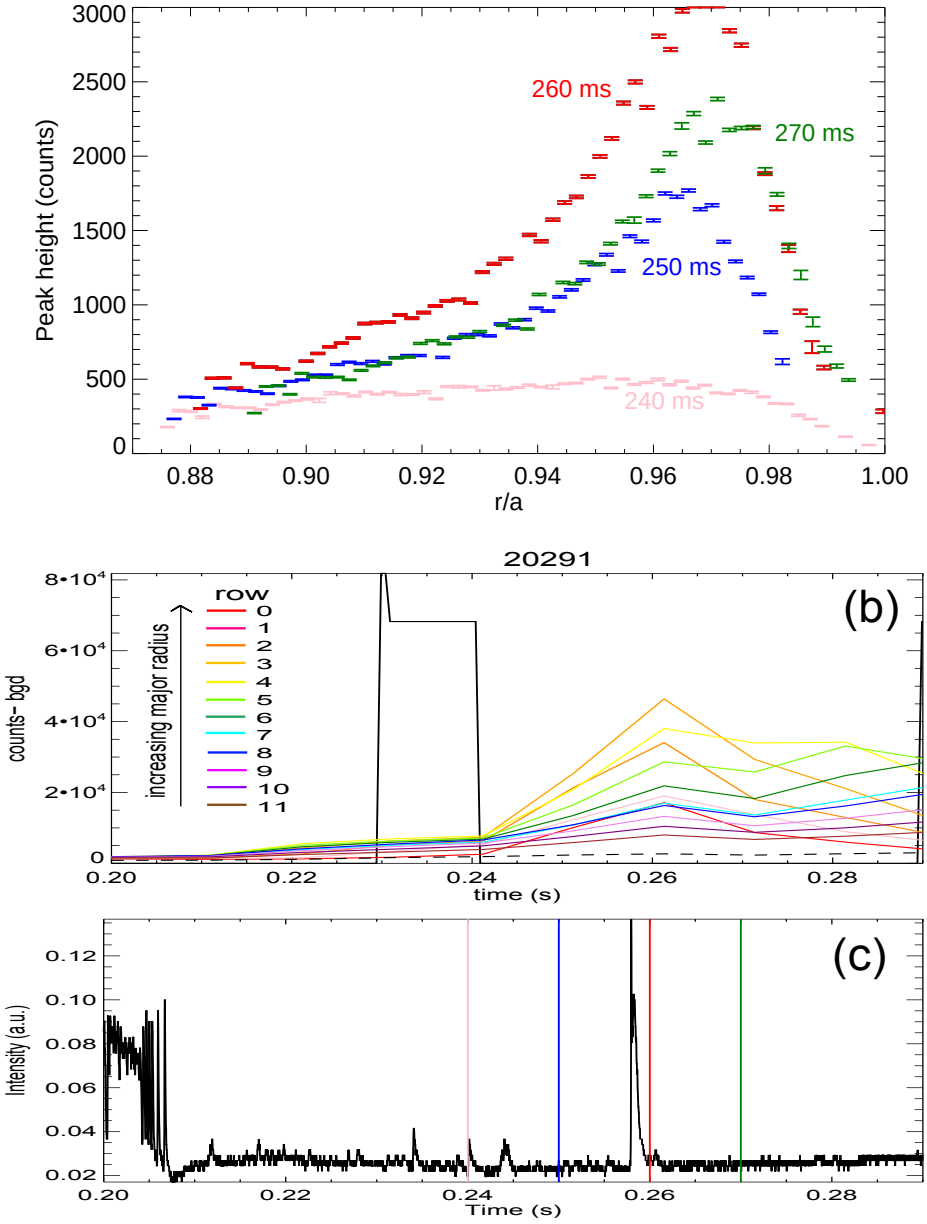


**Figure 5.9:** *(a) Recorded peak heights for shot 20291, times indicated are the time at the end of the 10 ms integration period, showing the lack of influence the ELM has on the intensity profiles. (b) Integrated line intensity showing the influence that the active gas puffing has across this time. The black line denotes the voltage signal to the HELIOS piezoelectric valve (i.e. when it is opened) and the black dashed line the recorded radial chord data (i.e. plasma background). (c) The D-alpha integrated emission recorded by a photomultiplier tube showing the time and duration of the recorded ELM and end times of each timeslice integration period.*

example, the plasma can hit the nozzle. This is both damaging to the nozzle as it can cause melting and halo currents, but can also cause a disruption in the plasma due to the ablation of boron and nitrogen from the nozzle head which cools the plasma through radiation from these heavy impurities. For this reason it is often necessary to situate the nozzle several cm from the expected plasma edge. This causes a corresponding loss in the response of the system as the gas puff is spread over a larger area as it enters the plasma, such that the stimulation is spread over a larger area and does not lead to as large a spike in the emission profile, due to less of the emission being observed. Furthermore, the observation is not as localised so the radial resolution is also poorer.

Beyond this the signal becomes reduced by degradation of window transmission over time, due to deposition onto the windows surface during plasma shots. Normally a shutter would be installed to reduce this effect, but unfortunately shortly after the start of the M7 MAST experimental campaign (January 2009 to April 2010) when most of the data was recorded, the shutter mechanism failed and was not available to be repaired until the end of this campaign. This is likely to have resulted in a reduction in overall signal level, but it is not possible to compare similar shots from the start and end of the campaign to quantify this as data was only recorded near the end of the campaign, although qualitatively there appears to be a large difference in comparison with data from the M6 experimental campaign prior to this. Transmission curves recorded for a new clean window, as installed at the start of the campaign, compared to transmission of the ECELESTE optics window at the end of the campaign, show that throughput is only 40% of what it was at the start of the M7 campaign at the 529 nm wavelength (see figure 5.10).

Due to poor signal to noise ratio as a result of the above limitations, it is necessary to record data over a time window of 5-10 ms. Therefore only evolutions in the plasma on this timescale can be accurately determined. For example, ELMs occur normally on a timescale of 100 $\mu$s and so will not be recorded. Similarly any movement of the outer radius of the plasma will be averaged over during the recording of the data, and this further reduces the spatial resolution when trying to determine features in the data. It therefore becomes desirable to only select data where the outer radius does not change significantly (as recorded by either the position of $D_\alpha$ peak emission [87], or from EFIT reconstruction [102] of the magnetic signals).

In order for the extra deuterium introduced by the gas puffing to be dispersed around the plasma, gas puffs must be spaced apart so that the active signal recorded by the ECELESTE system returns to background level so that background can be recorded, and so that the puffing does not significantly perturb the plasma. Data recorded as the puff

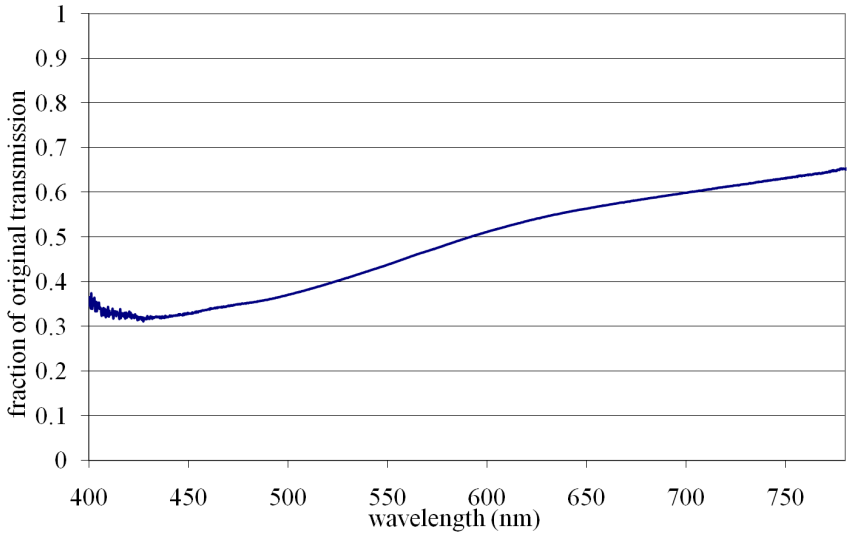


**Figure 5.10:** *Ratio of the transmission of the ECELESTE optics window at the end of the M7 campaign compared to that of a new and clean window. The absolute transmission of the clean window is over 90% at 529 nm.*

dies away are still valid but have a worse signal to background level as the neutrals are removed. Figures 5.1 and 5.2 show that the timescale for this is around 40 ms. Therefore it is also necessary to space the gas puffs at least 40 ms apart, leading to a further reduction in the number of useful timeslices.

In its original form therefore, the ECELESTE system cannot be utilised as a routine diagnostic to provide data at a fast rate throughout plasma shots. However, systemic improvements were made to increase availability and data quality, while further improvements are also being developed. These are outlined in section 5.4.

## 5.4 System Improvements

### 5.4.1 Introduction

Because of the limitations of the charge exchange technique used, several ideas were planned to improve the performance of the system. Improvements implemented or currently being added to the system included a new bandpass filter, a new camera, a new piezoelectric valve in the HELIOS nozzle and double-binning the data. The authors contribution in each case was full control of double-binning implementation and purchase and design of band pass filter, the contribution of the physics basis in the case of the piezoelectric valve and assistance in the commissioning of the new camera. At the time of writing the double-binned data and new filter had been fully installed with data recorded, while the camera

and valve are currently being installed. These are all discussed and their impact assessed, and further ways in which the system could be improved are discussed.

### 5.4.2 A new bandpass filter

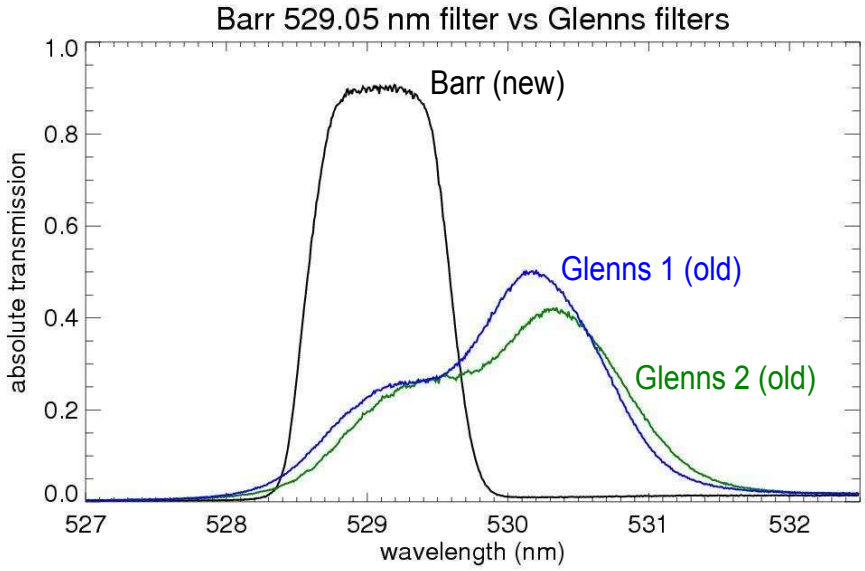


**Figure 5.11:** *Transmission profiles as a function of wavelength for both the new Barr Associates bandpass filter and the two original Glenns filters, measured using a PI Acton spectrometer.*

In particular in L-mode expected signal levels are small, since the $C^{6+}$ content in the edge is low. Hence, the throughput through the spectrometer needs to be optimised. The ECELESTE spectrometer had a choice of two similar bandpass filters manufactured by Glenns which were purchased many years ago and were designed for core CXRS measurements. These had had a transmission of only $\approx 30\%$ at the charge exchange wavelength and were too spectrally wide, potentially causing crosstalk between different chords if other emission lines were allowed to pass onto the CCD at close-lying wavelengths. Furthermore the filter shape was not flat in the bandpass region, which could lead to distortions in the shape of the emission spectrum (see figure 5.11). For these reasons it was decided to replace the bandpass filter with a more efficient design.

The main specifications were to maximise the transmission in the bandpass region and to get this area as flat as possible to minimise distortions. This had to be balanced against not making the filter too wide to avoid crosstalk from adjacent chords (because the slits are horizontally next to each other there may be spectral contamination from one spectrum to the other). This criteria was eased by using the chequerboard pattern in laying out the chords on the CCD (see figure 4.1). It was also necessary to determine how large a

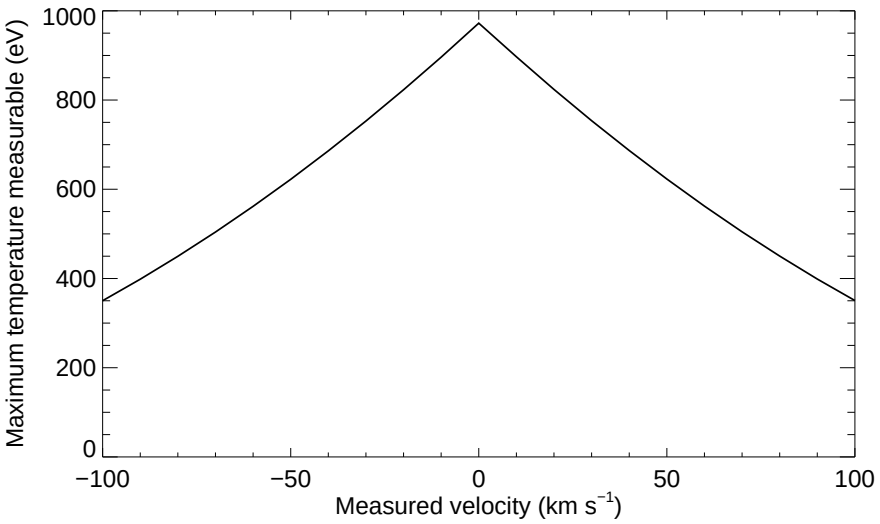


**Figure 5.12:** *Maximum temperature measurable as a function of plasma rotational velocity. At large velocities the maximum measurable ion temperature becomes smaller, so this accommodating the measurement of both must be balanced against the maximum possible spectral width of the filter when it is being designed.*

rotation and temperature could be accommodated before the edges of the filter distorted the shapes. Temperature can only be determined if at least 1 standard deviation of the Gaussian lineshape is visible on either side of the central wavelength position. Therefore movement of this position from the centre of the filter due to plasma rotation reduces the maximum temperature that can be determined. In the case of large rotations the Doppler shift could result in the position of the majority of the charge exchange Gaussian lying outside the transmission curve. Figure 5.12 illustrates the compromise between the maximum temperature measurable due to Doppler shift as a function of plasma rotational velocity. As shown in chapter 6 this should be more than adequate to accommodate the temperatures and velocities typically present at the plasma edge. The resultant design was a six-cavity filter manufactured by Barr Associates with a transmission spectrum shown in figure 5.11. The improvement in signal level is shown in a comparison between the recorded intensities in two similar shots at the same time, plasma density and outer radius, one with the original Glenns filter and one with the new Barr filter (figure 5.13). This shows that the signal level was increased by the expected factor of 2-4.

### 5.4.3 A new gas puffing piezoelectric valve and new nozzle head

As discussed in section 2.2.1 the gas injected through the HELIOS nozzle is controlled via a piezoelectric valve. This is located around 1.5 m from the end of the nozzle (see figure

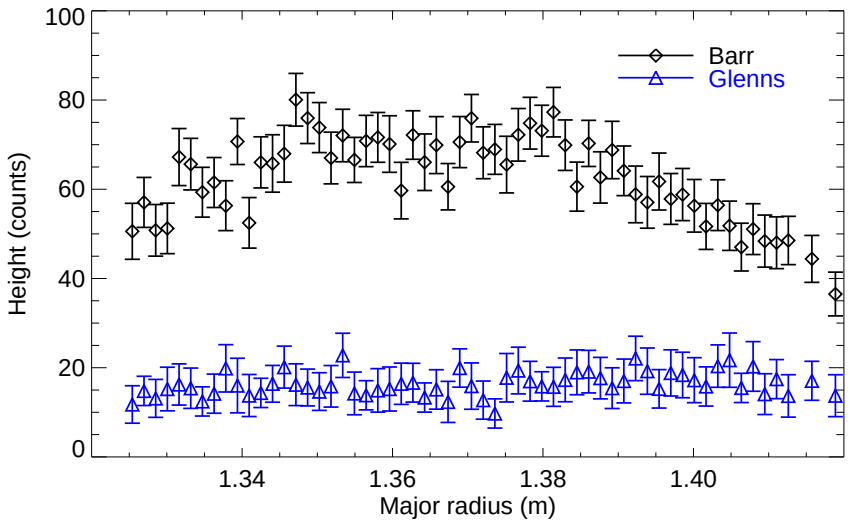


**Figure 5.13:** *Recorded ECELESTE emission as a function of major radius using the two spectral filters in similar shots. The comparison between the intensity profiles shows that the Barr filter transmits a greater signal than the Glenns filter by a factor of 2-4.*

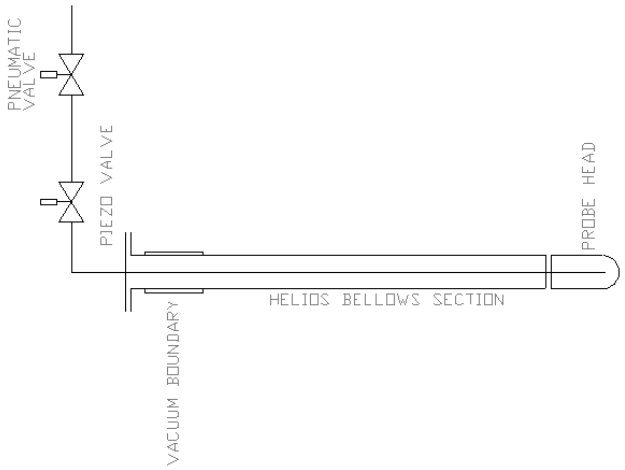


**Figure 5.14:** *Schematic of the HELIOS system showing the position of the pre-existing valves and nozzle head*

5.14). This results in a delay between the signal and entry of the gas into the plasma of $\sim$ 15 ms with $\pm$5 ms variability, and also means that the gas puff spreads out in space as it travels down the pipe due to the Maxwellian distribution of velocities of the gas. This means that the gas puff increases the signal above background for around 40 ms $\pm$10 ms (see figure 5.1). It was therefore decided to add an additional valve at the plasma facing end of the nozzle so that the delay time would be reduced, and the variability eliminated. The additional valve would also enable more intense, shorter puffs by delivering the same

volume of gas in a shorter time, as the gas would not have as large a distance to travel and expand as it moves along the piping. This would both increase the signal to noise ratio and allow more gas puffs to be fitted into each shot, providing more data. By adding the new valve the nozzle head had to be redesigned and a new nozzle head manufactured to accommodate it.

The design of the valve therefore required the opening and closing times of the valve to be as small as possible and the cycle time to be of the order 10 ms. The valve must also allow at least the same volume of gas to flow per opening, so that the conductivity of the system is as large as prior to the upgrade to avoid bottlenecks in the system due to the new valve. It is also desirable to locate the valve as close as possible to the plasma. However, this means that the valve must be mostly maintenance free as it is difficult to remove the nozzle head when not in an engineering break, and that the valve must be able to survive the bake out of the nozzle head ($\sim$ 65 °C).

A local plenum was added and the existing pipe diameter of 4.76 mm increased, which increases the conductivity limit on the system so that the limiting factor is now the new valve. The blocking force of the valve was also required to be larger than the force due to the gas pressure ($\sim$ 10 N) and the valve needed to fit within the approximately cylindrical nozzle head, the dimensions of which are 206 mm in length and 40 mm in inner diameter. The valve was also required to fail open in order for the system to be used as it was originally designed, in case of mechanical breakdown.

The plenum is large enough that the upstream pressure does not significantly change while the valve is open. Using the same model as in section 3.6.2 the mass flow rate is thus wholly determined by the area of the valve opening, i.e. $\dot{m}(t) = \rho v A(t)$. Therefore the flux is a time function of the effective blocking area of the ball as the valve moves in and out.

It was decided that the valve itself should be a 'ball-in-cone' design. This has two main advantages: firstly that a smooth self aligning fit is possible and secondly that the cone shape also expands the area of the valve to increase flow throughput at the valve and thus allow an actuator with a small movement to be used. The three main design possibilities to drive the valve were a piezoelectric actuator directly connected to the valve inside the nozzle head, a piezoelectric actuator outside the vessel driving the valve via a metal string, or a mechanical pneumatic piston outside the vessel driving the valve in the same way.

The mechanical actuator was found to have a significantly large response delay of around 50 ms which would not be acceptable, while the response of the piezo-actuator was smaller than 1 ms. The expansion of the string due to mechanical strain was determined to be too large for a piezoelectric actuator to work effectively ($\sim$ 750$\mu$m for a 1.5 m long, 0.5 mm

diameter steel string) compared to typical movement of a piezo-actuator of 100-1000 $\mu$m, so only the first option of using a piezoelectric actuator inside the nozzle head was viable.

**Figure 5.15:** *The amplified piezoelectric actuator used in the gas valve design. The elastic mechanical amplifier surrounding the crystal stack increases the movement by up to a factor of ten.*

An amplified piezoelectric actuator consists of a stack of piezoelectric crystals confined in an elastic mechanical amplifier (see figure 5.15). This can produce movements of around 1% of the actuator's length, up to a maximum of around 1 mm, and large blocking forces of up to $\sim$ 2000 N [103]. It has a high force to mass ratio which produces a fast response time, and as it is solid state it contains no moving parts to drive the actuator, making mechanical failure due to fatigue unlikely. The movement is proportional to an analogue voltage signal which makes the movement resolution very fine and it also can operate in high vacuum. However, the displacement is small and it is limited by its Curie temperature to less than 450 K [103]. It also cannot take large torsions.

In order to maximise the throughput area of the valve, the ball size and conical seat were made large, at 25 mm in diameter and 18 mm in diameter at the point of contact respectively. This allows the same volume of gas to flow past the valve as did prior to its installation. The piezoelectric actuator used was a Dynamic Structures and Materials leveraged piezo-actuator [104] with 110 $\mu$m of movement. Its small size ($26 \times 36 \times 12$ mm) allowed it to easily be accommodated within the nozzle head. When a positive voltage is applied the actuator expands, closing the valve (see figure 5.16). As it is pre-loaded a negative voltage can be used to drive it open, allowing a fast repetition rate. The actuator

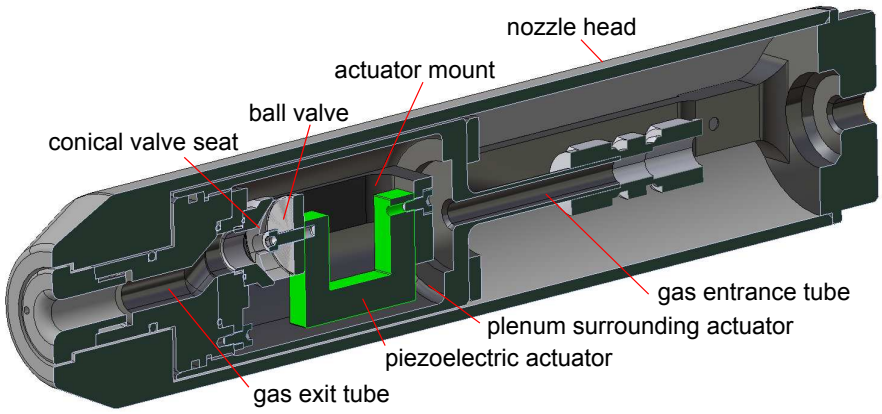


**Figure 5.16:** *The final design of the piezoelectric actuated gas valve with annotations of the major components.*

has a high resonant frequency of 3450 Hz [104], well below the expected frequency of use of approximately 550 Hz. As required, this will also fail in the open position.

The nozzle head is constructed from hexagonal Boron. This has a very low heat conductivity of 0.06 W $m^{-1}$ K [105]. ELMs and disruptions could hit the nozzle end and transfer heat from the plasma to it, potentially heating the piezoelectric material above its Curie temperature. However, it can be estimated that due to the insulating properties of the boron nitride the actuator should be heated by less than 5 K. In order to further insulate the actuator the gas flows into the space around the piezo-actuator, forming a small plenum which also acts to cool the actuator.

### 5.4.4 A new CCD camera

As mentioned in section 2.2.4 due to the design of the initially employed camera only 48 timeslices could be recorded. In order to be compatible with the MAST-Upgrade project the camera must be able to record data for at least 5 seconds, so this is entirely inadequate. Furthermore the quantum efficiency of the original camera is very low by modern standards at only around 18% at 529 nm. A new camera was also required as a back-up for the core charge exchange system. For these reasons and in order to upgrade the performance of ECELESTE in measuring the radial electric field ($E_R$) two new Princeton Instruments ProEM512B cameras were purchased.

These cameras have a similar area as the original camera (512 $\times$ 512 16 $\mu$m square pixels) so that the existing camera support system does not need modification, but have a much improved quantum efficiency of $\sim$ 95% at 529 nm. As the pixel size is smaller the number of pixels recording part of the spectrum is increased, improving spectral fitting

ability at a small cost to recorded intensity per pixel. They can also record continuously at a frame rate of less than 2 ms as either 5 Mhz or 10Mhz amplifiers were available, compared to 200 kHz in the original camera, and even faster for a limited time. The camera has two forms of gain: from the pre-amplifier (similar to the previous CCD camera) and electron multiplication gain. The former will improve slightly the signal to noise at higher gain, but reduce the dynamic range, since the full well cannot be used. The latter will increase the shot noise by 1.4 via the electron multiplication, but will almost eliminate the effect of read-out noise, by amplifying the signal by up-to a factor of 1000. If noise is a large problem a low noise amplifier at either 5 MHz, 1Mhz or 100 kHz is also available with reciprocal gains of 1.15, 0.81 and 0.72 electrons per count respectively, compared to 2.5 electrons per count in the original camera. Due to the combination of better quantum efficiency and improved reciprocal gain even at 5 MHz using the low noise amplifier the increase in signal should be a factor of $\sim 8$ per pixel. At lower speeds this can be improved further.

Unfortunately these new cameras were not installed in time to produce data for this thesis, but they should provide a significant improvement to the ECELESTE system and mostly negate the problem of insufficient signal to noise ratio. This should allow a combination of higher speed data recording or higher quality data recorded on a similar 5-10 ms timescale.

### 5.4.5 Double binning of data

A simple way used to improve the signal to noise ratio utilised prior to the installation of the new cameras was to combine the recorded data of two chords together to produce a single signal. This has the effect of doubling the signal but at the cost of halving the radial resolution and spatial resolution. The number of recorded chords is reduced to 29 from 59 (not including the radial chord). For the data recorded in M7 when the data quality was poor due to window degradation this improvement was therefore adopted. The result of this is shown in figure 5.17 where as in section 5.13 a comparison between the recorded intensities in two similar shots at the same time, plasma density and outer radius is made.

### 5.4.6 Further improvements

As well as the two new cameras, the poloidal optical system has been upgraded so that it will have a much larger aperture f/2 optics. This means it should couple a similar amount of light into the system as the toroidal optics. Furthermore a second spectrometer has been added with up to 120 slits to record the poloidal views using the second new camera. Using this system it should therefore be possible to record both toroidal ($v^i_\phi$) and poloidal ($v^i_\theta$)

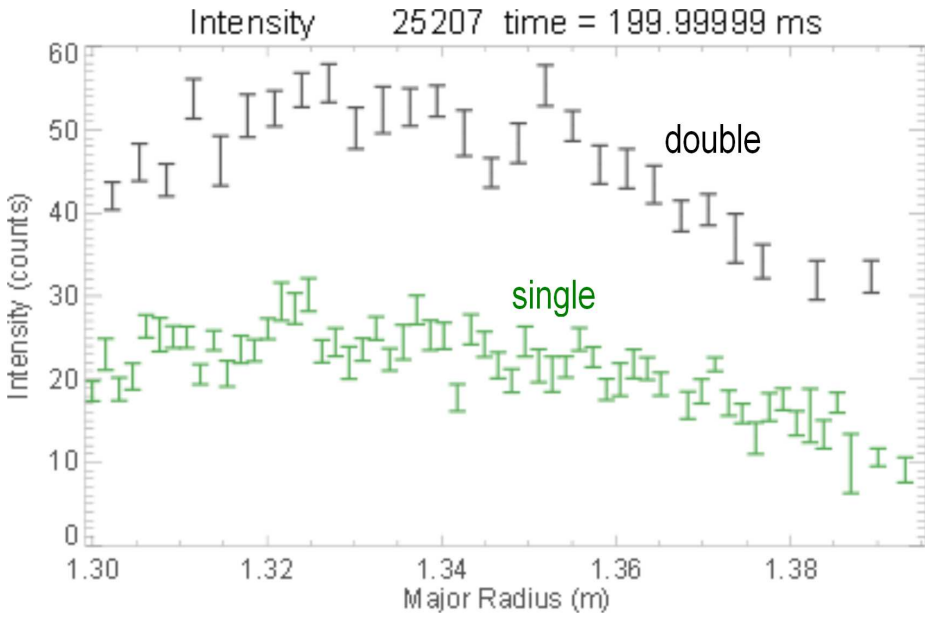


**Figure 5.17:** *Recorded ECELESTE emission as a function of major radius using either single-binning or double-binning of data in similar shots (25156 and 25207 respectively, both at 200 ms). The comparison between the intensity profiles shows the expected doubling of recorded signal.*

velocities simultaneously, as well as ion temperatures from poloidal and toroidal directions. This can be used either as a double check that the temperatures recorded are correct, or the toroidal system can be moved to extend the region where $T_i$ is measured in the edge. This would mean that temperatures could be measured for a wider range of plasma radii and during a longer part of the shot. Moreover the system could now be used exclusively to measure $C^{6+}$charge exchange emission as $v_\phi^i$ and $v_\theta^i$ can be used to determine $E_R$. This would remove the necessity of changing over between the two different measurements and decrease calibration uncertainties.

## 5.5 Conclusion

The impact that the gas puffing has on recorded intensity profiles in the ECELESTE spectrometer is shown to be significant in both H-mode and L-mode plasma shots. The effect of increased $C^{6+}$ density in H-mode results in a higher signal and therefore higher quality data as predicted in chapter 3. By using recorded values of $T_e$, $n_e$, and $T_i$ the forward modelled profiles shown in section 3.7.2 are improved upon and shown to generally agree with recorded intensity profiles in H-mode. In L-mode the agreement is weaker and this is most likely to be due to an underestimation of the extension of $C^{6+}$ ions to large radii in the model. The effects of ELMs on the data are also investigated and it is shown

that these are unlikely to affect the temperature and velocity profile shapes due to their fast transient nature. However, the ELMs do result in a density decrease due to particle losses and can thus reduce the signal level.

The limitations to the ECELESTE system due to the small spatial extent of the chords, positioning of the nozzle and required spacing of the gas puffing are discussed. Window degradation issues also have limited the throughput of the system, aggravating a low signal to background ratio for a large amount of data. To address these issues several system improvements were designed, including a new bandpass filter, double-binning of data, a new valve for the HELIOS nozzle and new CCD cameras. The new bandpass filter and the double binning of data have been implemented and their effect on the signal level assessed. The improvements due to the new fast HELIOS valve/nozzle, the second spectrometer and the new CCD cameras can not be shown, since no data has been collected, although the system is now fully implemented. These improvements and their impact on the performance of the system are discussed.

Having established the ECELESTE system performs closely to the predictions of chapter 3 the recorded temperature and velocity profiles are analysed in 6.

# Chapter 6

# Analysis of velocity and temperature results

## 6.1 Introduction

The performance of the ECELESTE system as discussed in chapter 5 indicates that using gas puffing of neutral deuterium in charge exchange with carbon ions to determine ion temperatures and toroidal velocities is feasible. In this chapter typical toroidal velocities for L-mode, Ohmic and H-mode shots are presented which have been deduced from the charge exchange emission spectra.

A large reverse velocity shear (positive gradient opposed to the generally negative gradient with increasing radius) in the plasma edge in H-mode, L-mode and Ohmic discharges is consistently observed close to the separatrix of the plasma. No reverse shear is observed in L-mode discharges in counter-rotation experiments while rotation becomes negative in the outer region close to the separatrix, indicating that the shear is linked to ion drifts. The Pfirsch-Schlüter flow is proposed as a likely candidate to produce these results and an estimation of the expected contribution from diamagnetic and $\mathbf{E} \times \mathbf{B}$ components of the flow is made.

Typical temperature results in H-mode and L-mode are presented and a comparison between measurements from ECELESTE of $T_i$ are compared to $T_e$ from Thomson scattering and $T_i$ from core CXRS where available. In some cases the ion temperature in H-mode does not display a similar steep gradient as the electrons in the pedestal region, resulting in a large ratio between $T_i$ and $T_e$ at the separatrix. An assessment of whether this is compatible with equilibration times between the ions and electrons is made. The effect a large disparity between $T_i$ and $T_e$ in the edge region would have on the power balance is also examined to ensure that this does not significantly effect the power fluxes in the edge

region, and to determine whether differences in the heating sources could be responsible for the difference.

A gyrokinetic formalism predicts that the gradient scale length of the ion temperature must be large in the banana collisionality regime, but that this requirement does not hold in more collisional regimes or for the electrons, indicating a possible connection between collisionality and ion temperature gradient. A dimensionless scan of collisionality has been made which supports this argument. The compatibility of this with predictions of ion to electron temperature ratio in the scrape-off layer is also assessed.

## 6.2 Toroidal velocity results

The true test of the ECELESTE system is its performance in measuring ion temperatures and velocities in the edge region. The velocity results are discussed here, with temperature results in section 6.3. The velocities are determined as discussed in section 1.5 with absolute values found using the radial chord when that is available and otherwise determined less accurately from calibration from a spectral lamp and ratio of spectrometer grating position (see appendix C). In the following all results use the radial chord method except in the case of the counter-rotation measurements. Positive rotation is designated as the direction of positive $I_p$ in normal operation which is counter-clockwise when viewing the tokamak from above. This is also the direction of neutral beam injection, while $B_\phi$ is negative in this case.

The results for L-mode and Ohmic rotation are shown in figure 6.1. The results in L-mode with beams on show good agreement with those from the core CXRS system when $r/a <\sim 0.95$ but show a large reverse shear outside this of up to $\sim 40$ km s$^{-1}$. The core CXRS system also records a reverse shear, but typically smaller in size than that measured by ECELESTE. The results for Ohmic discharges are very similar to those in L-mode, with a reverse shear of similar size. This implies that the inverse shear rotation is generally driven by intrinsic rotation processes in the outer edge region, not by neutral beam torque. This shear will be discussed in section 6.2.1. Average rotation velocity of the carbon ions at $r/a = 0.9$ from the available results with the standard deviation in values is $22 \pm 6$ km s$^{-1}$ for L-mode discharges, while for Ohmic discharges it is $13 \pm 7$ km s$^{-1}$. While this is not statistically significant it does indicate that it is likely that rotation inside the inverse shear region is driven at least partially by neutral beams.

Results for H-mode (see figure 6.2) generally show a much higher rotational velocity and greater negative gradient in the edge region compared to L-mode and Ohmic results. The higher rotation could be expected due to increased beam torque from NBI while large

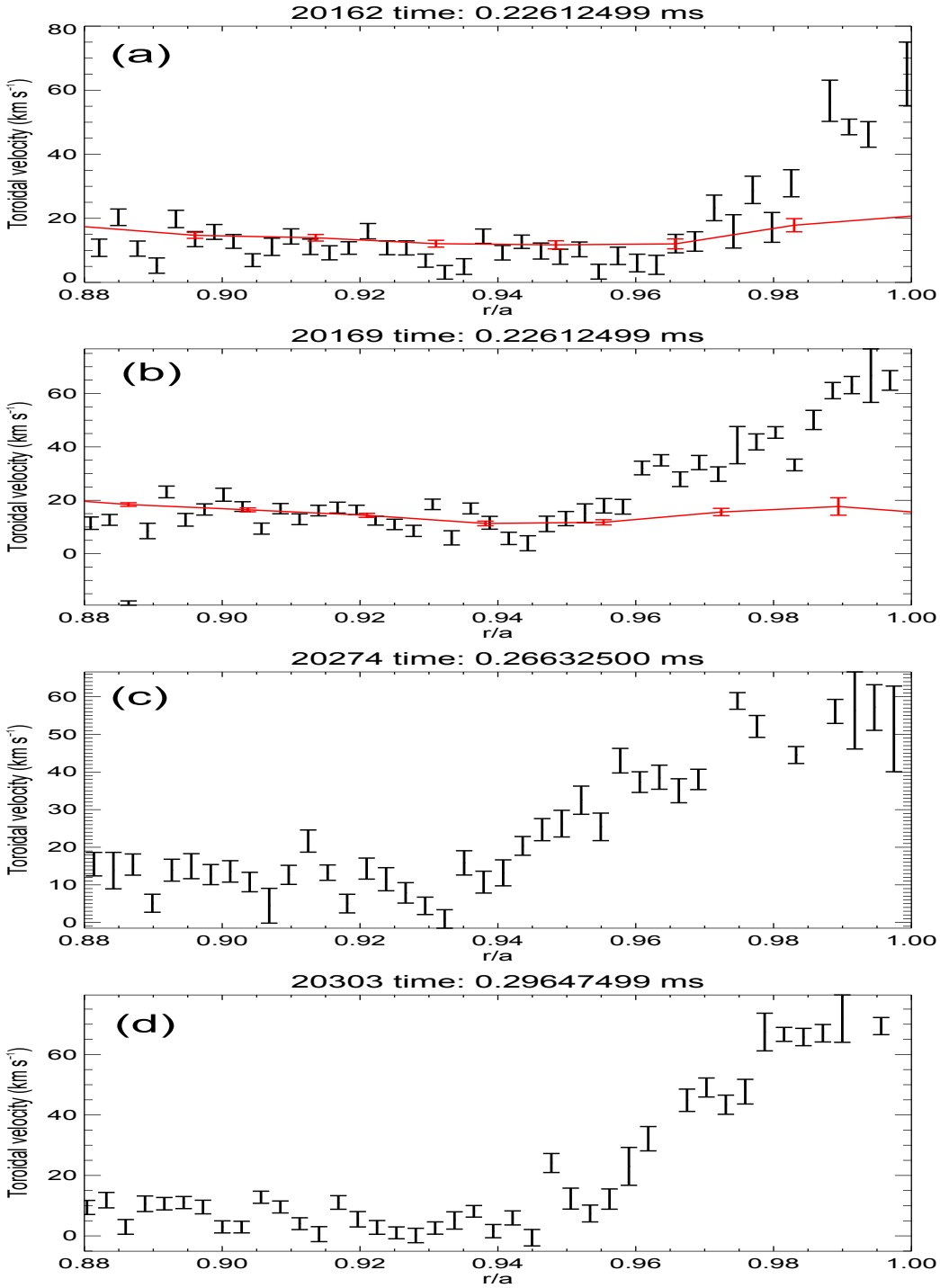


**Figure 6.1:** *Typical L-mode and Ohmic velocity profiles from ECELESTE (black data points) compared with $v_\phi$ data from the core CXRS system (red data points with line). Figures (a) (shot 20162, time = 226 ms) and (b) (shot 20169 time = 226 ms) are typical L-mode profiles, while figures (c) (shot 20274 time = 266 ms) and (d) (shot 20303 time = 296 ms) are typical Ohmic profiles.*

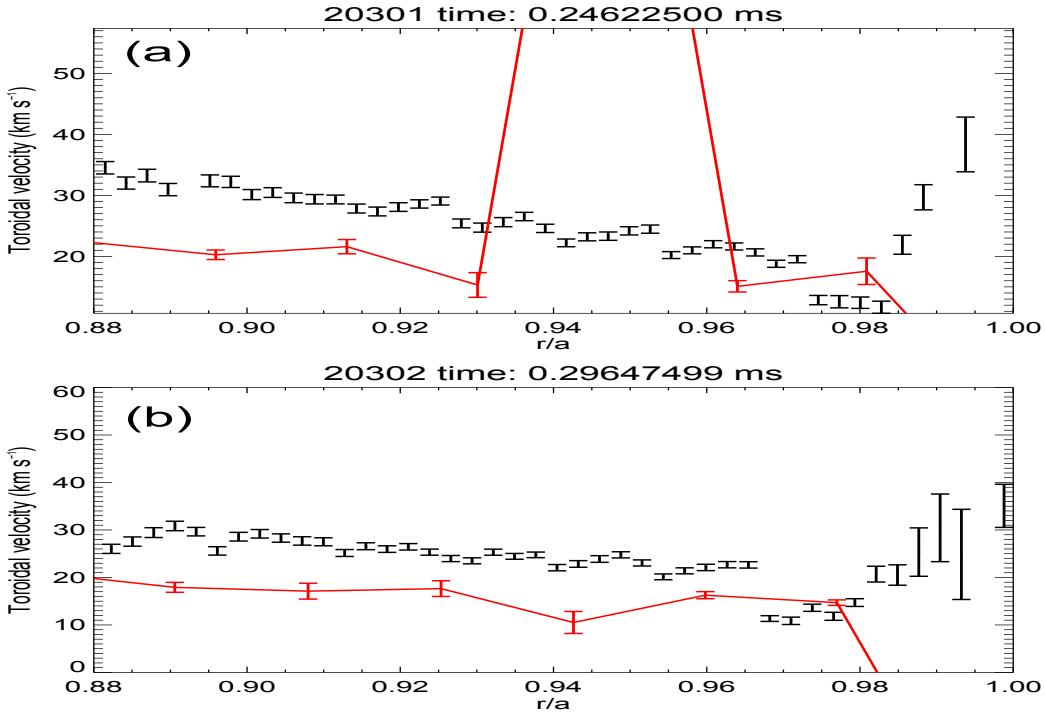


**Figure 6.2:** *Figures (a) (shot 20301, time = 246 ms) and (b) (shot 20302 time = 296 ms) show typical ECELESTE H-mode velocity profiles where reverse shear is observed (black data points) compared with $v_\phi$ data from the core CXRS system (red data points with line).*

gradients are linked to production of H-mode plasmas through suppression of turbulence [106]. The ECELESTE results are often larger than the results from core CXRS. It is unclear why there is a large discrepancy in some cases, although it could be linked to the uncertainties due to the large instrument function in the core CXRS system or a different value for the radial velocity recorded by the radial chord for each spectrometer (although both core CXRS and ECELESTE have a radial view from the same position). Relative values between chords have smaller uncertainties however.

In H-mode when measurements are available close to the separatrix a similar reverse shear to those recorded in L-mode/Ohmic shots is observed, generally with steeper gradient and located much closer to the plasma edge than in L-mode/Ohmic discharges. Due to the radial positioning uncertainties (see section 4.7) and the uncertainty in determining the separatrix position using EFIT [102] it is unclear whether the shear in this case occurs inside the LCFS or in the SOL, but in the L-mode/Ohmic case the reverse shear clearly lies inside the separatrix.

Counter-rotation experiments were made during June 2009, where both $I_p$ and $B_\phi$ are reversed so that the neutral beam torque opposes the current direction. L-mode measurements were made during this campaign and example results shown in figure 6.3. In all

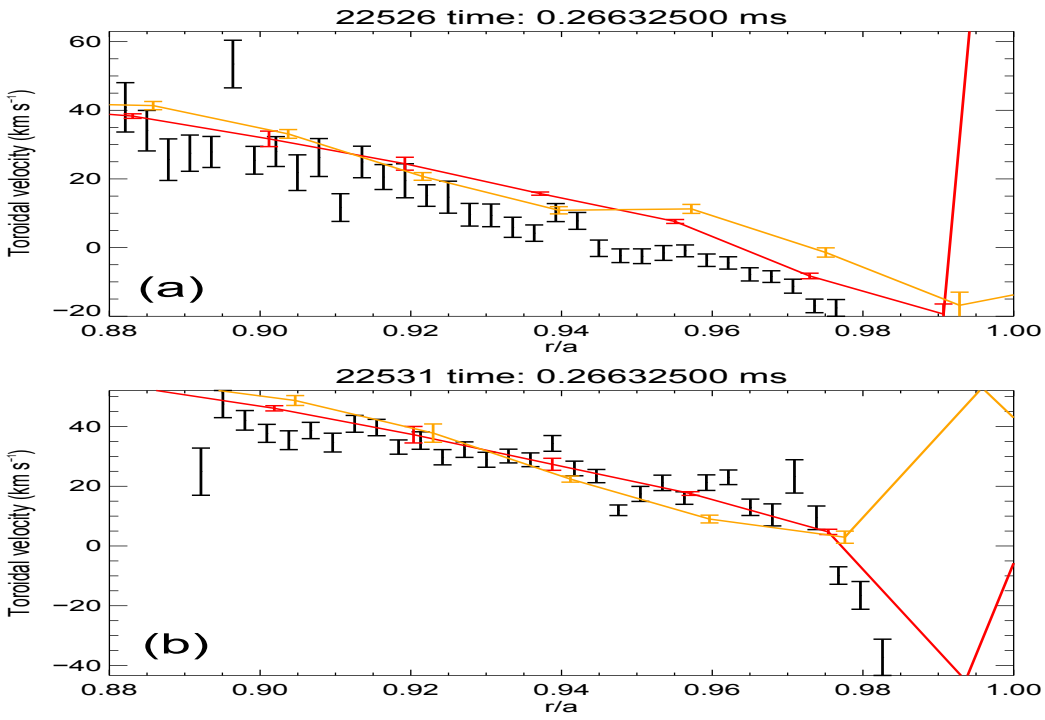


**Figure 6.3:** *Figures (a) (shot 22526, time = 266 ms) and (b) (shot 22531 time = 266 ms) show typical L-mode velocity profiles in counter-rotation MAST operation from ECELESTE (black data points) compared with $v_\phi$ data from the core CXRS system (SS beam red data points with line, SW beam orange data points with line).*

cases no reverse shear is observed, while the velocity often becomes negative close to the plasma edge. This could imply that the shear direction is reversed, which would indicate that it is driven by ion drifts, which reverse direction when $B_\phi$ is reversed. Possible causes of this reverse shear are discussed in the following section.

### 6.2.1 Driving mechanisms for edge shear

Reverse shear near the plasma edge has been observed in several tokamaks including ASDEX-U [101], DIII-D [107] and C-Mod [45] using CXRS from deuterium [101], helium [101], boron [45, 101] and carbon [101, 107]. Measurements showing a similar structure have also been made using Mach probes on the EAST tokamak [108] and in JET [109], which indicate the reverse shear extends into the SOL, and that this rotation is intrinsic, which is in agreement with the results from Ohmic discharges on MAST. The shear reversal in the CXRS cases are all in H-mode and are of order $\sim 12 - 17$ km s$^{-1}$ for ASDEX-U, $\sim 8$ km s$^{-1}$ for DIII-D and $\sim 10$ km s$^{-1}$ for C-Mod, which is much less than the values of up to $\sim 20 - 30$ km s$^{-1}$ and $\sim 40$ km s$^{-1}$ recorded by ECELESTE in H-mode and L-mode respectively. For the Mach probes the values recorded are up to $M = 0.6$ in the SOL for

JET in L-mode discharges which corresponds to $\sim 25$ km s$^{-1}$ while the change in velocity is $\sim 10$ km s$^{-1}$ for EAST in Ohmic discharges.

Chankin *et. al.* (2000) [110] use the SOL transport code EDGE2D [111] to model the parallel flows in the scrape-off-layer and near edge plasma of JET discharges. This suggests that flows in the SOL due to $\nabla B$ and centrifugal drifts are mostly responsible for the flow in this region. The intrinsic rotation due to these drifts in the near edge in this model qualitatively matches what is observed on MAST from ECELESTE data, with a positive gradient close to the separatrix in normal operation and negative in counter operation. However, the velocities measured by ECELESTE in counter-rotation and normal operation experiments are not symmetrical about zero, unlike the predictions of the EDGE2D modelling. However, if, as is suggested by the comparison of Ohmic and L-mode data, net positive rotation is driven by neutral beams, there is reasonable qualitative agreement between the model and observations. However, the predicted rotation speeds from EDGE2D are only up to $M = 0.2$ for JET SOL parallel flows, compared to $M = 0.6$ measured in JET [109], and predicts up to only $M = 0.1$ at the separatrix (see figure 6.4). ECELESTE measurements suggest Mach numbers for MAST in the range $M \sim 0.8 - 1.0$ at the separatrix in L-mode and Ohmic cases, and $M \sim 0.4 - 06$ in H-mode. It is not possible to directly compare the modelling with the measurements for MAST but it is likely that the predicted SOL flows would also not be large enough to account for all rotation.

The reversal of the edge flow direction in counter-rotation discharges indicates that the Pfirsch-Schlüter flow may be responsible for some of the flow. This is a parallel return current along the field lines to balance the poloidal ion drift velocity to ensure divergence free ion flux on the field lines, which is projected onto the toroidal velocity chords of ECELESTE. This can be calculated for a species $j$ as [112]

$$v_{\phi}^{PS} = 2qv_{\perp}cos\theta\left|\frac{B_{\phi}}{B}\right| \tag{6.1}$$

where $\theta$ is the angle of the position observed in the tokamak to the midplane, in the poloidal plane, so that $\theta = 0$ along the outer midplane radius. $v_{\perp}$ is given by [112]

$$\mathbf{v}_{\perp} = \left(\mathbf{E_R} - \frac{\nabla p_j}{en_j}\right) \times \frac{\mathbf{B}}{B^2} \tag{6.2}$$

By fitting a modified hyperbolic tangent function to the electron density [113] and a polynomial to the ion temperatures, while using $q \approx q_{95}$, it is possible to determine the diamagnetic flow contribution of the carbon ions to the Pfirsch-Schlüter flow (the second term inside the brackets of equation 6.2) as $\nabla p_C/en_C = \nabla p_i/en_i$ and we assume $n_i \approx n_e$. In L-mode and Ohmic plasmas typical values for the results shown above for the peak in

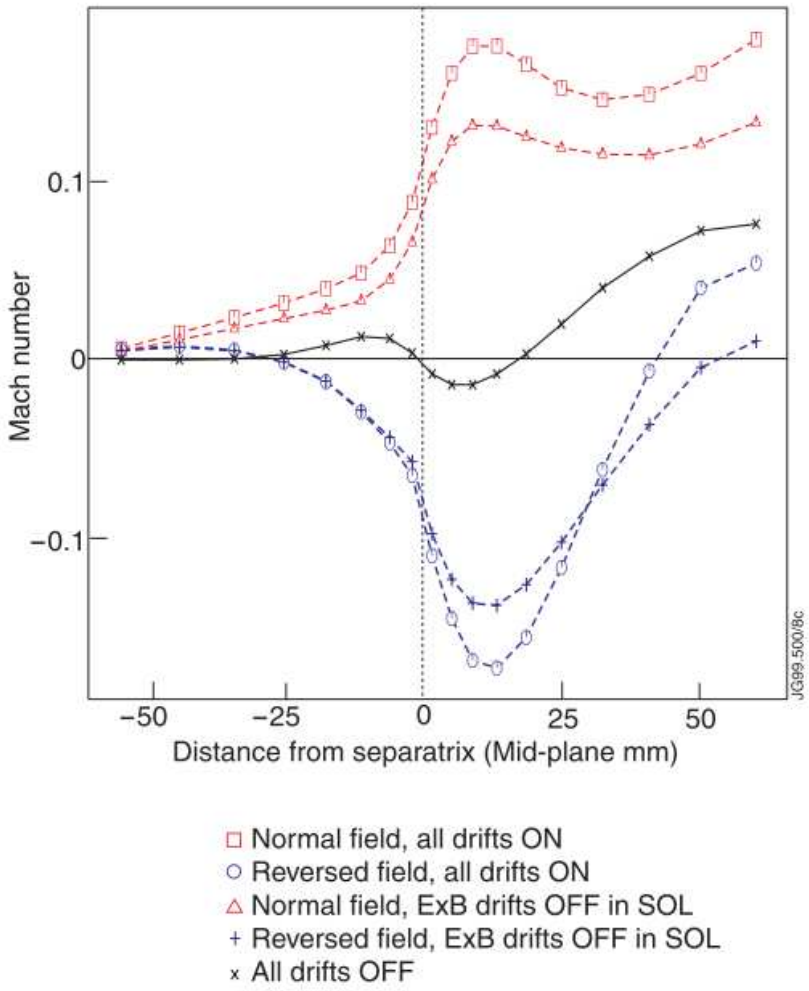


**Figure 6.4:** *EDGE2D code calculations for JET SOL parallel flows, showing the calculated symmetry about zero in the results and lack of flows when all drifts are turned off. In this case $I_p$ and $B_\phi$ were directed in the clockwise direction viewed from above, so positive flow is in the opposite direction from MAST although the $\nabla B$ is still in the downward direction. From Erents et. al. (2000) [109].*

the diamagnetic flow in the toroidal direction are $\sim$ 80 km s$^{-1}$ while in H-mode they are $\sim$ 180 km s$^{-1}$(see figure 6.5). However, the counter-balance to this is a radial electric field with typical minimum well value of +1 to -4 kV m$^{-1}$ in L-mode and -4 to -12 kV m$^{-1}$ in H-mode [53] which results in Pfirsch-Schlüter $\mathbf{E}\times\mathbf{B}$ flow velocity values of approximately 0 to -100 km s$^{-1}$ in L-mode and -60 to -120 km s$^{-1}$ in H-mode (see figure 6.5) at $r/a \sim 0.975$. These two tend to oppose and cancel in the pedestal resulting in a small or zero net flow. The position of the Pfirsch-Schlüter flow in the pedestal region is approximately correct to account for the reverse shear. Furthermore, the measurements indicate that $E_R$ can become positive close to the plasma edge [53] which would produce a net positive flow. In H-mode the gradient of $E_R$ is steeper and closer to the separatrix, which would also be compatible with observations. However, without simultaneous measurements of $E_R$ to determine its contribution to the Pfirsch-Schlüter flow it is impossible to determine if the observed rotation is due to a net flow resulting from the two drifts. Unfortunately ECELESTE is the measurement system used to determine $E_R$ in the MAST tokamak, meaning simultaneously finding $E_R$ and $v_\phi^C$ is not possible. However, this mechanism could explain the observed rotation profiles and the measurements are consistent with what could be expected from this flow. With the upgrade to the MAST poloidal system 5.4.6 simultaneous measurement of $E_R$ and $v_\phi$ will be available.

Xu *et. al.* (2011) [108] identify the dip in rotation with reverse shear outside this as the location of steep edge pressure gradients and large negative radial electric field ($E_R$) in EAST, which would support the suggestion that the reverse shear observed in MAST is connected to the Pfirsch-Schlüter flow. They further conclude that this flow dominates over turbulent Reynold's stress, ion orbit losses and collisional perpendicular shear viscosity as sources of drag in the edge, identifying charge exchange with neutrals as the main source of negative torque at the plasma edge. The neutrals have a rotational velocity much smaller than the equilibrated ions, producing a drag on the rotation.

To determine whether this is likely to be an important effect when considering the Pfirsch-Schlüter flow in the MAST tokamak the ratio of the torque from both the neoclassical Pfirsch-Schlüter flow and that from neutral charge exchange can be calculated as the torque due to charge exchange is given by [114]

$$T_{CX} = \langle J_{CX} R B_\theta \rangle \sim n_{D^0} n_i \langle \sigma v_i \rangle_{CX} m_i \left(v_i - v_{D^0}\right) \tag{6.3}$$

where $J$ is the current of the flow, $v_{D^0}$ the toroidal velocity of the neutrals and $\langle \sigma v_i \rangle_{CX}$ the rate coefficient for total charge exchange between deuterium and $C^{6+}$ carbon ions. Therefore the ratio can be estimated as

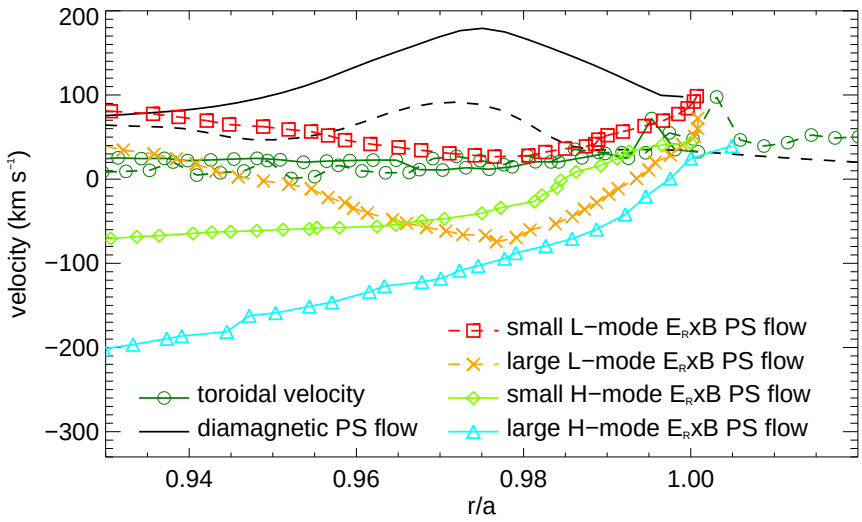


**Figure 6.5:** *Projection onto the toroidal viewing chords of the diamagnetic and* $\mathbf{E}\times\mathbf{B}$ *components of the Pfirsch-Schlüter flow for typical L-mode (dashed lines, shot 20167 time = 226 ms) and H-mode (solid lines, shot 20302, time = 296 ms). The measured toroidal rotation speeds measured by ECELESTE are also shown, indicating that non-zero cancellation between the two components could account for the reverse shear observed close to the edge of the plasma. The example* $E_R$ *data shows the typical range of measured* $E_R$ *in L-mode and H-mode [53].*

$$\begin{aligned}\frac{T_{CX}}{T_{PS}} &= \frac{\langle J_{CX}RB_\theta\rangle}{\langle J_{PS}RB_\theta\rangle} \\ &\approx \frac{n_{D^0}\langle\sigma v_i\rangle_{CX}m_i}{eRB_\theta}\end{aligned} \tag{6.4}$$

where $v_\phi^{PS} \approx v_i - v_{D^0}$ is assumed. For typical values in MAST at the plasma edge of $B_\theta \approx 0.2$, $R \sim 1.4$ m, $n_D^0 \approx 10^{17}$ and $\langle\sigma v_i\rangle_{CX} \approx 10^{-14}$ [115] this suggests a maximum ratio at $r/a = 1$ of $T_{CX}/T_{PS} \sim 1\times10^{-3}$, implying the impact of neutral drag should not significantly change the Pfirsch-Schlüter flow at the plasma edge. Although peak input from gas puffing is two orders of magnitude higher increased local torque due to the gas puffing is also not important as it is the global average influx which is the important quantity in determining the charge exchange torque [114].

## 6.3 Temperature results

Comparison with recorded measurements of $T_e$ from Thomson scattering and $T_i^{core}$ from the core CXRS system (when available) offers a way to assess the reliability of the ECELESTE measurements $T_i^{edge}$. Figure 6.6 shows examples of typical H-mode profiles. Generally there is good agreement between $T_e$ and $T_i^{edge}$ for all $r/a < 0.95$ with a large enough combined

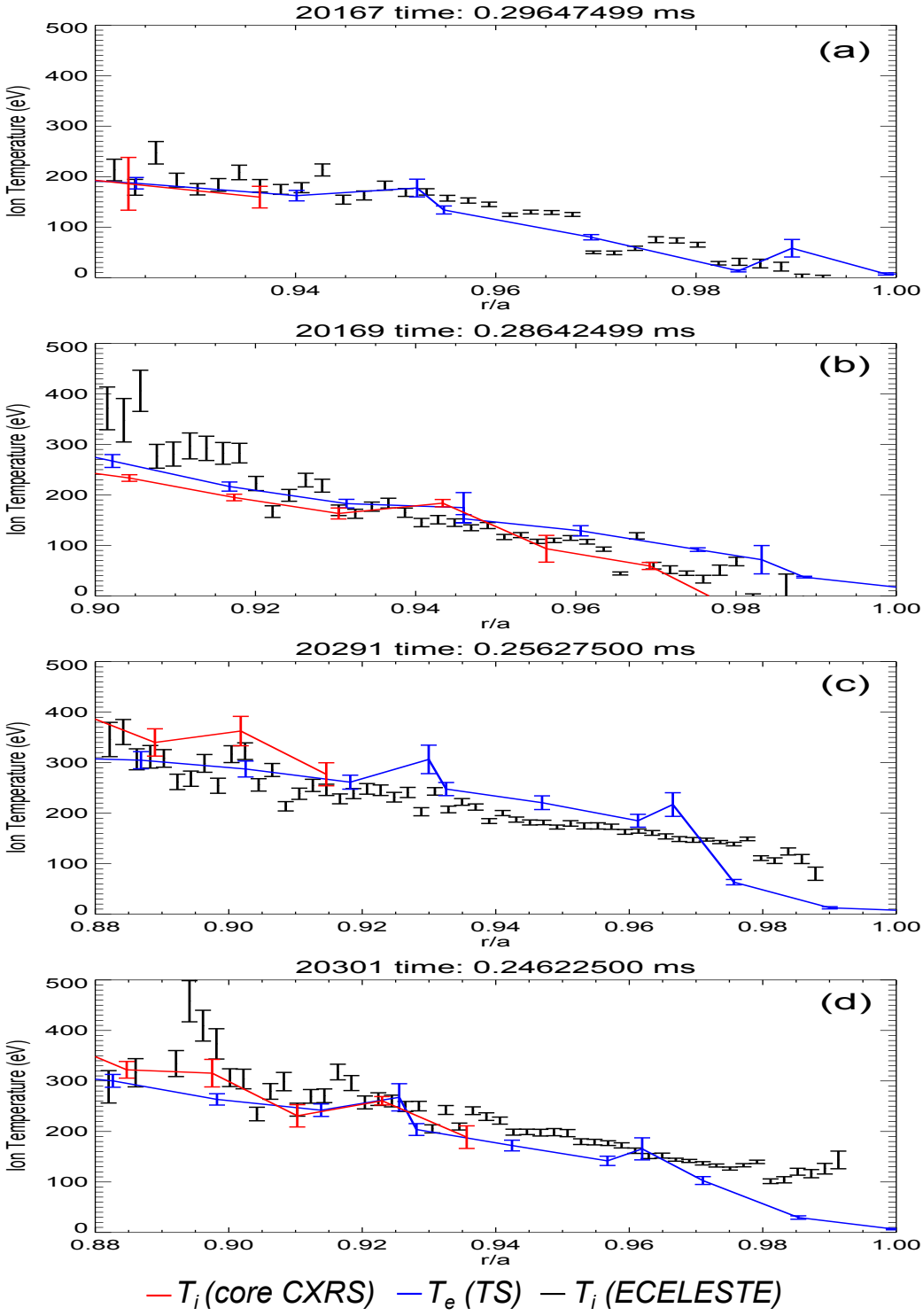


**Figure 6.6:** *Typical H-mode temperature profiles from ECELESTE compared with $T_i$ data from the core CXRS system and $T_e$ data from Thomson scattering. Figures (a) (shot 20167, time = 296 ms) and (b) (shot 20169 time = 286 ms) show examples where there is good agreement between $T_e$ and $T_i^(edge)$ across the entire edge region, while figures (c) (shot 20291 time = 256 ms) and (d) (shot 20301 time = 246 ms) show examples where the ion temperature remains high and maintains a small gradient across the pedestal region, in comparison to the large gradient in the electron temperature.*

error in the measured values of both that it seems likely that $T_i \sim T_e$ in this region. As expected, towards the inboard side the performance of the system deteriorates due to the reduced signal levels as the gas puff becomes ionized as it propagates into the plasma. In general the pedestal region (as defined by the position of the pedestal in $n_e$ measured by Thomson scattering) is the region of highest signal level and therefore the most reliable results. The region very close to the separatrix can also often have larger errors, in line with the recorded intensity measurements (see section 5.2). In H-mode the core CXRS system is often unable to provide reasonable values for $r/a > 0.9 - 0.95$ due to the small signal from the neutral beam. However, where available the measurements do again appear to be within error in most cases.

In many H-mode results the ions often do not appear to have a pedestal. The electron temperature often displays a large pedestal which is strongly correlated in position with the recorded pedestal in $n_e$. In many cases the ions do not show a large gradient and the temperatures of ions and electrons can diverge greatly from similar values at the top of the electron pedestal to extremely different ones at the separatrix. However in other cases the ions do display a similar gradient in line with the electrons so that $T_e \sim T_i$ across the entire edge region. This phenomenon will be investigated in the following sections.

In L-mode the errors are higher, again due to low signal levels, compared to H-mode (see figure 6.7). However the data is in good agreement with both $T_e$ and $T_i^{core}$. No significant consistent deviations from $T_e \sim T_i$ can be determined within the measurement ability of the system.

## 6.4 Are disparities between ion and electron temperatures permitted?

If the ion and electron temperatures differ significantly, this is only likely to be true if the thermalization time between the two species is significantly longer than the thermal transport time of the ions. The transport time is given by equation 3.2 while the ion-electron equilibration time is given by [5]

$$\tau_{ie} = \frac{3\sqrt{2}\pi^{3/2} m_e m_i}{n_i e^4 Z_i^2 \ln\Lambda} \left( \frac{k_B T_i}{m_i} + \frac{k_B T_e}{m_e} \right)^{3/2} \tag{6.5}$$

As the thermalization time of the ions and carbon impurities is always much shorter than that for equilibration between the electrons and either species the correct time to use is that for the equilibration between the bulk deuterium ions and electrons as collisions between the two will dominate over interactions between carbon and electrons in equili-

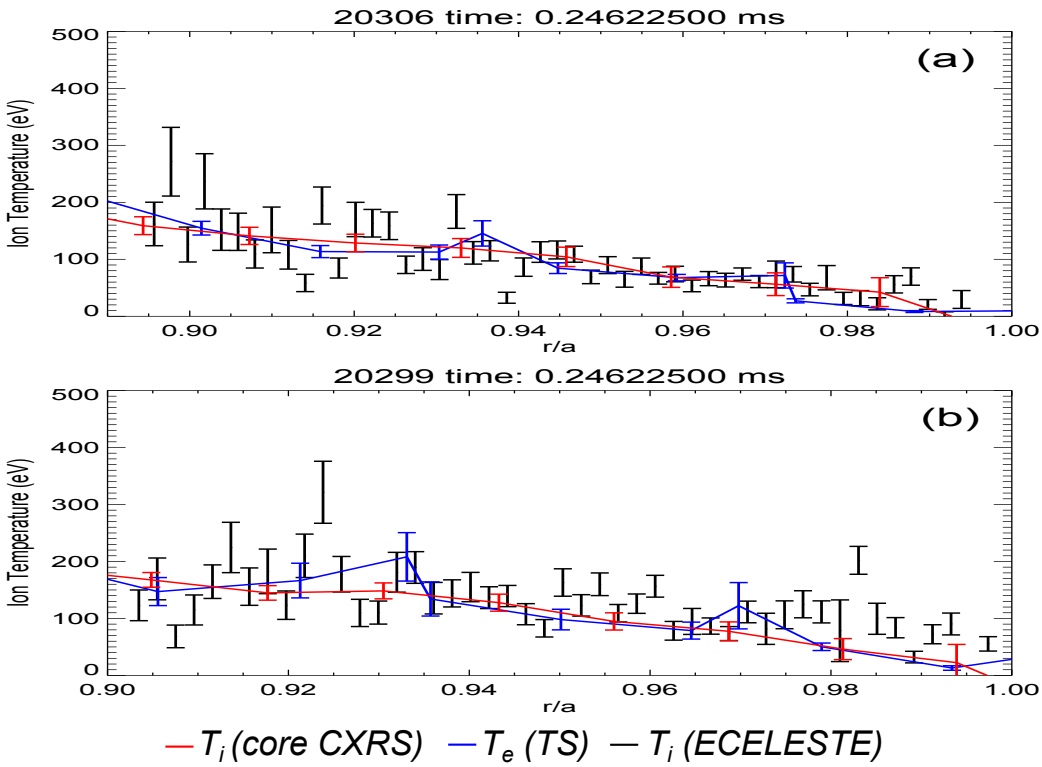


**Figure 6.7:** *Typical L-mode temperature profiles from ECELESTE compared with $T_i$ data from the core CXRS system and $T_e$ data from Thomson scattering. Figures (a) (shot 20306, time = 246 ms) and (b) (shot 20299 time = 246 ms) show there is good agreement between $T_e$, $T_i^(edge)$ and $T_i^{core}$ across the entire edge region*

bration between all species. Returning to the model profile for H-mode used in section 3.3 the transport times and thermalization times can be estimated. The thermalization time between deuterium ions and the electrons becomes larger than the transport time in the plasma edge at approximately $r/a \sim 0.9$. A higher flatter temperature across the pedestal region (defined as $0.95 \leq r/a \leq 1$ in the model), while maintaining $T_e$ as before (see figure 6.8), to simulate the high pedestal temperatures recorded makes little difference to the ratio between $\tau_{trans}$ and $\tau_{ie}$, although slightly reducing it (see figure 6.9).

Due to the uncertainties in estimating the heat diffusivity $\chi_i$ and pressure gradient scale length $L_p$, the modelling can only give an indication of the true values. However, it appears clear that a difference between the electron and ion temperature can be maintained in the pedestal region if $\tau_{ie}$ and $\tau_{trans}$ are of the same order as determined in this analysis. For a difference to be maintained though, there must be a driver of the temperature difference which applies to some shots and not others. This will be investigated in the following sections.

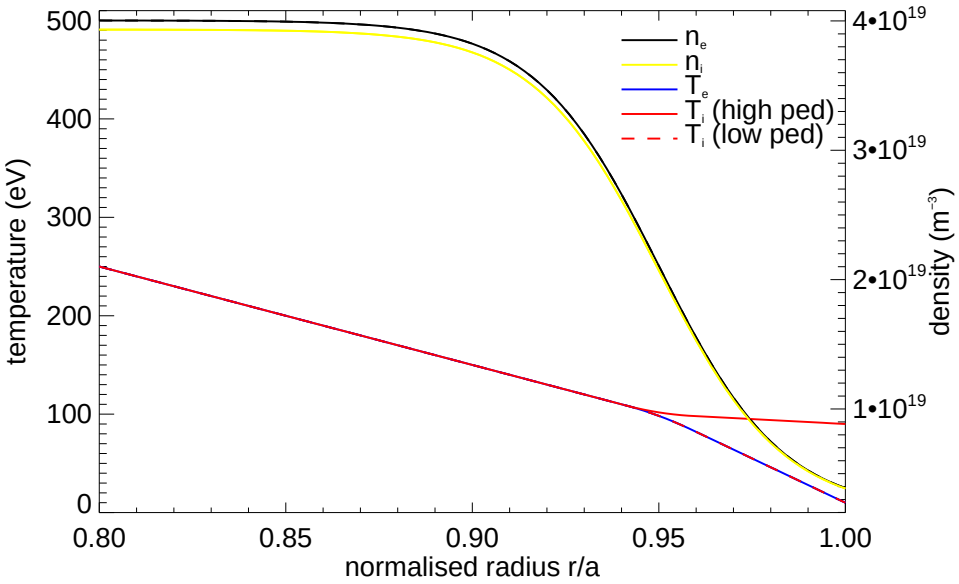


**Figure 6.8:** *The model profiles used to calculate $\tau_{ie}$, $\tau_{trans}$ and $\tau_{ci}$ in the case both of a low pedestal profile in the ions which matches $T_e$ and a high ion temperature in the pedestal region similar to those observed in figures 6.6(c) and 6.6(d)*

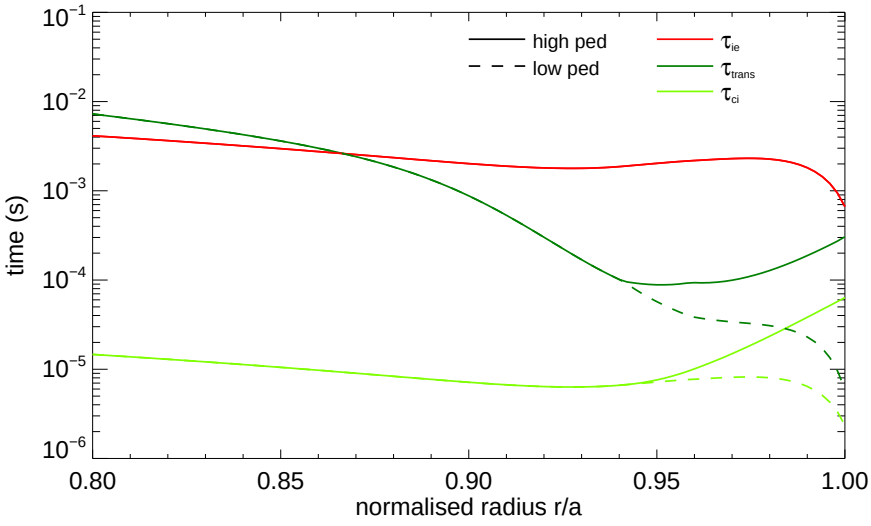


**Figure 6.9:** *Calculated values for $\tau_{ie}$, $\tau_{trans}$ and $\tau_{ci}$ from model profiles in the case both of a low pedestal profile in the ions which matches $T_e$ and a high ion temperature in the pedestal region similar to those observed in figures 6.6(c) and 6.6(d)*

## 6.5 Ion and electron power balance

In the plasma a radial power balance in the ions and electrons is maintained such that

$$\frac{3}{2}\frac{\partial}{\partial t}n_i T_i + \nabla_r \left(q_{conv} + q_{cond}\right) = P_{in} \tag{6.6}$$

The first term in this equation is the rate of change of energy, the next two refer to the radial fluxes due to convection and conduction, while these are balanced by the external heating power $P_{in}$.

For the ions the detailed radial balance equation is represented by [116]

$$\begin{aligned}\frac{3}{2}\frac{\partial}{\partial t}n_i T_i + \sum_j \left(\frac{1}{r}\frac{\partial}{\partial r}\left(\frac{5}{2}r n_j T_i V_j\right) - V_j \frac{\partial}{\partial r} n_j T_i\right) \\ -\frac{1}{r}\frac{\partial}{\partial r} r n_i \kappa_i \frac{\partial}{\partial r} T_i = P^i_{heat} + q_{ie} - P_{chx} + P_{neut} + P_{rot}\end{aligned} \tag{6.7}$$

where stress terms are neglected and $j$ refers to each ion species. The first term is again the rate of change of the thermal energy, while the next two terms relate to the power loss flows due to convection (the second referring to dissipation of the drifts by diffusion) and the next to flows due to conduction. This is balanced on the right hand side by an expansion of $P_{in}$ containing all sources and sinks. $P^i_{heat}$ is the heating power to the ions, which in MAST is dominated by the neutral beam heating. The ion electron heat exchange is given by $q_{ie}$ and is defined as negative if $T_i > T_e$ so that heat is transferred from the ions to the electrons. $P_{chx}$ gives the power loss by charged ions to neutrals at the plasma edge through charge exchange while $P_{neut}$ is the energy gained from hot (e.g. recycled) neutrals which are ionised. $P_{rot}$ is the heating of the ions due to frictional damping of the plasma rotation.

For the electrons there is a similar equation given by [116]

$$\begin{aligned}\frac{3}{2}\frac{\partial}{\partial t}n_e T_e + \left(\frac{1}{r}\frac{\partial}{\partial r}\left(\frac{5}{2}r n_e T_e V_e\right) + \sum_j V_j \frac{\partial}{\partial r} n_j T_i\right) \\ -\frac{1}{r}\frac{\partial}{\partial r} r n_e \kappa_e \frac{\partial}{\partial r} T_e = P^e_{heat} - q_{ie} - P_{ioniz} - P_{rad}\end{aligned} \tag{6.8}$$

where the left hand terms are the equivalent of those listed above (the second term in the convection terms being equal and opposite to that in the ion energy balance). The heating term for the electrons $P^e_{heat}$ includes both heating from neutral beams and a large contribution from Ohmic heating which overwhelmingly donates energy to electrons over the ions due to the mass difference between them. The terms $P_{ioniz}$ and $P_{rad}$ refer to the power lost by the electrons in ionising neutrals and the power radiated by impurities (which is produced through electron collisions) respectively.

By using the transport analysis code TRANSP [116, 117] to calculate this power balance for the ions and electrons, it is possible to determine whether a large discrepancy between the ion and electron temperatures in the edge region can be accommodated within the power balance equations. The power fluxes can be calculated from the power densities from Stoke's theorem by integrating over the volume enclosed by a given flux surface and divided by the surface area of each flux surface, as determined by EFIT [102]. In other words the power flux $F$ across each flux surface $\psi$ for each term $k$ in equations 6.7 and 6.8 is given by

$$F_j^k|_\psi = \frac{\int_0^{V(\psi)} P_j^k}{S(\psi)} \tag{6.9}$$

where $P$ is the power density on a given flux surface for each term $k$ while $S$ is the surface area enclosing volume $V$, so that everywhere $\sum_k F^k = 0$. In other words the power balance holds on each flux surface.

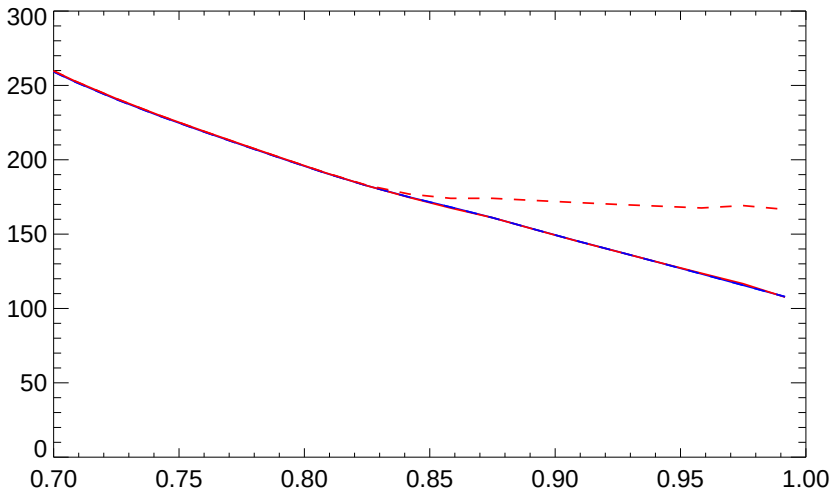


**Figure 6.10:** *Edge ion and electron temperature profiles (shot 25290, time =0.250 ms) used in TRANSP [116, 117], produced from measurements of $T_i$ and $T_e$ using the MC$^3$ analysis chain. Full lines denote the scenario where $T_i \approx T_e$ is assumed and dashed lines the scenario where $T_i > T_e$ in the edge region.*

The results of this for a typical shot where the edge temperature has been determined to be high compared to the electron temperature (shot 25290) are shown in figure 6.10 for two cases, firstly where it is assumed that $T_i = T_e$ and secondly for the case where $T_i$ is much larger than $T_e$ in the edge region, with an approximately flat profile, both produced in the integrated analysis chain MC$^3$ from measurements of $T_i$ and $T_e$.

Figure 6.11 shows that in the case of a large difference in temperature between the ions

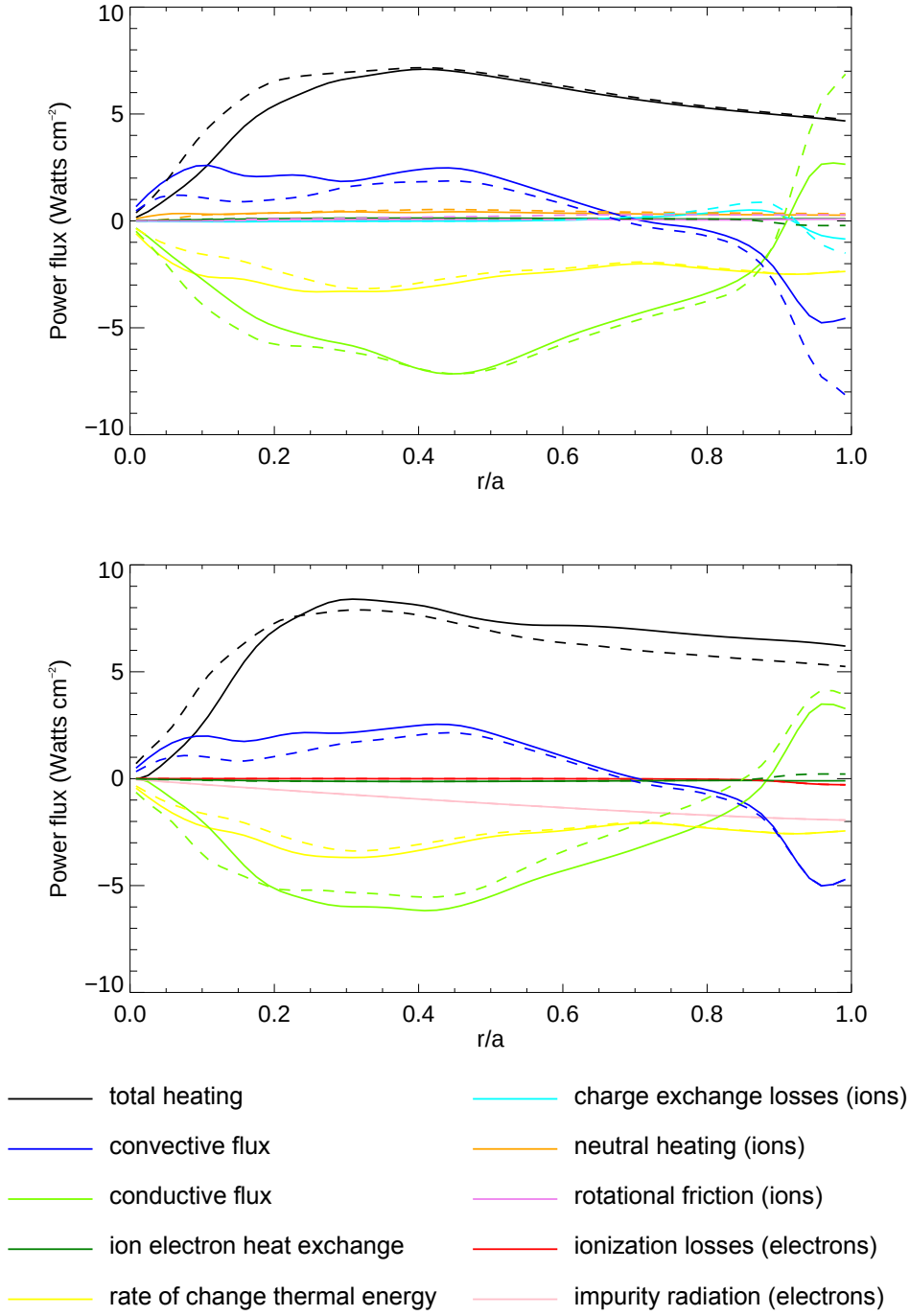


**Figure 6.11:** *Power flux across each flux surface at a given minor radius (LFS midplane) for each of the terms of equations 6.7 and 6.8 calculated from equation 6.9for the ions (top) and electrons (bottom) respectively. Full lines denote the scenario where $T_i \approx T_e$ is assumed and dashed lines the scenario where $T_i > T_e$ in the edge region.*

and electrons, the heat exchange term makes only a small contribution to the overall power balance, which is dominated by large inward heating flux from neutral beam heating (and Ohmic heating generated in the centre in the case of electrons) and a large outward flux by convective and conductive flows in the plasma edge in the case of both electrons and ions due to the steep pressure gradients in H-mode. This is essentially a cross over from outward heat transport by convection to conduction as the dominant mechanism (see figure 6.11). Therefore this implies that ion-electron temperature differences in the edge can easily be accommodated.

The power densities (see figure 6.12) also show that there are no significant heating sources in the edge from neutral beams for the ions. Furthermore the effect of charge exchange of neutrals with ions has a modest negative effect while the heating due to rotational damping and ionization of neutrals appears negligible. For the electrons the effect of the ionization losses and impurity radiation in the edge region also appear negligible, while the effect of ion electron heat exchange is also reasonably small. Therefore there are no obvious differences in heating between the ions and the electrons in the edge region which could account for the observed ion temperatures being much higher than electron temperatures in the edge.

## 6.6 The effect of collisionality

As shown in the previous section there are no obvious heating differences in the plasma edge which could drive a large temperature difference between the ions and electrons. Another possible cause is a difference in the behaviour of the plasma ions and electrons in different transport regimes.

Due to the variation in the magnetic field strength **B** in the poloidal direction from a maximum at the inner midplane ($B_{max}$) to a minimum at the outer midplane ($B_{min}$), particles with a small velocity component parallel to the magnetic field can undergo a magnetic mirror reflection when they are moving towards the region of higher field strength. The result of this is that the particle can be trapped bouncing back and forth in the outer midplane region of the plasma in a banana orbit (see figure 6.13). The transport regime at the edge then depends on the collisionality of the plasma. If collisions are frequent enough that the particles are detrapped from their orbits before completing a banana orbit then the result is that the transport becomes dominated by Pfirsch-Schlüter diffusion with a typical step length of [5]

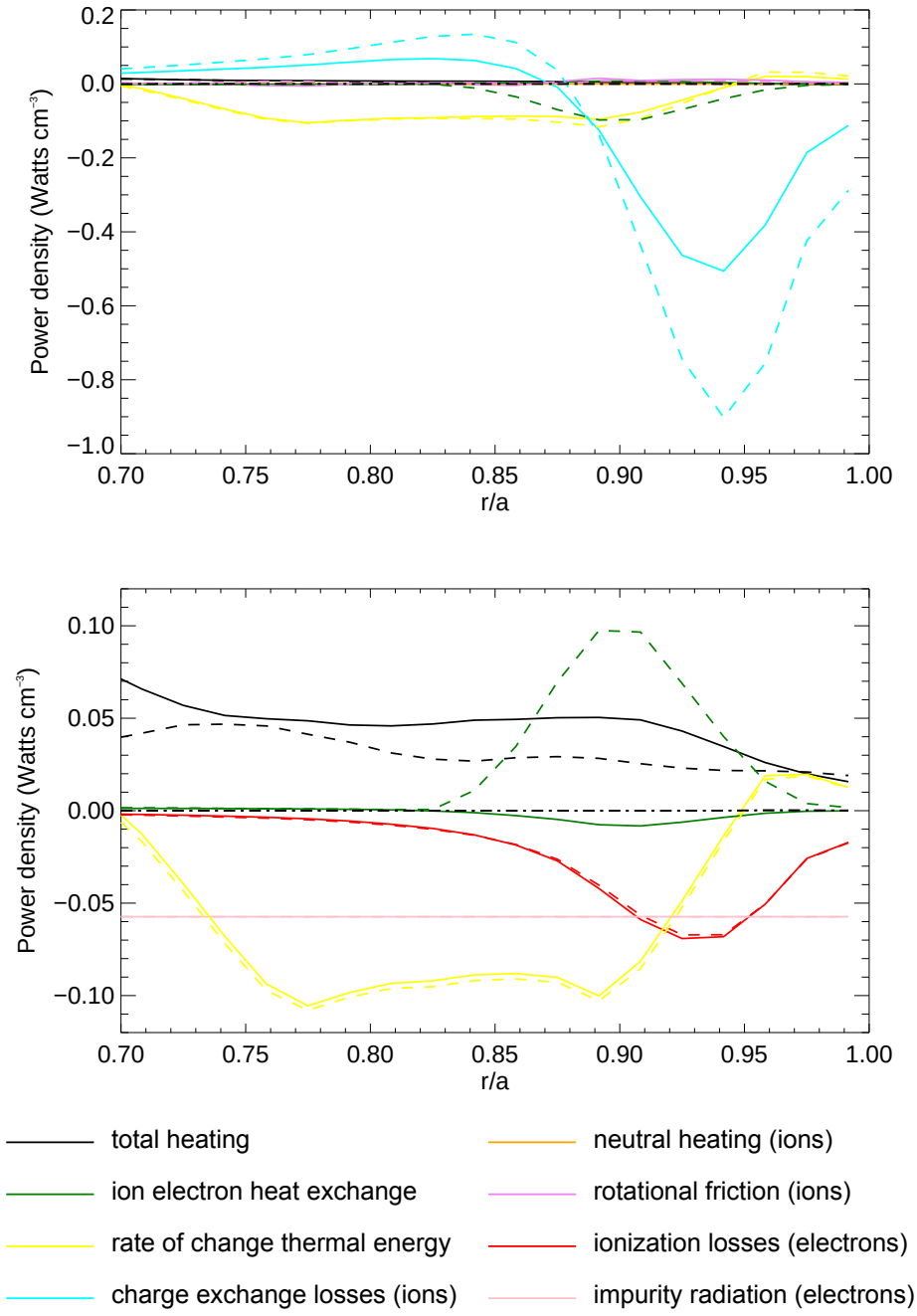


**Figure 6.12:** *Power density in the edge region for each of the terms of equations 6.7 and 6.8 for the ions (top) and electrons (bottom) respectively, excluding conduction and convection. Full lines denote the scenario where $T_i \approx T_e$ is assumed and dashed lines the scenario where $T_i > T_e$ in the edge region.*

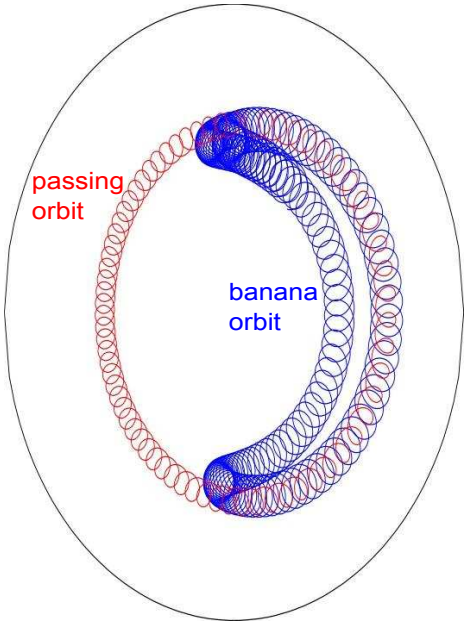


**Figure 6.13:** *Poloidal cross section of a particle in an elongated cylindrical geometry with either a passing orbit or a banana orbit, showing the typical shape of both [118]*

$$D_{PS} \sim \left(1 + 2\frac{\eta_{\|}}{\eta_{\perp}} q^2\right) D_{class} \tag{6.10}$$

where $\eta_{\|}, \eta_{\perp}$ is the resistivity or the plasma in the directions parallel and perpendicular to the magnetic field respectively, $q$ is the safety factor and $D_{class}$ the classical diffusivity. If the edge of the plasma is hot or the density low, the number of collisions between the ions can become small. Therefore a large fraction of the particles can complete whole banana orbits. In this case the thermal diffusion becomes large so that the typical step length of diffusion becomes [5]

$$D_{banana} \sim \left(\frac{q^2}{\epsilon^{3/2}}\right) D_{class} \tag{6.11}$$

where $\epsilon = r/R$ is the inverse aspect ratio of the magnetic surface. In this banana regime the diffusion step length is larger than in the Pfirsch-Schlüter regime by a factor $\sim 1/\epsilon^{3/2}$ (approximately 2 in MAST). The intermediate case between the two is called the plateau regime.

### 6.6.1 Gyrokinetic theory of ion pedestal behaviour

The gyrokinetic formalism developed by Kagan and Catto [119] makes a prediction which describes the observed behaviour in the MAST plasma edge ion temperatures. Gyrokinetics is a simplified form of the full kinetic equations where the Larmor orbit motion of the ions

and electrons (which has a much higher frequency than other processes of interest) has been averaged over. It is often used to study turbulence, most commonly in the core of the plasma but generally cannot make predictions about areas such as the plasma pedestal region and internal transport barriers (ITBs), due to the difficulties produced by large departures from flux surfaces in the steep gradient regions [119]. By changing the radial variable from the guiding centre location to canonical angular momentum this problem can be overcome, allowing predictions to be made about the pedestal region. This formulation concludes that in the pedestal an ion temperature pedestal is not permitted in the banana regime, and that a similar behaviour is expected in the plasma rotation [119].

The full derivation of the gyrokinetic formalism is beyond the scope of this thesis (see Kagan and Catto (2008) [119]), but a brief explanation of this prediction is described below, following the arguments of the paper.

The paper has been derived for conventional tokamaks of larger aspect ratio than spherical tokamaks, but the formalism should still be applicable in this case. It makes the assumptions that the gradient scale length of the magnetic field $L \equiv |\ln(B)|^{-1}$ is much greater than the gyroradius $\rho_i \equiv v^i_{th}/\omega^i_c$, i.e. that

$$\frac{\rho_i}{L} \ll 1, \tag{6.12}$$

and that the magnetic field is constant in time. Both of these are reasonable in the MAST tokamak for the purposes herein.

The distribution function $f$ evolves in time according to the equation

$$\frac{\mathrm{d}f}{\mathrm{d}t} = C\{f\} \tag{6.13}$$

where C is the collision operator. This includes all of the gyromotion, and so the distribution function is written such that $f = f(q_1, \ldots, q_n, \varphi)$ where $\varphi$ is the gyrophase. Therefore equation 6.13 becomes

$$\frac{\partial f}{\partial t} + \frac{\partial f}{\partial q_1}\frac{\partial q_1}{\partial t} + \ldots + \frac{\partial f}{\partial q_n}\frac{\partial q_n}{\partial t} + \frac{\partial f}{\partial \varphi}\frac{\partial \varphi}{\partial t} = C\{f\}. \tag{6.14}$$

This is then averaged over the gyrophase as

$$\langle \cdot \rangle \equiv \frac{1}{2\pi}\oint \mathrm{d}\varphi(\cdot) \tag{6.15}$$

where the variables $q_j$ are held fixed. These variables are such that their total time derivatives are gyroindependent as long as assumption 6.12 is true.

The radial variable chosen is the canonical angular momentum

$$\psi_\star \equiv \psi - \frac{m_i c}{Z_i e} R\mathbf{v}\cdot\hat{\phi} \tag{6.16}$$

(where $\mathbf{v_i} = v\|_i\hat{n} + v\perp_i(\hat{e_1}\cos\varphi + \hat{e_2}\sin\varphi)$, where $\hat{n} = \hat{e_1}\times\hat{e_2}$ is the normal vector to $\mathbf{B}$) while the other variables are chosen to be poloidal angle $\theta$, toroidal angle $\zeta$, magnetic moment $\mu$ and kinetic energy $E = v_i^2/2$. The canonical angular momentum is useful to choose as it is an invariant of the motion of the particle around its banana or passing orbit, unlike $\psi$.

Applying the gyrokinetic averaging to these variables $q$ results in the gyrokinetic variable $q_\star$ and its time derivative $\dot{q_\star}$ so that the gyroaveraged equation becomes

$$\frac{\partial\bar{f}}{\partial t} + \dot{\psi_\star}\frac{\partial\bar{f}}{\partial\psi_\star} + \dot{\theta_\star}\frac{\partial\bar{f}}{\partial\theta_\star} + \dot{\zeta_\star}\frac{\partial\bar{f}}{\partial\zeta_\star} + \dot{E_\star}\frac{\partial\bar{f}}{\partial E_\star} = \langle C\{f\}\rangle \tag{6.17}$$

where the magnetic moment $\mu_\star$ has been neglected as it is unimportant except at higher orders. For a stationary and axisymmetric plasma any function of the invariants of the motion $\varepsilon = E_\star + Ze/M\bar{\phi}$ and $\psi_\star$ will make the left side vanish. If $\bar{f}$ is a Maxwellian then the right hand side vanishes if the ion-ion collisions dominate (accepted as $C_{ii}\{f\}/C_{ie}\{f\} \sim \sqrt{(m_i/m_e)}$ so the average of the collision operator will be zero. Therefore an exact solution in this case is a rigidly rotating Maxwellian [120].

However, equation 6.17 has a dependence on the gyrokinetic poloidal angle $\theta_\star$, and in a non-stationary but still axisymmetric plasma it has a time dependent part as well as a dependence on the average potential $\bar{\phi}$ so that the equation becomes

$$\left.\frac{\partial\bar{f}}{\partial t}\right|_\varepsilon + \dot{\theta_\star}\left.\frac{\partial\bar{f}}{\partial\theta_\star}\right|_\varepsilon = \langle C\{f\}\rangle - \frac{Ze}{M}\frac{\partial\bar{\phi}}{\partial t}\frac{\partial\bar{f}}{\partial\varepsilon}. \tag{6.18}$$

The second term on the left hand side and first term on the right of equation 6.18 are of higher order than the other two so this simplifies to

$$\left.\dot{\theta_\star}\frac{\partial\bar{f}}{\partial\theta_\star}\right|_\varepsilon = \langle C\{f\}\rangle \tag{6.19}$$

to first order.

If one transit averages over this equation (i.e. average over either one banana orbit or one passing orbit for the trapped and passing particles respectively) then the average of the collisions is again zero and we return to the rigidly rotating Maxwellian solution.

If one assumes steep gradients in the ion distribution of order the poloidal gyroradius $\rho_\theta = (m_j v_\perp)/(e_j B_\theta)$ then the ordering assumed above still holds if $\rho_i \ll \rho_\theta$. This is strongly true in conventional tokamaks but in MAST $\rho_i \sim \rho_\theta$ at the low field side while $\rho_i \ll \rho_\theta$ at the high field side. By flux-surface averaging however the ordering will still hold. This

allows regions with steep gradients such as internal transport barriers and pedestals to be examined.

The paper then demonstrates that in the case of the core the spatial variation with respect to $\rho_\theta$ is small so the transit average is only over each flux surface and each flux surface equilibrates with itself. In the banana regime in the pedestal region the particles affect the equilibration of neighbouring flux surfaces due to the steep gradients and departures from the flux surface of order the poloidal gyroradius $\rho_\theta$, coupling adjacent flux surfaces together. Therefore the entire pedestal must be treated as a closed surface to be transit averaged over. In this case temperature and rotational frequency can only vary slowly compared to the $\rho_\theta$ scale length so that in the pedestal region

$$\rho_\theta \nabla \ln T_i \ll 1 \qquad \text{and} \tag{6.20}$$

$$\rho_\theta \nabla \ln \omega \ll 1. \tag{6.21}$$

where $\rho_\theta \nabla \ln X$ is the dimensionless inverse gradient scale length of variable $X$. In the Pfirsch-Schlüter regime this solution does not hold because the collisions start to dominate and change the ordering of the equation. Therefore the condition that the solution must be a Maxwellian to first order no longer holds. Physically the collisions reduce the scale length in the pedestal so that the coupling between all flux surfaces is broken. In the case of the electrons $\rho_\theta^e \ll \rho_\theta^i$ so that this analysis also does not hold. This allows the electrons and ions to have a different behaviour in the banana regime, and permits the large discrepancies in temperature that are observed.

### 6.6.2 Dimensionless scan of collisionality

The characteristic time to detrap the particles from their banana orbits is given by [121]

$$\tau_{detrap} = \tau_{coll} \left(\Delta\theta\right)^2 \tag{6.22}$$

where $\Delta\theta$ is the trapping angle of the magnetic mirror cone in velocity space. As equilibration between the deuterium and carbon ions is very fast (see figure 6.9) and as the density of $D^+$ is much greater than that of $C^{6+}$ it can be assumed that it is the collisionality of the deuterium ions that is important in determining the transport regime. The time taken for a particle to complete one banana orbit is called the bounce time $\tau_{bounce}$, and the collisionality is defined as

$$\nu^* \equiv \frac{\tau_{bounce}}{\tau_{detrap}} \tag{6.23}$$

so that $\nu^* < 1$ is defined as the banana regime and $\nu^* > \epsilon^{-3/2}$ is defined as the Pfirsch-Schlüter regime. The intermediate region $1 < \nu^* < \epsilon^{-3/2}$ is defined as the plateau regime. On MAST typical values are $a \approx 0.65$ m and $R \approx 0.85$ m so that $\epsilon^{-3/2}$ is typically about 1.5 in the MAST tokamak. The collisionality is calculated using the expression from Sauter *et. al.* (1999) [122] for arbitrary aspect ratio and collisionality as

$$\nu_i^* = 4.90 \times 10^{18} \frac{qRn_i Z^4 \ln \Lambda_{ii}}{T_i^2 \epsilon^{3/2}} \tag{6.24}$$

where $\ln \Lambda_{ii}$ is the coulomb logarithm given by [122]

$$\ln \Lambda_{ii} = 30 - \ln \left( \frac{Z^3 \sqrt{n_i}}{T_i^{3/2}} \right). \tag{6.25}$$

In order to assess the impact of the edge collisionality on the gradient of the ions at the plasma edge in H-mode a dimensionless scan of collisionality was made. This was conducted by adjusting the plasma current $I_p$ and toroidal magnetic field $B_\varphi$ in tandem so that $q$, $\beta$ etc remain approximately constant. Figure 6.14 shows the relationship between $\rho_\theta^i |\nabla \ln T_i|$ and $\nu^*$ for this set of measurements. The gradient is fitted across the pedestal region, which has been defined from the position of the pedestal in the electron density, while the collisionality is determined at the centre of the pedestal.

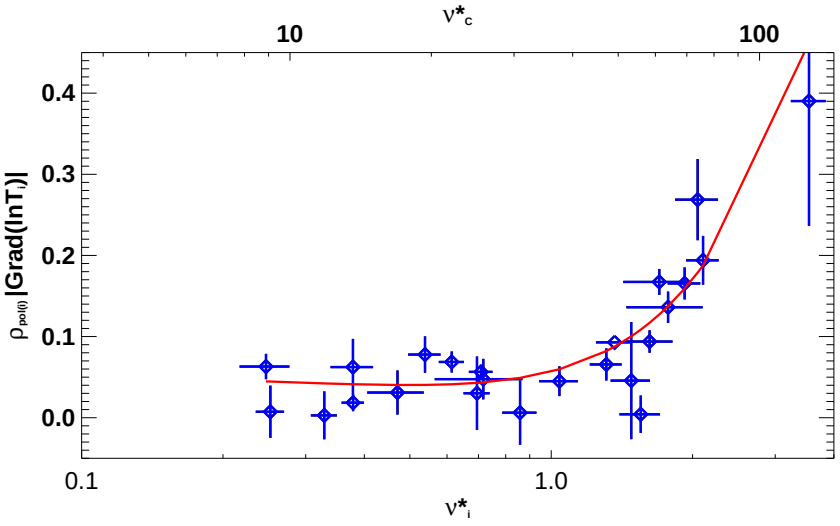


**Figure 6.14:** *The correlation between inverse ion temperature gradient scale length of the deuterium ions across the pedestal region with the collisionality of the deuterium ions recorded at the centre of the pedestal region is shown. The collisionality of the carbon ions is also shown on the top axis for comparison. The solid line is only to guide the eye.*

For the ions there is a strong correlation between the collisionality and the dimensionless

inverse gradient scale length of the ions. The recorded values straddle the region between the banana regime and the plateau/Pfirsch-Schlüter regimes. This implies that the arguments of section 6.6.1 are consistent with what is measured and provides evidence that the coupling of flux surfaces due to the larger step length in the banana regime could be responsible for the small gradients and large discrepancy between $T_i$ and $T_e$ in the plasma edge.

It is interesting to note that the edge is often in a mixed collisionality regime, as the carbon ions have a collisionality larger than the deuterium ions by a factor $(Z_C/Z_i)^2 = 36$ when deuterium-carbon collisions dominate. This indicates that, as predicted, it is the collisionality of the deuterium ions which is important.

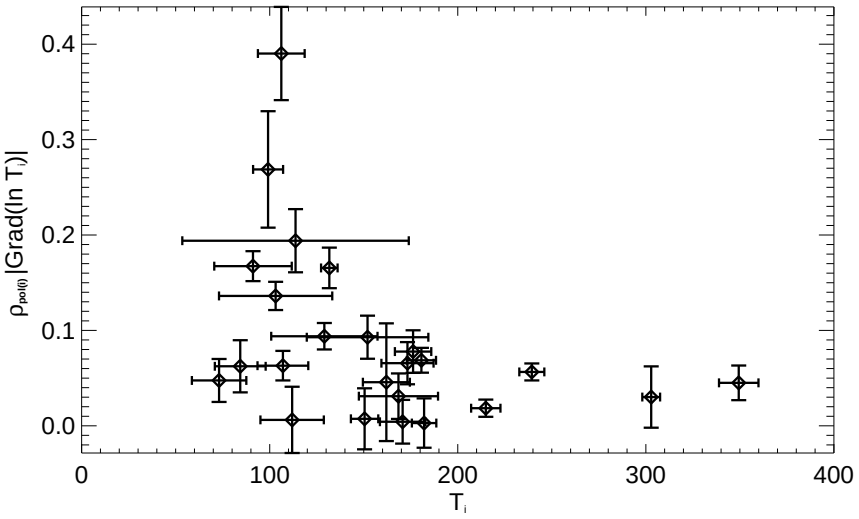


**Figure 6.15:** *A correlation plot between ion temperature at the pedestal centre and the dimensionless inverse gradient scale length across the pedestal for the ions, showing a weak or non-existent correlation between the two. This implies that collisionality, not simply ion temperature, is the driving factor in the gradient of the ions in the pedestal.*

It is also worth noting that $\nu^*$ is dependent upon the ion temperature as $\nu^* \propto 1/T_i^2$. The result of the flattened ion profiles would be to result in a smaller value of $\nu^*$ than would be the case if $T_i \approx T_e$. However, there appears to be no correlation between the ion temperature recorded at the pedestal centre and the inverse gradient scale length recorded across the pedestal (see figure 6.15). Therefore the relationship appears to truly be between collisionality and inverse gradient scale length which strongly implies that it is flux surface coupling which is responsible for the flattening of ion temperatures in the pedestal region, leading to a lack of pedestal in the ions in the banana regime.

The collisionality should also limit the gradient of the velocities recorded, as the pre-

diction in the banana regime is for a rigidly rotating Maxwellian, implying equation 6.21. Figure 6.16 shows the relationship between gradient scale length of velocity in the edge region and collisionality. The implications are that gradients are small irrespective of collisionality regime and so compatible with the predictions from section 6.6.1. This suggests that unlike in the case of the ion temperatures there are no drivers that would produce a large gradient in the Pfirsch-Schlüter regime that are restricted in the banana regime, and so the gradients are similar everywhere. The large reverse shear gradients that are observed in some H-mode cases (see section 6.2) are restricted here to the near SOL where measurements outside the separatrix are available, and so do not locally produce a large gradient.

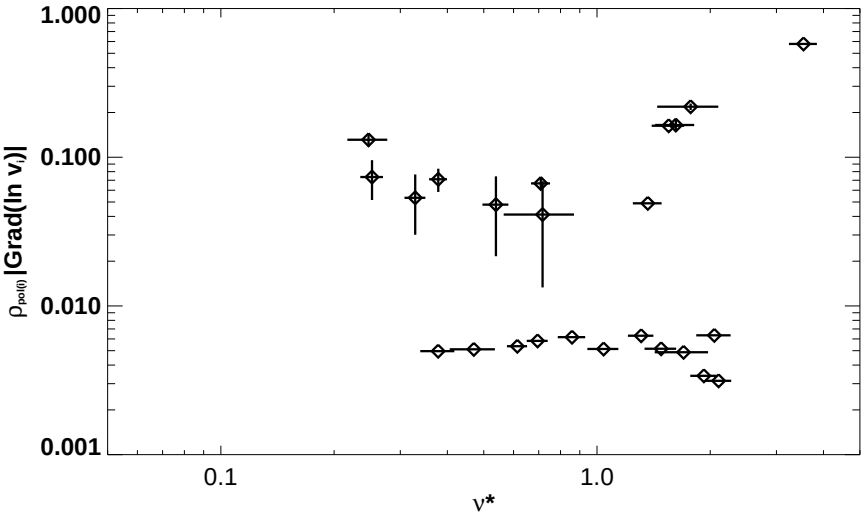


**Figure 6.16:** *Velocity dimensionless inverse gradient scale length of the deuterium ions across the pedestal region compared with the collisionality of the deuterium ions recorded at the centre of the pedestal region is shown. There appears to be no correlation between the two but the condition of equation 6.21 is fulfilled.*

### 6.6.3 Compatibility with the scrape-off layer

The result of the high ion temperatures in the pedestal is that at the separatrix the ion and electron temperature can differ by a factor of up to $\sim 8$. Figure 6.17 shows the influence of collisionality on the ratio $\tau = T_i/T_e$ at the separatrix. This shows that there is again a clear relationship between the collisionality and the ratio of ion and electron temperatures at $r/a = 1$, as would be expected if the gradient of $T_i$ in the pedestal is much shallower than $T_e$.

To assess whether the recorded temperature ratios are compatible with expectations

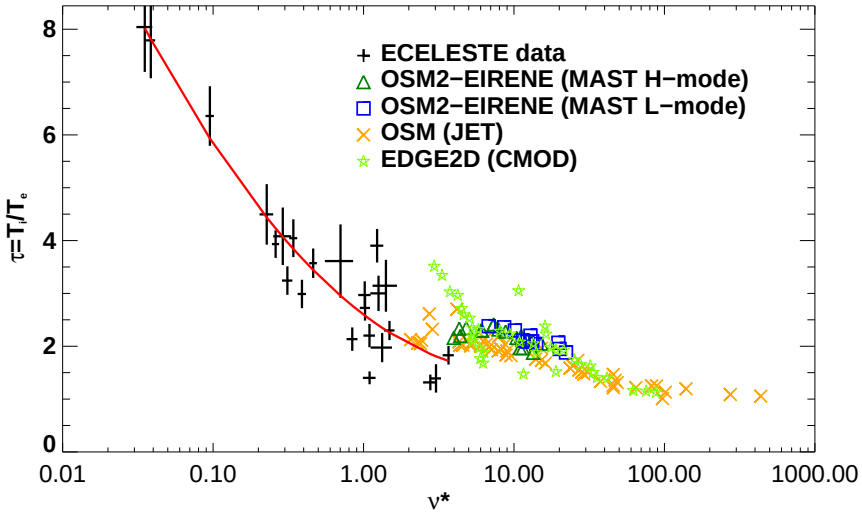


**Figure 6.17:** *Comparison of ion to electron temperature ratio ($\tau$) recorded by the ECELESTE spectrometer system and Thomson scattering system respectively at the separatrix, with collisionality at the separatrix. Modelling data from OSM2-EIRENE for MAST H-modes and L-modes [42], as well as modelled data from JET discharges using OSM [111] and CMOD discharges using EDGE2D [111] are also shown for comparison. The modelled and measured data indicates an increase in $\tau$ with decreasing collisionality, while the measured data also appears to be compatible with the edge code results shown.*

in the SOL comparisons are made in figure 6.17 with the predictions from modelling of $\tau$ upstream compared with upstream collisionality from several edge transport codes for transport. Predictions for MAST are from OSM2-EIRENE [42], while predictions for the ratio from CMOD are using the EDGE2D code [111] and from JET using onion-skin modelling [111]. Although these do not cover the same collisionality region as the measurements, there is nonetheless an increasing ratio between $T_i$ and $T_e$ as the collisionality decreases and extrapolation of this trend implies compatibility with the ratio determined by the ECELESTE measurements.

Ion temperature measurements in the SOL are often hard to come by, but in recent years progress has been made by using Segmented Tunnel Probes (STP's) [124, 125] as well as Retarding Field Analysers (RFA's) [123, 126, 127]. A comparison made by Kočan *et. al.* (2008) [123] of the measurements of $\tau$ as a function of $r/a$ on multiple machines show that a large ratio between $T_i$ and $T_e$ is common at the LCFS ($\sim 1.5 \leq \tau \leq \sim 5$), and can be even larger in the far SOL (see figure 6.18). A ratio greater than 1, and often 2-3, is also observed inside the LCFS. Measurements from the same paper (see figure 6.19 made 2-3 cm outside the separatrix on Tore Supra using an RFA show $\tau$ in the range 4-7

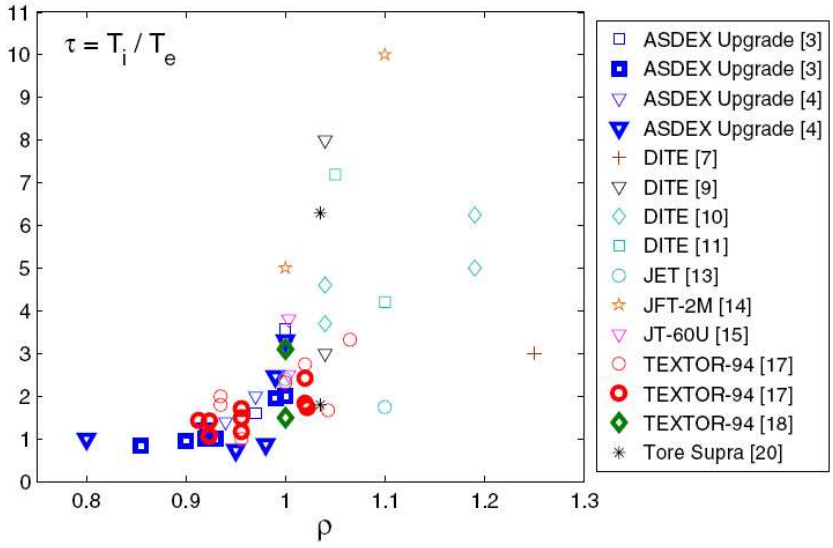


**Figure 6.18:** *Survey of ion to electron temperature ratio $\tau$ across the edge region as a function of $\rho = r/a$ in multiple machines in a variety of scenarios, showing that tau is often higher than one even inside the LCFS and often significantly higher at $r/a = 1$. From Kočan et. al. (2008) [123]*

and with a strong dependence on $n_e$, which collisionality is proportional to. All of this indicates that the measurements made are compatible with predictions and measurements in the SOL. An RFA for MAST [128] is currently installed and is undergoing commissioning at the time of writing. It is hoped that measurements made simultaneously with this and the ECELESTE system and core CXRS system should provide ion temperatures across the entire plasma radius from plasma core to the far SOL. This should also allow independent means of measuring $\tau$ at the separatrix of MAST for comparison with the measurements made by ECELESTE.

The sheath effect is a significant influence on the ion and electron energies in the SOL. This effect arises due to the negative potential $eV_{sf}$ of the target and other solid surfaces due to the flux difference between ions and electrons. This potential produces a repulsive effect upon the electrons. Therefore, assuming a Maxwellian distribution in the energies of the electrons, it is clear that only the most energetic electrons will overcome this repulsion to strike the target, the rest being reflected within the sheath region. Essentially this reduces the ensemble energy distribution of the electrons which cools them and sets up a flow towards the divertor. This lost energy is transferred to the ions, which are accelerated to hit the solid surface by the negative potential.

At low collisionality temperature gradients along the parallel direction are likely to be small and the simple SOL model [111] is appropriate. This description from Stangeby (2000) [129] gives the relationship between the particle fluxes and heat fluxes of each species

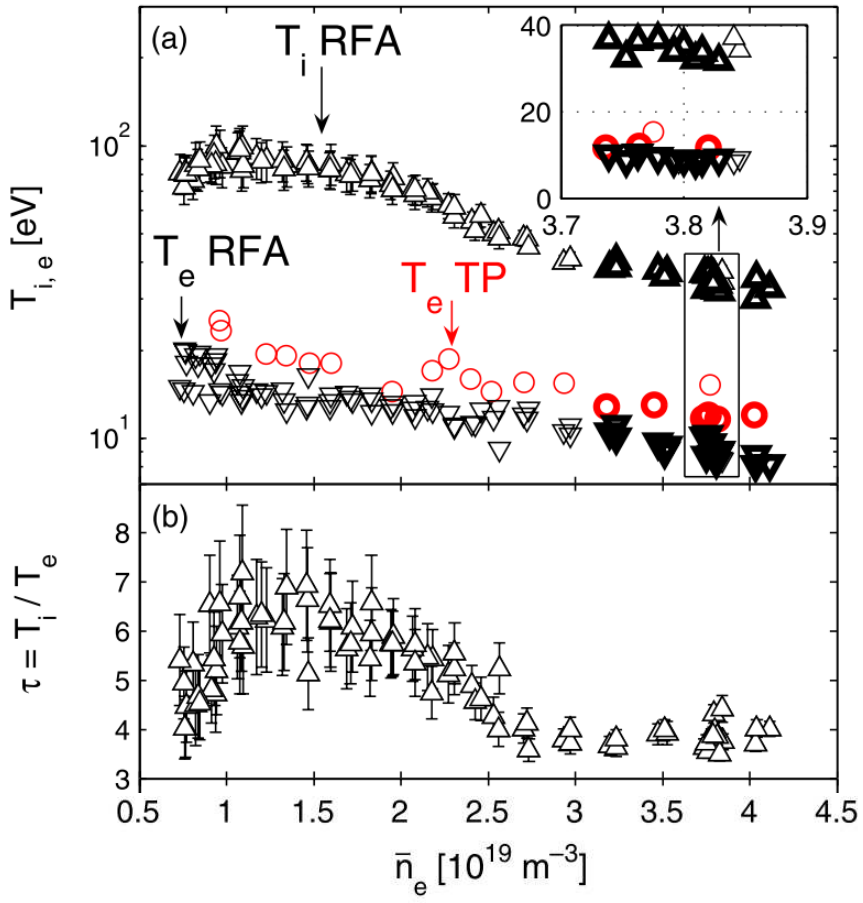


**Figure 6.19:** *(a) SOL $T_i$ data recorded by an RFA and $T_e$ data from the RFA and a tunnel probe (TP) as a function of electron density measured 2-3 cm outside the LCFS at the Tore-Supra tokamak. (b) The resultant ratio in $\tau$ as a function of density, from Kočan et. al. (2008) [123]*

at the sheath edge as

$$q_{se}^{j} = \gamma_j k_B T_j \Gamma_{se} \tag{6.26}$$

where $q_{se}^{j}$ and $\Gamma_{se}$ are the one-way heat and particle fluxes of species $j$ towards the surface at the sheath edge and $\gamma_j$ the sheath heat transmission coefficient of that species. For the electrons $\gamma_e \approx 5.5$ while for the ions the situation is more complicated as the ion velocity distribution is unlikely to be a Maxwellian and so a full kinetic analysis is required. However, a recommended value is $\gamma_i \approx 2.5$ [129]. In the assumption that the input power from the plasma $q_{in}^{j}$ is equal so that $q_{in}^{e} = q_{in}^{i}$ then if equipartition between the ions and electrons is low (i.e. low collisionality) then

$$q_{in}^{e} = q_{se}^{e} = 5.5 k_B T_e \Gamma_{se} = 2.5 k_B T_i \Gamma_{se} \approx q_{se}^{i} = q_{in}^{i} \tag{6.27}$$

The result of this is that in the SOL

$$\frac{T_i}{T_e} \approx 2.75. \tag{6.28}$$

Effectively, as the target acts as a heat sink for the electrons and the ions, it does so more effectively for the electrons, resulting in a lower electron temperature in the SOL.

If electron power fluxes from the plasma are larger than ion fluxes then this does not necessarily hold. However, calculations from the power balance of section 6.5 show that they are approximately equal. The effect of hydrogenic recycling is also generally an electron cooling process as the ionization is due to electron collisions. Similarly impurity radiation is generally driven by electron excitation. Overall, therefore, a high difference in temperature between $T_i$ and $T_e$ is compatible with predictions for the SOL. The cooling effect of the SOL may contribute significantly to the large gradient in electron temperature in the pedestal and significantly contribute to the temperature differences between the two species in the edge.

## 6.7 Conclusion

Typical results from ECELESTE for toroidal rotational velocity of the carbon ions are shown. These show a large reverse shear close to the separatrix in normal operation in both H-mode and L-mode. In counter rotation experiments no reverse shear is found, but negative rotation is observed, suggesting the edge shear is driven by ion drifts which have a dependence on $B_\phi$ which reverses in counter rotation operations. Systematic differences in the rotation speed of the ions in Ohmic and L-mode discharges indicate that some net positive rotation is driven by neutral beam torque, but the similar size of reverse shear in both types of discharge further indicate that this is likely to be intrinsic rotation.

Reverse shear in the plasma edge has been observed in several other tokamaks, indicating this unlikely to be an isolated phenomenon on MAST. Pfirsch-Schlüter flow is proposed as a possible driving mechanism for the reverse shear. The opposing components of this flow due to $\mathbf{E} \times \mathbf{B}$ and diamagnetic contributions are large enough that non-zero cancellation between them could accommodate the observed toroidal rotation measurements. Other possible contributors to the rotation are also discussed and the size of their contribution assessed to be inadequate to produce a large enough effect upon the rotation to account for the reverse shear.

Results for ion temperatures in H-mode and L-mode are also shown. In L-mode agreement between ECELESTE measurements, core CXRS and Thomson scattering is good, indicating that $T_i \approx T_e$ is a good assumption in this case in the edge. For H-mode the results indicate that this is not always true in the pedestal and small ion temperature

gradients compared to those in electron temperature can sometimes result in a large ratio between $T_i$ and $T_e$ at the separatrix. Calculations indicate that equilibration times between ions and electrons are long enough that discrepancies between the two are permitted in the pedestal. Power balance modelling using TRANSP [116, 117] indicates both that a difference between $T_i$ and $T_e$ can easily be accommodated within the power balance, and that there are no obvious heating sources in the pedestal region that could account for the difference between the two species.

A gyrokinetic formalism developed by Kagan and Catto (2008) [119] suggests a link between the collisionality regime of the ions and the gradient scale length, indicating that in the banana regime ion temperature gradient scale lengths should be small, while not imposing this restriction upon the ions in more collisional regimes and not for the electrons. Physically this arises due to flux surface coupling across the pedestal due to the larger diffusive step length due to banana orbits. A dimensionless scan of collisionality supports this theory with only small gradient scale lengths observed when the deuterium ions are in the banana regime and an increase in inverse gradient scale length outside this regime. The dimensionless scan also indicates a relationship between $\tau = T_i/T_e$ at the separatrix and collisionality as a result of these small gradients. This therefore has an influence on the SOL. Modelling from several tokamaks indicates that this is compatible with what is expected. Processes in the SOL which generally have a cooling effect upon the electrons are discussed as drivers to produce a large gradient in the electron temperature in the pedestal region.

# Chapter 7

# Conclusions and future work

## 7.1 Summary

A novel experimental method using gas puffing of neutrals to stimulate charge exchange emission has been developed to measure ion temperatures and toroidal rotation velocities in the plasma edge of a tokamak.

Various initial issues were first addressed in chapter 3 to enable the development of the diagnostic, including identifying appropriate spectral lines, the gas puff gas, the effects of background emission, the penetration of the gas puff and the level of signals that could be expected. The charge exchange emission from the $C^{6+}(n = 8 \rightarrow 7)$ transition was identified as the optimum line for use in the MAST tokamak due to its emission wavelength and the high density of carbon in the plasma. The cross section for charge exchange from ground state deuterium into the $n = 8$ state of $C^{6+}$ is extremely low at the temperatures in the edge. However the resonance in cross section between deuterium in the $n = 2$ state and the $n = 8$ level of carbon makes deuterium the optimal donor neutral and ensures that a large charge exchange signal from this line is possible. Collisional radiative modelling indicated that the population of $D^0(n = 2)$ is large enough to outweigh contributions from the ground state of deuterium and that this is the dominant charge exchange process. Calculations indicate that the assumption that impurity and deuterium ions temperature are equal is good in the edge of the MAST tokamak. The main background emission processes were identified as electron excitation of $C^{5+}$ and radiative recombination of electrons with $C^{6+}$ and their effective rate coefficients calculated.

Model profiles of the electron density, $C^{6+}$, $C^{5+}$ and background and active (gas puffed) neutral deuterium have been deduced using typical recorded measurements and the KN1D and GTNEUT codes. Modelling of the gas puff using GTNEUT indicated a penetration of up to 10 cm into the plasma with a narrow localised region of increased neutral density

above background, indicating that the gas puff did not significantly spread laterally. The gas puff profiles were combined with the calculated rate coefficients to produce model profiles of the background and active intensity profiles in both L-mode and H-mode scenarios. The models indicated that the background signal was dominated by charge exchange emission, but that electron excitation and radiative recombination (to a lesser extent) were significant components of the emission intensity. The charge exchange emission resulting from the gas puff was predicted to be stronger in H-mode than L-mode due to increased carbon density in H-mode.

Initial results showed a complex spectrum in the edge region of the plasma which arises due to emission from close lying emission lines to the charge exchange line. These lines were identified as molecular deuterium emission and a multi-Gaussian fitting routine was developed to accommodate this spectral complexity. Although fine structure and Zeeman splitting implies that the emission is the sum of hundreds of close lying emission lines it was found that the charge exchange line was well fitted by a single Gaussian if correction factors for all significant distortions were applied to the result. The main corrections found were for fine structure, Zeeman splitting and the broadening due to the instrument function, and correction factors were calculated in these cases. The fitting routine was benchmarked against simulated spectra to identify the region of validity within the parameter space and to detect systematic errors. Sources of noise were identified and the expected errors in temperatures and velocities evaluated, as well as uncertainties in radial positioning.

Having developed a fitting routine for the charge exchange emission line an assessment was made of the performance of the diagnostic by analysing recorded intensity results under different scenarios. The effect of gas puffing was shown to provide a good signal to background ratio, and that the modelling predictions that H-mode performance should exceed that in L-mode were observed. A comparison with modelling results showed good agreement of the measured spectra in H-mode and reasonable agreement in L-mode. The effect of ELMs upon the profiles was to expel carbons from the plasma but they did not greatly effect the profile shape. The limitations in the capability of the diagnostic were mainly identified as a limited spatial extent in minor radius of 10 cm limiting the size of measurable plasmas to a small range of radii. A low signal to background ratio lead to long integration times (typically 10 ms) in the measurements. A slow repetition rate for the measurements due to limitation in the gas puff rate was also identified as a limiting factor.

To help remedy the limitations of the diagnostic, a series of system improvements have been implemented or are in the process of being installed. These include a new bandpass

filter to improve signal throughput, double-binning of data to improve signal levels and statistics, a new camera which will also provide much greater recorded signal levels and a new gas valve located in the HELIOS nozzle head to improve repetition rate and time resolution.

Typical temperature and velocity profiles have been recorded and are presented. With the toroidal rotation velocity measurements, good agreement is generally seen between the core CXRS system and the results from ECELESTE in L-mode, although less good agreement is seen in H-mode. It is unclear why this is the case, as both instruments use the radial chord subtraction method. A large reverse shear appears present in Ohmic, L-mode and H-mode profiles in standard operation although the shape of this differs in H-mode from the L-mode and Ohmic cases. In counter rotation experiments, L-mode results do not show reverse shear but can become negative in the same region, suggesting that this shear is driven by ion drifts which reverses when the sign of the toroidal magnetic field also reverses. An asymmetry about the zero rotational velocity position is observed and is ascribed to neutral beam torque effects on the plasma. Pfirsch-Schlüter parallel flow is identified as the most likely candidate to explain the velocity shear observations, and an estimate of diamagnetic and $\mathbf{E} \times \mathbf{B}$ contributions is made (chapter 6).

With the ion temperature measurements, good agreement between core CXRS and temperatures from Thomson scattering is observed in L-mode. In H-mode good agreement is generally observed for radii smaller than the pedestal region. In the pedestal in some cases good agreement with Thomson scatter temperatures is still found, but in others a smaller temperature gradient in comparison to the Thomson electron temperature gradient is observed, leading to large ratios of the ion and electron temperatures at the separatrix. Calculations of equilibration times between the ions and electrons indicate that differences between the two species are permitted, while power balance analysis indicates that the observed ion and electron temperature differences could be present. However, no obvious heating sources can be identified to drive a temperature difference. Gyrokinetic theory suggests a link between ion temperature gradient and collisionality which places a limit on the ion temperature gradient scale to be small when the ions are in the banana regime. This limit does not hold in more collisional regimes and does not apply to the electrons. A dimensionless scan of collisionality supports this as only small gradients are observed in the banana regime, with larger gradients and a closer alignment between ion and electron temperatures observed when the edge collisionality is in the Pfirsch-Schlüter/Plateau region with an apparent transition from one to the other observed.

The compatibility of the temperature results from the developed diagnostic with the

scrape-off layer is assessed and comparison with modelling predictions from various machines and codes made which suggests the results are consistent with expectations (see Kocan et. al. 2008). Kočan *et. al.* (2008) suggest that a large ion to electron temperature ratio at the upstream position is not unusual. The sheath effect is calculated to be a contributing factor in this difference.

## 7.2 Suggestions for further work

There is scope for taking the results found here further. In the case of the velocity results further experiments in counter rotation could illuminate more fully the flows involved and ECELESTE $E_R$ measurements with helium puffing using repeated shots for direct comparison could provide more accurately the contribution from $\mathbf{E}\times\mathbf{B}$ flows to the Pfirsch-Schlüter flow. NCLASS modelling [130] could also allow a comparison of results with neoclassical theory. New poloidal views could also assess the effect of poloidal flows (see below). Furthermore the unexplained discrepancy between core CXRS and the ECELESTE results should be further investigated to obtain the source of disagreement.

In the case of the ion temperatures the effect of edge ion transport due to small ion temperature gradients could be further investigated and NCLASS and Chang-Hilton neoclassical values could be compared to the measured transport. SOL modelling using, for example, OSM2-EIRIENE in a low collisionality case would allow greater understanding of the results in this region and a direct comparison between model and experiment. The retarding field analyser recently installed on MAST should allow ion and electron temperature studies in the SOL which can be combined with ECELESTE measurements for further validation.

The system improvements due to newly installed cameras and new gas valve have yet to be fully installed but the potential for faster higher quality measurements should allow ECELESTE to become an even more effective diagnostic. The installation of a new camera and upgrade to fibre optic cables should improve intensity levels in the poloidal system and allow charge exchange measurements using these chords as well by using a second spectrometer. This presents the possibility of simultaneously measuring $T_i$, $v_\phi$, $v_\theta$ and $E_R$ using this setup. This should therefore provide a great deal of data to study edge shear and L-H transitions for example.

The potential of the ECELESTE diagnostic is large and it should be able to provide useful data in the edge for both MAST and MAST-Upgrade, allowing greater understanding of this important plasma region.

# Appendix A

# Derivation of semi-classical cross sections

## A.1 Low energy cross section

In the semi-classical atomic system $v_e$ can be found from the balance between the centripetal and Coulomb forces:

$$\frac{m_e {v_e}^2}{r} = \frac{Z_p e^2}{k_e r^2} \tag{A.1}$$

where $k_e = 1/4\pi\varepsilon_0$ is the Coulomb constant. Using this and the fact that $L = m_e v_e r = n\hbar$ and that $R_y = (k_e e^2)/2a_0$ we find that

$$v_e \approx \frac{Z_p}{n_p}\sqrt{\frac{2R_y}{m_e}}. \tag{A.2}$$

The resonance occurs when $E_{init} = E_{final}$, i.e. when

$$\frac{1}{2} m_e {v_{init}}^2 - \frac{k_e Z_p e^2}{r_r a_0} = \frac{1}{2} m_e {v_{final}}^2 - \frac{k_e Z_i e^2}{r_r a_0} \tag{A.3}$$

where $r_r$ is the normalised radius at this resonance position. Rearranging this we get

$$2R_y \left( \frac{{Z_p}^2}{2{n_p}^2} + \frac{Z_i}{r_r} \right) = 2R_y \left( \frac{{Z_i}^2}{2{n_i}^2} + \frac{Z_p}{r_r} \right). \tag{A.4}$$

The electron can exchange to the other nuclei if the potential at the saddle point between the two is low enough, i.e. approximately equal to the electrons binding energy. At the saddle point the electric field due to the two nuclei will be zero, i.e.

$$\mathbf{E} = \left( \frac{k_e Z_i e}{(r_i a_0)^2} - \frac{k_e Z_p e}{(r_p a_0)^2} \right) \hat{\mathbf{r}} = 0 \tag{A.5}$$

where $r_i$ and $r_p$ are the distance of the two nuclei from the saddle point respectively such that $r_r = r_i + r_p$. Substituting this in we can solve this to find a quadratic equation for either $r_i$ or $r_p$. Solving we find two solutions and take the positive one, which leads to

$$r_i = \frac{r_r\sqrt{Z_i}}{\sqrt{Z_p}+\sqrt{Z_i}} \quad \text{and} \quad r_p = \frac{r_r\sqrt{Z_p}}{\sqrt{Z_p}+\sqrt{Z_i}}. \tag{A.6}$$

We also know that the electric potential at the saddle point is equal to the potential of the electron, i.e.

$$V = \frac{R_y {Z_p}^2}{{n_p}^2} = \frac{2R_y Z_p}{r_p} + \frac{2R_y Z_i}{r_i}. \tag{A.7}$$

Substituting for $r_i$ and $r_p$ from equation A.6 we thus find that

$$\frac{R_y {Z_p}^2}{{n_p}^2} = \frac{2R_y}{r_r}\left(\sqrt{Z_p}+\sqrt{Z_i}\right)^2. \tag{A.8}$$

We therefore have two equations A.4 and A.8 which we can solve to find the two equations 3.4 and 3.5 used in section 3.4:

$$r_r = \frac{2{n_p}^2}{{Z_p}^2}\left(Z_p + 2\sqrt{Z_i Z_p}\right) = \frac{2{n_i}^2}{{Z_i}^2}\left(Z_p + 2\sqrt{Z_i Z_p}\right) \tag{A.9}$$

$$\frac{n_i}{n_p} = \left(\frac{Z_i}{Z_p}\right)^{3/4}\left(\frac{2\sqrt{Z_i}+\sqrt{Z_p}}{2\sqrt{Z_p}+\sqrt{Z_i}}\right)^{1/2}. \tag{A.10}$$

Thus by substituting fro $r_r$ from equation A.9 we can derive equation 3.6:

$$\sigma_{low} \approx \frac{1}{2}\pi {a_0}^2 {r_r}^2 = 8\frac{\pi {a_0}^2 {n_p}^4 Z_i}{{Z_p}^3}\left[1+\sqrt{Z_p/Z_i}+Z_p/4Z_i\right]. \tag{A.11}$$

## A.2 Intermediate energy cross section

In the intermediate energy case the electric potential at the saddle point must equal the kinetic energy of the ion, not the energy of the electron. Therefore we find that

$$V = \frac{1}{2}m_e v^2 = \frac{2R_y Z_p}{r_p} + \frac{2R_y Z_i}{r_i}. \tag{A.12}$$

Therefore following the same derivation as before we find that

$$b = a_0 2R_y \frac{\left(\sqrt{Z_p}+\sqrt{Z_i}\right)^2.}{\frac{1}{2}m_e v^2} = a_0 2R_y \frac{Z_m}{\frac{1}{2}m_e v^2} \tag{A.13}$$

where we have now defined $Z_m$. If P(Capture) $\approx (b/v)(v_e/a)$ where $a = (a_0 {n_p}^2)/Z_p$ then substituting equations A.13 and A.2 into this gives us

$$\mathrm{P(Capture)} \approx \frac{{Z_m}{Z_p}^2}{{n_p}^3}\left(\frac{2R_y}{\frac{1}{2}m_e v^2}\right)^{3/2}. \tag{A.14}$$

We therefore get an estimate for the cross section at intermediate energies as

$$\sigma_{med} \approx \pi b^2 \mathrm{P(Capture)} = \pi {a_0}^2 \frac{{Z_m}^3 {Z_p}^2}{\sqrt{2}{n_p}^3}\left(\frac{2R_y}{\frac{1}{2}m_e v^2}\right)^{7/2}. \tag{A.15}$$

Approximating so that $\sigma_{low} \approx \frac{8\pi {a_0}^2 {n_p}^4 Z_i}{{Z_p}^3}$ and that $Z_m \approx Z_i$ for large $Z_i$ we find that, defining $\varepsilon = (\frac{1}{2}m_e v^2)/(2R_y)$

$$\sigma_{med} \approx \sigma_{low}\frac{{Z_i}^2 {Z_p}^5}{2^7 \varepsilon^{7/2} n_p^7} = \sigma_{low}/\hat{\varepsilon} \tag{A.16}$$

where we have now defined $\hat{\varepsilon}$. We can thus interpolate by defining $\sigma_{interpol} = \sigma_{low}/(1+\hat{\varepsilon})$.

# Appendix B

# Derivation of the choked mass flow rate for an ideal gas under isentropic conditions

The mass flow rate can be defined as

$$\dot{m} = \rho v A \tag{B.1}$$

In the case of an ideal gas $v = Mv_s$ where $M$ is the Mach number and $v_s$ is the sound speed, given by

$$v_s = \sqrt{\frac{\gamma k_B T}{m}} \tag{B.2}$$

and

$$\rho = \frac{mp}{k_B T}. \tag{B.3}$$

Substituting equations B.2 and B.3 into equation B.1 gives

$$\dot{m} = A\sqrt{\frac{\gamma m}{k_B}} M \frac{p}{\sqrt{T}} \tag{B.4}$$

We wish to know the mass flow rate as a function of upstream absolute temperature and pressure of the gas $T_u$ and $p_u$ respectively. If the flow of the gas along the pipe is isentropic (i.e. adiabatic and reversible) then the following relations are true

$$p = p_u \left(\frac{T}{T_u}\right)^{\gamma/(\gamma-1)} \tag{B.5}$$

$$T = T_u \left(1 + \frac{1}{2}(\gamma - 1)M^2\right)^{-1} \tag{B.6}$$

Substituting these two equations into B.4 gives

$$\begin{aligned} \dot{m} &= A\sqrt{\frac{\gamma m}{k_B}} M \frac{p_u}{\sqrt{T_u}} \left(1 + \frac{1}{2}(\gamma - 1)M^2\right)^{\frac{-\gamma}{\gamma-1}+\frac{1}{2}} \\ &= A\sqrt{\frac{\gamma m}{k_B}} M \frac{p_u}{\sqrt{T_u}} \left(1 + \frac{1}{2}(\gamma - 1)M^2\right)^{-\frac{\gamma+1}{2(\gamma-1)}} \end{aligned} \tag{B.7}$$

For choked flow $M = 1$ so that the particle flow rate (molecules $s^{-1}$) is therefore

$$\dot{N} = \frac{\dot{m}}{m} = A\sqrt{\frac{\gamma}{m k_B}} \frac{p_u}{\sqrt{T_u}} \left(\frac{\gamma + 1}{2}\right)^{-\frac{\gamma+1}{2(\gamma-1)}} \tag{B.8}$$

# Appendix C

# Fitting calibrations

Prior to fitting the data it was necessary to calibrate the spectrometer by finding the instrument function and dispersion, as well as to calculate the sources of noise in the data. In order to produce radially accurate data the position of the viewing chords was also calibrated. These calibrations are discussed in this appendix.

If a line is monochromatic upon entering the ECELESTE system, any subsequent broadening measured is due to the instrument function. This is the additional broadening of a spectral line caused by the imperfections of the spectroscopic system used. It is a combination of contributions from all components of the system but is dominated by the Czerny-Turner spectrometer.

In order to measure the instrument function, a low pressure copper lamp was coupled into the toroidal optics using a diffuser to provide a uniform source of light. By doing this the dispersion of each chord in the $10 \times 12$ array can be measured simultaneously and any spectral aberrations detected. The dispersion of the spectrometer is wavelength dependent (see below) and copper produces a strong spectral line at 5292.52 Å which is sufficiently close to the emission line at 5290.50 Å to produce an accurate measurement of the instrument function. As the lamp is low pressure and low temperature the line is essentially monochromatic. A second spectral line from neon filler gas also lies nearby at 5298.19 Å and is used to measure the dispersion (see below). In order for other close lying spectral lines not to overlap and interfere the filter was retained within the system so that only these two lines were visible on the CCD from each chord. A white light calibration (essentially measuring the transmission shape of each chord) ensured that this was of sufficient spectral width that it did not effect the lineshape of the instrument function.

In order to quantify the instrument function the measured data was fitted with a Gaussian lineshape using the same least squares fitting routine as used to fit the measured data (see section 4.3). As shown in figure C.1 the full width half maximum (FWHM) of the

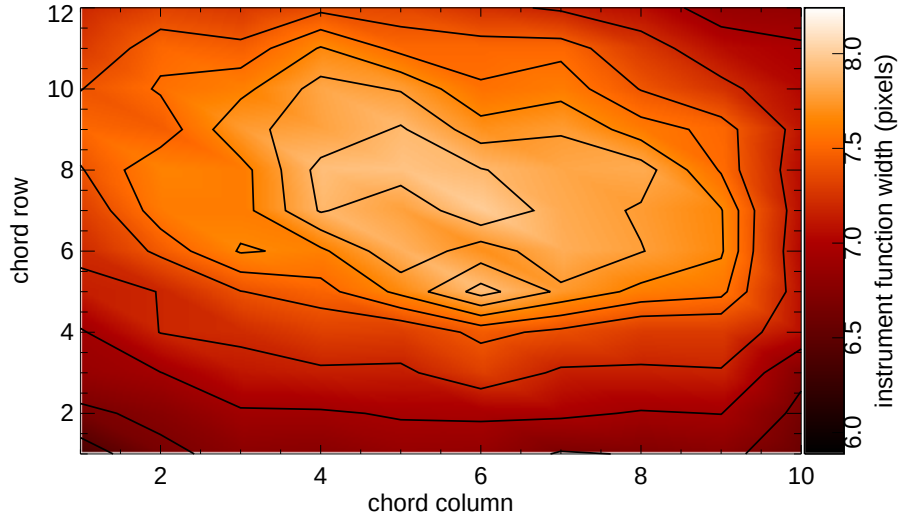


**Figure C.1:** *Variation in the full width half maximum (FWHM) of Gaussian fits to the instrument function of the ECELESTE spectrometer (in pixels)*

instrument functions varies considerably over the surface of the CCD. This is most likely to be due to barrel distortion from the demagnifying lens and means that dispersion and instrument function of every chord must be individually assessed to determine the effect of these variations.

The dispersion of the spectrometer can be calculated or measured. The equation for this is given as [131]

$$\frac{\Delta\lambda}{\Delta x} = \frac{d}{nf}\cos\left(\left(\arcsin\frac{n\lambda}{2d\cos\epsilon}\right) - \epsilon\right) \tag{C.1}$$

where $1/d$ is the lines per mm of the grating, $n$ is the order of the grating being used, $f$ is the focal length of the spectrometer, $\lambda$ the wavelength of light and $\epsilon$ the angle between the mirrors and the grating. For the ECELESTE spectrometer $\epsilon = 1.025 \pm 0.001$ radians, $f = 1 \pm 0.01$ m, $n = 1$ and $d = 1/2400$ mm per line, giving the dispersion as $3.463 \pm 0.002$ Å mm$^{-1}$. However, this does not take into account the variation due to optical abberrations and optical path differences.

By measuring two emission lines with a known wavelength separation the dispersion of each chord can be determined. The copper lamp contains a neon filler gas which has an emission line at 5298.19 Å. By measuring the distance on the CCD between the two lines the dispersion can be determined individually. The resulting measurement of Ångstroms per pixel can be converted to Ångstroms per mm to compare with equation C.1 if the width of a single pixel ($p = 22.5\mu$m) and magnification of the lens ($M = 2.0$) are known using

$$\frac{\Delta\lambda}{\Delta x_{mm}} = \frac{1}{pM}\frac{\Delta\lambda}{\Delta x_{pixels}} \tag{C.2}$$

This gives figures slightly larger than predicted by equation C.1, implying a better resolution for the velocities and temperatures, although the result is not large enough to make a great difference. Overall variation in the dispersion is over a total range of 3.462 to 3.526 Å mm$^{-1}$, with a mean and standard deviation of $3.480 \pm 0.010$ Å mm$^{-1}$ (see figure C.2). Using an average value for the dispersion would produce a maximum error (the largest discrepancy between mean and measured values) of 1.3% in the value of the measured velocity and temperature. Although this is small, individual dispersions have nonetheless been used to minimise error propagation.

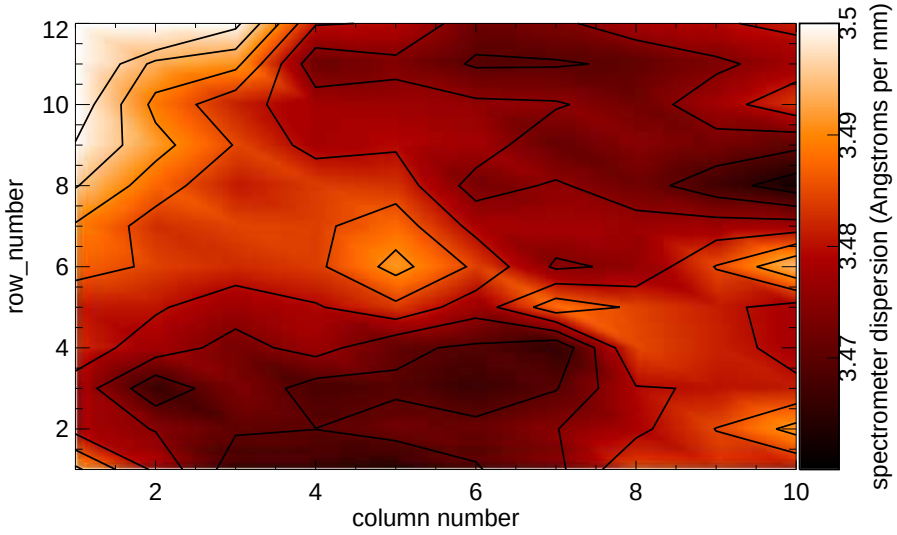


**Figure C.2:** *Variation in the dispersion of the spectrometer measured using Gaussian fitting of two emission lines of known spectral separation in Å per mm*

As the instrument functions are sufficiently close to Gaussian to be represented as such, the deconvolution of the instrument functions from the overall fit can be done algebraically using

$$\sigma_D = \sqrt{\sigma_M - \sigma_I} \tag{C.3}$$

where $\sigma_M$ is the measured broadening, $\sigma_D$ is the broadening due to the Doppler effect and $\sigma_I$ is the broadening due to the instrument. This removes the need for a complex forward model to account for the instrument function and greatly simplifies the calculation of ion temperatures with little to no loss of accuracy.

When the radial chord is employed the velocity can be measured by fitting a constant to the data as a function of time (see figure C.3). By using a cut in the normalised $\chi^2_N$

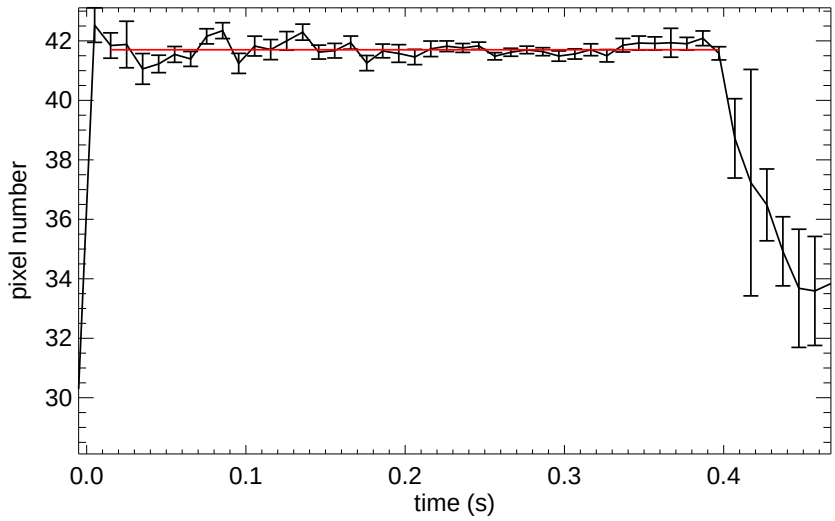


**Figure C.3:** *Timetrace of the measured position of the radial chord. A constant is fitted to the data to find the zero rotation velocity.*

value only correct points are selected for the fitting. The fitted result can be used as a zero reference point to calculate the velocities as

$$\lambda_S - \lambda_0 = \frac{p_i - c_i}{p_r - c_r}\frac{\Delta\lambda}{\Delta x} \tag{C.4}$$

where $p$ is the measured centroid position, and $c$ the measured calibration position of the measured chord ($i$) and radial chord ($r$). If the radial chord is not available then account must be made of the recorded position of the spectrometer grating, which is moved to take the measurement. The calibrated position $c_i$ is found from the measured pixel position by adjusting for the different measured wavelength and the different grating position. In this case $c_i$ is found as

$$c_i = c_{meas} - \Delta\lambda_{cal} + \Delta A \quad \text{pixels} \tag{C.5}$$

where $\Delta\lambda_{cal}$ and $\Delta A$ are the shifts in wavelength between the calibration wavelength and the charge exchange emission's natural wavelength in pixels, given by

$$\Delta\lambda_{cal} = \frac{(5292.52 - 5290.5)}{\frac{\Delta\lambda}{\Delta x}} \quad \text{pixels} \tag{C.6}$$

and $\Delta A$ is the shift in the position in the dial given by

$$\Delta A = \frac{A_{cal} - A_{meas}}{2\frac{\Delta\lambda}{\Delta x}} \quad \text{pixels} \tag{C.7}$$

where the factor 2 arises because the display reads double the actual wavelength orientation of the spectrometer. The Doppler shift can then be calculated as

$$\lambda_S - \lambda_0 = (p_i - c_i)\,\frac{\Delta\lambda}{\Delta x} \tag{C.8}$$

Because the $c_i$ cancel in equation C.4 the uncertainties in dial position and wavelength value are eliminated.

For the velocity measurements therefore the errors in the case with a radial chord are calculated as

$$\sigma_{Dopp} = \sqrt{\sigma^2_{disp} + \sigma^2_{meas} + \sigma^2_{cal} + \sigma^2_{radcal} + \sigma^2_{radfit}}\frac{\Delta\lambda}{\Delta x} \tag{C.9}$$

where each term is, in order, the total Doppler shift error, the error in the dispersion calculation, the error in the calibration line fitting, the calibration in the radial chord's calibration line fitting and the error in the fit to the timetrace of the radial chord. In the case without a radial chord the error is given by

$$\sigma_{Dopp} = \sqrt{\sigma^2_{disp} + \sigma^2_{meas} + \sigma^2_{cal} + \sigma^2_{wl} + \sigma^2_{A}}\frac{\Delta\lambda}{\Delta x} \tag{C.10}$$

where $\sigma_{wl}$ is the uncertainty in wavelength position and $\sigma_A$ the error in the dial position. As $\sigma_A$ is large and because the $c_i$ cancel in equation C.4 the uncertainties in dial position and wavelength value are eliminated, so this is the preferred methodology.

In terms of velocity the error in velocity can be calculated as

$$\sigma_v = \frac{\sigma_{Dopp}}{\lambda_0}c \tag{C.11}$$

For the temperatures the error is calculated as

$$\sigma_{T(pixels)} = \sqrt{\sigma^2_{disp} + \sigma^2_{meas} + \sigma^2_{cal}}\frac{\Delta\lambda}{\Delta x} \tag{C.12}$$

where the measurement and calibration errors in this case refer to the widths of the measured lines. This is transformed to a temperature error as

$$\sigma_{T(eV)} = \sqrt{2T(eV)\frac{\sigma^2_{T(Pixels)}}{T(pixels)}}. \tag{C.13}$$

# Appendix D

# Acronyms and Symbols

| Symbol | Meaning |
|---|---|
| $\theta$ | Poloidal direction in tokamak geometry |
| $\phi$ | Toroidal direction in tokamak geometry |
| $T$ | Temperature |
| $v_\phi$ | Toroidal velocity |
| $v_\theta$ | Poloidal velocity |
| $n$ | Density |
| $p$ | Pressure |
| $e$ | Electrons or electric charge of an electron |
| $i$ | Bulk ions (deuterium) |
| $z$ | Impurity ions |
| $C$ | Carbon |
| $\omega_p$ | Plasma frequency |
| $\omega_c$ | Cyclotron frequency |
| $\tau_{coll}$ | Collision time |
| $R_y$ | Rydberg energy (13.61 eV) |
| $v_{th}$ | Thermal velocity |
| $R$ | Major radius |
| $r$ | Minor radius |
| $a$ | Separatrix position such that $r/a = 1$ |
| $E_R$ | Radial electric field |
| CXRS | Charge Exchange Recombination Spectroscopy |
| LCFS | Last Closed Flux Surface |
| ELM | Edge Localised Mode |

# Bibliography


[1] U. Nations, "World population to 2050," 2004.

[2] U.S. Energy Information Administration (EIA), *Annual Energy Outlook 2011.* 2011.

[3] L. L. Lucas and M. P. Unterweger, "Comprehensive Review and Critical Evaluation of the Half-Life of Tritium," *Journal of Research of the National Institute of Standards and Technology*, vol. 105, no. 4, pp. 541–549, 2000.

[4] U. G. Survey, "MINERAL COMMODITY SUMMARIES 2010," 2010.

[5] J. Wesson, *Tokamaks (3rd Ed.).* 2004.

[6] JET/EFDA, "Cyclotron," 1999.

[7] F. Troyon, R. Gruber, H. Saurenmann, S. Semenzato, and S. Succi, "MHD limits to plasma confinement," *Plasma Physics and Controlled Fusion*, vol. 26, no. 1A, pp. 209–215, 1984.

[8] Y.-K. M. Peng and D. J. Stricker, "Features of spherical torus plasmas," *Nuclear Fusion*, vol. 26, p. 769, 1986.

[9] Y.-K. M. Peng, "The physics of spherical torus plasmas," *Physics of Plasmas*, vol. 7, no. 5, p. 874048, 2000.

[10] A. R. Field, P. G. Carolan, R. J. Akers, E. R. Arends, K. Axon, R. J. Buttery, N. J. Conway, G. F. Counsell, G. Cunningham, S. J. Fielding, M. Gryaznevich, A. Kirk, I. P. Lehane, B. Lloyd, M. A. McGrath, H. Meyer, C. Ribeiro, A. Sykes, A. Tabasso, M. R. Tournianski, M. Valovic, M. J. Walsh, and H. R. Wilson, "H-mode plasmas in the MAST spherical tokamak," *Plasma Physics and Controlled Fusion*, vol. 44, pp. 113–121, 2002.

[11] A. Sykes, "Progress on Spherical Tokamaks," *Plasma Physics and Controlled Fusion*, vol. 36, pp. B93–B106, 1994.

[12] M. Gryaznevich, R. Akers, P. G. Carolan, N. J. Conway, D. Gates, A. R. Field, T. C. Hender, I. Jenkins, R. Martin, M. P. S. Nightingale, C. Ribeiro, D. C. Robinson, A. Sykes, M. Tournianski, M. Valovic, and M. J. Walsh, "Achievement of Record $\beta$ in the START Spherical Tokamak," *Physical Review Letters*, vol. 80, no. 18, pp. 3972–3975, 1998.

[13] S. M. Kaye, M. G. Bell, R. E. Bell, J. Bialek, T. Bigelow, M. Bitter, P. Bonoli, D. Darrow, P. Efthimion, J. Ferron, E. Fredrickson, D. Gates, L. Grisham, J. Hosea, D. Johnson, R. Kaita, S. Kubota, H. Kugel, B. LeBlanc, R. Maingi, J. Manickam, T. K. Mau, R. J. Maqueda, E. Mazzucato, J. Menard, D. Mueller, B. Nelson, N. Nishino, M. Ono, F. Paoletti, S. Paul, Y.-K. M. Peng, C. K. Phillips, R. Raman, P. Ryan, S. A. Sabbagh, M. Schaffer, C. H. Skinner, D. Stutman, D. Swain, E. Synakowski, Y. Takase, J. Wilgen, J. R. Wilson, W. Zhu, S. Zweben, A. Bers, M. Carter, B. Deng, C. Domier, E. Doyle, Finkenthal, M. Hill, T. Jarboe, S. Jardin, H. Ji, L. Lao, K. C. Lee, N. Luhmann, R. Majeski, S. Medley, H. Park, T. Peebles, R. I. Pinsker, G. Porter, A. Ram, M. Rensink, T. Rognlien, D. Stotler, B. Stratton, G. Taylor, W. Wampler, G. A. Wurden, X. Q. Xu, and L. Zeng, "Initial physics results from the National Spherical Torus Experiment," *Physics of Plasmas*, vol. 8, no. 5, pp. 1977–1987, 2001.

[14] D. Gates, J. Ahn, J. Allain, R. Andre, R. Bastasz, M. Bell, R. Bell, E. Belova, J. Berkery, R. Betti, J. Bialek, T. Biewer, T. Bigelow, M. Bitter, J. Boedo, P. Bonoli, a. Boozer, D. Brennan, J. Breslau, D. Brower, C. Bush, J. Canik, G. Caravelli, M. Carter, J. Caughman, C. Chang, W. Choe, N. Crocker, D. Darrow, L. Delgado-Aparicio, S. Diem, D. D'Ippolito, C. Domier, W. Dorland, P. Efthimion, a. Ejiri, N. Ershov, T. Evans, E. Feibush, M. Fenstermacher, J. Ferron, M. Finkenthal, J. Foley, R. Frazin, E. Fredrickson, G. Fu, H. Funaba, S. Gerhardt, a. Glasser, N. Gorelenkov, L. Grisham, T. Hahm, R. Harvey, a. Hassanein, W. Heidbrink, K. Hill, J. Hillesheim, D. Hillis, Y. Hirooka, J. Hosea, B. Hu, D. Humphreys, T. Idehara, K. Indireshkumar, a. Ishida, F. Jaeger, T. Jarboe, S. Jardin, M. Jaworski, H. Ji, H. Jung, R. Kaita, J. Kallman, O. Katsuro-Hopkins, K. Kawahata, E. Kawamori, S. Kaye, C. Kessel, J. Kim, H. Kimura, E. Kolemen, S. Krasheninnikov, P. Krstic, S. Ku, S. Kubota, H. Kugel, R. La Haye, L. Lao, B. LeBlanc, W. Lee, K. Lee, J. Leuer, F. Levinton, Y. Liang, D. Liu, N. Luhmann, R. Maingi, R. Majeski, J. Manickam, D. Mansfield, R. Maqueda, E. Mazzucato, D. McCune, B. McGeehan, G. McKee, S. Medley, J. Menard, M. Menon, H. Meyer, D. Mikkelsen, G. Miloshevsky, O. Mitarai, D. Mueller, S. Mueller, T. Munsat, J. Myra, Y. Nagayama, B. Nelson, X. Nguyen, N. Nishino, M. Nishiura, R. Nygren, M. Ono, T. Osborne, D. Pacella,

H. Park, J. Park, S. Paul, W. Peebles, B. Penaflor, M. Peng, C. Phillips, a. Pigarov, M. Podesta, J. Preinhaelter, a. Ram, R. Raman, D. Rasmussen, a. Redd, H. Reimerdes, G. Rewoldt, P. Ross, C. Rowley, E. Ruskov, D. Russell, D. Ruzic, P. Ryan, S. Sabbagh, M. Schaffer, E. Schuster, S. Scott, K. Shaing, P. Sharpe, V. Shevchenko, K. Shinohara, V. Sizyuk, C. Skinner, a. Smirnov, D. Smith, S. Smith, P. Snyder, W. Solomon, a. Sontag, V. Soukhanovskii, T. Stoltzfus-Dueck, D. Stotler, T. Strait, B. Stratton, D. Stutman, R. Takahashi, Y. Takase, N. Tamura, X. Tang, G. Taylor, C. Taylor, C. Ticos, K. Tritz, D. Tsarouhas, a. Turrnbull, G. Tynan, M. Ulrickson, M. Umansky, J. Urban, E. Utergberg, M. Walker, W. Wampler, J. Wang, W. Wang, a. Welander, J. Whaley, R. White, J. Wilgen, R. Wilson, K. Wong, J. Wright, Z. Xia, X. Xu, D. Youchison, G. Yu, H. Yuh, L. Zakharov, D. Zemlyanov, and S. Zweben, "Overview of results from the National Spherical Torus Experiment (NSTX)," *Nuclear Fusion*, vol. 49, p. 104016, Oct. 2009.

[15] M. Cox, "The Mega Amp Spherical Tokamak," *Fusion Engineering and Design*, vol. 46, no. 2-4, pp. 397–404, 1999.

[16] A. Sykes, "The spherical tokamak programme at Culham," *Nuclear Fusion*, vol. 39, no. 9Y, pp. 1271–1281, 1999.

[17] A. Sykes, "Overview of recent spherical tokamak results," *Plasma Physics and Controlled Fusion*, vol. 43, no. 12A, pp. A127–A139, 2001.

[18] H. Meyer, R. Akers, F. Alladio, L. Appel, K. Axon, N. B. Ayed, P. Boerner, R. Buttery, P. Carolan, D. Ciric, C. Challis, I. Chapman, G. Coyler, J. Connor, N. Conway, S. Cowley, M. Cox, G. Counsell, G. Cunningham, a. Darke, M. DeBock, G. DeTemmerman, R. Dendy, J. Dowling, a. Y. Dnestrovskij, Y. Dnestrovskij, B. Dudson, D. Dunai, M. Dunstan, a.R. Field, a. Foster, L. Garzotti, K. Gibson, M. Gryaznevich, W. Guttenfelder, N. Hawkes, J. Harrison, P. Helander, T. Hender, B. Hnat, M. Hole, D. Howell, M. D. Hua, a. Hubbard, M. Istenic, N. Joiner, D. Keeling, a. Kirk, H. Koslowski, Y. Liang, M. Lilley, S. Lisgo, B. Lloyd, G. Maddison, R. Maingi, a. Mancuso, S. Manhood, R. Martin, G. McArdle, J. McCone, C. Michael, P. Micozzi, T. Morgan, a.W. Morris, D. Muir, E. Nardon, G. Naylor, M. O'Brien, T. O'Gorman, a. Patel, S. Pinches, J. Preinhaelter, M. Price, E. Rachlew, D. Reiter, C. Roach, V. Rozhansky, S. Saarelma, a. Saveliev, R. Scannell, S. Sharapov, V. Shevchenko, S. Shibaev, H. Smith, G. Staebler, D. Stork, J. Storrs, a. Sykes, S. Tallents, P. Tamain, D. Taylor, D. Temple, N. Thomas-Davies, a. Thornton, a. Thyagaraja, M. Turnyanskiy, J. Urban, M. Valovic, R. Vann, F. Volpe, G. Voss, M. Walsh, S. Warder,

R. Watkins, H. Wilson, M. Windridge, M. Wisse, a. Zabolotski, S. Zoletnik, and O. Zolotukhin, "Overview of physics results from MAST," *Nuclear Fusion*, vol. 49, p. 104017, Oct. 2009.

[19] D. Temple, *Experimental Investigations into The Radial Electric Field of MAST*. PhD thesis, 2010.

[20] R. Scannell, M. J. Walsh, M. R. Dunstan, J. Figueiredo, G. Naylor, T. O'Gorman, S. Shibaev, K. J. Gibson, and H. Wilson, "A 130 point Nd:YAG Thomson scattering diagnostic on MAST.," *The Review of scientific instruments*, vol. 81, p. 10D520, Oct. 2010.

[21] M. Manso, "Reflectometry in fusion devices," *Plasma Physics and Controlled Fusion*, vol. 35, pp. B141–BI55, 1993.

[22] F. Wagner, G. Becker, K. Behringer, D. Campbell, A. Eberhagen, W. Engelhardt, G. Fussmann, O. Gehre, J. Gernhardt, G. v. Gierke, G. Haas, M. Huang, F. Karger, M. Keilhacker, O. Klüber, M. Kornherr, K. Lackner, G. Lisitano, G. G. Lister, H. M. Mayer, D. Meisel, E. R. Müller, H. Murmann, H. Niedermeyer, W. Poschenrieder, H. Rapp, H. Röhr, F. Schneider, G. Siller, E. Speth, A. Stäbler, K. H. Steuer, G. Venus, O. Vollmer, and Z. Yü, "Regime of Improved Confinement and High Beta in Neutral-Beam-Heated Divertor Discharges of the ASDEX Tokamak," *Physical Review Letters*, vol. 49, no. 19, pp. 1408–1412, 1982.

[23] F. Wagner, "A quarter-century of H-mode studies," *Plasma Physics and Controlled Fusion*, vol. 49, pp. B1–B33, Dec. 2007.

[24] J. W. Connor, R. J. Hastie, H. R. Wilson, and R. L. Miller, "Magnetohydrodynamic stability of tokamak edge plasmas," *Physics of Plasmas*, vol. 5, no. 7, p. 2687, 1998.

[25] G. Federici, P. Andrew, P. Barabaschia, J. Brooks, R. Doerner, A. Geier, Herrmanne A., G. Janeschitz, K. Krieger, A. Kukushkin, A. Loarte, R. Neue, G. Saibene, M. Shimada, G. Strohmayer, and M. Sugihara, "Key ITER plasma edge and plasmamaterial interaction issues," *Journal of Nuclear Materials*, vol. 313-316, pp. 11–22, 2003.

[26] J. Callen, A. Cole, and C. Hegna, "Toroidal Rotation In Tokamak Plasmas," *Nuclear Fusion*, vol. 49, no. 8, p. 085021, 2009.

[27] V. Afrosimov, Y. Gordeev, A. Zinov'ev, and A. Korotkov, "Active diagnostics of impurity ions in the plasma of a T-4 tokamak," *JETP letters*, vol. 28, no. 8, p. 500, 1978.

[28] A. Zinov'ev, A. Korotko, E. Krzhizhanovski, V. Afrosimov, and Y. Gordeev, "Radial distribution of the concentration of oxygen nuclei in the plasma of the T-10 Tokamak," *JETP letters*, vol. 32, no. 9, p. 540, 1980.

[29] R. Fonck, R. Goldston, R. Kaita, and D. Post, "Plasma ion temperature measurements via charge exchange recombination radiation," *Applied Physics Letters*, vol. 42, no. 3, p. 239, 1983.

[30] R. Groebner, N. Brooks, K. Burrell, and L. Rottler, "Measurements of plasma ion temperature and rotation velocity using the HeII 4686-A line produced by charge transfer," *Applied Physics Letters*, vol. 43, no. 10, p. 920, 1983.

[31] R. C. Isler and L. Murray, "Plasma rotation measurements using spectral lines from charge-transfer reactions," *Applied Physics Letters*, vol. 42, no. 4, p. 355, 1983.

[32] R. Fonck, D. Darrow, and K. Jaehnig, "Determination of plasma-ion velocity distribution via charge-exchange recombination spectroscopy," June 1984.

[33] R. C. Isler, "An overview of charge-exchange spectroscopy as a plasma diagnostic," *Plasma Physics and Controlled Fusion*, vol. 36, pp. 171–208, 1994.

[34] A. Boileau, M. von Hellermann, L. Horton, J. Spence, and H. P. Summers, "The deduction of low-Z ion temperature and densities in the JET tokamak using Charge Exchange Recombinatoin Spectroscopy," *Plasma Physics and Controlled Fusion*, vol. 31, no. 5, pp. 779–804, 1989.

[35] E. Busche, H. Euringer, and R. Jaspers, "Measurement of deuterium ion temperature profiles at TEXTOR-94," *Plasma Physics and Controlled Fusion*, vol. 39, pp. 1327–1338, Sept. 1997.

[36] K. Ida, S. Kado, and Y. Liang, "Measurements of poloidal rotation velocity using charge exchange spectroscopy in a large helical device," *Review of Scientific Instruments*, vol. 71, no. 6, p. 2360, 2000.

[37] Y. Koide, a. Sakasai, Y. Sakamoto, H. Kubo, and T. Sugie, "Multichordal charge exchange recombination spectroscopy on the JT-60U tokamak," *Review of Scientific Instruments*, vol. 72, no. 1, p. 119, 2001.

[38] M. Reich, E. Wolfrum, J. Schweinzer, H. Ehmler, L. D. Horton, J. Neuhauser, and A. U. Team, "Lithium beam charge exchange diagnostic for edge ion temperature measurements at the ASDEX Upgrade tokamak," *Plasma Physics and Controlled Fusion*, vol. 46, pp. 797–808, May 2004.

[39] Y. Andrew, N. C. Hawkes, and K. Crombe, "Improved charge exchange spectroscopy on the Joint European Torus for ion temperature and rotation velocity profiles," *Review of Scientific Instruments*, vol. 77, no. 10, p. 10E913, 2006.

[40] N. J. Conway, P. G. Carolan, J. McCone, M. J. Walsh, and M. Wisse, "High-throughput charge exchange recombination spectroscopy system on MAST," *Review of Scientific Instruments*, vol. 77, no. 10, p. 10F131, 2006.

[41] H. Meyer, C. Bunting, P. G. Carolan, N. J. Conway, M. R. Dunstan, a. Kirk, R. Scannell, D. Temple, M. Walsh, t. M. Teams, and Nbi, "The structure, evolution and role of the radial edge electric field in H-mode and L-mode on MAST," *Journal of Physics: Conference Series*, vol. 123, p. 012005, July 2008.

[42] A. Kirk, G. F. Counsell, W. Fundamenski, J.-W. Ahn, D. Taylor, M. J. Walsh, and Y. Yang, "A comparison of mid-plane scrape-off-layer measurements with model predictions in MAST and the calculation of cross-field transport coefficients," *Plasma Physics and Controlled Fusion*, vol. 46, pp. 1591–1603, Oct. 2004.

[43] J. McCone, *Spectroscopic diagnostics on MAST*. PhD thesis, 2011.

[44] M. Wisse and N. J. Conway, "Private communication," 2008.

[45] R. M. McDermott, B. Lipschultz, J. W. Hughes, P. J. Catto, a. E. Hubbard, I. H. Hutchinson, R. S. Granetz, M. Greenwald, B. LaBombard, K. Marr, M. L. Reinke, J. E. Rice, and D. Whyte, "Edge radial electric field structure and its connections to H-mode confinement in Alcator C-Mod plasmas," *Physics of Plasmas*, vol. 16, no. 5, p. 056103, 2009.

[46] K. D. Marr, *Comparison of Charge-Exchange Recombination Spectroscopy Measurements of the Pedestal Region of Alcator C-Mod with Neoclassical Flow Predictions by*. PhD thesis, 2010.

[47] I. D. Paton, *On the neutral gas puff as a tokamak edge diagnostic*. PhD thesis, 2005.

[48] P. G. Carolan, N. J. Conway, C. a. Bunting, P. Leahy, R. OConnell, R. Huxford, C. R. Negus, and P. D. Wilcock, "Fast charged-coupled device spectrometry using zoom-wavelength optics," *Review of Scientific Instruments*, vol. 68, no. 1, p. 1015, 1997.

[49] P. G. Carolan, N. J. Conway, a. R. Field, P. B. Jones, and H. F. Meyer, "Synergy of multiviewing spectroscopic diagnostics on COMPASS-D (invited)," *Review of Scientific Instruments*, vol. 72, no. 1, p. 881, 2001.

[50] A. R. Field, S. J. Fielding, P. Helander, H. R. Wilson, J. M. A. Ashbourn, P. G. Carolan, P. B. Jones, M. G. O. Mullane, and S. Giles, "H-mode studies using the HELIOS (HELium Injection and Optical Spectroscopy) diagnostic on COMPASS-D tokamak," *26th EPS Conference on controlled fusion and plasma physics proceedings*, vol. 23J, pp. 273 – 276, 1999.

[51] N. J. Conway, *Study of ion behaviour on tokamaks using active and passive spectroscopy.* PhD thesis, 1998.

[52] O. Jitrik and C. F. Bunge, "Transition Probabilities for Hydrogen-Like Atoms," *Journal of Physical and Chemical Reference Data*, vol. 33, no. 4, p. 1059, 2004.

[53] H. Meyer, "Private communication," 2011.

[54] H. Summers, *The ADAS User Manual, version 2.6 http://www.adas.ac.uk.* 2004.

[55] J. E. Sansonetti, "Handbook of Basic Atomic Spectroscopic Data," *Journal of Physical and Chemical Reference Data*, vol. 34, no. 4, p. 1559, 2005.

[56] G. Erickson, "Energy Levels of One-Electron Atoms," *Journal of Physical and Chemical Reference DataJournal of Physical and Chemical Reference Data*, vol. 6, no. 3, p. 831, 1977.

[57] I. H. Hutchinson, *Principles of Plasma Diagnostics.* 2005.

[58] W. M. Stacey and R. J. Groebner, "Thermal transport analysis of the edge region in the low and high confinement stages of a DIII-D discharge," *Physics of Plasmas*, vol. 14, no. 1, p. 012501, 2007.

[59] M. Wisse, *Charge-Exchange Spectroscopy in the MAST Tokamak.* PhD thesis, 2007.

[60] R. E. Olson and D. R. Schultz, "n, l Distributions for electon-capture from H(1s) by C6+ and O8+," *Physica Scripta*, vol. 28, pp. 71–76, 1989.

[61] R. E. Olson, "n, l distributions in Aq+ + H electron-capture collisions," *Physical Review A*, vol. 24, no. 4, p. 1726, 1981.

[62] T. Green, M. Riley, E. Shipsey, and J. Browne, "Semiclassical trajectory effects on C6+-H charge-exchange cross sections at low energy," Dec. 1982.

[63] W. Fritsch and C. Lin, "Atomic-orbital-expansion studies of electron transfer in bare-nucleus Z (Z=2, 4-8) - hydrogen-atom collisions," *Physical Review A*, vol. 29, no. 6, p. 3039, 1984.

[64] M. Kimura and C. Lin, "Unified treatment of slow atom-atom and ion-atom collisions. II. Application to H+ +H and C6+ + H collisions," *Physical Review A*, vol. 32, no. 3, p. 1357, 1985.

[65] H. Tawara and W. Fritsch, "Electron Transfer Data fro Cq+ and Oq+ Ions in Collisions w i t h H, H2, and He Targets - Present Status and Some Related Data Needs in Applications t o Fusion Research," *Physica Scripta*, vol. 28, pp. 58–66, 1989.

[66] R. Hoekstra, D. Ciric, F. J. D. Heer, and R. Morgenstern, "State Selective Electron Capture in Collisions of C 6+ and O 8+ on Atomic and Molecular Hydrogen Studied by Photon Emission Spectroscopy," *Physica Scripta*, vol. T28, pp. 81–90, Jan. 1989.

[67] R. Hoekstra, H. Anderson, F. W. Bliek, M. V. Hellermann, C. F. Maggi, R. E. Olson, and H. P. Summers, "Charge exchange from D( n = 2) atoms to low- Z receiver ions," *Plasma Physics and Controlled Fusion*, vol. 40, pp. 1541–1550, Aug. 1998.

[68] H. Suno and T. Kato, "Recommended Cross Section Data for Carbon Ions and Atoms: Electron-impact Excitation, Ionization and Charge Exchange," *Journal of Physics: Conference Series*, vol. 72, p. 012018, June 2007.

[69] I. Mančev, "Four-body continuum-distorted-wave model for charge exchange between hydrogenlike projectiles and atoms," *Physical Review A*, vol. 75, May 2007.

[70] R. Janev, R. Phaneuf, H. Tawara, and T. Shirai, "Recommended Cross Sections for State-Selective Electron Capture in Collisions of C6+ and O8+ Ions with Atomic Hydrogen," *Atomic Data and Nuclear Data Tables*, vol. 55, no. 2, pp. 201–232, 1993.

[71] H. Tawara, "Total and partial cross sections of electron transfer processes for Beq+ and Bq+ ions in collisions with H, H2 and He gas targets," tech. rep., 1991.

[72] N. Toshima and H. Tawara, "Excitation, ionization and electron capture cross sections of atomic hydrogen in collisions with multiply charged ions," tech. rep., 1995.

[73] K. Ida and S. Hidekuma, "Space- and time-resolved measurements of ion temperature with the CVI 5292-A charge-exchange recombination line after subtracting background radiation," *Review of Scientific Instruments*, vol. 60, no. 5, p. 867, 1989.

[74] P. Gohil, K. Burrell, R. Groebner, J. Kim, W. Martin, E. McKee, and R. Seraydarian, "The charge exchange recombination diagnostic system on the DIII-D tokamak," *[Proceedings] The 14th IEEE/NPSS Symposium Fusion Engineering*, pp. 1199–1204, 1991.

[75] P. Bogen, J. Hey, E. Hintz, Y. Lie, D. Rusbüldt, and U. Samm, "Spectroscopic measurements of the ion temperature in front of a tokamak limiter," *Journal of Nuclear Materials*, vol. 220-222, pp. 472–477, Apr. 1995.

[76] H. Suno and T. Kato, "Cross section database for carbon atoms and ions: Electron-impact ionization, excitation, and charge exchange in collisions with hydrogen atoms," *Atomic Data and Nuclear Data Tables*, vol. 92, pp. 407–455, July 2006.

[77] W. Fritsch, "Description of high-n state population in electron transfer collisions," *Journal de Physique Colloque*, vol. 50, no. C1, pp. 87–92, 1989.

[78] H. Ryufuku, "Ionization excitation and charge transfer from inpacts of H+ Li3+ B5+ C6+ Si14+ ions on atomic hydrogen," *Physical Review A*, vol. 25, no. 2, p. 720, 1982.

[79] J. Spence and H. P. Summers, "The recombination and level populations of ions: III. The role of charge exchange from neutral hydrogen," *Journal of Physics B: Atomic, Molecular and Optical Physics*, vol. 19, p. 3749, 1986.

[80] M. Seaton, "Radiative recombination of hydrogenic ions," *Monthly Notices of the Royal Astronomical Society*, vol. 119, p. 81, 1959.

[81] R. E. Bell, "Carbon ion plume emission produced by charge exchange with neutral beams on National Spherical Torus Experiment," *Review of Scientific Instruments*, vol. 77, no. 10, p. 10E902, 2006.

[82] B. Labombard, "KN1D : A 1-D Space , 2-D Velocity , Kinetic Transport Algorithm for Atomic and Molecular Hydrogen in an Ionizing Plasma," tech. rep., 2001.

[83] J. Huang, S. Lisgo, and G. Maddison, "Analysis of fuel retention on MAST by global gas balance," *Plasma Physics and Controlled Fusion*, vol. 52, p. 075012, July 2010.

[84] J. Mandrekas, "GTNEUT: A code for the calculation of neutral particle transport in plasmas based on the Transmission and Escape Probability method," *Computer Physics Communications*, vol. 161, pp. 36–64, Aug. 2004.

[85] R. Janev, W. Langer, K. Evans, and D. Post, *Elementary Processes in Hydrogen-Helium Plasmas, Cross Sections and Reaction Rate Coefficients*. 1987.

[86] A. Kirk, T. O'Gorman, S. Saarelma, R. Scannell, and H. R. Wilson, "A comparison of H-mode pedestal characteristics in MAST as a function of magnetic configuration and ELM type," *Plasma Physics and Controlled Fusion*, vol. 51, p. 065016, June 2009.

[87] J. Storrs, J. Dowling, G. Counsell, and G. Mcardle, "Real-time optical plasma edge detection and position control on MAST," *Fusion Engineering and Design*, vol. 81, pp. 1841–1845, July 2006.

[88] R. S. Freund, J. A. Schiavone, and H. M. Crosswhite, "The electronic spectrum and energy levels of the Deuterium molecule," *Journal of Physical and Chemical Reference Data*, vol. 14, no. 1, p. 235, 1985.

[89] G. Nave, S. Johannson, R. Learner, A. Thorne, and J. Brault, "A new multiplet table for Fe I," *The Astrophysical Journal supplement series*, vol. 94, no. 1, pp. 221–459, 1994.

[90] Y. Ralchenko, A. E. Kramida, and J. Reader, "NIST Atomic Spectra Database (version 4.0) [online]," 2010.

[91] N. J. Conway, M. F. M. De Bock, C. A. Michael, M. J. Walsh, P. G. Carolan, N. C. Hawkes, E. Rachlew, J. F. G. McCone, S. Shibaev, and G. Wearing, "The MAST motional Stark effect diagnostic.," *The Review of scientific instruments*, vol. 81, p. 10D738, Oct. 2010.

[92] C. Markwardt, "Non-Linear Least Squares Fitting in IDL with MPFIT," in *Astronomical Data Analysis Software and Systems XVIII (ASP Conference Series, Vol. 411)*, pp. 251–254, 2008.

[93] W. H. Press, B. P. Flannery, S. A. Teukolsky, and W. T. Vetterling, *Numerical Recipes in C*. 1998.

[94] R. C. Isler, "A Review of Charge-Exchange Spectroscopy and Applications to Fusion Plasmas," *Physica Scripta*, vol. 35, pp. 650–661, May 1987.

[95] H. Kuhn, *Atomic Spectra*. 1962.

[96] A. Blom and C. Jupen, "Parametrization of the Zeeman effect for hydrogen-like spectra in high-temperature plasmas," *Plasma Physics and Controlled Fusion*, vol. 44, pp. 1229–1241, July 2002.

[97] W. L. Wiese and J. R. Fuhr, "Accurate Atomic Transition Probabilities for Hydrogen, Helium, and Lithium," *Journal of Physical and Chemical Reference Data*, vol. 38, p. 565, 2009.

[98] H. Griem, *Spectral line broadening by plasmas*. 1974.

[99] R. E. Bell and E. J. Synakowski, "New Understanding of Poloidal Rotation Measurements in a Tokamak Plasma," Tech. Rep. May, 2000.

[100] R. Scannell, D. Dickinson, A. Kirk, C. M. Roach, and S. Saarelma, "Evolution of the edge pressure gradient during the ELM cycle on MAST," in *38th EPS Conference on Plasma Physics proceeedings*, pp. 3–4, 2011.

[101] T. Pütterich, E. Wolfrum, R. Dux, and C. Maggi, "Evidence for Strong Inversed Shear of Toroidal Rotation at the Edge-Transport Barrier in the ASDEX Upgrade," *Physical Review Letters*, vol. 102, pp. 1–4, Jan. 2009.

[102] L. Lao, H. St John, R. Stambaugh, A. Kellman, and W. Pfeiffer, "Reconstruction of current profile parameters and plasma shapes in tokamaks," *Nuclear Fusion*, vol. 25, no. 11, p. 1611, 1985.

[103] CEDRATTechnologies, *Piezo actuators and electronics catalogue.* 2005.

[104] M. Johns, "PA-100 Leveraged piezo-electric actuator," 2011.

[105] C. H. Henager and W. T. Pawlewicz, "Thermal conductivities of thin, sputtered optical films," *Applied Optics*, vol. 32, pp. 91–101, 1993.

[106] P. Terry, "Suppression of turbulence and transport by sheared flow," *Reviews of Modern Physics*, vol. 72, pp. 109–165, Jan. 2000.

[107] J. DeGrassie, R. Groebner, K. Burrell, and W. Solomon, "Intrinsic toroidal velocity near the edge of DIII-D H-mode plasmas," *Nuclear Fusion*, vol. 49, p. 085020, Aug. 2009.

[108] G. Xu, V. Naulin, B. Wan, H. Guo, W. Zhang, J. Chang, N. Yan, S. Ding, L. Zhang, L. Wang, S. Liu, P. Liu, M. Jiang, H. Wang, J. Rasmussen, A. Nielsen, C. Xiao, X. Gao, L. Hu, S. Zhu, Z. Wu, J. Qian, and X. Gong, "A Dip Structure in the Intrinsic Toroidal Rotation Near the Edge of the Ohmic Plasmas in EAST," *Plasma Science and Technology*, vol. 13, no. 4, p. 397, 2011.

[109] S. K. Erents, A. Chankin, G. F. Matthews, and P. Stangeby, "Parallel flow in the JET scrape-off layer," *Plasma Physics and Controlled Fusion*, vol. 42, pp. 905–915, 2000.

[110] A. Chankin, J. Coad, G. Corrigan, S. Davies, S. Erents, H. Guo, G. Matthews, G. Radford, J. Spence, P. Stangeby, and A. Taroni, "Modelling of SOL Flows and

Target Asymmetries in JET Field Reversal Experiments with EDGE2D Code," *Contributions to Plasma Physics*, vol. 40, pp. 288–294, June 2000.

[111] P. Stangeby, "A tutorial on some basic aspects of divertor physics," *Plasma Physics and Controlled Fusion*, vol. 42, p. 271, 2000.

[112] N. Asakura, S. Sakurai, N. Hosogane, M. Shimada, K. Itami, Y. Koide, and O. Naito, "Heat and particle transport of SOL and divertor plasmas in the W shaped divertor on JT-60U," *Nuclear Fusion*, vol. 39, no. 11, pp. 1983–1994, 1999.

[113] R. Groebner and T. Carlstrom, "Critical edge parameters for H-mode transition in DIII-D," *Plasma Physics and Controlled Fusion*, vol. 40, pp. 673–677, 1998.

[114] T. W. Versloot, P. C. de Vries, C. Giroud, M. Brix, M. G. von Hellermann, P. J. Lomas, D. Moulton, M. O. Mullane, I. M. Nunes, a. Salmi, T. Tala, I. Voitsekhovitch, and K.-D. Zastrow, "Momentum losses by charge exchange with neutral particles in H-mode discharges at JET," *Plasma Physics and Controlled Fusion*, vol. 53, p. 065017, June 2011.

[115] C. F. Maggi, L. D. Horton, and H. P. Summers, "The effect of charge exchange with neutral deuterium on carbon emission in JET divertor plasmas," *Plasma Physics and Controlled Fusion*, vol. 42, pp. 669–700, 2000.

[116] R. Hawryluk, "An empirical approach to tokamak transport," tech. rep., 1980.

[117] R. Goldston, "Basic physical processes of toroidal fusion plasmas," in *Proceedings of Course and Workshop, Varenna*, p. 165, 1985.

[118] D. Van Eester, "http://iter.rma.ac.be/en/physics/tokamak/index.php (Accessed 01/09/11)," 2011.

[119] G. Kagan and P. J. Catto, "Arbitrary poloidal gyroradius effects in tokamak pedestals and transport barriers," *Plasma Physics and Controlled Fusion*, vol. 50, p. 085010, Aug. 2008.

[120] P. J. Catto and R. D. Hazeltine, "Isothermal tokamak," *Physics of Plasmas*, vol. 13, no. 12, p. 122508, 2006.

[121] W. Mandl, K. Burrell, R. Groebner, J. Kim, R. P. Seraydarian, M. R. Wade, and J. T. Scoville, "Ion edge temperature behaviour using CER spectroscopy at DIII-D," *Nuclear Fusion*, vol. 35, no. 3, p. 347, 1995.

[122] O. Sauter, C. Angioni, and Y. R. Lin-Liu, "Neoclassical conductivity and bootstrap current formulas for general axisymmetric equilibria and arbitrary collisionality regime," *Physics of Plasmas*, vol. 6, no. 7, p. 2834, 1999.

[123] M. Kočan, J. P. Gunn, J.-Y. Pascal, G. Bonhomme, C. Fenzi, E. Gauthier, and J.-L. Segui, "Edge ion-to-electron temperature ratio in the Tore Supra tokamak," *Plasma Physics and Controlled Fusion*, vol. 50, p. 125009, Dec. 2008.

[124] P. Balan, R. Schrittwieser, J. Adámek, O. Baina, P. D. Beule, I. uran, J. P. Gunn, R. Hrach, M. Hron, C. Ioni, E. Martines, R. Pánek, J. Stöckel, G. V. D. Berge, G. V. Oost, T. V. Rompuy, and M. Vicher, "Measurements of the Parallel and Perpendicular Ion Temperatures by Means of an Ion-sensitive Segmented Tunnel Probe," *Contributions to Plasma Physics*, vol. 44, no. 7-8, pp. 683–688, 2004.

[125] J. P. Gunn, R. Schrittwieser, P. Balan, C. Ionita, J. Stockel, J. Adamek, I. Duran, M. Hron, R. Panek, O. Barina, R. Hrach, M. Vicher, G. Van Oost, T. Van Rompuy, and E. Martines, "Tunnel probes for measurements of the electron and ion temperature in fusion plasmas," *Review of Scientific Instruments*, vol. 75, no. 10, p. 4328, 2004.

[126] H. Y. Guo, G. F. Matthews, S. J. Davies, S. K. Erents, L. D. Horton, R. D. Monk, and P. C. Stangeby, "Ion Temperature Measurements in JET Boundary Plasmas Using a Retarding Field Analyser," *Contributions to Plasma Physics*, vol. 36, pp. 81–86, 1996.

[127] R. A. Pitts, R. Chavan, S. J. Davies, S. K. Erents, G. Kaveney, G. F. Matthews, G. Neill, J. E. Vince, and I. Duran, "Retarding field energy analyzer for the JET plasma boundary," *Review of Scientific Instruments*, vol. 74, no. 11, p. 4644, 2003.

[128] P. Tamain, M. Kočan, J. Gunn, A. Kirk, J.-Y. Pascal, and M. Price, "Ion energy measurements in the scrape-off layer of MAST using a Retarding Field Analyzer (in press)," *Journal of Nuclear Materials*, Dec. 2010.

[129] P. Stangeby, *The plasma boundary of magnetic fusion devices*. 2000.

[130] W. A. Houlberg, K. C. Shaing, S. P. Hirshman, and M. C. Zarnstorff, "Bootstrap current and neoclassical transport in tokamaks of arbitrary collisionality and aspect ratio," *Physics of Plasmas*, vol. 4, no. 9, p. 3230, 1997.

[131] F. Maessen and J. Tielrooij, "Dispersion of grating monochromators," *Journal of Analytical Chemistry*, vol. 323, no. 5, p. 490, 1985.